Dennis Johannes Wouter Belleter

Control of Underactuated Marine Vehicles in the Presence of Environmental Disturbances

Thesis for the degree of philosophiae doctor
Trondheim, August 2016

Norwegian University of Science and Technology
Faculty of Information Technology, Mathematics and Electrical Engineering
Department of Engineering Cybernetics

NTNU – Trondheim
Norwegian University of
Science and Technology

NTNU
Norwegian University of Science and Technology

Thesis for the degree of philosophiae doctor

Faculty of Information Technology, Mathematics and Electrical Engineering
Department of Engineering Cybernetics

ISBN 978-82-326-2014-2 (printed version)
ISBN 978-82-326-2015-9 (electronic version)
ISSN 1503-8181
2016-17-W

Doctoral theses at NTNU, 2016:337

Printed by

To my parents and brother

Summary

This thesis presents several topics on the subject of controlling underactuated marine vessels and the rejection of environmental disturbances.

To address disturbances caused by waves, an observer is introduced for the wave encounter frequency. To estimate the wave encounter frequency we utilise an estimator intended to estimate the frequency of sinusoidal signals. The estimator is used to estimate the frequency of motion signals of the ship which are directly related to the wave encounter frequency and are sinusoidal in nature, e.g. the roll angle and pitch angle of the ship. Consequently, no model of the ship is required. The frequency estimator is equipped with a gain-switching mechanism to assure good performance in situations of high and low excitation. It is shown that when applied to sinusoidal signals with a time-varying, amplitude the frequency estimation error of the filter equipped with a gain switching-mechanism is globally exponentially stable. The theoretical results are verified using experimental data. The frequency estimator is applied to data from several towing tank tests and data gathered during an Atlantic passage of a container ship. To assess the performance of the filter, the frequency estimate is compared to the peak of a frequency spectrum of the data that is created using fast Fourier transform frequency spectral analysis.

The next part of the thesis is concerned with multi-agent control strategies of marine vessels. In this part results are presented to achieve coordinated path-following of underactuated marine vehicles in the presence of unknown constant ocean currents. Both marine surface vessels and autonomous underwater vehicles are considered. The vehicles are individually guided to the path using an integral line-of-sight guidance law to reject the ocean current disturbances. To achieve coordination, the vehicles communicate their along-path distance. The along-path distance is used in a decentralised coordination law to achieve the desired along-path distances between the vehicles. The theoretical results are verified using numerical simulations and experimental results with three autonomous underwater vehicles.

A coordinated control strategy based on leader-follower synchronisation is also presented for underactuated marine surface vessels. This strategy is based on a constant bearing guidance algorithm from the marine system literature. First we show that the guidance algorithm is semi-globally exponentially stable and give explicit bounds on the solution. We then analyse the synchronisation properties using the constant bearing guidance when it is used on curved trajectories rather then the straight lines it is designed for. From an analysis of the guidance in closed loop with a heading and velocity controller we show that on curved trajectories the

synchronisation errors between leader and follower are integral input-to-state stable when the sway velocity is considered as a disturbance input to the synchronisation error dynamics. The theoretical results are verified using numerical simulations.

The third part first presents two strategies to follow curved paths in the presence of unknown constant ocean currents. In both strategies the paths are parametrised by a path variable that is used to propagate a path-tangential reference frame. In one strategy the frame is propagated to makes sure the vessel stays on the normal of the path tangential reference frame. This results in a singularity in the update law and make the strategy only usable locally. In the other strategy a parametrisation is used that is globally valid. An appropriate guidance law is defined for both parametrisations. The controllers use the input from the guidance law and from an ocean current observer to reject the ocean current and converge to the path. The closed-system with the controllers and observer is analysed and it is shown that the path-following errors are globally asymptotically stable. The theoretical results are verified using numerical simulations.

A novel curved path-following strategy that does not require parametrisation of the path is also presented in the third part of the thesis. This strategy is based on principles from geometric control and hierarchical control design. In this strategy the path is defined implicitly as a manifold of the state space. It is shown that using three geometric objects, i.e. the normal to the path, the tangent to the path, and the curvature of the path, we can define controllers that make the manifold that describes the path asymptotically stable. The theoretical results are verified using numerical simulation. This work does not consider environmental disturbances.

Contents

List of figures

List of tables

Preface

This thesis is submitted in partial fulfilment of the requirements for the degree of philosophiae doctor (PhD) at the Norwegian University of Science and Technology (NTNU). The work has been carried out at the department of Engineering Cybernetics and the Center for Autonomous Marine Operations and System (AMOS). My main supervisor has been Professor Kristin Ytterstad Pettersen and my co-supervisors have been Professor Asgeir Sørensen from the Marine Technology department and Professor Henk Nijmeijer from the department of Mechanical Engineering at the Eindhoven University of Technology.

Acknowledgement

I would first of all like to thank Professor Kristin Ytterstad Pettersen for giving me the opportunity to pursue the PhD-degree in her group. She has been a great supervisor and I could not have completed this process without her support and guidance throughout the process. The inspiration and motivation from her positive attitude and her advice during our meetings has helped lift this work to a higher level. I would also like to thank my co-supervisor Professor Asgeir Sørensen for making his time available to me, for his motivational talks at AMOS events, and for urging the PhDs in AMOS to discuss as much as possible, which gave us all valuable insights. I would also like to thank my other co-supervisor Professor Henk Nijmeijer, who has supported me both during my Master's education in Eindhoven and during the process of pursuing the PhD-degree. He has always made time for me despite of his busy schedule and has given me valuable advice and feedback throughout my career. It is also thanks to Professor Henk Nijmeijer that I first came to Trondheim during my Master's education in the Fall of 2011 for an internship with Professor Thor Inge Fossen. Without this internship I would have never got to know the research environment and the people that inspired me to return. Moreover, Professor Nijmeijer was willing to receive me in Eindhoven for a period during the PhD where I got to work with Erjen Lefeber. I would like to thank Erjen Lefeber for the inspiring brainstorming sessions and for making time for me in his busy schedule. Hopefully, the results of our joint work will be completed soon.

During this work I also had the good fortune to meet more great people to work with and I would like to take the opportunity to also thank them for their contributions to this work. I would like to thank Professor Thor Inge Fossen who first gave me the aforementioned internship in 2011, was willing to co-supervise the graduation project of my Master's education, and continued to work with me on

the topic of wave frequency estimation during the first part of the PhD project. For this I would also like to thank Dominik Breu, who during the process of pursuing his PhD-degree under supervision of Professor Fossen, made time to support me during my first attempts at doing research. I would also like to thank Roberto Galeazzi from the Technical University Denmark for his involvement in extending the work on wave frequency estimation and providing experimental data. I would like to thank Professor Randal Beard for welcoming me for Brigham Young University in Utah for two weeks for an inspirational visit. I am also grateful for the opportunity to do experiments with underwater vehicles from the group of Professor João Sousa at the University of Porto. I would like to extend these thanks to the whole group at the underwater systems and technology laboratory (LSTS) and in particular José Braga who has helped me get the code ready and perform the experiments. I would like to thank Professor Manfredi Maggiore from the University of Toronto, who inspired me with his excellent scientific advice and positive attitude during the two times he visited our group in Trondheim. The discussions we had, have led to some joint work that is a great asset to this thesis. I would also like to thank Mohamed Maghenem who has visited our department to work with us. His cheerful personality, his great work drive, and theoretical understanding has allowed us to do some great work in a short time.

I would like to thank all of my current and former colleagues at AMOS and at the department of Engineering Cybernetics. You have all attributed to creating a great working environment over the past three years. I would like to thank you all for the coffee and lunch breaks, parties, and the pleasant conversations and discussions we have had over the years. The list of incredible people I have met and friends I have made would be too long to be contained here, but I would especially like to thank Claudio Paliotta and Albert Sans Muntadas who have had the biggest impact on my daily life in Trondheim and who have not only been great colleagues but I am proud to call them friends. Claudio has been the best office mate anyone could have. Our discussions and the joint work we have done have been a great asset to this thesis and his encouraging words helped to keep me motivated even when confronted with setbacks. I will always remember the daily coffee breaks with Claudio, Albert, and others in which we shared many jokes, and the conversations ranged from the most trivial things, to us trying to solve global problems. Their interesting perspectives have given me new perspectives on many things that I will always take with me.

During my time at the university I had support from the administrative personnel both at AMOS and at the department of Engineering Cybernetics and I would like to thank them for allow everything to operate in the smooth way it does. Moreover, I would like to thank the organisers and everybody that participated in the cageball games every week on Friday and I am sorry for missing so many of them during the last part of the project.

I would also like to thank my family and friends in the Netherlands, who have supported me during my time abroad and have always made me feel most welcome when I came back home. It is a great feeling that when you get home you are able to pick things up as if you have never left in the first place.

Last but not least, I would like to thank my parents Wout and Lisette and my brother Joey for their love and support. I thank them for supporting me during

everything I have done in my life and for stimulating me to do my best at everything I undertake. I thank my parents for raising me and my brother with the values that they did, for always setting a great example, and for the sacrifices they have made to help us achieve our goals.

Chapter 1

Introduction

This thesis considers the control of underactuated marine vehicles in the presence of environmental disturbances. The thesis is divided into three parts. The first part considers modelling of marine vehicles in the presence of environmental disturbances. The second part considers multi-vehicle path-following approaches. The third part considers curved path following for underactuated vehicles.

1.1 Background and Motivation

This section gives the background information and motivation of the topics considered in the thesis. Moreover, it gives an overview of previous works on these topics. The different parts of the thesis are considered separately in three subsections.

1.1.1 Modelling of Marine Vehicles and Environmental Disturbances

As in many fields of technology, and especially robotics, the need for increased autonomy and intelligent control systems has also increased in the control of marine vehicles. Although nowadays almost all commercial ships are equipped with GPS based navigational systems, radar systems, guidance autopilots, and speed controllers, the introduction of autonomous and unmanned vehicles have increased the need for further development. The introduction of these systems with increased autonomy has both economical and practical motives. In particular, increased autonomy can make operations more efficient and thereby decrease the time a vessel and crew need to be out at sea, and thus reduce operational costs. Moreover, for underwater operations with remotely operated vehicles (ROVs) that require a tether connection to a support ship, can be replaced by autonomous vehicles that do not require a tether. This allows for more freedom of motion and reduces the amount of support needed and thereby reducing costs. Moreover, unmanned operations in hostile environments and for dangerous tasks, e.g. mine detection and sweeping, can greatly improve safety.

Autonomous marine vehicles can be subdiveded in two main catergories: autonomous surface vessels (ASVs) and autonomous underwater vehicles (AUVs).

Both ASVs and AUVs need to be able to operate without operator intervention. This implies that they should be equipped with control systems that can actively attenuate the environmental disturbances that affect them during their operations. To develop these control systems, mathematical models of both the vehicle and the disturbances are required. The type of model used depends on the desired control purposes and the operation conditions. Based on the operational conditions the mathematical models can be subdivided into low velocity models and higher velocity models. Low velocity models are used for station keeping and dynamic positioning where the vessel is required to remain at a desired fixed position, and higher velocity models are used for manoeuvring applications such as path following [60]. Moreover, the complexity of the model should also depend on the purpose of the model. In Sørensen [131], two main categories are defined. The first being control plant models which give a simplified mathematical description containing only the main physical properties of the plant, and which is suitable for control design purposes and theoretical analysis. The second category consists of process plant models which give a comprehensive description of the actual process and should be as detailed as needed, and which are suited for high-fidelity simulations and robustness analysis.

When modelling disturbances, the complexity of the model should also depend on the application of the model. The model should capture the effects of the disturbances that affect the control system most. For the control of marine vehicles three types of disturbances play a role, i.e. ocean currents, wave disturbances, and wind disturbances.

When studying the effect of ocean currents on path-following control strategies for marine vehicles, it is a widely accepted practice to model them as a constant drift force. This captures the behaviour of an irrotational constant ocean current which for the purpose of control design is a good approximation for a slowly time-varying disturbance [60].

When considering wave disturbances the effects can be separated into first-order and second-order effects [60]. The first-order wave-induced forces cause wave-frequency induced motion and are observed as zero-mean oscillatory motions. The second-order wave-induced forces are wave drift forces that are observed as nonzero slowly varying components. These two types of forces have to be taken into account differently by the control system. The second-order wave-induced forces cause a drift force similar to the ocean current and can be lumped together with the ocean current drift in the model. The first-order wave-induced forces cause zero-mean oscillatory motions that should not be compensated for by the vehicles actuators since this would cause oscillations in the ship's propulsion and rudder system, something which is undesirable. Therefore, these motions should be removed from from the feedback controllers, something which is usually done by filtering out the oscillations by using a cascaded notch and low-pass filter [60]. This process is usually referred to as wave filtering. This requires knowledge of the wave frequency to determine the pole placement of the notch frequency. In the case of a moving vessel, a Doppler shift of the wave frequency should be taken into account. The Doppler shifted frequency that is experienced by the ship is called the wave encounter frequency.

Wind disturbances also have a constant and a non-constant effect. The con-

stant effects of wind disturbances are often modelled as having a constant pressure and direction [60]. This pressure and direction cause forces and moments on the vessel depending on its exposed surface area, its direction with respect to the wind direction, and load condition coefficients that can be obtained from wind tunnel tests. The non-constant effects of wind disturbances, e.g. wind gusts, should not be compensated for by the propulsion system to avoid frequent control action. These effects are often removed from the control system by filtering, and moreover, for larger vessels are often attenuated by the inertia of the vessels. For small autonomous surface vehicles and autonomous underwater vehicles at the surface, the area exposed to wind is small and the effect of wind disturbances is less than that of the drift forces caused by ocean currents.

1.1.2 Multi-Vehicle Path Following

This part is concerned with multi-vehicle path following for underactuated marine vessels. Multi-vehicle systems, or more generally multi-agent systems, have attracted a lot of attention from the research community, see for instance Bai et al. [10], Kumar et al. [83] , and Pettersen et al. [117] and the references therein.

A lot of the work in the multi-agent systems literature has focused on consensus and agreements protocols. The goal of these works is to derive theoretical conditions for synchronisation of states between systems, e.g. to achieve a common velocity or a desired inter-agent distance. To achieve synchronisation, communication between agents is required. Powerful tools to model this type of communication and to analyse the synchronisation behaviour can be found in the literature of algebraic graph theory, see for instance Mesbahi and Egerstedt [98] and Godcil and Royle [68]. Algebraic graph theory can be used to model multi-agent systems as a set of vertices (the agents) which are connected by a set of edges (the communication channels). Synchronisation can be achieved depending on the topology of the network, that is, if the network satisfies certain properties to allow the information to spread to all agents. More advanced works dealing with consensus can be found for instance in Moreau [101] and Moreau [102] in which time delays are also taken into account using set based stabilisation of the consensus dynamics. Work on dynamic graphs can be found in Lin et al. [92]. For a survey on consensus problems see Ren et al. [121].

These theoretical works have found applications to more practically motivated studies of formation control and cooperative/coordinated motion of robotic systems. Multi-agent systems can offer several advantages over operations with single robot systems. When using multiple robots a lot of tasks can be executed more time effectively. This especially hold for spatially distributed tasks since multiple robots can cover a larger area, but also having multiple robots to execute tasks in parallel or together increases this efficiency. Moreover, multiple robots can take over tasks of more complex and costly single robots and can introduce some redundancy for operations in harsh environments. In particular, if a vehicle malfunctions or is lost in a sub-sea environment or under the Arctic, repairing or recovering the robot can be difficult or impossible, making redundancy desirable to continue operations.

One of the fields for the applications that has received a lot of interest from the research community is formation control. Comprehensive reviews of the literature

in this field are given in Chen and Wang [44] and Oh et al. [108]. Formation control strategies aim to drive agents to adhere to prescribed constraints on their states. Usually this includes a desired relative inter-agent distance such that the vehicles achieve a formation. This goal can be achieved in different ways. The choice for one of the different methods is often motivated by the constraints of the vehicles and their inter-agent communication capacities and the intended application for the formation. Four major research directions within the formation control field are

1. Leader-follower synchronisation
2. Virtual structure approach
3. Behaviour-based approach
4. Coordinated path following

In the following a sample of the wide range of literature available in each of these fields is given. Some references from applications in other fields of robotics are provided followed by a review of works in the marine systems literature.

Leader-follower synchronisation is conceptually one of the simplest strategies for formation control. This is a hierarchical formation control approach in which there is a leader and there are followers. Due to this hierarchical approach it is sometimes also referred to as master-slave synchronisation. The leader can be allowed to move freely or has the task to follow a certain path or trajectory. However, the leader does not carry any responsibility for the achievement of the formation. This responsibility falls on the followers, which have the task to control their inter-agent position and/or orientation with respect to the leader to a desired value. The advantage of the leader-follower structure is that only local information needs to be used to achieve the formation. The disadvantages is that there is limited fault tolerance. In particular, if the leader fails the entire formation breaks down, and if one or more of the followers fail the leader does not change its behaviour accordingly and the formation breaks down. A special form of leader-follower formation control is the one-to-one communication formation control, where each vehicle only receives information from one vehicle, its leader, and sends information to only one vehicle, its follower. Leader-follower behaviour can also be used to steer the coordination between groups of agents to provide a common reference. This is one of the cases considered in the seminal work of Jadbabaie et al. [78].

Leader-follower synchronisation is widely applied for coordinated control applications. Applications include master-slave synchronisation of robot manipulators of which an in-depth treatment is given in Nijmeijer and Rodriguez-Angeles [106]. In Nijmeijer and Rodriguez-Angeles [106] several output-feedback schemes are given for synchronisation of fully actuated Euler-Lagrange systems representing robot manipulators with both rigid and flexible joints. Moreover, a scheme for mutual synchronisation is given. Leader-follower synchronisation for control of mobile robots is studied in Desai et al. [47] which focuses on cases of synchronising the distance with respect to multiple leaders and the case of synchronising the distance and orientation with respect to one leader. This approach is extended in Desai et al. [48] to allow for changing formations. In Dasdemir and Loria [46] the case of one-to-one communication is investigated to build up a formation of mobile robots

along straight-line paths. One-to-one communication is also investigated in Poonawala et al. [118] in which an estimator is used to find the leader's velocity and only position measurements are used for synchronisation. In Aguirre [3] leader-follower synchronisation is investigated for mobile robots connected over a network which induces a delay in the communication. Theoretical results are presented and these are verified with experiments. A strategy for leader-follower based formations for unmanned aerial vehicles can be found in Stipanović et al. [132], in which several leader-follower strings are combined by selecting a common leader to build up a formation.

Leader-follower synchronisation for marine vessels is considered in Breivik et al. [36], in which a leader-follower scheme for fully actuated marine vessels is presented that can be used both in a centralised and a decentralised control strategy. In the marine systems literature work on leader-follower synchronisation has played an important part in research on underway replenishment of ships, see for instance Fu and Haddad [65], Kyrkjebø et al. [85], and Skejic et al. [125]. For these operations the supply-ship is usually responsible for synchronising its motion with the ship it is supplying. In Kyrkjebø et al. [85] the case of a fully actuated follower that synchronises its output with a leader with unknown dynamics is investigated. An observer-controller scheme is utilised to achieve synchronisation where the observers are used to estimate the unknown velocities of the leader and follower. The observer-controller scheme utilised in Kyrkjebø et al. [85] is based on the theory for master-slave synchronisation of robotic manipulators investigated in Nijmeijer and Rodriguez-Angeles [106]. In Skejic et al. [125] the focus is on the interaction forces between two vessels during underway replenishment operations. For control purposes the constant bearing guidance algorithm from Breivik and Fossen [35] is used to synchronise the ships along a straight-line path. The vessels are underactuated, but no analysis of the underactuated internal dynamics are given. In Fu and Haddad [65] underway replenishment between fully actuated vessels is investigated and adaptive backstepping controllers are designed to reject exogenous disturbances. In Peng et al. [114] formation control of underactuated vessels under the influence of constant disturbances is considered using neural network adaptive dynamic surface control in a leader-follower scheme.

In the virtual structure approach the goal is for the individual vehicles to converge to different points of a virtual structure. The virtual structure is usually a geometrically-rigid object that defines the shape of the formation. Consequently, when each vehicle is at its desired point on the virtual structure the vehicles are in formation. Using this approach it is very straightforward to describe the desired overall behaviour of the formation by appropriately designing the virtual structure and its motion. The virtual structure approach was first proposed in Tan and Lewis [134] and Lewis and Tan [90]. The controllers are usually derived in three steps. In the first step the virtual structure is defined. In the second step the desired motion of the virtual structure is translated to the desired motion of individual vehicles. In the third step tracking controllers are defined for the individual vehicles to follow the desired motion designed in the second step. An optional fourth step can be added in which each of the vehicles provides feedback to the virtual structure and the motion can be adjusted if necessary. This fourth step is called formation feedback. In Tan and Lewis [134] and Lewis and Tan [90], the concept of a virtual

structure is introduced and the proposed methodology is verified using simulations and experiments for a mobile robot platform. Moreover, it is shown that the virtual structure can be used bi-directionally to add fault tolerance, i.e. the motion of the virtual structure can be adjusted based on limitations of the vehicles. However, no stability guarantees are given for the formation. Stability guarantees for the formation using a virtual structure were given in Beard et al. [12], in which a unified control architecture is presented for the control of a formation of spacecraft. The architecture includes a virtual structure but also utilises ideas from leader-follower formation control and the behaviour-based approach. The disadvantage of this architecture is however that formation feedback is not included. The work of Lewis and Tan [90] and Beard et al. [12] is combined in Young et al. [139] which presents a virtual structure approach with stability guarantees for a mobile robot platform that also allows for formation feedback. These ideas are further developed in Ren and Beard [120] where an extension is made that allows for a decentralised implementation. Based on the idea of a virtual structure with formation feedback an application of an output feedback scheme for mobile robots with a dynamic model is investigated in Do and Pan [52]. For marine systems a virtual structure is used in the work of Skjetne et al. [127]. The approach uses a centralised control law to control the formation that generates inputs for the decentralised controllers of the vessels to achieve and maintain their position in the formation. This approach is decentralised and validated experimentally in Ihle et al. [73]. Another decentralised approach for marine surface vessels is developed in Ihle et al. [75], in which the virtual structure is modelled as a set of mechanical constraints on the vehicles using Lagrangian mechanics. The reaction forces generated from violating these constraints are then used to control each vessel to keep the formation.

In the behaviour-based approach several behaviours are prescribed for the agents. The control action is then typically a weighted average of the control action for each behaviour of individual agents and the group as a whole. Different behaviours can include collision avoidance, obstacle avoidance, goal keeping, and formation keeping. This type of averaging of the behaviours makes the resulting behaviour unpredictable and makes it difficult to describe desired formation behaviour and to show stability. An advantage however is that the averaging of behaviours within the group introduces formation feedback in a straightforward manner. These approaches have their origins in studies aiming to recreate behavioural studies of animals such as flocking and the behaviour of herds and schools. One of the first works to reproduce such behaviour using computer simulations is Reynolds [122]. This type of formation control is still widely used when recreating animal behaviour, since this is often a process of consensus that is not steered by a desired reference. This biologically inspired type of interaction amongst neighbours is shown Vicsek et al. [137] to achieve common behaviour using numerical simulations. The work in Vicsek et al. [137] inspired [78] to perform the first mathematical analysis of these types of interactions and provide conditions for convergence of such strategies based on nearest-neighbour communication. An early application for mobile robots of the behaviour-based approach is found in Balch and Arkin [11], in which the generated behaviour is analysed using simulations and experiments. Later works have focused on finding theoretical proofs for different types of behaviour based on specific types of interaction rules, see for instance Olfati-Saber

[109] and Tanner et al. [135]. An application for marine vessels can be found in Arrichiello et al. [9] in which different tasks, i.e. obstacle avoidance and keeping a formation, are weighted against each other based on priorities.

Coordinated path following is a two-fold approach to formation control. That is, a path is assigned to each vehicle individually. The vehicle is individually responsible to follow this path. The formation is then achieved by coordinating the motion of the vehicles among their given paths. This allows for decentralised approaches in which only minimal information such as inter-agent distances need to be communicated. This type of formation control is best suited for formation control along straight-lines and identical parallel curved paths since when vehicles are on different curved paths it is non-trivial to find a suitable metric of inter-agent distance to synchronise the vehicles' positions. Therefore, this problem is mainly investigated in the marine systems literature since these types of paths are common trajectories in the marine systems literature.

In [88] path following of two underwater vehicles is investigated. The vehicles follow parallel paths, whilst achieving and maintaining a desired along-path distance. Similar results can be found in Børhaug et al. [28] for surface vessels and Børhaug et al. [29] for underwater vehicles. The work from Børhaug et al. [28] is extended in Børhaug et al. [31] to include a thorough study of the coordination dynamics using techniques from graph theory. The work in [88] is a simplified version of this problem where one of the vehicles is responsible for coordinating the inter-agent distances along the path which results in a leader-follower type coordinated path following. The work in Børhaug et al. [31] is analysed for a much wider range of communication topologies. The work in Ghabcheloo et al. [66] and Ghabcheloo et al. [67] considers coordinated path following in the presence of communication failures and time delays. In Ghabcheloo et al. [66] and Ghabcheloo et al. [67] the individual vehicles converge to a virtual target on the path to achieve path following. The motion of these virtual targets is then adjusted around their common nominal value based on their relative distances, to achieve coordination of the virtual targets and indirectly of the vehicles. In all the formation control approaches discussed above the effects of ocean currents are not taken into account. Ocean current are considered in, for instance, Almeida et al. [4] and Ihle et al. [76]. However these works consider fully actuated marine vehicles. In Almeida et al. [4] backstepping based controllers are derived for path following while coordination along the paths is performed using measurements of the inter-agent distances between vehicles. In Ihle et al. [76] a path-following approach is used that is shown to satisfy passivity properties. This passive path-following strategy is combined with a coordination law that is also passive, which results in a passive closed-loop system. In [38] line-of-sight (LOS) path-following with a conditional integrator is used for path following under the influence of unknown disturbances. However, the coordination dynamics are not analysed in this work.

1.1.3 Curved Path Following for Underactuated Marine Vessels

This part is concerned with curved path-following for underactuated marine vessels. While the literature for straight-line path following of underactuated marine vessels is, by now, well established even in the presence of unknown disturbances, the

literature for curved paths is much less rich and has some caveats. This is due to the complexity caused by the underactuation which causes several necessary conditions to be satisfied. In particular, these conditions pertain to the well definedness of the controllers and boundedness of the state.

In the literature three main approaches are considered when considering control of ships along paths

1. *The path-following problem* focuses on stabilising a given path for a vehicle without any time specifications, i.e. without putting a constraint on where the vehicle needs to be on the path at a certain time.
2. *The trajectory-tracking problem* aims to let the vehicle's output track a desired time-varying output, i.e. the desired position of the vehicle is a time dependent reference, e.g. $(x_p(t), y_p(t))$.
3. *The manoeuvring problem* requires two tasks to be satisfied: a *geometric task* and a *speed assignment*. More specifically, for a θ-parametrised path the vehicle needs to track a θ dependent output, e.g. $(x_p(\theta(t)), y_p(\theta(t)))$, and one or more additional requirements such as a time assignment, speed assignment, or an acceleration assignment.

Some of these definitions have been used interchangeably in the literature by different authors. Partly because the definitions have not been established from the beginning and partly because sometimes the differences can only be subtle such that multiple cases can be argued to classify the result. In the following a review is given of some of the literature on each of the problems given above.

The problem of curved path following for underactuated marine vessels has its parallel in the field of mobile robotics. Although the nature of the underactuation between mobile robots and marine vessels are different, the powerful tools to parametrise paths and define the problem developed in the seminal works Samson [124] and Micaelli and Samson [99] can still be utilised. A solution for 2D path following based on the tools developed in [99, 124] was proposed in Encarnaçao et al. [57]. In Encarnaçao et al. [57] the path representation from Micaelli and Samson [99] is used to define the path-following problem and a solution is presented using a nonlinear controller. An observer is used to incorporate the effects of unknown, but constant ocean current. Part of the state is shown to be stable and the zero dynamics are analysed and shown to be well behaved. However, this is done under the assumption that the total speed is constant. This requires active control of the forward velocity to cancel the effect of the sideways velocity induced by turning. Moreover, the parametrisation from Micaelli and Samson [99] is only valid locally, making the path-following result only valid locally. The work in Encarnaçao et al. [57] was extended to the 3D case in Encarnaçao and Pascoal [56]. Another local result based on the parametrisation of [99, 124], is obtained in Do and Pan [49]. In this work a practical stability result is shown for the path-following states of an underactuated surface vessel in the presence of an environmental disturbance. However, a simplified model with diagonal system matrices is used and the interconnection between the total velocity and the sideways velocity is not taken into account in the analysis of the zero dynamics. In Lapierre et al. [87] and Lapierre and Soetanto [86] the work of Encarnaçao et al. [57] is extended to solve the path-following problem globally. This is done using another result first

described for the control of mobile robots in Soetanto et al. [130]. In particular, it is achieved by adapting the parametrisation of the path such that propagation of the path-tangential reference frame can be used as an extra degree of freedom in the controller design in order to avoid singularities in the parametrisation of the path. The work in [86, 87] does not consider environmental disturbances, it focuses on stabilisation of the path-following states but does not analyse the zero dynamics. A similar approach to Lapierre et al. [87] is taken in Børhaug and Pettersen [27] in which the frame is propagated differently and the controllers are also analysed in closed loop. In Børhaug and Pettersen [27] a look-ahead based steering law is used to guide the vehicle to the path. Stability of the path-following errors is shown using cascaded systems theory and the zero dynamics are analysed and shown to be well behaved. To take into account ocean currents, the work in Børhaug and Pettersen [27] is extended in Børhaug et al. [30] by adding integral action to the steering laws. However, the results in Børhaug et al. [30] are only valid for straight-line path following. The work in Børhaug et al. [30] was revisited in Caharija et al. [40] for surface vessels and Caharija et al. [41] for AUVs. Experimental results were added in Caharija et al. [43]. The works of Caharija et al. consider straight-line path following in the presence of ocean currents and reformulate the work of Børhaug et al. [30] to consider relative velocities which provide a simpler structure for controller design and a more direct control of energy expenditure. Using the model formulation based on relative velocities from Caharija et al. [40] the work of Børhaug and Pettersen [27] is extended with an ocean current observer in Moe et al. [100] for curved path-following. However, in Moe et al. [100] the zero dynamics are not analysed and the suggested input signals would contain the unknown ocean current. Another LOS guidance for path-following is presented in Fossen et al. [59]. The strategy is based on following a path made of straight-line sections connecting way points. These concepts are further developed to circles in Breivik and Fossen [32] where the vessel is regulated to the tangent of its projection on the circle. The work is extended to the three dimensional case in Breivik and Fossen [33] and Breivik and Fossen [34]. However, these works do not consider environmental disturbances.

One of the first solutions to the full-state stabilisation problem for an underactuated 3-DOF surface vessel was developed in Pettersen and Nijmeijer [115]. In this work a trajectory tracking controller is developed for a simplified model to guarantee exponential tracking. The approach is based on backstepping and the recursive design technique for systems in chained form developed in Jiang and Nijmeijer [80]. This result requires a persistently exciting (PE) yaw rate with some additional condition on the curvature of the path, which implies that the path should have a non-zero curvature, i.e. straight-lines are excluded. These limitations were partly relaxed in Pettersen and Nijmeijer [116] where only the PE condition for the yaw rate is required. The results in Pettersen and Nijmeijer [116] is extended to global exponential tracking in Lefeber et al. [89] by using a cascaded systems approach. In this work the problem is divided in two subsystem, i.e. a subsystem for the yaw control and a subsystem for the velocity control. In Jiang [79] two solutions for global trajectory tracking under the assumption of a persistently exciting yaw rate are presented. Both approaches are base on Lyapunov's direct method. The first method is a passivity-based approach which under a sufficient PE condition for the

yaw rate provides asymptotically convergent tracking errors. The second method is based on a combination of backstepping and cascaded systems theory to derive an exponentially convergent tracking controller. A solution that does not require the yaw rate to be persistently exciting is given in Do et al. [53] and extended to include point stabilisation in Do et al. [54]. Both of these works are based on a combination of backstepping and Lyapunov's direct method. In all of the aforementioned works on trajectory tracking the model was simplified. In particular, these works assume diagonal mass and damping matrices which significantly simplifies the controller design. In Do and Pan [50] nonzero off-diagonal terms in the mass and damping matrices are added and environmental disturbances were considered. This method introduced a coordinate transform to transform the dynamics back into diagonal form and then followed the same approach as previous works. Nonlinear damping terms were included in Do and Pan [51] to allow for high-speed applications. Another interesting approach can be found in Aguiar and Hespanha [1] in which a tracking controller is developed that is combined with an adaptive switching supervisory control to develop a hybrid controller. The controller guarantees global boundedness, convergence of the position tracking error to a small neighbourhood, and robustness against parametric model uncertainties.

The manoeuvring problem combines aspects of both the path-following and trajectory-tracking control problem. Its geometric task aims at stabilising a subset of the state space as is done in path-following. However, for the manoeuvring problem this is combined with a dynamic task that can prescribe a time-dependent assignments as is done in trajectory tracking, or a velocity assignment depending on the path parametrisation as is done in Do and Pan [51]. The manoeuvring problem is introduced in Skjetne et al. [126]. In Skjetne et al. [126] a recursive control design technique is developed for fully actuated nonlinear plants in vectorial strict feedback form of any relative degree. This work is extended to handle disturbances in Skjetne et al. [128]. The results of [128] are used in Skjetne et al. [129] to develop and experimentally validate a manoeuvring controller for a fully actuated model ship. In Ihle et al. [74] this work is extended to the output feedback case for fully actuated ships. Moreover, unknown environmental disturbances are included in this work.

The three problems treated above have their own set of advantages and disadvantages depending on the desired application and system under consideration. The path-following is most convenient when simply satisfying the geometric task of path following is the single most important task. In particular when the speed to travel along the path is irrelevant or if the speed assignment is independent of the velocity along the path. This is the case for instance in Børhaug and Pettersen [27] and Moe et al. [100], where the vehicle is regulated towards the path using a parametrisation of the path but the speed assignment is independent of the parametrisation. When the speed assignment, or another dynamic task, is connected to the parametrisation the problem is best treated as a manoeuvring problem. This is the case for instance in Do and Pan [51] where the parametrisation is used to generate a desired velocity of the vehicle to guarantee path following, which is an approach similar to the ones listed above in the review on the manoeuvring problem. When it is important to converge to a certain place along the path at a specific time the problem is best treated as a trajectory-tracking problem. This is for instance the case when

performing docking with a moving target or other coordinated tasks, or tasks that are time critical such as reconnaissance and search and rescue missions where the vehicle is required to be at a certain place at a certain time that is relevant to the mission.

1.2 Scope and Contributions of the Thesis

This section discusses the scope of the thesis and lists the contributions of the work. This section is divided into three subsections corresponding two the three main parts of the thesis. Within the three subsections each chapter is treated separately.

1.2.1 Modelling of Marine Vehicles and Environmental Disturbances

Part I of the thesis considers modelling of the vehicles studied in the thesis and the environmental disturbances encountered by the vehicles studied in this thesis. The different types of disturbances, i.e. ocean current and waves, and their effects on the vehicles are described.

Chapter 2 considers modelling of underactuated marine vehicles and presents a convenient way to model the effect of ocean currents on the motion of a marine vehicle. The material in this chapter is based on Fossen [60] and Caharija [39]. Two models are presented that are used in this thesis. The first model represents an underactuated surface vessel or an AUV moving in the horizontal plane. Hence, it describes planar motion and has three degrees-of-freedom (DOF), i.e. two positions and an angle. This model is used in Chapter 4 and Chapters 6-8. The second model is the model of an AUV moving in three dimensional space. This model has five degrees-of-freedom, i.e. three positions and two angles. The third angle, which is the roll angle along the longitudinal axis, is not considered since it is self-stabilising and does not influence the motion for the AUVs considered. This model is used in Chapter 5.

Chapter 3 considers wave disturbances and presents a frequency estimator that can measure the wave frequency encountered by a ship. The contribution in this chapter is the development and experimental verification of a wave frequency estimator that is designed to estimate the dominant wave frequency of a wave spectrum on-line. The frequency estimator takes motion signals, such as measurements of the pitch or roll angle, of the vessel as input. The frequency estimator is based on a filter developed in Aranovskiy et al. [8] to estimate the frequency of sinusoidal signals with fixed amplitudes. The work of Aranovskiy et al. [8] is extended to show that the origin of the estimation error is globally exponentially stable even when the amplitude is time-varying. It is shown that these stability properties hold when the estimator is equipped with a gain-switching mechanism. The gain-switching mechanism is triggered by the amplitude of the measured signal and allows the estimator to function in both situations of high excitation and low excitation. Moreover, it is shown that the theoretical results hold if a low-pass filter is added to smooth the estimates if necessary. The theoretical results derived in this chapter are then

verified using an experimental case study. The experimental verification consists of two parts. In the first part the estimator is verified using data gathered in towing tank tests using a model ship. Frequency spectra are made for the data sets gathered in the towing tank and the estimate of the filter is compared against the peaks in those spectra. In the second part the wave frequency estimator is verified using data gathered on a container ship during a passage of the Atlantic Ocean. The work in Chapter 3 is based on Belleter et al. [19] and Belleter et al. [20].

Wind disturbances are not considered in this thesis. Certain aspects of wind disturbances may be captured by the model of the ocean current. However, dynamic effects are not taken into account.

1.2.2 Multi-Vehicle Path Following

Part II consists of three chapters. Chapter 4 presents a control strategy for coordinated path following for underactuated marine vehicles in the presence of ocean currents. In this chapter integral line-of-sight guidance from Caharija et al. [40] is used to control an underactuated marine vessel to follow a straight-line path in the presence of a constant unknown ocean current. This is a task each vehicle has to satisfy individually. To achieve coordination along the paths, a coordination subsystem is added which uses measurements of the relative positions between vessels to adjust the velocity of the vessel around a nominal value common to all the vehicles, which is a coordination strategy based on the ideas in Børhaug et al. [31]. The closed loop of the path-following and coordination subsystems is then analysed using a technique from Loría [93], which allows us to consider the feedback interconnection between the two subsystems as a cascaded connection. A simulation case study with three vehicles is given to verify the results. The main contribution of this work is that it presents an approach to coordinated path following that considers underactuated vessels and ocean currents together, whereas in the previous literature results are available for both separately but not together in one framework. Chapter 5 considers a similar problem to that of Chapter 4 but for AUVs. This means that an extra subsystem is added to control the vehicle in the vertical plane. The analysis follows along the same lines of that in Chapter 4 and a simulation case study is given. Moreover, Chapter 5 presents experimental results using three light autonomous underwater vehicles (LAUVs) to verify the theoretical results. The material in Chapter 4 is based on Belleter and Pettersen [13] and Belleter and Pettersen [15]. The material in Chapter 5 is based on Belleter and Pettersen [14].

Chapter 6 considers leader-follower synchronisation along an arbitrary trajectory chosen by the leader. The underactuated follower is responsible for synchronisation with the motion of the leader. The follower uses a constant bearing guidance algorithm from Breivik et al. [37] to follow the leader. A proof is given to show that the constant bearing guidance algorithm results in USGES tracking error dynamics for which we can give an explicit bound on the error, rather than UGAS and ULES by linearisation about the origin as shown in Fossen [60] which provided no such bound. The constant bearing guidance algorithm from Breivik et al. [37] is intended for straight-line target tracking, while in this work the leader's trajectory can be arbitrary. Therefore, the remainder of the chapter analyses the closed-loop system

when the constant bearing guidance algorithm is used for curved leader trajectories. It is shown that for a straight line, synchonisation can be achieved. However, on a curved trajectory only integral input-to-state stability of the synchronisation error with respect to the sway velocity can be shown. Simulation results are given to verify the theoretical results. The material in Chapter 6 is based on Belleter and Pettersen [16] and Belleter and Pettersen [17].

1.2.3 Curved Path Following for Underactuated Marine Vessels

Inspired by the interesting dynamical effects that appeared in the application on curved paths in Chapter 6, Part III presents three approaches to curved path following for underactuated marine vehicles. Contrary to the straight-line guidance used in Chapter 6, the guidance strategies in this part are designed to overcome the difficulties encountered in Chapter 6. Three approaches are considered, all of them are path-following approaches. The first two strategies presented in Chapter 7 and Chapter 8 use parametrisation of the path to achieve this. In particular, a path-tangential frame is propagated along the path and the goal is to let the vessel converge to the path-frame in the presence of an unknown constant ocean current. The third strategy presented in Chapter 9 presents a strategy to follow unparametrised paths, but ocean currents are not considered.

Chapter 7 considers path-following of underactuated marine vessels in the presence of constant ocean currents. A line-of-sight guidance law, an ocean current observer, and a local parametrisation of the path are used in this work. The parametrisation that is used is the parametrisation introduced for mobile robots in Samson [124] with an adaptation to include the effect of the unknown ocean currents. This parametrisation aims to keep the vessel on the normal of a path-tangential reference frame. However, this is only possible when the ocean current is known and therefore the adaptation to the parametrisation includes a restoring term that assures that the vessel is brought back to the normal of the path-tangential reference frame once the estimate of the ocean current has converged. Due to the locality of the parametrisation it can only be used in a certain tube around the path whose size depends on the maximum curvature of the path. When in this tube it is shown that the closed-loop system of the controllers and the ocean current observer provides global asymptotic stability of the path-following error dynamics. This work considers a path-following scenario similar to Do and Pan [49]. In Do and Pan [49] the mass and damping matrices are assumed diagonal while in Chapter 7 these matrices may have non-zero off-diagonal terms. Moreover, in Do and Pan [49] the coupling between the total speed and the underactuated side-ways velocity is not considered when showing boundedness of the sideways velocity. This coupling may actually cause unbounded growth of the sideways velocity, which is shown and prevented in Chapter 7.

Chapter 8 considers path-following of underactuated marine vessels in the presence of constant ocean currents. Contrary to the parametrisation in Chapter 7 the parametrisation in this chapter is valid globally, i.e. the initial path-following errors can be arbitrarily large. To accommodate this the guidance law is adapted, resulting in a line-of-sight like guidance for which the look-ahead distance is adapted based on the path-following errors. Like in the local case an ocean current observer

is used to compensate for the unknown ocean current. The full closed-loop system is then analysed and it is shown that under appropriate conditions for the look-ahead distance and path curvature the path-following errors are globally asymptotically stable. The guidance considered in this work is an adaptation of the guidance in Moe et al. [100], which investigates the same problem. It is shown that this modification is necessary to guarantee boundedness of the zero dynamics which were not analysed in Moe et al. [100].

Chapter 9 presents a novel strategy to follow unparametrised paths with underactuated marine vessels. The path is defined implicitly by using a describing function that is zero when on the path. Then using three geometric objects, i.e. the normal to the path, the tangent to the path, and the curvature of the path, a control approach is introduced that drives the describing function to zero and hence controls the vessel to the path. The controller is based on principles from geometric control and the hierarchical control design method from El-Hawwary and Maggiore [55]. Using the hierarchical control design method, the closed-loop system is analysed and the underactuated zero dynamics are shown to be well behaved. The main contribution of this work is in the introduction of a new geometric controller that allows path-following of unparametrised paths. This is a 'purer' form of path-following than the approach taken in Chapters 7 and 8 and the other approaches available in the literature, since parametrisation of the path technically only makes any point on the path attractive instantaneously rather than the path in general. The material in Chapter 9 is based on Belleter et al. [23].

1.2.4 Publications

The following is a list of publications relating to the work in the thesis. It contains publications in journals, a book chapter, and publications at several international peer-reviewed conferences. The list contains both accepted and submitted works.

Journal Papers and Book Chapter

- D. J. W. Belleter, R. Galeazzi, and T. I. Fossen. Experimental verification of a global exponential stable nonlinear wave encounter frequency estimator. *Ocean Engineering*, 97:48–56, 2015
- D. J. W. Belleter and K. Y. Pettersen. Leader-follower synchronisation for a class of underactuated systems. In N. van de Wouw, E. Lefeber, and I. Lopez Arteaga, editors, *Nonlinear Systems*, chapter 8, pages 157–179. Springer, 2017
- D. J. W. Belleter, J. Braga, and K. Y. Pettersen. Experimental verification of a coordinated path following strategy for underactuated marine vehicles. *To be submitted to Elsevier Ocean Engineering*, 2016
- D. J. W. Belleter, M. Maghenem, C. Paliotta, and K. Y. Pettersen. Observer based path following for underactuated marine vessels in the presence of ocean currents: a global approach. *To be submitted to IEEE Transactions of Control Systems Technology*, 2016

Conference Papers

- D. J. W. Belleter, D. A. Breu, T. I. Fossen, and H. Nijmeijer. A globally K-exponentially stable nonlinear observer for the wave encounter frequency. *IFAC Proceedings Volumes, Presented at: 9th IFAC Conference on Control Applications in Marine Systems*, 46(33):209–214, 2013
- D. J. W. Belleter and K. Y. Pettersen. Path following for formations of underactuated marine vessels under influence of constant ocean currents. In *Proceedings of the 53th IEEE Conference on Decision and Control, Los Angeles, USA, Dec. 15-17*, pages 4521–4528, 2014
- D. J. W. Belleter and K. Y. Pettersen. Path following with disturbance rejection for inhomogeneous formations with underactuated agents. In *European Control Conference (ECC), Linz, Austria*, pages 1023–1030. IEEE, 2015
- D. J. W. Belleter and K. Y. Pettersen. Underactuated leader-follower synchronisation for multi-agent systems with rejection of unknown disturbances. In *American Control Conference (ACC), Chicago, USA*, pages 3094–3100, 2015
- D. J. W. Belleter and K. Y. Pettersen. 3D coordinated path following with disturbance rejection for formations of under-actuated agents. In *54th IEEE Conference on Decision and Control (CDC)*, pages 1040–1047. IEEE, 2015
- D. J. W. Belleter, C. Paliotta, M. Maggiore, and K. Y. Pettersen. Path following for underactuated marine vessels. In *10th IFAC Symposium on Nonlinear Control Systems (NOLCOS), To Appear*. IFAC, 2016
- M. Maghenem, D. J. W. Belleter, C. Paliotta, and K. Y. Pettersen. Observer based path following for underactuated marine vessels in the presence of ocean currents: a local approach. *Submitted to IFAC world congress*, 2017

Publications not part of the thesis

- D. J. W. Belleter, D. A. Breu, T. I. Fossen, and H. Nijmeijer. Nonlinear observer design for parametric roll resonance. In *Proceedings of the 11th International Conference on the Stability of Ships and Ocean Vehicles*, pages 699–705, 2012
- C. Paliotta, D. J. W. Belleter, and K. Y. Pettersen. Adaptive source seeking with leader-follower formation control. *IFAC-PapersOnLine, Presented at: 10th IFAC Conference on Manoeuvring and Control of Marine Craft*, 48(16): 285–290, 2015

1.3 Outline of the Thesis

This thesis is build up of ten chapters and three appendices. Some chapters have their own subappendices for material that is specific to that chapter and is not necessary in the main body of the text.

Chapter 2 presents a dynamical model for motion in two dimensional space to model marine surface vessels, and a dynamical model for motion in three dimensional space to model autonomous underwater vehicles (AUVs).

Chapter 3 presents the design of a frequency estimator to estimate the wave encounter frequency of a ship. The estimation algorithm can be used online and is equipped with a gain-switching mechanism to function in situations with high and low excitation. The theoretical results are verified using experimental data.

Chapter 4 presents a coordinated straight line path-following strategy for underactuated surface vessels in the presence of constant ocean currents. The combination of an integral line-of-sight guidance to achieve path-following and a nonlinear coordination law to achieve desired along-path distances is investigated and it is shown that coordinated path following can be achieved.

Chapter 5 presents a coordinated straight line path-following strategy for autonomous underwater vehicles in the presence of constant ocean currents. Compared to the previous chapter an extra step in the guidance is added for the depth control and the extra degree of underactuation is taken into account in the coordination error dynamics.

Chapter 6 considers leader-follower synchronisation for underactuated surface vessels, where a straight-line guidance is applied to curved trajectories to analyse the synchronisation behaviour under these circumstances.

Chapter 7 presents an approach for curved path following in the presence of unknown ocean currents for underactuated marine surface vessels. It combines a line-of-sight guidance law with an ocean current observer to achieve path following. The result from this chapter is valid only locally due to the particular parametrisation of the path which has a singularity.

Chapter 8 presents an approach for curved path following in the presence of unknown ocean currents for underactuated marine surface vessels. Compared to the previous chapter this approach uses a different parametrisation and different guidance that makes the result globally valid.

Chapter 9 presents a novel curved path-following strategy that does not require parametrisation of the path. This strategy is based on principles from geometric control and hierarchical control design.

Chapter 10 presents concluding remarks and gives recommendations for future work and developments.

Appendix A presents some of the mathematical notations, definitions, and tools used in the thesis.

Appendix B presents model transformations that are used in the derivation of the dynamical models of Chapter 2.

Appendix C presents the numerical simulation models used in the thesis.

Part I

Modelling of Marine Vehicles and Environmental Disturbances

Chapter 2

Modelling of Marine Vehicles in the Presence of Environmental Disturbances

This chapter considers modelling of underactuated marine vehicles in the presence of environmental disturbances. The first section presents a general model for marine vehicles based on a rigid-body approximation. In subsequent sections several aspects of this model are specified further to derive some of the models that are used for the controller designs throughout this thesis. The models presented in this chapter are for the purpose of control design and stability analysis. The models give a good representation of the kinematics and dynamics of the ship's motion but do not capture complex effects such as hydrodynamic interactions between the hull and the water, details of the propulsion system and its interactions with the environment.

2.1 Modelling of Ocean Current for Control of Marine Vehicles

To derive the models used for control design in this thesis we start from a general manoeuvring model as presented in Fossen [60]. This model is based on a rigid-body approximation of a marine vehicle subjected to hydrodynamic and hydrostatic forces which results in a nonlinear mass-spring-damper system with constant coefficients. The model describes motion in three dimensional space. In the marine systems literature it is common to express this motion in two frames: the inertial north-east-down (NED) frame expressed by i and the body-fixed frame b which is attached to the body of the marine vehicle as depicted in Figure 2.1. This section only gives a brief presentation of the model a more comprehensive discussion and other variations of models can be found in Fossen [60]. The model is then given by

$$\dot{\boldsymbol{\eta}} = \boldsymbol{J}(\boldsymbol{\eta})\boldsymbol{\nu}, \tag{2.1a}$$

$$\boldsymbol{M}_{RB}\dot{\boldsymbol{\nu}} + \boldsymbol{C}_{RB}(\boldsymbol{\nu})\boldsymbol{\nu} + \boldsymbol{M}_A\dot{\boldsymbol{\nu}}_r + \boldsymbol{C}_A(\boldsymbol{\nu}_r)\boldsymbol{\nu}_r + \boldsymbol{D}(\boldsymbol{\nu}_r)\boldsymbol{\nu}_r + \boldsymbol{g}(\boldsymbol{\eta}) = \boldsymbol{\tau} + \boldsymbol{\tau}_w. \tag{2.1b}$$

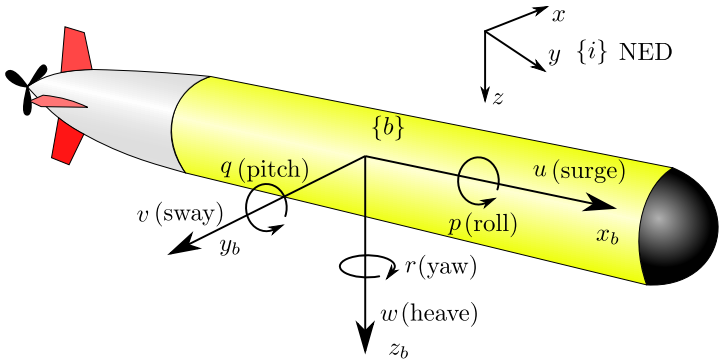

Figure 2.1: Definition of the coordinates.

The vector $\boldsymbol{\eta} \triangleq [x, y, z, \phi, \theta, \psi]^T$ is defined in i and represents the position in Cartesian coordinates and orientation in Euler angles roll-pitch-yaw of the vehicle with respect to i. The matrix $\boldsymbol{J}(\boldsymbol{\nu})$ is the velocity transformation matrix between b and i. The term $\boldsymbol{\nu} \triangleq [u, v, w, p, q, r]^T$ is the vector of generalised velocities with respect to b. The linear velocities u, v, and w are the surge, sway, and heave velocity respectively and the angular velocities p, q, and r are the roll rate, pitch rate, and yaw rate respectively. The relative velocity vector, i.e. the velocity with respect to the ocean current, is defined as $\boldsymbol{\nu}_r \triangleq \boldsymbol{\nu} - \boldsymbol{\nu}_c$ where $\boldsymbol{\nu}_c$ is the velocity of the ocean current expressed in b. The matrices $\boldsymbol{M}_{RB} = \boldsymbol{M}_{RB}^T > 0$ and $\boldsymbol{C}_{RB}(\boldsymbol{\nu})$ are the rigid-body mass matrix and Coriolis and centripetal matrix respectively. The matrices $\boldsymbol{M}_A = \boldsymbol{M}_A^T > 0$ and $\boldsymbol{C}_A(\boldsymbol{\nu})$ are the hydrodynamic added mass matrix and the added mass Coriolis and centripetal matrix, respectively. The matrix $\boldsymbol{D}(\boldsymbol{\nu}_r)$ is the hydrodynamic damping matrix. The vector $\boldsymbol{g}(\boldsymbol{\eta})$ is the vector of gravitational/buoyancy forces and moments. The control input in body-frame b is given by $\boldsymbol{\tau}$ and the vector $\boldsymbol{\tau}_w \triangleq \boldsymbol{\tau}_{\text{wind}} + \boldsymbol{\tau}_{\text{wave}}$ represents the vector of added wind and wave-induced forces.

The general model (2.1) is specified further in the two subsequent sections of this chapter. However, we first specify the nature of the disturbances considered in this thesis. As specified in Chapter 1, the disturbance considered in this thesis are ocean currents and wave forces. The wave forces are considered to be filtered out using a wave filter that utilises estimates of the wave encounter frequency from the wave frequency estimator that is presented in the next chapter. Moreover, as specified in Chapter 1, wind disturbances are out of the scope of this thesis. Therefore, the vector of added wind and wave-induced forces $\boldsymbol{\tau}_w$ is not considered in the models for control design in the next subsections. We now rewrite the model (2.1) in a more convenient form to incorporate ocean currents. To do this we assume that the ocean current is constant and irrotational with respect to the inertial frame. Hence, we define the current vector $\boldsymbol{V}_c \triangleq [V_x, V_y, V_z]^T$ which has constant components and where for surface vessels it holds that $V_z = 0$. Moreover, we assume the current is bounded by a maximum value $V_{\max} > 0$ such that $\|\boldsymbol{V}_c\| = \sqrt{V_x^2 + V_y^2 + V_z^2} \leq V_{\max}$.

The ocean current can be expressed in the body frame according to

$$\boldsymbol{v}_c = \boldsymbol{R}(\phi, \theta, \psi)^T \boldsymbol{V}_c, \tag{2.2}$$

where $\boldsymbol{R}(\phi, \theta, \psi)$ is the rotation matrix from b to i and where $\boldsymbol{v}_c \triangleq [u_c, v_c, w_c]^T$. In an irrotational fluid this results in $\boldsymbol{\nu}_c \triangleq [u_c, v_c, w_c, 0, 0, 0]^T$. Furthermore, it shown in Fossen [60] that if the current is constant and irrotational it holds that

$$\boldsymbol{M}_{RB}\dot{\boldsymbol{\nu}} + \boldsymbol{C}_{RB}(\boldsymbol{\nu})\boldsymbol{\nu} = \boldsymbol{M}_{RB}\dot{\boldsymbol{\nu}}_r + \boldsymbol{C}_{RB}(\boldsymbol{\nu}_r)\boldsymbol{\nu}_r. \tag{2.3}$$

Using (2.2), (2.3), and the definition of $\boldsymbol{\nu}_r$ we rewrite (2.1) to

$$\dot{\boldsymbol{\eta}} = \boldsymbol{J}(\boldsymbol{\eta})\boldsymbol{\nu}_r + [\boldsymbol{V}_c, \boldsymbol{0}_{1\times 3}]^T, \tag{2.4a}$$

$$\boldsymbol{M}\dot{\boldsymbol{\nu}}_r + \boldsymbol{C}(\boldsymbol{\nu}_r)\boldsymbol{\nu}_r + \boldsymbol{D}(\boldsymbol{\nu}_r)\boldsymbol{\nu}_r + \boldsymbol{g}(\boldsymbol{\eta}) = \boldsymbol{\tau}, \tag{2.4b}$$

where $\boldsymbol{M} \triangleq \boldsymbol{M}_{RB} + \boldsymbol{M}_A$ and $\boldsymbol{C}(\boldsymbol{\nu}_r) = \boldsymbol{C}_{RB}(\boldsymbol{\nu}_r) + \boldsymbol{C}_A(\boldsymbol{\nu}_r)$. The model (2.4) now represents a marine vehicle moving in the presence of an ocean current that causes a kinematic drift. The first-order wave forces are assumed to be filtered from this model, and the vehicle is considered in the absence of wind. In this thesis we choose to control the relative velocity. This gives direct control over the energy consumption since the hydrodynamic damping depends on $\boldsymbol{\nu}_r$ [39]. Furthermore, using the relative velocity representation of the model leads to more straightforward controller design. In the next two sections the models are specified further to represent a surface vessel and an autonomous underwater vehicle.

2.2 The Manoeuvring Model in 3 DOF

In this section the model (2.4) is further simplified to a 3 DOF model. This model can be used to describe an autonomous surface vessel or an autonomous underwater vehicle moving in a plane and is used in several subsequent chapters of the thesis. This means that there is no motion in the vertical direction and that there is no need to consider motion along the z-axis and rotation along the y-axis, i.e. the z position and the pitch angle θ can be removed from the model. Furthermore the roll angle ϕ is assumed to be passively stabilised and is also not considered in the reduced model.

In line with the previous section the position in the plane is denoted by $\boldsymbol{p} \triangleq [x, y]^T \in \mathbb{R}^2$ and the heading, i.e. yaw, angle is denoted by $\psi \in \mathbb{R}$. The linear velocities in the longitudinal (surge) and lateral direction (sway) of the body-fixed frame are denoted by u and v respectively. The yaw rate is denoted by r. The vessel has two control inputs available, the surge trust T_u and the rudder angle T_r. The vessel in this case is only disturbed by an ocean current denoted by $\boldsymbol{V}_c \triangleq [V_x, V_y]^T$ in the inertial frame. The ocean current is assumed to be constant and irrotational with respect to the inertial frame and it is bounded by $V_{\max} > 0$ such that $\|V_c\| = \sqrt{V_x^2 + V_y^2} \leq V_{max}$.

The relative velocity vector also reduces to two components resulting in $\boldsymbol{\nu}_r \triangleq [u_r, v_r]^T$ with $u_r \triangleq u - u_c$ the relative surge velocity and $v_r \triangleq v - v_c$ relative sway velocity where u_c and v_c are the components of the current expressed in the body

frame. The total speed is defined as $u_t \triangleq \sqrt{u_r^2 + v_r^2}$ and the angle between the direction of the surge velocity and total speed, i.e. the side-slip angle, is defined as $\beta \triangleq \text{atan}(v_r/u_r)$. An illustration of the variables is given in Figure 2.2. In Fossen [60] a 3-DOF manoeuvring model expressed in these variables is given by:

$$\dot{\boldsymbol{\eta}} = \boldsymbol{R}(\psi)\boldsymbol{\nu}_r + [V_x, V_y, 0]^T \tag{2.5a}$$

$$\boldsymbol{M}\dot{\boldsymbol{\nu}}_r + \boldsymbol{C}(\boldsymbol{\nu}_r)\boldsymbol{\nu}_r + \boldsymbol{D}\boldsymbol{\nu}_r = \boldsymbol{B}\boldsymbol{f}. \tag{2.5b}$$

where $\boldsymbol{\eta} \triangleq [x, y, \psi]^T$, $\boldsymbol{\nu}_r \triangleq [u_r, v_r, r]^T$, $\boldsymbol{f} \triangleq [T_u, T_r]^T$, and

$$\boldsymbol{R}(\psi) \triangleq \begin{bmatrix} \cos(\psi) & -\sin(\psi) & 0 \\ \sin(\psi) & \cos(\psi) & 0 \\ 0 & 0 & 1 \end{bmatrix}. \tag{2.6}$$

If we assume the vessel is port-starboard symmetric an the body-fixed frame is located along the centreline of the vessel, the matrices $\boldsymbol{M}$, $\boldsymbol{D}$, and $\boldsymbol{B}$ can be defined as

$$\boldsymbol{M} \triangleq \begin{bmatrix} m_{11} & 0 & 0 \\ 0 & m_{22} & m_{23} \\ 0 & m_{23} & m_{33} \end{bmatrix}, \boldsymbol{D} \triangleq \begin{bmatrix} d_{11} & 0 & 0 \\ 0 & d_{22} & d_{23} \\ 0 & d_{32} & d_{33} \end{bmatrix}, \boldsymbol{B} \triangleq \begin{bmatrix} b_{11} & 0 \\ 0 & b_{22} \\ 0 & b_{32} \end{bmatrix},$$

with $\boldsymbol{M} = \boldsymbol{M}^T > 0$ the symmetric positive definite inertia matrix including added mass, $\boldsymbol{D} > 0$ is the hydrodynamic damping matrix, and $\boldsymbol{B}$ is the actuator configuration matrix. The matrix $\boldsymbol{C}(\boldsymbol{\nu}_r)$ is the matrix of Coriolis and centripetal forces and can be obtained from $\boldsymbol{M}$ (see [60]) resulting in

$$\boldsymbol{C}(\boldsymbol{\nu}_r) \triangleq \begin{bmatrix} 0 & 0 & -m_{22}v_r - m_{23}r \\ 0 & 0 & m_{11}u_r \\ m_{22}v_r + m_{23}r & -m_{11}u_r & 0 \end{bmatrix}. \tag{2.7}$$

Remark 2.1. Note that nonlinear damping is not considered in this thesis. This choice is made to reduce the complexity of the proposed controllers. However, the passive nature of the nonlinear hydrodynamic damping forces should only enhance the directional stability [42].

To make the stability properties of the sway dynamics easier to analyse we perform a change of coordinates by moving the origin of the body frame over a distance ϵ along the center-line of the vessel. Following Fredriksen and Pettersen [64] there exists a constant ϵ such that the resulting dynamics have mass and damping matrices satisfying this relation: $\boldsymbol{M}^{-1}\boldsymbol{B}\boldsymbol{f} = [\tau_u, 0, \tau_r]^T$. Details of this coordination transformation can be found in Appendix B. Using these conditions, the model of the marine vessel (2.5) can be represented in component form as

$$\dot{x} = u_r \cos(\psi) - v_r \sin(\psi) + V_x, \tag{2.8a}$$

$$\dot{y} = u_r \sin(\psi) + v_r \cos(\psi) + V_y, \tag{2.8b}$$

$$\dot{\psi} = r, \tag{2.8c}$$

$$\dot{u}_r = F_{u_r}(v_r, r) - \tfrac{d_{11}}{m_{11}}u_r + \tau_u, \tag{2.8d}$$

$$\dot{v}_r = X(u_r)r + Y(u_r)v_r, \tag{2.8e}$$

$$\dot{r} = F_r(u_r, v_r, r) + \tau_r, \tag{2.8f}$$

The expressions for $X(u_r)$, $Y(u_r)$, F_u, and F_r are

$$F_{u_r} \triangleq \frac{1}{m_{11}}(m_{22}v_r + m_{23}r)r, \tag{2.9a}$$

$$X(u_r) \triangleq \frac{m_{23}^2 - m_{11}m_{33}}{m_{22}m_{33} - m_{23}^2 u_r + \frac{d_{33}m_{23} - d_{23}m_{33}}{m_{22}m_{33} - m_{23}^2}}, \tag{2.9b}$$

$$Y(u_r) \triangleq \frac{(m_{22} - m_{11})m_{23}}{m_{22}m_{33} - m_{23}^2}u_r - \frac{d_{22}m_{33} - d_{32}m_{23}}{m_{22}m_{33} - m_{23}^2}, \tag{2.9c}$$

$$\begin{aligned} F_r(u_r, v_r, r) \triangleq & \frac{m_{23}d_{22} - m_{22}(d_{32} + (m_{22} - m_{11})u_r)}{m_{22}m_{33} - m_{23}^2}v_r \\ & + \frac{m_{23}(d_{23} + m_{11}u_r) - m_{22}(d_{33} + m_{23}u_r)}{m_{22}m_{33} - m_{23}^2}r. \end{aligned} \tag{2.9d}$$

Note that the functions $X(u_r)$ and $Y(u_r)$ are linear and that $Y(u_r)$ satisfies the following assumption throughout the thesis.

Assumption 2.1. The function $Y_{v_r}(u_r)$ satisfies

$$Y(u_r) \leq -Y^{\min} < 0, \, \forall u_r \in [-V_{\max}, u_{rd}],$$

where u_{rd} is the desired surge speed.

Remark 2.2. Assumptions 2.1 is satisfied for commercial vessels by design, since the converse would imply an undamped or nominally unstable vessel in sway.

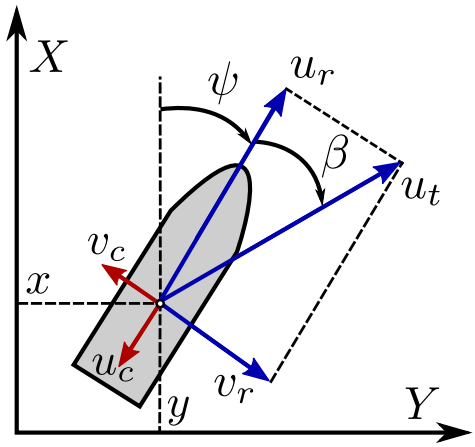

Figure 2.2: Definition of the ship's kinematic variables.

2.3 The Manoeuvring Model in 5 DOF

The model considered in this section is a 5-DOF model of an AUV which describes the motion of the AUV in surge, sway, heave, pitch and yaw. The roll angle is

assumed to be passively stabilised by fins or by gravity and is therefore neglected. Consequently, the state of the vehicle w.r.t to i is given by $\boldsymbol{\eta} \triangleq [x, y, z, \theta, \psi]^T$ with three spatial coordinates x, y, and z and two angles θ and ψ which are the pitch and yaw angle respectively. The vector of linear and angular velocities of the vehicle $\boldsymbol{\nu} \triangleq [u, v, w, q, r]^T$ is expressed with respect to the body-fixed frame b and contains the surge velocity u, the sway velocity v, the heave velocity w, the pitch rate q, and the yaw rate ψ. The vehicles are affected by the ocean current described in Section 2.1 such that $\boldsymbol{V}_c \triangleq [V_x, V_y, V_z]^T$ expressed in the inertial frame i is assumed to be constant, irrotational and upper-bounded, i.e. $\exists V_{\max} > 0$ such that $\|\boldsymbol{V}_c\| = \sqrt{V_x^2 + V_y^2 + V_z^2} \leq V_{\max}$.

The ocean current velocities in the body-fixed frame b are given by $\boldsymbol{\nu}_c \triangleq [u_c, v_c, w_c, 0, 0]^T$, and are obtained from $[u_c, v_c, w_c]^T = \boldsymbol{R}^T(\theta, \psi)\boldsymbol{V}_c$ where $\boldsymbol{R}(\theta, \psi)$ is the rotation matrix from b to i defined as

$$\boldsymbol{R}(\theta, \psi) \triangleq \begin{bmatrix} \cos(\psi)\cos(\theta) & -\sin(\psi) & \cos(\psi)\sin(\theta) \\ \sin(\psi)\cos(\theta) & \cos(\psi) & \sin(\psi)\sin(\theta) \\ -\sin(\theta) & 0 & \cos(\theta) \end{bmatrix} \tag{2.10}$$

Using the ocean current velocity we can define the relative velocity in the body-fixed frame as $\boldsymbol{\nu}_r \triangleq \boldsymbol{\nu} - \boldsymbol{\nu}_c = [u_r, v_r, w_r, q, r]^T$ [60]. It is shown in Fossen [60] that if the current is constant, bounded, and irrotational an underwater vehicle can be described using the 5-DOF manoeuvring model:

$$\dot{\boldsymbol{\eta}} = \boldsymbol{J}(\boldsymbol{\eta})\boldsymbol{\nu}_r + [V_x, V_y, V_z, 0, 0]^T, \tag{2.11a}$$

$$\boldsymbol{M}\dot{\boldsymbol{\nu}}_r + \boldsymbol{C}(\boldsymbol{\nu}_r)\boldsymbol{\nu}_r + \boldsymbol{D}\boldsymbol{\nu}_r + \boldsymbol{g}(\boldsymbol{\eta}) = \boldsymbol{B}\boldsymbol{f} \tag{2.11b}$$

The block diagonal velocity transformation matrix maps the body-frame velocities and rotation to the inertial frame and is defined as $\boldsymbol{J}(\eta) \triangleq \text{bdiag}(\boldsymbol{R}(\theta, \psi), \boldsymbol{T}(\theta))$, with $\boldsymbol{T}(\theta) \triangleq \text{diag}(1, 1/\cos(\theta))$, $|\theta| \neq \pm\pi/2$. The matrix $\boldsymbol{M} = \boldsymbol{M}^T > 0$ is the mass and inertia matrix, matrix $\boldsymbol{D} > 0$ is the hydrodynamic damping matrix, and $\boldsymbol{B}$ is the actuator configuration matrix.

The AUVs considered here are assumed to be slender-body AUVs, i.e. they have a large length-to-width ratio. The AUV are assumed to be xz-plane symmetric, which is the parallel of the port-starboard symmetry assumption in the previous subsection. The AUVs are assumed to be neutrally buoyant, that is, they do not move in the vertical plane unless active depth control is applied. Moreover, the center of gravity (CG) and the center of buoyancy (CB) are located along the same vertical axis in the body-fixed frame. The surge mode is decoupled from the other degrees of freedom and consider only the dominating interconnections, i.e. the interconnections between sway and yaw and between heave and pitch.

Remark 2.3. The assumptions made in the preceding discussion are common assumptions in manoeuvring control of slender-body AUVs [60].

The matrices $\boldsymbol{M}$, $\boldsymbol{D}$, and $\boldsymbol{B}$ can now be defined to have the following structure

$$\boldsymbol{M} \triangleq \begin{bmatrix} m_{11} & 0 & 0 & 0 & 0 \\ 0 & m_{22} & 0 & 0 & m_{25} \\ 0 & 0 & m_{33} & m_{34} & 0 \\ 0 & 0 & m_{43} & m_{44} & 0 \\ 0 & m_{52} & 0 & 0 & m_{55} \end{bmatrix},$$

$$\boldsymbol{D} \triangleq \begin{bmatrix} d_{11} & 0 & 0 & 0 & 0 \\ 0 & d_{22} & 0 & 0 & d_{25} \\ 0 & 0 & d_{33} & d_{34} & 0 \\ 0 & 0 & d_{43} & d_{44} & 0 \\ 0 & d_{52} & 0 & 0 & d_{55} \end{bmatrix}, \quad \boldsymbol{B} \triangleq \begin{bmatrix} b_{11} & 0 & 0 \\ 0 & 0 & b_{23} \\ 0 & b_{32} & 0 \\ 0 & b_{42} & 0 \\ 0 & 0 & b_{53} \end{bmatrix}.$$

Remark 2.4. Note that nonlinear damping is not considered in this thesis. This choice is made to reduce the complexity of the proposed controllers. However, the passive nature of the nonlinear hydrodynamic damping forces should only enhance the directional stability [42].

The matrix $\boldsymbol{C}$ is the coriolis and centripetal matrix and can be derived from $\boldsymbol{M}$ (see [60]) to obtain

$$\boldsymbol{C}(\boldsymbol{\nu}_r) \triangleq \begin{bmatrix} 0 & 0 & 0 & m_{33}w_r + m_{34}q & -m_{22}v_r - m_{25}r \\ 0 & 0 & 0 & 0 & m_{11}u_r \\ 0 & 0 & 0 & -m_{11}u_r & 0 \\ -m_{33}w_r - m_{34}q & 0 & m_{11}u_r & 0 & 0 \\ m_{22}v_r + m_{25}r & -m_{11}u_r & 0 & 0 & 0 \end{bmatrix}$$

The gravity vector in CG is given as $\boldsymbol{g}(\boldsymbol{\eta}) \triangleq [0, 0, 0, BG_z W \sin(\theta), 0]^T$, with BG_z the vertical distance between CG and CB, and W is the weight of the vehicle. The control input vector $\boldsymbol{f}$ is defined as $\boldsymbol{f} \triangleq [T_u, T_q, T_r]^T$ and contains the surge thrust T_u, the pitch rudder angle T_q, and the yaw rudder angle T_r. The location of the body-fixed frame is chosen to be at $(x_g^*, 0, 0)$ such that $\boldsymbol{M}^{-1}\boldsymbol{B}\boldsymbol{f} = [\tau_u, 0, 0, \tau_q, \tau_r]^T$. Note that the model is under-actuated in sway and heave. The point $(x_g^*, 0, 0)$ always exists for AUVs of cylindrical shape employing symmetric steering and diving control surfaces [29] and the body-fixed frame can always be translated to this location [60], details of this coordination transformation can be found in Appendix B.

The model can be expanded into component form as

$$\dot{x} = u_r \cos(\psi)\cos(\theta) - v_r \sin(\psi) + w_r \cos(\psi)\sin(\theta) + V_x \tag{2.12a}$$
$$\dot{y} = u_r \sin(\psi)\cos(\theta) + v_r \cos(\psi) + w_r \sin(\psi)\sin(\theta) + V_y \tag{2.12b}$$
$$\dot{z} = -u_r \sin(\theta) + w_r \cos(\theta) + V_z \tag{2.12c}$$
$$\dot{\theta} = q \tag{2.12d}$$
$$\dot{\psi} = r/\cos(\theta) \tag{2.12e}$$
$$\dot{u}_r = F_{u_r}(v_r, w_r, q, r) - (d_{11}/m_{11})u_r + \tau_u \tag{2.12f}$$
$$\dot{v}_r = X_{v_r}(u_r)q + Y_{v_r}(u_r)v_r \tag{2.12g}$$
$$\dot{w}_r = X_{w_r}(u_r)q + Y_{w_r}(u_r)w_r + Z_{w_r}\sin(\theta) \tag{2.12h}$$
$$\dot{q} = F_q(\theta, u_r, w_r, q) + \tau_q \tag{2.12i}$$
$$\dot{r} = F_r(u_r, v_r, r) + \tau_r \tag{2.12j}$$

The definitions of F_{u_r}, X_{v_r}, Y_{v_r}, X_{w_r}, Y_{w_r}, Z_{w_r}, F_q, and F_r are given by

$$F_{u_r}(v_r, w_r, r, q) \triangleq \frac{1}{m_{11}}[(m_{22}v_r + m_{25}r)r - (m_{33}w_r + m_{34}q)q], \tag{2.13a}$$

$$X_{v_r}(u_r) \triangleq \frac{m_{25}^2 - m_{11}m_{55}}{m_{22}m_{55} - m_{25}^2}u_r + \frac{d_{55}m_{25} - d_{25}m_{55}}{m_{22}m_{55} - m_{25}^2}, \tag{2.13b}$$

$$Y_{v_r}(u_r) \triangleq \frac{(m_{22} - m_{11})m_{25}}{m_{22}m_{55} - m_{25}^2}u_r - \frac{d_{22}m_{55} - d_{52}m_{25}}{m_{22}m_{55} - m_{25}^2}, \tag{2.13c}$$

$$X_{w_r}(u_r) \triangleq \frac{-m_{34}^2 + m_{11}m_{44}}{m_{33}m_{44} - m_{34}^2}u_r + \frac{d_{44}m_{34} - d_{34}m_{44}}{m_{33}m_{44} - m_{34}^2}, \tag{2.13d}$$

$$Y_{w_r}(u_r) \triangleq \frac{(m_{11} - m_{33})m_{34}}{m_{33}m_{44} - m_{34}^2}u_r - \frac{d_{33}m_{44} - d_{43}m_{34}}{m_{33}m_{44} - m_{34}^2}, \tag{2.13e}$$

$$Z_{w_r} \triangleq \frac{BG_zWm_{34}}{m_{33}m_{44} - m_{34}^2}, \tag{2.13f}$$

$$\begin{aligned} F_q(\theta, u_r, w_r, q) \triangleq{}& \frac{m_{34}d_{33} - m_{33}(d_{43} - (m_{33} - m_{11})u_r)}{m_{33}m_{44} - m_{34}^2}w_r \\ &+ \frac{m_{34}(d_{34} - m_{11}u_r) - m_{33}(d_{44} - m_{34}u_r)}{m_{33}m_{44} - m_{34}^2}q \\ &- \frac{BG_zWm_{33}}{m_{33}m_{44} - m_{34}^2}\sin(\theta), \end{aligned} \tag{2.13g}$$

$$\begin{aligned} F_r(u_r, v_r, r) \triangleq{}& \frac{m_{25}d_{22} - m_{22}(d_{53} + (m_{22} - m_{11})u_r)}{m_{22}m_{55} - m_{25}^2}v_r \\ &+ \frac{m_{25}(d_{25} + m_{11}u_r) - m_{22}(d_{55} + m_{25}u_r)}{m_{22}m_{55} - m_{25}^2}r. \end{aligned} \tag{2.13h}$$

Assumption 2.2. The function $Y_{v_r}(u_r)$ satisfies

$$Y_{v_r}(u_r) \leq -Y_{v_r}^{\min} < 0, \, \forall u_r \in [-V_{\max}, u_{rd}],$$

where u_{rd} is the desired surge speed.

Assumption 2.3. The function $Y_{w_r}(u_r)$ satisfies

$$Y_{w_r}(u_r) \leq -Y_{w_r}^{\min} < 0, \, \forall u_r \in [-V_{\max}, u_{rd}],$$

where u_{rd} is the desired surge speed.

Remark 2.5. Assumptions 2.2 and 2.3 are satisfied for commercial vessels by design, since the converse would imply an undamped or nominally unstable vessel in sway and heave respectively.

Chapter 3

Wave Frequency Estimation

Estimation of the wave encounter frequency is an important part of sea-state prediction, which is of great importance in many marine operations as well as control systems design. Sea-state estimation also provides information to increase both the safety of operations at sea and the performance of control systems for ships affected by waves.

To increase the safety of operations, knowledge of the wave encounter frequency can be used for prediction of extreme waves, parametric roll resonance and in-service monitoring. Knowledge of the sea-state, and in particular the encounter frequency, is also important to increase the performance of marine control systems. For ship autopilot and dynamic positioning (DP) systems, knowledge of the encounter frequency allows for better tuning of the low-pass and notch filters used in wave filtering [60, Ch. 11]. On-line adjustment of controller and observer gains also require knowledge of the wave encounter frequency [61]. This allows for automatic gain scheduling of autopilots and DP systems.

As an exception in this thesis, this chapter has its own section with background information. This is done since this chapter presents a topic not related to the other chapters in the thesis which consider control of marine vehicles whilst this chapter considers estimation of an environmental parameter. The material presented in this chapter is based on Belleter et al. [19] and Belleter et al. [20].

3.1 Background

3.1.1 Sea-state estimation

In the literature several techniques for estimation of the wave encounter frequency or wave spectra have been presented. The classical method is to obtain the wave spectrum from *Fast Fourier Transform* (FFT) frequency spectral analysis [58]. Unfortunately, creating a FFT frequency spectrum takes time and consequently it results in back-dated information when estimating the time-varying wave encounter frequency. This is due to the moving window necessary for applying the FFT frequency spectral analysis. Hence, it is impossible to estimate a time-varying wave encounter frequency without lag.

More advanced spectral estimation techniques allow estimation of directional wave spectra [105]. This can be done by parametric or non-parametric modelling. The parametric modelling approach typically assumes that the wave spectrum is parametrized such that it can be estimated using least-squares parameter matching of a bimodal spectrum for stationary vessels [136] and moving vessels [105]. The non-parametric modelling or Bayesian approach uses stochastic processes to match the frequencies for stationary vessels [77] and moving vessels [105]. These techniques have the same disadvantages with respect to acquisition times as the FFT frequency spectral analysis. However, besides the frequency of the waves, they also supply directional information.

Another approach to wave encounter frequency estimation is to estimate the peak frequency instead of the entire wave spectrum. This is a valid approach for application of sea-state estimation when designing control systems, since the peak frequency of the spectrum is used for wave filtering [60, Ch. 11]. Approaches using Kalman filters can be found in Belleter et al. [18] and Hassani et al. [69]. However, these approaches require a dynamic model of the vessel.

3.1.2 Frequency estimation

Frequency estimation of oscillating signals is a well studied problem in the signal processing literature. A discrete-time algorithm for a multifrequency signal based on an adaptive notch filtering was first proposed by Regalia [119]. A continuous-time version of this algorithm was presented in Bodson and Douglas [25], while Hsu et al. [72] have derived a globally convergent continuous-time frequency estimator for a single frequency signal.

An adaptive technique based on the persistency of excitation (PE) of oscillating signals was proposed in Marino and Tomei [97], and extended by Xia [138] and Hou [71]. Two discrete-time algorithms based on PE can also be found in Stotsky [133].

The approach taken by the authors is based on the internal model principle for identification of a single frequency. This was first introduced in Nikiforov [107] and further extended by Aranovskiy et al. [8], Bobtsov [24], and Aranovskiy and Bobtsov [7].

3.1.3 Main contribution

The main result of this chapter is a nonlinear signal-based wave encounter frequency estimator, which effectively estimates the ship wave encounter frequency from heave, pitch or roll motion measurements. The wave encounter frequency estimator under consideration is designed to estimate the frequency of a sinusoid with unknown frequency, amplitude and phase by modifying the algorithm of Aranovskiy et al. [8] to include an adaptive gain-switching mechanism. The frequency estimator with gain-switching mechanism is shown to have GES error dynamics even for signals with a time-varying amplitude.

The main motivation for introducing a gain-switching mechanism is that it is important to improve the convergence of the estimator in situations with little excitation (e.g. small roll and pitch angles) and vice versa. Typical applications are marine craft control and decision-support systems where it is important to

know the sea state and wave frequency. The wave encounter frequency estimator is experimentally verified through towing tank tests in both regular and irregular waves. The estimator is also verified for 9-hours of data gathered onboard the container vessel *Clara Maersk* during a storm across the North Atlantic Ocean.

The wave estimator is implemented in real-time and consequently it is much faster than the real-time requirement of the ship autopilot and DP control systems, which typically samples data at 1–10 Hz. FFT is an off-line algorithm, which use batches of data (moving window). The computational footprint is higher and significantly affected by the acquisition time and numerical processing of the data.

3.1.4 Organization of the chapter

This chapter is organized as follows: In Section 2 the wave encounter frequency estimation problem is introduced and the Aranovskiy fixed-gain frequency estimator is reviewed. Section 3 presents the switching-gain frequency estimator and GES of the equilibrium point of the estimation error dynamics is proven. Section 4 contains experimental verification using towing tank experiments and full-scale data of a container ship. The material in this chapter is based on Belleter et al. [19] and Belleter et al. [20].

3.2 Estimation of the Wave Spectrum Encounter Frequency

Characterization of the sea state for marine operations is generally done in terms of a limited number of fundamental parameters, which are used to calculate approximations of the wave spectrum. Those parameters are the significant wave height H_s, the wave modal frequency (peak frequency) ω_0, and the wave encounter angle β_e that is the relative angle between the vessel heading and the the main direction of the wave train. Knowledge of those parameters may reveal to be of extreme importance in order to schedule and perform activities at sea in a safe, reliable and cost effective manner.

For vessels in transit at forward speed $U > 0$ the experienced wave excitation does not occur at the modal frequency ω_0 because of the *Doppler shift*. The frequency observed from the vessel in motion is given by:

$$\omega_e(\omega_0, U, \beta_e) = \left| \omega_0 - \frac{\omega_0^2}{g} U \cos(\beta_e) \right| \tag{3.1}$$

which is known as the wave encounter frequency. Awareness about ω_e would allow performance enhancement of ship control systems. For instance autopilots and DP systems use wave filters, which are tuned to suppress oscillations at the encounter frequency, in order to reduce the workload of the steering and propulsion systems.

Although waves are usually described as narrow-band stochastic processes, the associated spectrum is certainly richer in frequency content than a single sinusoid. Nevertheless spectral analysis of wave-induced vessel motions usually displays a dominant frequency associated with the peak of the spectrum. During the transient the natural frequencies of the different modes can be observed in the spectrum

giving rise to multiple peaks. However, If the waves are large enough the ship will oscillate at ω_e in all 6 degrees-of-freedom in steady state. For multi-peaked wave spectra with a dominant peak the proposed method will provide an estimate close to the frequency of the highest peak. Analytically the problem can be formulated as:

Problem definition (Wave encounter frequency estimation)
Given the signal in the form:

$$y(t) = A(t)\sin(\omega_e t + \epsilon) \tag{3.2}$$

with $A(t)$ the unknown amplitude, ω_e the unknown frequency and ϵ the unknown phase, reconstruct on-line the frequency ω_e based solely on noisy measurements of $y(t)$.

3.2.1 The Aranovskiy fixed-gain frequency estimator

Before presenting the main contribution of the chapter (Theorem 3.1), we first review the signal-based frequency estimator proposed by Aranovskiy et al. [8], which is instrumental in our design.

The sinusoidal signal (3.2) can be represented by the differential equation:

$$\ddot{y} = \varphi y \tag{3.3}$$

where $\varphi := -\omega_e^2$ is treated as an unknown parameter. The frequency ω_e of the signal (3.2) can be estimated using an auxiliary filter [7]:

$$\dot{\zeta}_1 = \zeta_2 \tag{3.4}$$
$$\dot{\zeta}_2 = -2\omega_f\zeta_2 - \omega_f^2\zeta_1 + \omega_f^2 y \tag{3.5}$$

where the filter cut-off frequency must be chosen such that $0 < \omega_e < \omega_f$. The transfer function corresponding to (3.4)–(3.5) is found by Laplace transformation:

$$\zeta_1(s) = \frac{\omega_f^2}{(s+\omega_f)^2} y(s) \tag{3.6}$$

From (3.3) it follows that $s^2 y(s) = \varphi y(s)$ and

$$\begin{aligned} y(s) &= \frac{\varphi + 2\omega_f s + \omega_f^2}{(s+\omega_f)^2} y(s) \\ &= \frac{2\omega_f s + \omega_f^2 + \varphi}{\omega_f^2} \zeta_1(s) \end{aligned} \tag{3.7}$$

Transforming this expression to the time domain gives:

$$y = \frac{1}{\omega_f^2}\left(2\omega_f\zeta_2 + \omega_f^2\zeta_1 + \varphi\zeta_1\right) \tag{3.8}$$

The Aranovskiy et al. [8] parameter update law for φ uses the computed measurement:

$$y' := \dot{\zeta}_2 = -2\omega_f \zeta_2 - \omega_f^2 \zeta_1 + \omega_f^2 y = \varphi \zeta_1 \tag{3.9}$$

Let $\hat{\varphi}$ denote the parameter estimate and define:

$$\hat{y}' := \hat{\varphi} \zeta_1 \tag{3.10}$$

The parameter update law is chosen as:

$$\dot{\hat{\varphi}} = k_0 \, \zeta_1 (y' - \hat{y}') \tag{3.11}$$

where $k_0 > 0$ is the constant observer gain. Consequently, the resulting frequency estimator becomes:

$$\dot{\zeta}_1 = \zeta_2 \tag{3.12}$$

$$\dot{\zeta}_2 = -2\omega_f \zeta_2 - \omega_f^2 \zeta_1 + \omega_f^2 y \tag{3.13}$$

$$\dot{\hat{\varphi}} = k_0 \, \zeta_1 (\dot{\zeta}_2 - \hat{\varphi} \zeta_1) \tag{3.14}$$

The differential equation for the parameter estimation error $\tilde{\varphi} = \varphi - \hat{\varphi}$ where φ is assumed to be constant becomes:

$$\dot{\tilde{\varphi}} = -k_0 \, \zeta_1^2 \tilde{\varphi} \tag{3.15}$$

The wave component (3.2) has a positive amplitude $0 < A_{\min} \leq A$ for $\forall t \geq 0$ and frequency $\omega_e > 0$. For frequencies $\omega_e < \omega_f$, the time-domain solution of (3.6) for a sinusoidal input (3.2) is $\zeta_1 = A \sin(\omega_e t + \epsilon_1)$ where ϵ_1 is the phase. The signal ζ_1 is persistently exciting (PE) since there exist a positive μ and T such that

$$\mu \leq \int_t^{t+T} \zeta_1^2 (\tau) \, \mathrm{d}\tau, \quad \forall t \geq 0 \tag{3.16}$$

The PE-condition (3.16) is used to prove that the the equilibrium point of the estimation error dynamics (3.15) is GES for constant adaptation gain $k_0 > 0$ and $A > 0$. This result will be generalized to time-varying adaptation gain and wave amplitude in Section 3.

The solutions of (3.15) satisfy:

$$\begin{aligned} \|\tilde{\varphi}\| &= \|\tilde{\varphi}(t_0)\| e^{-k_0 \int_{t_0}^t \zeta_1^2(\tau) \, \mathrm{d}\tau} \\ &= \|\tilde{\varphi}(t_0)\| \, e^{-k_0 \int_{t_0}^t A^2 \sin^2(\omega_e \tau + \epsilon_1) \, \mathrm{d}\tau} \end{aligned} \tag{3.17}$$

with

$$\begin{aligned} \int_{t_0}^t A^2 \sin^2(\omega_e \tau + \epsilon_1) \, \mathrm{d}\tau = \frac{A^2}{2}(t - t_0) - \frac{A^2}{4\omega_e} \sin(2\omega_e t + 2\epsilon_1) \\ + \frac{A^2}{4\omega_e} \sin(2\omega_e t_0 + 2\epsilon_1) \end{aligned} \tag{3.18}$$

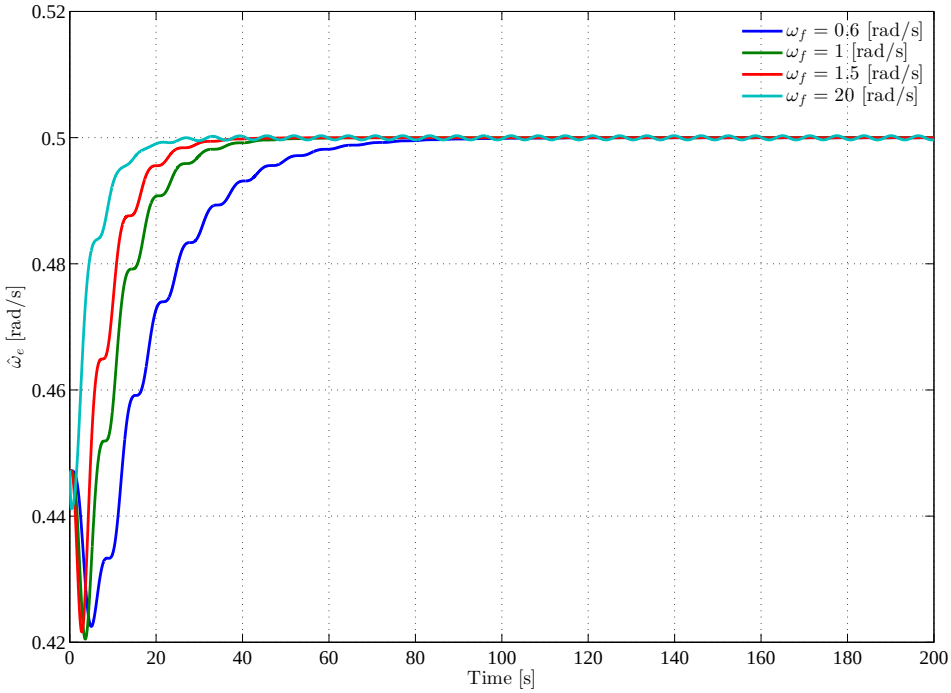

Figure 3.1: Frequency estimates using different cut-off frequencies ω_f.

Substituting (3.18) in (3.17) gives:

$$\begin{aligned} \|\tilde{\varphi}\| &= \|\tilde{\varphi}(t_0)\| \, e^{-\frac{k_0 A^2}{2}(t-t_0)} e^{\frac{k_0 A^2}{4\omega_e}[\sin(2\omega_e t + 2\epsilon_1) - \sin(2\omega_e t_0 + 2\epsilon_1)]} \\ &\leq c \, \|\tilde{\varphi}(t_0)\| \, e^{-\lambda(t-t_0)} \end{aligned} \tag{3.19}$$

where $c = e^{k_0 A^2/2\omega_e} > 0$ and $\lambda = k_0 A^2/2 > 0$. Hence, by Khalil [82, Definition 4.5], given in Appendix A as Definition A.4, the equilibrium point $\tilde{\varphi} = 0$ of (3.15) is GES.

3.2.2 Filter cut-off frequency

The choice of the cut-off frequency ω_f should be made based on desired performance – i.e. convergence rate and steady-state error – and noise filtering capabilities. ω_f clearly influences the convergence rate of the estimator as shown in Figure 3.1, where the frequency of a sinusoidal function oscillating at 0.5 [rad/s] is estimated for increasing value of the cut-off frequency. Small cut-off frequencies result in a slow convergence rate. However, higher cut-off frequencies introduce some oscillations in steady state, as visible from the estimate done with $\omega_f = 20$ [rad/s]. It is interesting to note that moderately increasing the cut-off frequency can significantly increase the convergence rate while the increase in steady-state error is negligible.

3.3 Switching-Gain Wave Encounter Frequency Estimator

The GES stability proof for the Aranovskiy frequency estimator (Section 3.2.1) is based on a constant observer gain $k_0 > 0$. For marine craft the roll and pitch angles may be quite small when operating in low sea states. Consequently, it is advantageous to switch between a high and low gain in the parameter update law depending on the amplitude of the pitch angle. In Belleter et al. [19] it was shown that the frequency estimator (3.14) could be modified to include a switching gain $k(A)$, which depends on the amplitude A of the measured signal. Moreover,

$$k(A) = \begin{cases} k_{\text{init}} & \text{if}, t \leq t_{\text{init}} \\ k_{\min} & \text{if}, t > t_{\text{init}} \ \wedge \ A > A_0 \\ k_{\max} & \text{if}, t > t_{\text{init}} \ \wedge \ A \leq A_0 \end{cases} \tag{3.20}$$

Here $k_{\text{init}} \geq k_{\min} > 0$ is the initial gain used to increase the convergence rate at start up. During normal operation the gain is switched between the positive gains $k_{\min}$ and $k_{\max}$. Moreover, the gain $k(A)$ will switch to the high value if the amplitude $A \leq A_0$ and to the low gain when $A > A_0$.

To implement the switching mechanism (3.20) online we need to know the amplitude A of the measured signal y. Since we cannot measure A an estimator based on the squared signal of (3.2) can be used for switching. Moreover,

$$y^2 = \frac{A^2}{2}(1 - \cos(2\omega_e t + 2\epsilon)) \tag{3.21}$$

The signal (3.21) can be low-pass filtered to obtain the amplitude $A^2/2$ of the squared signal y^2. For instance,

$$\chi = \frac{1}{Ts + 1} y^2 \tag{3.22}$$

where $T > 0$ implies that the estimated amplitude becomes:

$$\hat{A} = \sqrt{2\chi} \tag{3.23}$$

3.3.1 Wave encounter frequency estimator with switching-gain

The results are in this section extended to be GES for time-varying wave amplitude $A(t)$ and adaptation gain $k_f(t)$ by introducing a low-pass filter for the gain $k(\hat{A})$ according to:

$$T_f \dot{k}_f + k_f = k(\hat{A}) \tag{3.24}$$

where $T_f > 0$ is the filter time constant and $k(\hat{A}) \leq \max(k_{\max}, k_{\text{init}})$. The parameter update law (3.14) is modified according to:

$$\dot{\hat{\varphi}} = k_f \, \zeta_1 \left(\dot{\zeta}_2 - \zeta_1 \hat{\varphi} \right) \tag{3.25}$$

and GES is guaranteed by Theorem 3.1, which is presented below. The effect of low-pass filtering on the gain switching is illustrated in Figure 3.2.

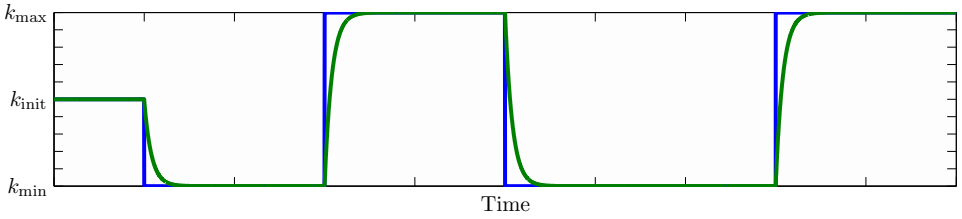

Figure 3.2: Illustration of low-pass filtered gain changes for step inputs $k(\hat{A})$.

Theorem 3.1 (GES switching-gain estimator). *Let the time-varying wave amplitude satisfy* $0 < A_{\min} \leq A(t)$ *for all* $t \geq 0$. *Assume that* $\varphi = -\omega_e^2$ *is constant and that* $k_f(t)$ *is the solution of* (3.24) *for* $T_f > 0$ *and step input* $k(\hat{A})$ *given by* (3.20). *Then the equilibrium point* $\tilde{\varphi} = 0$ *of the estimation error dynamics:*

$$\dot{\tilde{\varphi}} = -k_f \, \zeta_1^2 \tilde{\varphi} \tag{3.26}$$

is GES.

Proof. From Formulae (3.20) and (3.24) it follows that $0 < k_{\min} \leq k_f(t) \leq k_{\max}$ for all $\hat{A}$. The solutions of (3.26) satisfy:

$$\begin{aligned} \|\tilde{\varphi}\| &= \|\tilde{\varphi}(t_0)\| e^{-\int_{t_0}^{t} k_f \zeta_1^2(\tau) \, \mathrm{d}\tau} \\ &\leq \|\tilde{\varphi}(t_0)\| \, e^{-k_{\min} \int_{t_0}^{t} A^2 \sin^2(\omega_e \tau + \epsilon_1) \, \mathrm{d}\tau} \\ &\leq \|\tilde{\varphi}(t_0)\| \, e^{-k_{\min} A_{\min}^2 \int_{t_0}^{t} \sin^2(\omega_e \tau + \epsilon_1) \, \mathrm{d}\tau} \end{aligned} \tag{3.27}$$

Application of (3.18) to (3.27) gives:

$$\begin{aligned} \|\tilde{\varphi}\| &\leq \|\tilde{\varphi}(t_0)\| \, e^{-\frac{k_{\min} A_{\min}^2}{2}(t - t_0)} e^{\frac{k_{\min} A_{\min}^2}{2\omega_e}} \\ &\leq c \, \|\tilde{\varphi}(t_0)\| \, e^{-\lambda(t - t_0)} \end{aligned} \tag{3.28}$$

where $c = e^{k_{\min} A_{\min}^2 / 2\omega_e} > 0$ and $\lambda = k_{\min} A_{\min}^2 / 2 > 0$. Hence, by Khalil [82, Definition 4.5], given in Appendix A as Definition A.4, the equilibrium point $\tilde{\varphi} = 0$ of (3.26) is GES. □

3.3.2 Low-pass filtering of the wave encounter frequency estimate

Since the measured ship motions in general display a non-pure sinusoidal behaviour due to the narrow-band spectral characteristic of the wave motions, the estimate $\hat{\varphi}$ provided by (3.25) will show high-frequency fluctuations as a result. Therefore, if the encounter frequency estimator is to be used in applications such as adaptive wave filtering or gain-scheduling control, the high-frequency variations are certainly undesirable since they may introduce chattering in the system. A straightforward solution to this problem is to apply a low-pass filter at the output of the estimator

(3.25), to obtain a running mean of the encounter frequency estimate. Consider the system:

$$\dot{\hat{\varphi}} = k_f\, \zeta_1 \left(\dot{\zeta}_2 - \zeta_1 \hat{\varphi} \right) \tag{3.29}$$

$$\dot{\boldsymbol{\varphi}}_f = \mathbf{A}\boldsymbol{\varphi}_f + \mathbf{b}\hat{\varphi} \tag{3.30}$$

where $\boldsymbol{\varphi}_f \in \mathbb{R}^n$ is the vector whose first component $\varphi_{f,1}$ is the low-pass filtered $\hat{\varphi}$. The *Hurwitz* design matrix $\mathbf{A}$ and the vector $\mathbf{b} = [0, 0, 0, \ldots, 1]^{\mathrm{T}}$ define the low-pass filter. By rewriting (3.29) in terms of the estimation error $\tilde{\varphi}$, and by applying a change of coordinates $\boldsymbol{\xi} = \boldsymbol{\varphi}_f + \mathbf{A}^{-1}\mathbf{b}\varphi$ the following cascaded system is obtained:

$$\Sigma_1 : \quad \dot{\tilde{\varphi}} = -k_f\, \zeta_1^2 \tilde{\varphi} \tag{3.31}$$

$$\Sigma_2 : \quad \dot{\boldsymbol{\xi}} = \mathbf{A}\boldsymbol{\xi} + \mathbf{b}\tilde{\varphi} \tag{3.32}$$

GES of the cascade Σ_1–Σ_2 is guaranteed by Corollary 3.2.

Corollary 3.2 (GES cascade)**.** *The origin of the cascade Σ_1–Σ_2 is GES.*

Proof. The origin of (3.31) is GES according to Theorem 3.1. For $\tilde{\varphi} = 0$ the differential equation (3.32) reduces to $\dot{\boldsymbol{\xi}} = \mathbf{A}\boldsymbol{\xi}$ (nominal system) whose origin is GES since $\mathbf{A}$ is *Hurwitz*. In addition, the linear growth condition $\|\mathbf{b}\tilde{\varphi}\| \leq |\tilde{\varphi}|$ is satisfied for all $\tilde{\varphi}$. Hence, according to Loría and Panteley [94, Theorem 2.1, Proposition 2.3], see Theorem A.3 and Proposition A.1 in Appendix A, the origin of the cascade Σ_1–Σ_2 is GES. □

3.4 Experimental Verification

The performance of the estimator (3.20)–(3.25) in Section 3.3 is tested on experimental and full-scale data using heave and pitch data. This to demonstrate that the wave frequency estimator performs equally well for both signals. Operationally this will provide flexibility for the operator, which could use measurements provided by either a heave accelerometer or a pitch rate gyro. First, the wave encounter frequency estimator is applied to experimental data gathered through towing tank experiments. Subsequently, the estimator is applied to full-scale sea trial data gathered aboard the container vessel *Clara Maersk* in an Atlantic passage during a storm.

3.4.1 Towing tank experiments

The experimental data considered here was gathered through towing tank tests with a 1:45 scale model of 281[m] long container ship with volume displacement 76 000[m]^3 (see Figure 3.3). The detailed model and all the hydrodynamic coefficients can be found in Holden et al. [70].

The experimental conditions are reported in Table 3.1. For the regular wave experiments (R–1173 and R–1189) ω_0 is the wave frequency and H_w is the wave amplitude. For the irregular wave experiment (I–1195) ω_0 is the peak wave frequency and H_w is the significant wave height. U and ω_e are the ship forward speed and the wave encounter frequency, respectively.

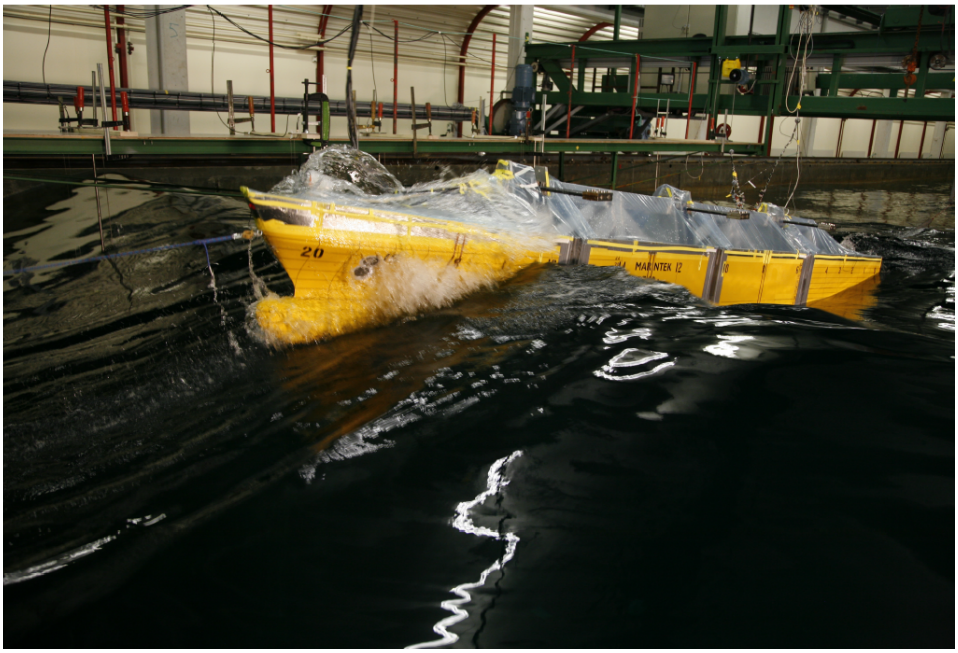

Figure 3.3: Model ship in the towing tank. Photo courtesy of Dr I. Drummen.

Table 3.1: Towing-tank experiment (full scale equivalents)

Exp.	U [m/s]	ω_0 [rad/s]	H_w [m]	ω_e [rad/s]
R–1173	5.4806	0.4425	2.5	0.5519
R–1189	7.6675	0.4640	2.5	0.6324
I–1195	6.0240	0.4640	9	0.5963

Comparative study of the fixed and variable gain estimators

The data set R-1173 is used for comparing the performance of the Aranovskiy fixed-gain frequency estimator with the proposed switching-gain solution (Theorem 1). This data set is well suited for this comparison because the amplitude variations of the pitch angle emphasizes the importance of the switching mechanism. The parameters settings for both estimators can be fond in Table 3.2. Note that the value of k_0 is chosen equal to $k_{\min}$. This choice guarantees a small steady-sate error during the first 15 minutes of the measurement where the pitch angle shows large amplitudes.

Figure 3.4 illustrates the results of the comparative study. The use of the very large initialization gain k_{init} (Figure 3.4(b)) boosts the convergence rate of the switching-gain estimator, which settles to the true value of the encounter frequency approximately 4 minutes before the fixed-gain estimator (Figure 3.4(c)). After both filters have converged they have the same gain, and hence the same small steady-state error. When the encounter frequency changes the estimators initially converge

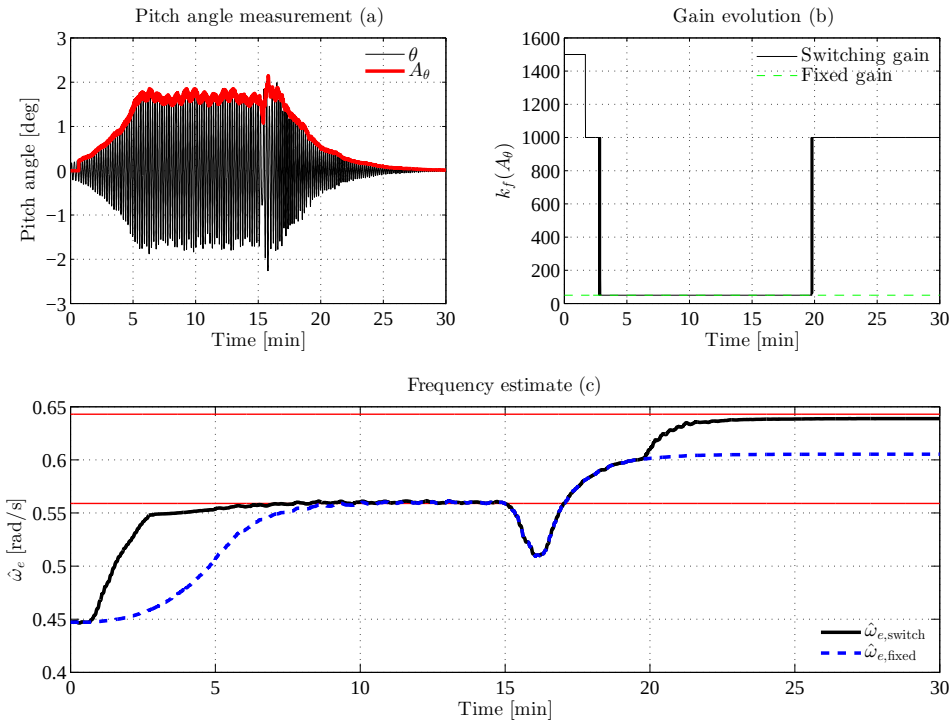

Figure 3.4: Comparison of the frequency estimator with and without a gain switching mechanism.

Table 3.2: Parameter settings for the comparative study.

Quantity	**Symbol**	**Value**	**Unit**
Switching time constant	T_f	0.05	s
Filter cut-off frequency	ω_f	1	rad/s
Switching amplitude pitch	$A_{\theta,0}$	0.01	rad
Initialization time	t_{init}	100	s
Initialization gain	k_{init}	1500	-
Filter low gain	k_{low}	50	-
Filter high gain	k_{high}	1000	-
Fixed gain	k_{fixed}	50	-

to the new value at the same rate. However, when the amplitude gets below the switching threshold A_0 the switching-gain estimator switches to the much high gain $k_{\max}$, as shown in Figure 3.4(b). This allows faster convergence towards the correct frequency before the excitation becomes too small. The fixed-gain estimator does not converge to the true value because the gain is to small for limited excitation.

Table 3.3: Switching-gain estimator parameter settings for towing-tank data.

Quantity	Symbol	Value	Unit
Switching time constant	T_f	0.05	s
Filter cut-off frequency	ω_f	1	rad/s
Switching amplitude pitch	$A_{\theta,0}$	0.01	rad
Switching amplitude heave	$A_{z,0}$	0.6	m
Initialization time	t_{init}	100	s
Initialization gain	k_{init}	500	-
Filter low gain	$k_{\min}$	250	-
Filter high gain	$k_{\max}$	1000	-

Performance assessment on towing tank data

The estimator is tested on pitch and heave measurements gathered during experiments R–1173 and R–1189, and on a heave measurement gathered during the experiment I–1195. The settings for the filter and gain switching parameters are given in Table 3.3.

At the first the frequency estimator is tested on a measurement of the pitch angle $\theta(t)$, as shown in Figure 3.5(a). The 30 minutes long time series is obtained by joining the pitch angles measured in experiments R–1173 and R–1189, and the last 15 minutes of the recording have been amplitude modulated through a decaying exponential function. This behaviour has been appositely introduced in order to test the capability of the estimator to track frequency variations in vanishing signals.

The spectral analysis shown in Figure 3.5(b) clearly shows a frequency shift between the first 15 minutes of the experiments and the second ones in total agreement with the data reported in Table 3.1. Moreover, the nature of the excitation used in the regular wave experiments determines a very narrow-band power spectral density (PSD) denoted $\Theta(\omega)$, and this will ease the estimation process.

The estimate of the wave encounter frequency $\hat{\omega}_e$ and the changes in the gain k_f can be seen in Figures 3.5(c)–(d). The two horizontal lines in the frequency estimate plot correspond to the peaks in the PSD's. Figure 3.5(c) shows that the estimate $\hat{\omega}_e$ rapidly converges to the frequency associated to the largest peak of $\Theta_1(\omega)$. During the transition to the exponential decaying pitch angle the frequency estimate drops to values in the neighborhood of the small side-lobe of the PSD $\Theta_2(\omega)$ and then converges to the frequency value associated with the largest peak of $\Theta_2(\omega)$.

Figure 3.6(a) presents the measurement of the heave displacement $z(t)$ recorded during the regular wave experiments. The power spectral density $Z(\omega)$ shown in Figure 3.6(b) obviously confirms the position of the peak frequencies already identified in the PSD of the pitch angle. The estimate of the wave encounter frequency is not as sharp as seen in relation to the pitch measurement, as shown in Figure 3.6(c). This reduced precision in estimating the correct value of ω_e may be explained by the presence of side lobs in both PSDs $Z_1(\omega)$ and $Z_2(\omega)$. If fact for both tranches of the heave measurement the estimate $\hat{\omega}_e$ is pulled towards slightly higher frequency values clearly addressing the influence of the side lobes in the estimation process. Last, Figure 3.6(d) shows that the switching-gain strategy is

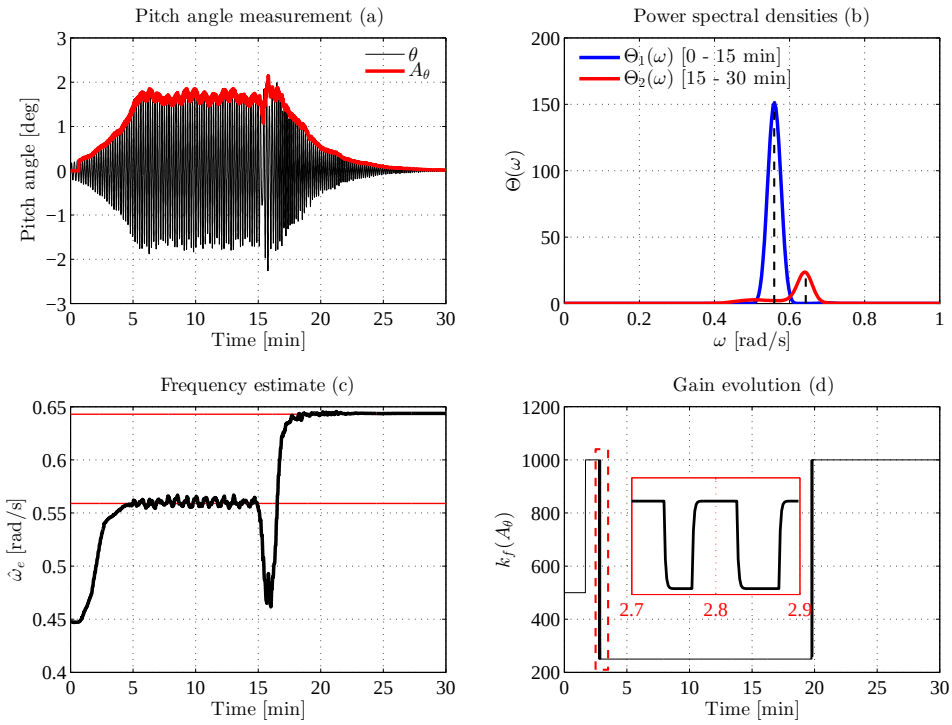

Figure 3.5: Test I: estimation of wave encounter frequency from exponentially modulated pitch angle measurements collected during regular wave experiments R–1173 and R–1189. The estimator rapidly converges to and track the peak frequency of the power spectral density $\Theta(\omega)$.

very active due to the large variability of the heave amplitude A_z.

At last the switching-gain frequency estimator is tested on measurements of the heave displacement recorded during the irregular waves experiment I–1195, as shown in Figure 3.7(a). The large significant wave height together with the irregular pattern of the wave train exciting the vessel determine repeated large and asymmetric variations of the heave displacement. This behaviour largely differs from the sinusoidal one and challenges the frequency estimator, as shown in Figure 3.7(c). The estimate $\hat{\omega}_e$ of the encounter frequency shows larger variations as a result of the broader frequency range the power spectral density $Z(\omega)$ spans over. Moreover the presence of multiple peaks of almost equal magnitude in the PSDs, as for $Z_2(\omega)$ and $Z_3(\omega)$, increases the difficulty of identifying the main frequency carrier.

Figure 3.7(c) shows that the estimator slightly overestimates the peak frequency of $Z_1(\omega)$, which can be explained by the skewness of the PSD towards the higher frequencies. Between 6 and 12 minutes the estimates varies between 0.5 and 0.7 [rad/s], which can be expected since $Z_2(\omega)$ shows not clear dominant peak during this time interval. For the last 5 minutes $\hat{\omega}_e$ first oscillates around 0.6 [rad/s], and than decreases to around 0.5 [rad/s], which once again nearly matches the location

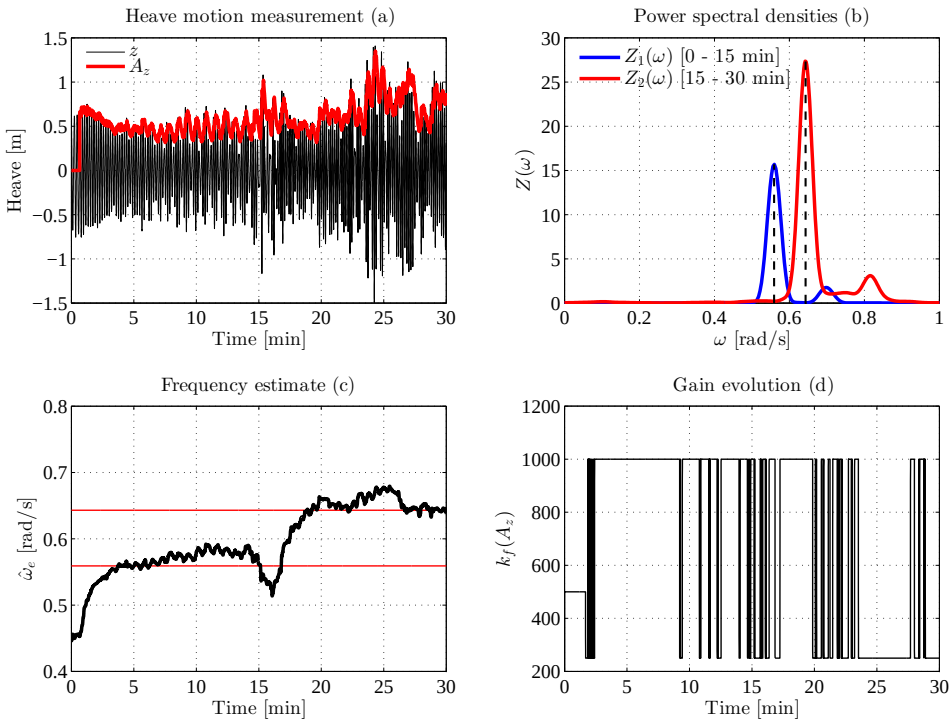

Figure 3.6: Test II: estimation of wave encounter frequency from heave displacement measurements collected during regular wave experiments R–1173 and R–1189. The encounter frequency estimator converges towards the true value of the two main peak frequencies of $Z(\omega)$, however the presence of side lobs in the power spectral density influences the estimation process pulling $\hat{\omega}_e$ towards slightly higher values.

Table 3.4: Switching-gain estimator parameter settings for full-scale data.

Quantity	**Symbol**	**Value**	**Unit**
Switching time constant	T_f	0.05	s
Filter cut-off frequency	ω_f	1	rad/s
Switching amplitude pitch	$A_{\theta,0}$	0.01	rad
Initialization time	t_{init}	100	s
Initialization gain pitch angle	k_{init}	50	-
Filter low gain pitch angle	k_{min}	25	-
Filter high gain pitch angle	k_{max}	100	-

of the two peaks of the power spectral density $Z_3(\omega)$.

In order to reduce these fluctuations a low-pass filter is added at the output of the switching-gain estimator. This smooths the behaviour of the frequency estimate of the encounter wave, which now stays much closer to the true value at all times, as shown by the green line in Figure 3.7(c).

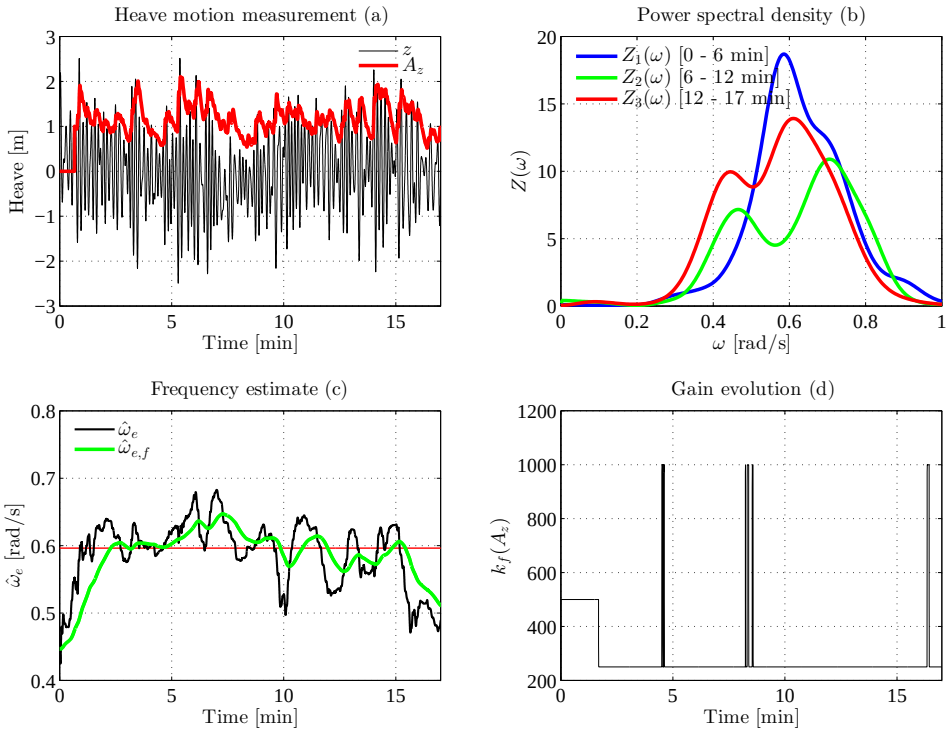

Figure 3.7: Test III: estimation of wave encounter frequency from heave displacement measurements collected during irregular wave experiment I–1195. The encounter frequency estimator converges towards the true value of the two main peak frequencies of $Z(\omega)$, however the presence of side lobs in the power spectral density influences the estimation process pulling $\hat{\omega}_e$ towards slightly higher values.

3.4.2 Atlantic passage full-scale data

The final test of the switching-gain frequency estimator is run on a data set of full-scale ship motions' data recorded on board the container ship *Clara Maersk* crossing the North Atlantic Ocean during a storm. The length of the vessel was 197[m] and its displacement volume was 33 000[m]^3. Time series used here correspond to the pitch angle recorded during nine hours of navigation. Due to the larger amplitudes induced by the stormy weather different settings of the gain switching mechanism have been chosen. The settings for the filter and the gain switching mechanism are given in Table 3.4.

Performance assessment on full-scale data

The measurement of the pitch angle aboard the ship is presented in Figure 3.8(a). The measurements show that the amplitude of the pitch angle is fairly constant over a long period of time, with the exception of few larger peaks. Figure 3.9 presents

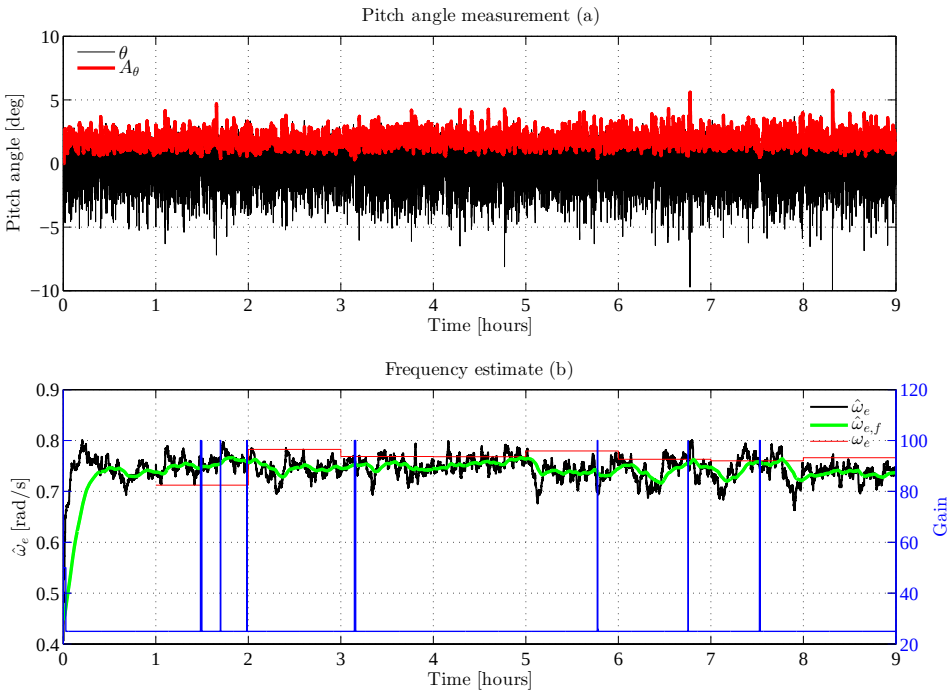

Figure 3.8: Test IV: estimation of wave encounter frequency from pitch angle measurements collected aboard *Clara Maersk* during a passage through the North Atlantic. The wave encounter frequency estimator succeeds in rapidly identifying the range of frequencies where the dominant spectral components fall into.

the evolution of the pitch power spectral density $\Theta(\omega)$ over the nine hours, and the wave encounter frequency identified as the frequency of the largest peak of each PSD. The power spectral density spans over a very broad range of frequencies with a multitude of peaks; however, the main spectral components are in the range 0.7–0.8 [rad/s].

The estimate of the encounter frequency based on the pitch measurement is given in Figure 3.8(b), which shows that $\hat{\omega}_e$ is also in the range 0.7–0.8 [rad/s]. Comparing the estimate of the encounter frequency with ω_e identified through the analysis of the power spectral density it can be noted that $\hat{\omega}_e$ converges to values in close proximity to ω_e. Application of a low-pass filter to the output of the switching-gain frequency estimator helps in smoothing the obtained frequency estimate. Figure 3.8(b) also shows the switching gain strategy. Since the amplitude A_θ of the measured pitch angle is rather constant and sufficiently exciting for rapid adaptation there are only few gain switches.

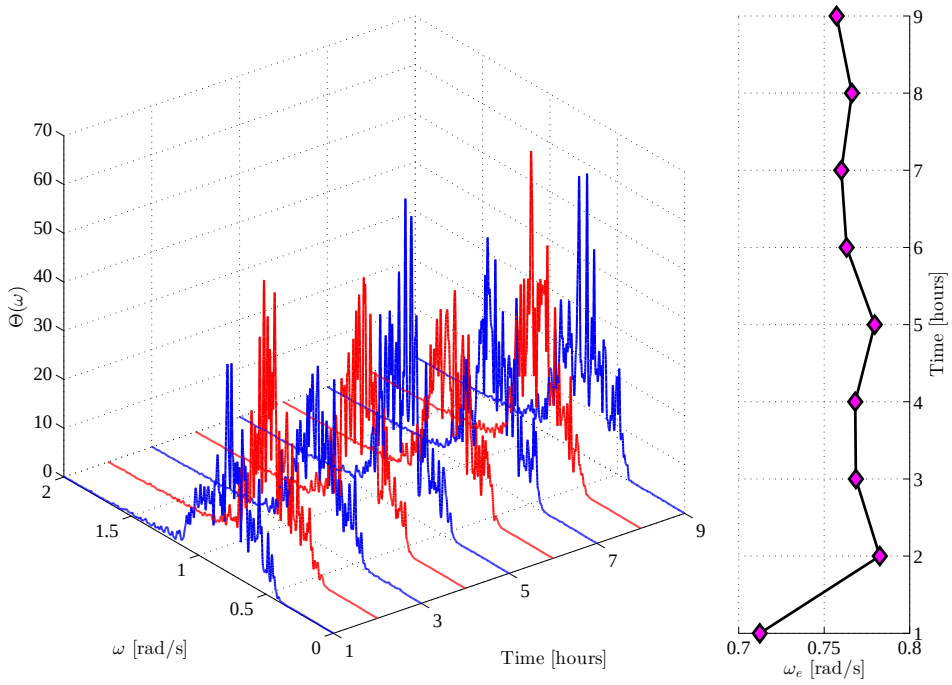

Figure 3.9: Evolution of the pitch power spectral density over 9 hours of navigation across a storm.

3.5 Conclusions

Knowledge of the parameters characterizing the sea state is of extreme value in order to carry out marine operations in a safe, reliable and cost effective ways. This chapter has derived a signal-based nonlinear observer for the estimation of the wave encounter frequency. The kernel of the designed estimator is a second-order nonlinear observer with a switching-gain mechanism designed to estimate the frequency of a sinusoid with unknown frequency, amplitude and phase. The origin of the estimation error dynamics is proven to be global exponentially stable.

The frequency estimator has been extensively tested on model-scale motion data of a container ship gathered during towing tank experiments in regular and irregular waves, and on full-scale motion data of a container ship recorded in an Atlantic passage during a storm. In all scenarios the nonlinear switching-gain frequency estimator succeeds in identifying the frequency range where the encounter frequency falls into. Extremely good results in terms of fast convergence and tracking are obtained for the model-scale data collected in the regular wave experiments, since the ship responses in pitch and heave closely resemble pure sinusoidal signals. The broadening of the spectral content of the heave and pitch responses recorded in the irregular wave experiment and in the sea trial clearly challenges the capabilities of the observer to converge to the true value of the wave encounter frequency. Nev-

ertheless, the frequency estimator achieves its objective, by providing an estimate within the frequency range where the main spectral components are.

Acknowledgment

Data from model tests were kindly provided by Dr I. Drummen (Maritime research institute Netherlands), Professor T. Perez (Queensland University of Technology) and Dr G. Storhaug (DNV-GL). Data from the Atlantic passage were provided by Professor M. Blanke (Technical University of Denmark) and they were presented with the permission from Maersk Lines.

Part II

Multi-Vehicle Path Following

Chapter 4

Straight-Line Coordinated Path-Following for Underactuated Marine Vessels in the Presence of Ocean Currents

In this chapter the straight line path-following problem is considered for formations of underactuated marine vessels. The vessels are affected by a constant ocean current that is bounded and irrotational with respect to the inertial frame. This is a problem of interest in applications such as sea-bed scanning or measuring of environmental parameters, since in such applications the vehicles have to cover an area often by performing a lawn-mover pattern with long straight-line sections. Hence, by using multiple vehicles a large area can be covered at once, reducing the time and costs of the operation. A Line-of-Sight (LOS) guidance law with two feedback linearising controllers is used to achieve path following of each individual vessel. Integral action is added to the LOS guidance law to compensate the effects of the ocean current acting on each vessel. In addition to the individual geometric task of path convergence, the vessels must also achieve the formation control task. More specifically, the vessels have to move along the desired path with a specified relative inter-vessel distance and with a constant desired velocity. This task is accomplished using a nonlinear coordination law. The closed-loop dynamics are analysed using theory that allows the analysis of feedback-interconnected systems as cascaded systems under certain conditions Loría [93]. It is shown that the origin of the closed-loop error dynamics of the combined path-following dynamics and formation dynamics is uniformly globally asymptotically stable. Simulation results are presented in a case study.

To achieve the goal of coordinated path following, the work aims to unify the results for integral LOS (iLOS) path following for underactuated marine vessels in the presence of ocean currents from Børhaug et al. [30] and Caharija et al. [40], with LOS path-following results for formations of underactuated marine vessels from Børhaug et al. [31]. This is done in order to achieve path-following control of formations of underactuated marine vessels in a two dimensional plane that also

takes into account the ocean currents.

Motivated by [30, 40], and [31] we use a cascaded systems approach. It is interesting to note that the combination of the integral LOS guidance control, which has adaptive properties, together with the formation keeping control, introduces a feedback-loop in the system that is not present when only one of these features is present in the system. The approach of cascaded control used in [30, 40], and [31] can therefore not be directly applied. In particular, the combination of adaptation and formation keeping makes it necessary to "break the loop" [93]. Using this approach, we prove that the origin of the closed-loop error dynamics is uniformly globally asymptotically stable.

The chapter is organized as follows. In Section 4.1 the model of an underactuated surface vessel is given and the control objectives are stated. In Section 4.2 the controllers to solve the control problem are presented. Section 4.3 contains the derivation of the closed-loop system. The main result is formulated and the closed loop is analysed in Section 4.4. A case study is presented in Section 4.5. Finally Section 4.6 gives the conclusions of the work. The material presented in this chapter is based on Belleter and Pettersen [13] and Belleter and Pettersen [15].

4.1 Model

In this chapter underactuated marine surface vessels are considered. Therefore, the model under consideration is the model from Section 2.2. Recall the model can be written in component form as

$$\dot{x} = u_r \cos(\psi) - v_r \sin(\psi) + V_x, \tag{4.1a}$$
$$\dot{y} = u_r \sin(\psi) + v_r \cos(\psi) + V_y, \tag{4.1b}$$
$$\dot{\psi} = r, \tag{4.1c}$$
$$\dot{u}_r = F_{u_r}(v_r, r) - \tfrac{d_{11}}{m_{11}} u_r + \tau_u, \tag{4.1d}$$
$$\dot{v}_r = X(u_r) r + Y(u_r) v_r, \tag{4.1e}$$
$$\dot{r} = F_r(u_r, v_r, r) + \tau_r, \tag{4.1f}$$

The definitions of F_{u_r}, $X(u_r)$, $Y(u_r)$, and F_r are given in Appendix 4.A. Note that $X(u_r)$ and $Y(u_r)$ are bounded for bounded arguments and linear in u_r. We assume the following assumptions are satisfied

Assumption 4.1. The ocean current is assumed to be constant and irrotational with respect to the inertial frame, i.e. $\boldsymbol{V_c} \triangleq [V_x, V_y, 0]^T$. Furthermore, it is bounded by $V_{\max} > 0$ such that $\|V_c\| = \sqrt{V_x^2 + V_y^2} \leq V_{\max}$.

Assumption 4.2. It is assumed that $Y(u_r)$ satisfies

$$Y(u_r) \leq -Y_{\min} < 0, \, \forall u_r \in [-V_{\max}, U_{rd} + a],$$

with U_{rd} the constant desired velocity and a a parameter of the formation control law to be defined later.

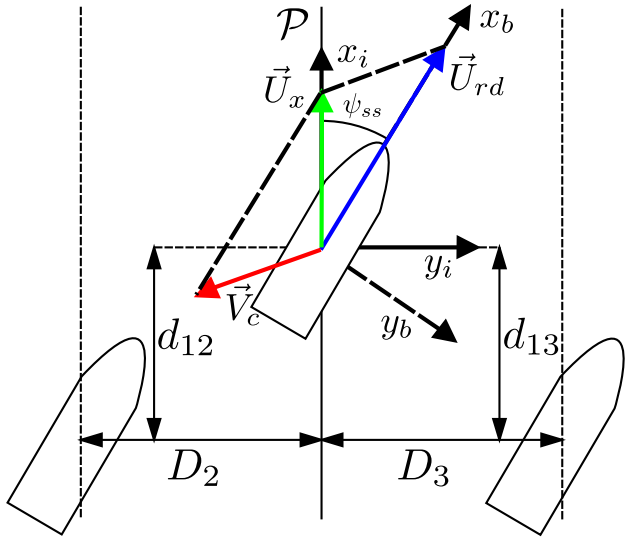

Figure 4.1: Example of a desired formation.

Remark 4.1. This assumption is satisfied for commercial vessels by design, since $Y(u_r) \geq 0$ would imply an undamped or nominally unstable vessel is sway direction.

Assumption 4.3. It is assumed that $V_{\max} + a < U_{rd} < U_{\max} - a$ where $U_{\max}$ is the maximum attainable surge velocity of the vessel.

Remark 4.2. Assumption 4.3 requires that the desired speed of the vessel is higher than the maximum of the ocean current and the constant a which is a parameter of the formation control law. In general, Assumption 4.3 is easily satisfied since vessel propulsion systems are rated for much higher speeds then typical ocean current magnitudes.

4.1.1 Control Objectives

The goal is to coordinate the motion of n vessels along a straight-line path defined as $\mathcal{P} \triangleq \{(x, y) \in \mathbb{R}^2 : y = 0\}$. An example formation is given in Figure 4.1. Note that this definition implies that, without loss of generality, the x-axis of the inertial frame is aligned with the path. The desired potion of jth vessel can than be described by the distance D_j with respect to the path $\mathcal{P}$ and the relative along-path distance d_{ji} with respect to vessel i. This leads to a decentralised control strategy where each vessel determines it's own control input dependent on its own position measurements and that of its neighbours.

$$\lim_{t\to\infty} y_j(t) - D_j = 0, \tag{4.2a}$$

$$\lim_{t\to\infty} \psi_j(t) = \psi_{ss}, \quad \psi_{ss} \in \left(-\tfrac{\pi}{2}, \tfrac{\pi}{2}\right), \tag{4.2b}$$

$$\lim_{t\to\infty} x_j(t) - x_i(t) - d_{ji} = 0, \tag{4.2c}$$

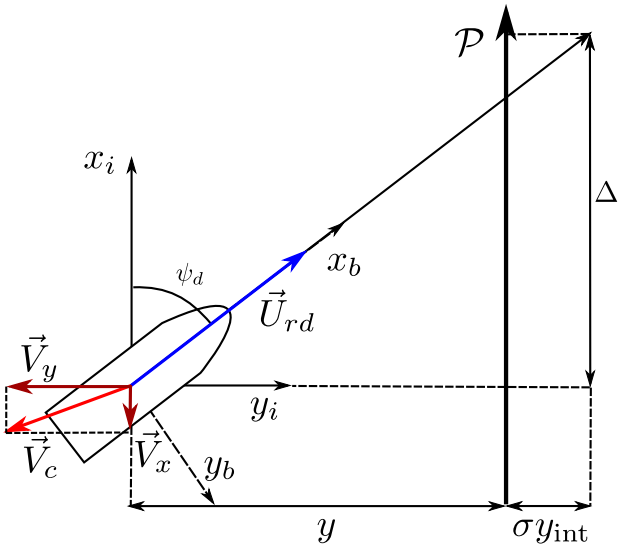

Figure 4.2: Illustration of the integral line-of-sight guidance.

for $i, j = 1, \ldots, n$. Note that according to (4.2b) the desired yaw angle is required to converge to a constant value in the interval $\left(-\frac{\pi}{2}, \frac{\pi}{2}\right)$. This constant side-slip angle, whose magnitude is dependent on the magnitude of the current, is required to compensate for the component of the ocean current perpendicular to the path.

4.2 Guidance Law, Communication Topology and Coordination Law

This section presents the guidance law that is used to steer the vessel to the desired path, the coordination law that is used to achieve the desired along-path distances, and the controllers to achieve the desired values prescribed by the guidance law and coordination law.

4.2.1 Guidance law

The guidance law that is used is an integral line-of-sight guidance law. This guidance law was first introduced by Børhaug et al. [30] and assigns the desired heading angle based on the cross-track error $y - D_j$, an adaptive part to add the integral action that is used to compensate for the unknown ocean current σy_{int}, and the look-ahead distance Δ. Resulting in the desired heading angle assignment:

$$\psi_d \triangleq -\tan^{-1}\left(\frac{(y - D_j) + \sigma y_{\text{int}}}{\Delta}\right), \quad \Delta > 0, \tag{4.3a}$$

$$\dot{y}_{\text{int}} = \frac{\Delta(y - D_j)}{((y - D_j) + \sigma y_{\text{int}})^2 + \Delta^2}, \tag{4.3b}$$

where σ is the integral gain. An illustration of the guidance law can be seen in Figure 4.2. As shown in Børhaug et al. [30] the integral action allows the yaw angle assignment (4.3a) to be non-zero when the vehicle is on the desired path, which in turn allows the vessel to compensate for the ocean current component perpendicular to the path. To reduce the risk of integrator wind-up the integrator update law (4.3b) is defined such that adaptation becomes small when the cross-track error is large. To track the desired yaw angle we apply the following feedback linearising PD controller to (4.1f):

$$\tau_r = -F_r(u_r, v_r, r) + \ddot{\psi}_d - k_\psi(\psi - \psi_d) - k_r(\dot{\psi} - \dot{\psi}_d), \tag{4.4}$$

with $k_\psi > 0$ and $k_r > 0$ constant controller gains. This controller assures that ψ and r exponentially track ψ_d and $\dot{\psi}_d$ respectively.

Remark 4.3. Note that technically implementation of the feedback linearising controller (4.4) used here and in the works of Caharija et al. is not possible with just measurements of the relative velocities, since $\dot{\psi}_d$ contains unknown signals. More specifically, from (4.3a) it can be seen that $\dot{\psi}_d$ contains $\dot{y}$, and from (2.8b) it can be seen that $\dot{y}$ depends on the unknown ocean current component V_y. This can be solved in various ways. The easiest solution is to use measurements of $\dot{y}$ from the GPS for ships and through a DVL with bottom lock for an AUV. Alternatively, an ocean current observer can also be used which is the approach taken in Chapter 7 and Chapter 8 of this thesis. Moreover, it should be noted that for practical applications this problem usually does not arise, since typically existing ASVs and AUVs do not allow force or torque inputs to the control system, but rather have autopilots that only allow the heading angle as input. The control input is thus given by the guidance angle in (4.3a).

4.2.2 Communication topology and coordination law

The control objective (4.2c) is defined in terms of the along-path position of multiple vessels. Hence, the vessels need to communicate their along-path position. Graph theory (see for instance Mesbahi and Egerstedt [98]) is used to describe the communication.

The communication network is represented by a directed graph or digraph $\mathcal{G}(V, E)$, where V is a set of vertices and E a set of edges. The vertices represent the vessels in the formation and the number of vertices is equal to the number of vessels. The edges represent communication channels and are represented by pairs of vertices. More specifically, if there is information transfer from vertex v_i to v_j then the pair $(v_j, v_i) \in E$.

The neighbourhood $\mathcal{A}_j$ of v_j is the set of vertices $v_i \in V$ such that there is an edge from v_j to v_i. Hence, when controlling vessel j only the along-path position x_i of the vessels where $i \in \mathcal{A}_j$ may be used. The above allows us to give some definitions, based on Godcil and Royle [68], that are used in the analysis of the formation dynamics. A vertex $v_k \in V$ reachable from vertex $v_i \in V$ if there is a path from v_i to v_k. A vertex is globally reachable if it can be reached, either directly or indirectly, from every vertex in $\mathcal{G}(V, E)$. The graph is said to be strongly connected, if all vertices of $\mathcal{G}(V, E)$ are globally reachable.

Assumption 4.4. It is assumed the communication graph has at least one globally reachable vertex.

Coordination is achieved by a coordination law at the velocity level using the desired surge speed assignment

$$u_{c_j} = U_{rd} - g\Big(\sum_{i\in\mathcal{A}_j}(x_j - x_i - d_{ji})\Big), \tag{4.5}$$

consisting of the desired constant relative surge velocity U_{rd} and $g(x) : \mathbb{R} \to \mathbb{R}$ should be a continuously differentiable saturation-like function that satisfies

$$\begin{aligned} -a \leq g(x) \leq a, \quad \forall x \in \mathbb{R}, \quad g(0) = 0, \\ 0 < g'(x) \leq \mu, \forall x \in \mathbb{R}, \quad g'(x) \triangleq dg/dx \end{aligned} \tag{4.6}$$

where a is the parameter from Assumptions 4.2 and 4.3, and $\mu > 0$ is an arbitrary constant. This also implies that the function $g(x)$ should be a sector function belonging to the sector $[0, \mu]$. A suitable choice for $g(x)$ is for example

$$g\,(x) \triangleq \frac{2a}{\pi}\tan^{-1}(x)\,. \tag{4.7}$$

To make $u_{r_j}(t)$ track u_{c_j} the following feedback linearising P controller is applied to (4.1d) (omitting the vessel-specific subscript):

$$\tau_u = -F_{u_r}(v_r, r) + \frac{d_{11}}{m_{11}}u_c + \dot{u}_c - k_{u_r}(u_r - u_c), \tag{4.8}$$

with $k_{u_r} > 0$ a constant controller gain.

4.3 The Closed-Loop System

This section presents the closed-loop systems of the model (4.1) with the yaw rate (4.4) and surge velocity (4.8) controllers. First we consider the actuated dynamics for each vehicle and analyse the control errors $\boldsymbol{\xi} \triangleq [\tilde{u}_r, \tilde{\psi}, \tilde{r}]^T$, where $\tilde{u}_r \triangleq u_r - u_c$ is the surge velocity error, $\tilde{\psi} \triangleq \psi - \psi_d$ is the yaw angle error, and $\tilde{r} \triangleq r - r_d$ is the yaw rate error. The derivative of $\boldsymbol{\xi}$ can be found by applying (4.4) and (4.8) to the dynamical system (4.1), resulting in

$$\dot{\boldsymbol{\xi}} = \begin{bmatrix} -k_{u_r} - \frac{d_{11}}{m_{11}} & 0 & 0 \\ 0 & 0 & 1 \\ 0 & -k_\psi & -k_r \end{bmatrix} \triangleq \Sigma\boldsymbol{\xi}. \tag{4.9}$$

The system (4.9) is linear and time-invariant and k_{u_r}, k_ψ, k_r, and d_{11}/m_{11} are strictly positive. Consequently, Σ is Hurwitz and the origin of (4.9) is uniformly globally exponentially stable.

The underactuated part is considered next and we consider the cross-track error kinematics (4.1b), the sway velocity dynamics (4.1e), and the guidance (4.3). To

simplify notation we define $y_j \triangleq y - D_j$ The dynamics of the y_j-v_r subsystem is given by:

$$\dot{y}_{\text{int}} = \frac{\Delta y_j}{(y_j + \sigma y_{\text{int}})^2 + \Delta^2} \tag{4.10}$$

$$\dot{y}_j = (\tilde{u}_r + u_c)\sin(\tilde{\psi} + \psi_d) + v_r \cos(\tilde{\psi} + \psi_d) + V_y \tag{4.11}$$

$$\dot{v}_r = X(\tilde{u}_r + u_c)(\dot{\tilde{\psi}} + \dot{\psi}_d) + Y(\tilde{u}_r + u_c)v_r. \tag{4.12}$$

The equilibrium of the $y_j - v_r$ systems for $u_c = U_{rd}$ satisfies:

$$y_{\text{int}}^{\text{eq}} = \frac{\Delta}{\sigma}\frac{V_y}{\sqrt{U_{rd}^2 - V_y^2}},\ y_j^{\text{eq}} = 0,\ v_r^{\text{eq}} = 0. \tag{4.13}$$

The equilibrium is moved to the origin by defining $e_1 \triangleq y_{\text{int}} - y_{\text{int}}^{\text{eq}}$ and $e_2 \triangleq y_j + \sigma e_1$. Substituting (4.3a) for ψ_d and factorizing the result w.r.t. $\boldsymbol{\xi}$ leads to the interconnected dynamics

$$[\dot{e}_1, \dot{e}_2, \dot{v}_r]^T = \boldsymbol{A}[e_1, e_2, v_r]^T + \boldsymbol{B}f(e_2) + \boldsymbol{C}g(x) - \boldsymbol{H}\boldsymbol{\xi} \tag{4.14a}$$

$$\dot{\boldsymbol{\xi}} = \Sigma\boldsymbol{\xi}. \tag{4.14b}$$

with $\boldsymbol{A}$ as in (4.50) and $\boldsymbol{B}$, $\boldsymbol{C}$, and $\boldsymbol{H}$ defined as:

$$\boldsymbol{B}(e_2) \triangleq \begin{bmatrix} 0 & V_y & -\frac{\Delta X^{u_c} V_y}{(e_2 + \sigma y_{\text{int}}^{\text{eq}})^2 + \Delta^2} \end{bmatrix}^T \tag{4.15}$$

$$\boldsymbol{C}(e_2) \triangleq \begin{bmatrix} 0 & \frac{\sigma y_{\text{int}}^{\text{eq}}}{(e_2 + \sigma y_{\text{int}}^{\text{eq}})^2 + \Delta^2} & \frac{\Delta X^{u_c} \sigma y_{\text{int}}^{\text{eq}}}{\left((e_2 + \sigma y_{\text{int}}^{\text{eq}})^2 + \Delta^2\right)^{3/2}} \end{bmatrix}^T \tag{4.16}$$

$$\boldsymbol{H}(y, y_{\text{int}}, \psi_d, v_r, \boldsymbol{\xi}) \triangleq \begin{bmatrix} 0 & 0 \\ 1 & 0 \\ -\frac{\Delta X(\tilde{u}_r + u_c)}{(e_2 + \sigma y_{\text{int}}^{\text{eq}})^2 + \Delta^2} & 1 \end{bmatrix} \begin{bmatrix} \boldsymbol{h}_y^T \\ \boldsymbol{h}_{v_r}^T \end{bmatrix} \tag{4.17}$$

with $\boldsymbol{h}_y^T$ and $\boldsymbol{h}_{v_r}^T$ defined in Appendix 4.A and

$$f(e_2) = 1 - \frac{\sqrt{(\sigma y_{\text{int}}^{\text{eq}})^2 + \Delta^2}}{\sqrt{(e_2 + \sigma y_{\text{int}}^{\text{eq}})^2 + \Delta^2}}. \tag{4.18}$$

Note that $f(e_2)$ satisfies the following bound:

$$|f(e_2)| \leq \frac{|e_2|}{\sqrt{(e_2 + \sigma y_{\text{int}}^{\text{eq}})^2 + \Delta^2}} \tag{4.19}$$

and that $\boldsymbol{H}(\cdot)\boldsymbol{\xi}$ contains the terms vanishing at $\boldsymbol{\xi} = \boldsymbol{0}$. The above describes the path-following error dynamics for each vehicle, which is decoupled from every other vehicle. We now turn our attention to our attention to the interconnected dynamics.

Coordination takes place along the direction of the path, i.e. the x-axis. Therefore, we analyse the along-path kinematics to analyse the coordination error. The along-path kinematics are given by

$$\dot{x} = u_r \cos(\psi) - v_r \sin(\psi) + V_x. \tag{4.20}$$

Using the expressions $u_r = \tilde{u}_r + u_c$, $\psi = \tilde{\psi} + \psi_d$, and $u_c = U_{rd} - g(x)$, with $g(x)$ defined as in (4.6), (4.20) can be rewritten as

$$\dot{x} = U_{rd}\cos(\psi) - g(x)\cos(\psi_d) + V_x + \boldsymbol{h}^T(\boldsymbol{\zeta}, x)\boldsymbol{\zeta}, \tag{4.21}$$

where $\boldsymbol{\zeta} \triangleq [e_1, e_2, v_r, \boldsymbol{\xi}^T]^T$ and $\boldsymbol{h}^T(\boldsymbol{\zeta}, x)\boldsymbol{\zeta}$ contains the terms vanishing at $\boldsymbol{\zeta} = \mathbf{0}$. Furthermore, we can split $\psi_d = \psi_{ss} + \psi_t$ where ψ_{ss} is the steady-state path-following angle (see Figure 4.1) and ψ_t a transient part that disappears when $e_2 = 0$ resulting in

$$\dot{x} = U_{rd}\cos(\psi) - g(x)\cos(\psi_{ss}) + V_x + \boldsymbol{h}_x^T(\boldsymbol{\zeta}, x)\boldsymbol{\zeta}. \tag{4.22}$$

Consequently, $\boldsymbol{h}_x^T(\boldsymbol{\zeta}, x) \triangleq [h_{x,1}, \ldots, h_{x,6}]^T$ is given by

$$\begin{aligned}
h_{x,1} &= h_{x,6} = 0;\ h_{x,3} = \sin(\tilde{\psi} + \psi_d) \\
h_{x,2} &= g(x)\left[\frac{\sin(\psi_t)}{e_2}\sin(\psi_{ss}) - \frac{\cos(\psi_t) - 1}{e_2}\cos(\psi_{ss})\right] \\
h_{x,4} &= \cos(\tilde{\psi} + \psi_d) \\
h_{x,5} &= g(x)\left[\frac{\sin(\tilde{\psi})}{\tilde{\psi}}\sin(\psi_d) - \frac{\cos(\tilde{\psi}) - 1}{\tilde{\psi}}\cos(\psi_d)\right]
\end{aligned} \tag{4.23}$$

where $h_{x,5}$ is related to ψ_t and disappears when $e_2 = 0$. Note that $\boldsymbol{h}_x^T(\boldsymbol{\zeta}, x)$ has less then linear growth in x. More specifically the growth of $\boldsymbol{h}_x^T(\boldsymbol{\zeta}, x)$ is bounded by the constant a.

From the geometry of the problem (see Figure 4.2) it can be verified that the following holds

$$U_{rd}\cos(\psi) = u_x(t) - V_x \tag{4.24}$$

where $u_x(t)$ is the along-path component of the velocity, which allows us expresses the relative velocity term in an equivalent inertial frame term. We now substitute (4.24) in (4.22) to obtain

$$\dot{x} = u_x(t) - g(x)\cos(\psi_{ss}) + \boldsymbol{h}_x^T(\boldsymbol{\zeta}, x)\boldsymbol{\zeta}. \tag{4.25}$$

More specifically, for the formation we can write (4.25) as

$$\dot{x}_j = u_x(t) - g\Big(\sum_{i \in \mathcal{A}_j}(x_j - x_i - d_{ji})\Big)\cos(\psi_{ss_j}) + \boldsymbol{h}_{x_j}^T\boldsymbol{\zeta}_j \tag{4.26}$$

with $j = 1, \ldots, n$. Based on the preceding substitution we now perform a change of coordinates, as is done in Børhaug et al. [31], by defining $\theta_j \triangleq x_j - d_j - \int_{t_0}^{t} u_x(s)ds$ for $j = 1, \ldots, n$ where d_j is such that $d_j - d_i = d_{ji}$, for $j, i = 1, \ldots, n$. This results in

$$\dot{\theta}_j = -g\Big(\sum_{i \in \mathcal{A}_j}(\theta_j - \theta_i)\Big)\cos(\psi_{ss_j}) + \boldsymbol{h}_{x_j}^T(\boldsymbol{\zeta}_j, \theta)\boldsymbol{\zeta}_j, \tag{4.27}$$

for $j = 1, \ldots, n$. It can be verified that $\theta_j - \theta_i = 0\ \forall\ i, j = 1, \ldots, n$ implies that the control goal (4.2c) is achieved.

We now write the system in vector form by defining the aggregate state $\boldsymbol{\theta} \triangleq [\theta_1, \ldots, \theta_n]^T$, the aggregate function $\boldsymbol{g(x)} \triangleq [g(x_1), \ldots, g(x_n)]^T$, and the aggregate matrices $\boldsymbol{\Lambda} \triangleq [\mathbf{diag}\{\cos(\psi_{ss_1}), \ldots, \cos(\psi_{ss_n})\}]$, $\boldsymbol{\zeta} \triangleq [\boldsymbol{\zeta}_1^T, \ldots, \boldsymbol{\zeta}_n^T]^T$, and $\boldsymbol{H}_x \triangleq [\boldsymbol{h}_{x_1}, \ldots, \boldsymbol{h}_{x_n}]^T$. Such that (4.27) can be written as

$$\dot{\boldsymbol{\theta}} = -\boldsymbol{\Lambda} \boldsymbol{g}(\boldsymbol{L}\boldsymbol{\theta}) + \boldsymbol{H}_x(\boldsymbol{\zeta}, \boldsymbol{\theta})\boldsymbol{\zeta} \tag{4.28}$$

where the $\boldsymbol{L}$ is the Laplacian matrix of the graph $\mathcal{G}$ with elements:

$$l_{ji} \triangleq \begin{cases} \delta_j & \text{if } j = i \\ -1, & \text{if } j \neq i \ \wedge \ (j,i) \in E, \ j,i = 1, \ldots, n \\ 0, & \text{otherwise} \end{cases} \tag{4.29}$$

with δ_j the number of outgoing edges from v_j. By definition the Laplacian has one or more eigenvalues at zero with the vector of all ones as eigenvector. If the graph is stronlgy connected -i.e. it has n globally reachable vertices- then the zero eigenvalue is simple and $\boldsymbol{L}$ is symmetric and positive semi-definite (see [68, 98]).

Remark 4.4. The graph Laplacian is a well known tool from the literature of graph theory and is used to express the structure of the communication network mathematically. For more information see for instance Mesbahi and Egerstedt [98].

Remark 4.5. Although the system equation has differences, the structure (4.28) is equivalent to the system considered in Børhaug et al. [31] except for the multiplication with the matrix $\boldsymbol{\Lambda}$, which is a diagonal positive definite matrix. In the following we will adapt some of the tools used in Børhaug et al. [31] to show stability of the coordination error dynamics to account for the addition of the matrix $\boldsymbol{\Lambda}$.

As stated in Børhaug et al. [31], the consensus properties of the along-path dynamics cannot be determined by simply analysing its stability properties, since any state of consensus is an equilibrium point of (4.28). Therefore, a coordinate transform is proposed in Børhaug et al. [31, Lemma 2] which can also be derived for system equation (4.28).

Lemma 4.1 (Børhaug et al. [31, Lemma 2])**.** *Consider system (4.28).Provided Assumption 4.4 is satisfied, there exists a coordinate transformation $\boldsymbol{\phi} \triangleq \boldsymbol{T}\boldsymbol{\theta}$, $\boldsymbol{T} \in \mathbb{R}^{(n-1)\times n}$, such that the following holds:*

1. *$\boldsymbol{\phi} = \mathbf{0}$ implies that $\theta_1 = \ldots = \theta_n$;*
2. *the dynamics of $\boldsymbol{\phi}$ are of the form*

$$\dot{\boldsymbol{\phi}} = \boldsymbol{f}(\boldsymbol{\phi}) + \boldsymbol{G}(\boldsymbol{\zeta}, \boldsymbol{\phi})\boldsymbol{\zeta} \tag{4.30}$$

   with $\boldsymbol{G}(\boldsymbol{\zeta}, \boldsymbol{\phi})$ globally bounded, uniformly in $\boldsymbol{\zeta}$ and $\boldsymbol{\phi}$;
3. *$\dot{\boldsymbol{\phi}} = \boldsymbol{f}(\boldsymbol{\phi})$ is UGAS with positive definite and radially unbounded Lyapunov function $V = V(\boldsymbol{\phi})$ satisfying*

$$\frac{\partial V}{\partial \boldsymbol{\phi}}(\boldsymbol{\phi})\boldsymbol{f}(\boldsymbol{\phi}) \leq -W(\boldsymbol{\phi}) < 0, \ \forall \boldsymbol{\phi} \in \mathbb{R}^{n-1} \setminus \{\mathbf{0}\} \tag{4.31}$$

$$\left\| \frac{\partial V}{\partial \boldsymbol{\phi}}(\boldsymbol{\phi}) \right\| \leq C_1, \ \forall \boldsymbol{\phi} \in \mathbb{R}^{n-1}. \tag{4.32}$$

The proof of Lemma 4.1 is given in Appendix 4.B.
We are now ready to formulate the full closed system as:

$$\dot{\boldsymbol{\phi}} = \boldsymbol{f}(\boldsymbol{\phi}) + \boldsymbol{G}(\boldsymbol{\zeta}, \boldsymbol{\phi})\boldsymbol{\zeta} \tag{4.33a}$$

$$[\dot{e}_1, \dot{e}_2, \dot{v}_r]^T = \boldsymbol{A}[e_1, e_2, v_r]^T + \boldsymbol{B}f(e_2) + \boldsymbol{C}g(x) - \boldsymbol{H}\boldsymbol{\xi} \tag{4.33b}$$

$$\dot{\boldsymbol{\xi}} = \Sigma\boldsymbol{\xi}. \tag{4.33c}$$

where (4.33a) describes the synchronization dynamics, (4.33b) is the path-following error dynamics, and (4.33c) are the controller error dynamics. In the next section we formulate the main theorem and show stability of the closed-loop dynamics (4.33).

Remark 4.6. Note that by a slight abuse of notation (4.33b) contains $g(x)$ instead of $g(\boldsymbol{\phi})$ and that the cross-track error system is in a non-aggregate form. This is done to make the analysis more clear, since path following is considered for individual vessels, while the along-path dynamics (4.33a) considers multiple vessels.

Remark 4.7. Note that (4.33b) contains a term depending on $g(x)$, hence (4.33) is a feedback-interconnected system and not a cascaded system. Consequently, we cannot use classical cascaded systems theory to prove stability of the path following problem as is done in Caharija et al. [40] and for the formation path following problem in the absence of ocean currents as in Børhaug et al. [31]. Note that the term $\boldsymbol{C}g(x)$ is a result of the combination of integral action/adaptation and formation control. Having only one of these features, as in Caharija et al. [40] and Børhaug et al. [31], this term would be zero. Therefore the feedback-interconnection structure is a result of the combination of integral effect/adaptation together with the formation keeping scheme.

4.4 Main Result

Using the following notation to denote the maximum and minimum of $X(u_c)$ and $Y(u_c)$ respectfully

$$X_j^{\max} \triangleq \max_{u_{c_j} \in [U_{rd}-a, U_{rd}+a]} |X_j(u_{c_j})| \tag{4.34}$$

$$Y_j^{\min} \triangleq \min_{u_{c_j} \in [U_{rd}-a, U_{rd}+a]} |Y_j(u_{c_j})| \tag{4.35}$$

we formulate the main result as

Theorem 4.2. *Consider n vessels described by the dynamical system (4.1). If Assumptions 4.1-4.3 hold, and if the communication digraph $\mathcal{G}(V, E)$ has at least one globally reachable vertex, and the look-ahead distance Δ and the integral gain σ satisfy the conditions*

$$\Delta > \frac{|X_j^{\max}|}{|Y_j^{\min}|}\left[\frac{5}{4}\frac{U_{rd} + V_{\max} + a + \sigma}{U_{rd} - V_{\max} - a - \sigma} + 1\right], \tag{4.36}$$

$$0 < \sigma < U_{rd} - V_{\max} - a, \tag{4.37}$$

for $j = 1, \ldots, n$, then the controllers (4.4) *and* (4.8) *guarantee achievement of the control objectives (4.2a)-(4.2c).*

To proof Theorem 4.2 we study stability of the origin of closed-loop error dynamics (4.33). The system (4.33) has a cascaded structure however there is a feedback from the synchronisation error kinematics to the path-following error dynamics because of the influence of the synchronisation error kinematics on the surge velocity. This feedback perturbs the path-following error dynamics and changes the equilibrium of the integral line-of-sight guidance. The resulting structure is analysed in Loría [93], where it is shown that a system of the form:

$$\dot{x}_1 = f_1(t, x_1) + g(t, x_1, x_2) \tag{4.38a}$$
$$\dot{x}_2 = f_2(t, x_1, x_2) \tag{4.38b}$$

can be analysed as a cascaded system of the form

$$\dot{\xi}_1 = f_1(t, \xi_1) + g(t, \xi_1, \xi_2)\xi_2 \tag{4.39a}$$
$$\dot{\xi}_2 = f_2(t, x_1(t), \xi_2) = \tilde{f}_2(t, \xi_2) \tag{4.39b}$$

where $f_2(t, x_1(t), \xi_2)$ depends on the *parameter* x_1, with $x_1(t)$ denoting solutions of (4.38a), under the conditions that

1. $x_1 = 0$ is a UGAS equilibrium for $\dot{x}_1 = f_1(t, x_1)$.
2. The solutions of (4.38) are uniformly globally bounded.

In Loría [93] it is shown that if these conditions are satisfied in the manner presented in the remainder of this section, then the solutions of the system (4.39) will coincide with that of (4.38) for an appropriate choice of initial conditions.

Condition 1) translates to the closed-loop system (4.33) satisfying the following condition:

Condition 4.1 (1)**.** *$\boldsymbol{\phi} = 0$ is a UGAS equilibrium for $\dot{\boldsymbol{\phi}} = \boldsymbol{f}(\boldsymbol{\phi})$.*

Condition 4.1 is verified by claim 3) from Lemma 4.1, which establishes stability of the nominal coordination dynamics.

Verifying condition 2) requires satisfying the following three subconditions 2a), 2b), and 2c).

Condition 4.2 (2a)**.** *There exists a $\mathcal{C}^1$ positive definite radially unbounded function $\tilde{V} : \mathbb{R} \times \mathbb{R}^{n_1} \to \mathbb{R}_{\geq 0}, \alpha_1 \in \mathcal{K}_\infty$ and continuous non-decreasing functions $\alpha_4, \alpha_4' : \mathbb{R}_{\geq 0} \times \mathbb{R} \to \mathbb{R}_{\geq 0}$ such that*

$$\tilde{V}(t, x_1) \geq \alpha_1(|x_1|) \tag{4.40}$$

and that,

$$\dot{\tilde{V}}_{(4.33a)}(t, x_1) \leq \alpha_4(|x_1|)\alpha_4'(|x_2|); \tag{4.41}$$
$$\int_a^\infty \frac{\mathrm{d}\tilde{v}}{\alpha_4(\alpha_1^{-1}(\tilde{v}))} = \infty \tag{4.42}$$

This condition is used to verify that (4.33a) has no finite escape times uniform in $\boldsymbol{\zeta}$. We define $\alpha_1(\|x_1\|)$ as the lower bound of the radially unbounded Lyapunov function from Appendix 4.B. More specifically, $\alpha_1(\|\boldsymbol{\phi}\|) \triangleq \ln(V+1)$, where V is given in (4.56). Now using Lemma 4.1 and its proof in Appendix 4.B we have

$$\begin{aligned}\dot{\tilde{V}}_{(4.33a)}(t,x_1) &\leq -W(\boldsymbol{\phi}) + \left\| \frac{\partial V}{\partial \boldsymbol{\phi}}(\boldsymbol{\phi}) \right\| \|\boldsymbol{G}(\boldsymbol{\zeta},\boldsymbol{\phi})\| \|\boldsymbol{\zeta}\| \\ &\leq \left[\frac{\delta\|\boldsymbol{\phi}_2\|}{\frac{\delta}{2}\|\boldsymbol{\phi}_2\|^2+1} + \|\boldsymbol{g}_1(\boldsymbol{\phi})\| \, \|\boldsymbol{\Lambda}_1\| \, \|\boldsymbol{P}\| \right] C_2\|\boldsymbol{\zeta}\| \\ &\leq \left[\frac{\delta\|\boldsymbol{\phi}_2\|}{\frac{\delta}{2}\|\boldsymbol{\phi}_2\|+1} + \|\boldsymbol{g}_1(\boldsymbol{\phi})\| \, \|\boldsymbol{\Lambda}_1\| \, \|\boldsymbol{P}\| \right] C_2\|\boldsymbol{\zeta}\|\end{aligned} \tag{4.43}$$

where the existence of the constant $C_2 > 0$ above is a consequence of $\boldsymbol{G}(\boldsymbol{\zeta},\boldsymbol{\phi})$ being bounded in its arguments. Moreover, it should be noted from the definition of $g(\cdot)$ in (4.6) that $g(\cdot)$ is upper bounded by a constant a and that the growth of $g(\cdot)$ in its argument is upper-bounded by μ and lower-bounded by zero. This implies that $g(\cdot)$ has its maximal growth around the origin, outside the origin it keeps growing at a smaller rate as it approaches the upper-bound. Therefore, any function $g(\|\boldsymbol{\phi}\|)$ can be bounded by a function of the form $\beta\|\boldsymbol{\phi}\|/(\|\boldsymbol{\phi}\|+\gamma)$ for which there exists constants $\beta > 0$ sufficiently larger than a and $\gamma > 0$ sufficiently small to dominate the growth of $g(\cdot)$. Consequently, we can bound (4.43) as

$$\begin{aligned}\dot{\tilde{V}}_{(4.33a)}(t,x_1) &\leq \left[\frac{\delta\|\boldsymbol{\phi}_2\|}{\frac{\delta}{2}\|\boldsymbol{\phi}_2\|+1} + \|\boldsymbol{g}_1(\boldsymbol{\phi})\| \, \|\boldsymbol{\Lambda}_1\| \, \|\boldsymbol{P}\| \right] C_2\|\boldsymbol{\zeta}\| \\ &\leq \frac{\varepsilon\|\boldsymbol{\phi}\|}{\|\boldsymbol{\phi}\|+\kappa} C_2\|\boldsymbol{\zeta}\|\end{aligned} \tag{4.44}$$

where $\varepsilon > 0$ is sufficiently large and $\kappa > 0$ is sufficiently small. From the above we can satisfy (4.41) by choosing $\alpha_4(\|\boldsymbol{\phi}\|) \triangleq \|\boldsymbol{\phi}\|/(\|\boldsymbol{\phi}\|+\kappa)$ and $\alpha_4'(\|\boldsymbol{\zeta}\|) \triangleq \varepsilon C_2\|\boldsymbol{\zeta}\|$. Computation of the inverse of $\alpha_1(\|\boldsymbol{\phi}\|)$ is not an easy tasks and results in a complicated function. However, to verify (4.42) we do not need to calculate $\alpha_1^{-1}(\|\boldsymbol{\phi}\|)$ if we note that $\alpha_1(\|\boldsymbol{\phi}\|)$ is a function in class $\mathcal{K}_\infty$ and from Khalil [82, Lemma 4.2] (see Lemma A.1), we know that it holds that $\alpha_1^{-1}(\|\boldsymbol{\phi}\|)$ is defined on $[0,\infty)$ and belongs to class $\mathcal{K}_\infty$. With the definition for $\alpha_4(\|\boldsymbol{\phi}\|)$ above, for (4.42) we have

$$\begin{aligned}\int_a^\infty \frac{\mathrm{d}\tilde{v}}{\alpha_4(\alpha_1^{-1}(\tilde{v}))} &= \int_a^\infty \frac{\alpha_1^{-1}(\tilde{v})+\kappa}{\alpha_1^{-1}(\tilde{v})}\mathrm{d}\tilde{v} \\ &= \int_a^\infty 1 \, \mathrm{d}\tilde{v} + \int_a^\infty \frac{\kappa}{\alpha_1^{-1}(\tilde{v})}\mathrm{d}\tilde{v} = \infty\end{aligned} \tag{4.45}$$

since the integral from a to ∞ of 1 is infinity and the integral of $\kappa/\alpha_1^{-1}(\tilde{v}) \geq 0$ because $\alpha_1^{-1}(\tilde{v}) \in \mathcal{K}_\infty$, and consequently (4.42) is satisfied. Therefore, Condition 4.2 is satisfied.

Remark 4.8. The fact that (4.33a) has no finite escape times uniform in $\boldsymbol{\zeta}$ can also be verified by the following observations on the growth rate of $\boldsymbol{\phi}$. It can be seen from

(4.54a) that the nominal dynamics $\boldsymbol{f}(\boldsymbol{\phi})$ have a growth rate dependent on $g(\boldsymbol{L}\boldsymbol{\phi})$, which has at most linear growth and is bounded by constants according to the definitions in (4.6). From (4.23) we can see that same holds for the perturbing term $\boldsymbol{G}(\boldsymbol{\zeta}, \boldsymbol{\phi})\boldsymbol{\zeta}$. Consequently, the growth rate of (4.33a) is less then linear everywhere, which implies no finite escape times uniform in $\boldsymbol{\zeta}$.

Condition 4.3 (2b)**.** *We dispose of a $\mathcal{C}^1$ function $V : \mathbb{R} \times \mathbb{R}^{n_1} \to \mathbb{R}_{\geq 0}$, $\alpha_1, \alpha_2 \in \mathcal{K}_\infty$, and a positive semidefinite function W such that*

$$\alpha_1(\|x_1\|) \leq V(t, x_1) \leq \alpha_2(\|x_1\|) \tag{4.46}$$

$$\frac{\partial V}{\partial t} + \frac{\partial V}{\partial x_1} f_1(t, x_1) \leq -W(x_1) \tag{4.47}$$

for all $t \in [t_o, t_{\max})$ and all $x_1 \in \mathbb{R}^{n_1}$.

This condition is verified by Lemma 4.1. In particular, in Lemma 4.1 it is shown that this condition is satisfied for $t_{\max} = \infty$.

Condition 4.4 (2c)**.** *There exists $\beta \in \mathcal{KL}$ such that the solutions $x_2(t, t_o, x_{2o}, x_1)$ of $\dot{x}_2 = \tilde{f}_2(t, x_2)$ satisfy*

$$\|x_2(t, t_o, x_{2o}, x_1)\| \leq \beta(\|x_{2o}\|, t - t_o) \quad \forall t \in [t_o, t_{\max}). \tag{4.48}$$

It should be noted that $\|x_2(t, t_o, x_{2o}, x_1)\|$ represents the solutions of (4.38b) for fixed values of the parameter x_1 with initial conditions (t_o, x_{2o}), i.e. solutions of the path-following error dynamics (4.33b)-(4.33c) for fixed values of the coordination error $\boldsymbol{\phi}$ and hence fixed values of the velocity. Consequently, Condition 4.4 implies that the solutions of x_2, i.e. subsystem (4.33b)-(4.33c), are required to asymptotically decreasing to zero for all possible values of the parameter x_1. For (4.33) it suffices to show that (4.33b)-(4.33c) is UGAS for all velocities constant velocities $u_c \in [U_{rd} - a, U_{rd} + a]$. Hence, for all possible states of the synchronisation error (4.33a) the adaptation function $g(\cdot)$ that appears in the (4.33b)-(4.33c) takes values in the range $[-a, a]$.

Consequently, a proof that the error dynamics of the integral line-of-sight path-following strategy is UGAS is sufficient to proof Condition 4.4. This proof is available from the work in Caharija et al. [40] and Caharija [39], where it is shown that the origin of the error dynamics of the integral line-of-sight path following is in fact UGAS and ULES. In fact, if we choose Δ and σ as in Theorem 4.2, then the conditions of the proof in Caharija et al. [40] are satisfied for all $u_c \in [U_{rd} - a, U_{rd} + a]$. Therefore, we can show that there is a stable equilibrium on the path for each value of the coordination function.

Condition 2) is now verified with the following theorem:

Theorem 4.3. *The solutions of (4.33) are uniformly globally bounded.*

Proof. The proof of this theorem follows from Loría [93, Theorem 2], which is given as Theorem 4.5 in Appendix 4.C. In the case presented here, it is straightforward

to verify that item 2) of Theorem 4.5 holds. In particular, in this case

$$\|[L_g V]\| = \left\| \frac{\partial V(x_1)}{\partial x_1} g(t, x_1, x_2) \right\| \tag{4.49a}$$

$$\leq \left\| \frac{\partial V}{\partial \boldsymbol{\phi}}(\boldsymbol{\phi}) \right\| \|\boldsymbol{G}(\boldsymbol{\zeta}, \boldsymbol{\phi})\| \|\boldsymbol{\zeta}\| \tag{4.49b}$$

$$\leq \left[\frac{\delta \|\boldsymbol{\phi}_2\|}{\frac{\delta}{2}\|\boldsymbol{\phi}_2\|^2 + 1} + \|\boldsymbol{g}_1(\boldsymbol{\phi})\| \, \|\boldsymbol{\Lambda}_1\| \, \|\boldsymbol{P}\| \right] C_2 \|\boldsymbol{\zeta}\| \tag{4.49c}$$

$$\leq \frac{\varepsilon \|\boldsymbol{\phi}\|}{\|\boldsymbol{\phi}\| + \kappa} C_2 \|\boldsymbol{\zeta}\| \leq C_1 C_2 \|\boldsymbol{\zeta}\| \tag{4.49d}$$

where C_1 is the constant from (4.32) and note that we have used the results from the verification of Condition 4.2. From (4.49d) it can be seen that to bound $\|[L_g V]\|$, we can choose $\alpha_5(\|\boldsymbol{\phi}\|) \in \mathcal{K}$ as a function of the form $\|\boldsymbol{\phi}\|/(\|\boldsymbol{\phi}\|+\kappa)$ for an appropriate choice of $\kappa > 0$. Having chosen a suitable family of functions for $\alpha_5(\|\boldsymbol{\phi}\|)$, we then note that forward completeness of (4.33a) is implied by the fulfilment of Condition 4.2 and Condition 4.3 [93]. Therefore, the solutions of the cascade (4.33) exist for all time. Moreover, we know that according to Condition 4.4, $\|\boldsymbol{\zeta}\|$ decreases for all values of $\boldsymbol{\phi}$ since there is always an equilibrium on the path. Therefore, after a certain time, $W(\boldsymbol{\phi})$ dominates $\|[L_g V]\| \leq C_1 C_2 \|\boldsymbol{\zeta}\|$. More specifically, there exists a certain time after which it holds that $\alpha_5'(\|\boldsymbol{\zeta}\|) \triangleq \varepsilon C_2 \|\boldsymbol{\zeta}\| \leq \lambda_r$, such that $\alpha_5(\|\boldsymbol{\phi}\|) \leq \lambda_r W(\boldsymbol{\phi})$. Consequently, item 2) of Theorem 4.5 is satisfied. Moreover, since it is shown that Condition 4.2, 4.3, and 4.4 hold, Theorem 4.5 holds and consequently Theorem 4.3 holds. □

Theorem 4.4. *The origin of (4.33) is UGAS if Condition 4.1 and the conditions of Theorem 4.3 hold.*

Proof. It is shown that both Condition 4.1 and Theorem 4.3 hold and hence we can invoke Loría [93, Proposition 2], given as Proposition 4.1 in Appendix 4.C, for system (4.33). □

This implies that the control goals (4.2) are achieved and thus the proof of Theorem 4.2 is complete.

4.5 Case Study

In this case study we consider three vessels described by the ship model from Fredriksen and Pettersen [63], which are given in Section C.1. The three vessels each have to follow their specified path $\mathcal{P}_i$, whilst being affected by a current with an intensity $|\boldsymbol{V}_c| = \sqrt{2}$ [m/s]. The components of the current are chosen as $V_x = -1.1028$ [m/s] and $V_y = 0.8854$ [m/s]. The integral gain for the ILOS guidance law is chosen as $\sigma = 1.5$ [m/s] and the look-ahead distance is chosen to be $\Delta = 200$ [m], which satisfies conditions (4.36-4.37) for the given vessels. The gains for the feedback linearising controllers are chosen as $k_{u_r} = 0.1$, $k_\psi = 0.04$,

and $k_r = 0.9$, following the tuning of the path-following controller in Caharija et al. [40]. All initial velocities are set to zero and the initial positions and angles (in degrees) are chosen as

$$\begin{bmatrix} x_{1o} \\ y_{1o} \\ \psi_{1o} \end{bmatrix} = \begin{bmatrix} 0 \\ -1000 \\ 180 \end{bmatrix}, \begin{bmatrix} x_{2o} \\ y_{2o} \\ \psi_{2o} \end{bmatrix} = \begin{bmatrix} 0 \\ 500 \\ 90 \end{bmatrix}, \begin{bmatrix} x_{3o} \\ y_{3o} \\ \psi_{3o} \end{bmatrix} = \begin{bmatrix} 0 \\ -500 \\ -90 \end{bmatrix}.$$

The desired relative surge velocity is chosen to be $U_{rd} = 5$ [m/s] and the velocity adaptation parameter as $a = 0.5$ [m/s] to have sufficient freedom to adapt the velocity. Ship 1 can communicate its position to ship 2 and 3, while only ship 3 can communicate its position to ship 1. The path-following distances for the formation are $d_{12} = 200$ [m], $d_{13} = 100$ [m], $D_2 = -200$ [m], and $D_3 = 200$ [m]. In Figure 4.3 it can be seen that the ships converge to their specified paths and attain the desired formation. We also see how the ships side-slip in order to keep the desired path despite the ocean current acting in the transverse direction of the path. This is confirmed by the plot of the cross-track error $y - D_j$ for each vessel given in Figure 4.4, which show that the path-following errors converge to zero. Furthermore, the side-slipping behaviour can be seen from the heading angle assignments given in Figure 4.5, which shows that the heading angle for the vessels is nonzero when it has converged to the paths in order to compensate for the ocean current. In Figure 4.6 the relative surge velocity over time can be seen. We can see that at first ship 1 is at maximal speed while ship 2 and 3 wait until they are at the desired distance by slowing down. After about 340 [s] ship 2 is at the desired position w.r.t. ship 1 and matches its velocity to ship 1. After about 540 [s] the desired formation is achieved and the velocities all converge to the desired surge velocity. The along-path formation errors can be seen in Figure 4.7, from which it can be observed that the formation errors converge to zero.

Remark 4.9. Collision avoidance is not taken into consideration during this case study, which is intended to illustrate the combined path-following and formation control strategy.

4.6 Conclusions

In this chapter, the problem of path following for formations of underactuated surface vessels under the influence of constant ocean currents was considered. It was shown that n underactuated surface vessels can be controlled to follow a straight-line path whilst attaining and maintaining a desired formation. This has been achieved by making each vehicle converge to a desired path individually using a ILOS-based cross-track controller, combined with a formation keeping control scheme controlling the along-path position of the vessels using only locally available information. The closed-loop system of the path following and formation control strategy were analysed using theory for nonlinear cascaded systems. This was done by showing that the system, which is feedback interconnected, can be analysed as a cascaded system under certain conditions. Simulation results are presented to validate the theory.

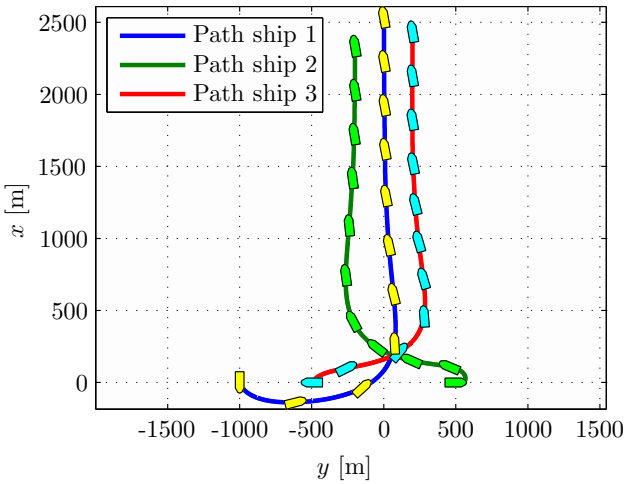

Figure 4.3: The paths of the vessels attaining formation. The small boats give the orientation of the vessels at certain times.

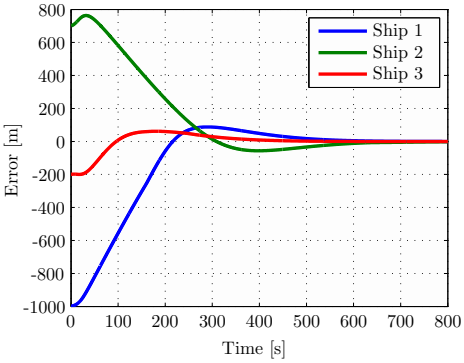

Figure 4.4: The cross-track error between the vehicles and the path.

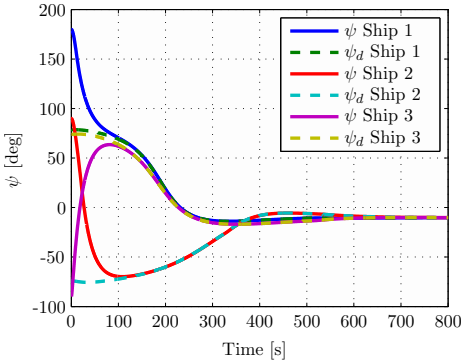

Figure 4.5: Yaw angle and its desired value ψ_d.

4.A Function Definitions

The functions F_{u_r}, $X(u_r)$, $Y(u_r)$, and F_r are given by:

$$
\begin{aligned}
F_{u_r}(v_r, r) &\triangleq \frac{1}{m_{11}}(m_{22}v_r + m_{23}r)r, \\
X(u_r) &\triangleq \frac{m_{23}^2 - m_{11}m_{33}}{m_{22}m_{33} - m_{23}^2}u_r + \frac{d_{33}m_{23} - d_{23}m_{33}}{m_{22}m_{33} - m_{23}^2}, \\
Y(u_r) &\triangleq \frac{(m_{22} - m_{11})m_{23}}{m_{22}m_{33} - m_{23}^2}u_r - \frac{d_{22}m_{33} - d_{32}m_{23}}{m_{22}m_{33} - m_{23}^2},
\end{aligned}
$$

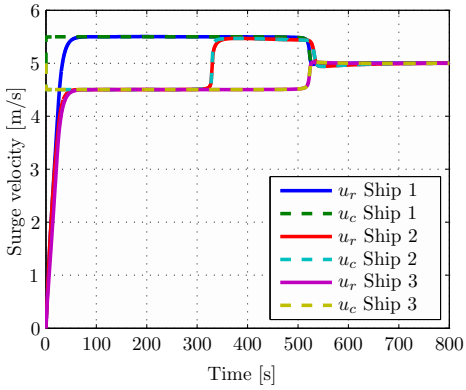

Figure 4.6: The relative surge velocities u_r and their desired values u_c.

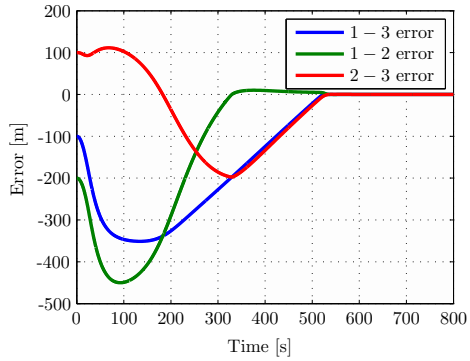

Figure 4.7: The along-path formation keeping error between the vehicles.

$$F_r(u_r, v_r, r) \triangleq \frac{m_{23}d_{22} - m_{22}(d_{32} + (m_{22} - m_{11})u_r)}{m_{22}m_{33} - m_{23}^2} v_r + \frac{m_{23}(d_{23} + m_{11}u_r) - m_{22}(d_{33} + m_{23}u_r)}{m_{22}m_{33} - m_{23}^2} r.$$

Functions $\boldsymbol{h}_y \triangleq [h_{y_1}, h_{y_2}, h_{y_3}]^T$ and $\boldsymbol{h}_{v_r} \triangleq [h_{v_{r1}}, h_{v_{r2}}, h_{v_{r3}}]^T$ are given by:

$$h_{y,1} = \sin(\tilde{\psi} + \psi_d),\ h_{y,3} = 0,$$
$$h_{y,2} = u_c \left[\frac{\sin(\tilde{\psi})}{\tilde{\psi}} \cos(\psi_d) + \frac{\cos(\tilde{\psi}) - 1}{\tilde{\psi}} \sin(\psi_d) \right] + v_r \left[\frac{\cos(\tilde{\psi}) - 1}{\tilde{\psi}} \cos(\psi_d) - \frac{\sin(\tilde{\psi})}{\tilde{\psi}} \sin(\psi_d) \right],$$

$$h_{v_r,1} = \frac{X(\tilde{u}_r + u_c) - X^{u_c}}{\tilde{u}_r} \gamma(y_{\text{int}}, y, v_r) + v_r \frac{Y(\tilde{u}_r + u_c) - Y^{u_c}}{\tilde{u}_r},$$
$$h_{v_r,2} = 0,\ h_{v_r,3} = X(\tilde{u}_r - u_c),$$

with $\gamma(y_{\text{int}}, y, v_r)$ defined as:

$$\gamma(y_{\text{int}}, y, v_r) \triangleq \frac{\Delta(u_c(y + \sigma y_{\text{int}}^{\text{eq}}) - \Delta v_r)}{((e_2 + \sigma y_{\text{int}}^{\text{eq}})^2 + \Delta^2)^{3/2}} - \frac{\Delta V_y}{(e_2 + \sigma y_{\text{int}}^{\text{eq}})^2 + \Delta^2} - \frac{\sigma\Delta}{((e_2 + \sigma y_{\text{int}}^{\text{eq}})^2 + \Delta^2)^2}(y - D_j).$$

$$\boldsymbol{A}(e_2) \triangleq \begin{bmatrix} -\frac{\sigma\Delta}{(e_2+\sigma y_{\text{int}}^{\text{eq}})^2+\Delta^2} & \frac{\Delta}{(e_2+\sigma y_{\text{int}}^{\text{eq}})^2+\Delta^2} & 0 \\ -\frac{\sigma^2\Delta}{(e_2+\sigma y_{\text{int}}^{\text{eq}})^2+\Delta^2} & \left(\frac{\sigma\Delta}{(e_2+\sigma y_{\text{int}}^{\text{eq}})^2+\Delta^2} - \frac{u_c}{\sqrt{(e_2+\sigma y_{\text{int}}^{\text{eq}})^2+\Delta^2}}\right) & \frac{\Delta}{\sqrt{(e_2+\sigma y_{\text{int}}^{\text{eq}})^2+\Delta^2}} \\ \frac{\sigma^2\Delta^2 Y u_c}{((e_2+\sigma y_{\text{int}}^{\text{eq}})^2+\Delta^2)^2} & \left(\frac{u_c\Delta X^r u_c}{((e_2+\sigma y_{\text{int}}^{\text{eq}})^2+\Delta^2)^{3/2}} - \frac{\sigma\Delta^2 X^{u_c}}{((e_2+\sigma y_{\text{int}}^{\text{eq}})^2+\Delta^2)^2}\right) & \left(Y^{u_c} - \frac{\Delta^2 X^{u_c}}{((e_2+\sigma y_{\text{int}}^{\text{eq}})^2+\Delta^2)^{3/2}}\right) \end{bmatrix} \tag{4.50}$$

4.B Proof of Lemma 4.1

The proof for Lemma 4.1 follows along the lines of the proof given in Børhaug et al. [31]. However, we now have to account for the matrix $\boldsymbol{\Lambda}$ in the dynamics (in addition to the interconnection term $\boldsymbol{H}_x\boldsymbol{\zeta}$ being different). According to Assumption 4.3 the communication graph $\mathcal{G}$ has at least one globally reachable vertex. Therefore in this proof we assume that $\mathcal{G}$ has $1 \leq r < n$ globally reachable vertices. This allows us, without loss of generality, to partition $\boldsymbol{L}$ as

$$\boldsymbol{L} = \begin{bmatrix} \boldsymbol{L}_1 & \boldsymbol{L}_2 \\ \boldsymbol{0} & \boldsymbol{L}_3 \end{bmatrix} \tag{4.51}$$

where $\boldsymbol{L}_1 \in \mathbb{R}^{(n-r)\times(n-r)}$ is anti-Hurwitz, i.e., $-\boldsymbol{L}_1$ is Hurwitz, and satisfies

$$\boldsymbol{P}\boldsymbol{L}_1 + \boldsymbol{L}_1^T\boldsymbol{P} = \boldsymbol{Q}, \qquad \boldsymbol{Q} = \boldsymbol{Q}^T > 0 \tag{4.52}$$

for some positive definite diagonal matrix $\boldsymbol{P}$ [91]. The sub-graph corresponding to $\boldsymbol{L}_3 \in \mathbb{R}^{r\times r}$, i.e. $\mathcal{G}(\boldsymbol{L}_3)$, is strongly connected. Hence $\boldsymbol{L}_3$ is positive semi-definite, with zero as a simple eigenvalue and a corresponding eigenvector $\boldsymbol{1}_r = [1, ..., 1]^T \in \mathbb{R}^r$. Consequently, $\boldsymbol{L}_3$ can be decomposed into $\boldsymbol{L}_3 = \boldsymbol{M}_3\boldsymbol{M}_3^T$, where $\boldsymbol{M}_3 \in \mathbb{R}^{r\times(r-1)}$ has full column rank. A coordinate transform is then given by

$$\boldsymbol{\phi} \triangleq \begin{bmatrix} \boldsymbol{L}_1 & \boldsymbol{L}_2 \\ \boldsymbol{0} & \boldsymbol{M}_3^T \end{bmatrix} \boldsymbol{\theta} \triangleq \boldsymbol{T}\boldsymbol{\theta}. \tag{4.53}$$

We can now verify the claims of Lemma 4.1.

Claim 1):

$$\boldsymbol{\phi} = \boldsymbol{0} \;\Rightarrow\; \begin{bmatrix} \boldsymbol{I} & \boldsymbol{0} \\ \boldsymbol{0} & \boldsymbol{M}_3 \end{bmatrix} \boldsymbol{\phi} = \boldsymbol{L}\boldsymbol{\theta} = \boldsymbol{0} \;\Rightarrow\; \boldsymbol{\theta} = \alpha\boldsymbol{1}_n,\ \alpha \in \mathbb{R}.$$

Consequently, $\boldsymbol{\phi} = \boldsymbol{0}$ implies that $\theta_j = \theta_i$, $j, i = 1, ..., n$.

Claim 2): Differentiating (4.53) w.r.t time we obtain

$$\dot{\boldsymbol{\phi}} = \begin{bmatrix} -\boldsymbol{L}_1\boldsymbol{\Lambda}_1\boldsymbol{g}_1(\boldsymbol{\phi}_1) - \boldsymbol{L}_2\boldsymbol{\Lambda}_2\boldsymbol{g}_2(\boldsymbol{\kappa}) \\ -\boldsymbol{M}_3^T\boldsymbol{\Lambda}_2\boldsymbol{g}_2(\boldsymbol{\kappa}) \end{bmatrix} + \boldsymbol{T}\boldsymbol{H}_x(\boldsymbol{\zeta}, \boldsymbol{\theta})\boldsymbol{\zeta} \tag{4.54a}$$

$$\triangleq \boldsymbol{f}(\boldsymbol{\phi}) + \boldsymbol{G}(\boldsymbol{\zeta}, \boldsymbol{\phi})\boldsymbol{\zeta} \tag{4.54b}$$

where $\boldsymbol{\phi} = [\boldsymbol{\phi}_1^T, \boldsymbol{\phi}_2^T]^T$, with $\boldsymbol{\phi}_1 \in \mathbb{R}^{n-r}$ and $\boldsymbol{\phi}_2 \in \mathbb{R}^r$, and we defined $\boldsymbol{\kappa} \triangleq \boldsymbol{M}_3\boldsymbol{\phi}_2$ to simplify notation. Moreover, using (4.23) it is straightforward to verify that $\boldsymbol{G}(\boldsymbol{\zeta}, \boldsymbol{\phi}) \triangleq \boldsymbol{T}\boldsymbol{H}_x(\boldsymbol{\zeta}, \boldsymbol{\theta})$ is globally bounded in its arguments.

Claim 3): Consider the stability properties of the nominal system

$$\begin{bmatrix} \dot{\boldsymbol{\phi}}_1 \\ \dot{\boldsymbol{\phi}}_2 \end{bmatrix} = \begin{bmatrix} -\boldsymbol{L}_1\boldsymbol{\Lambda}_1\boldsymbol{g}_1(\boldsymbol{\phi}_1) - \boldsymbol{L}_2\boldsymbol{\Lambda}_2\boldsymbol{g}_2(\boldsymbol{\kappa}) \\ -\boldsymbol{M}_3^T\boldsymbol{\Lambda}_2\boldsymbol{g}_2(\boldsymbol{\kappa}) \end{bmatrix} = \boldsymbol{f}(\boldsymbol{\phi}). \tag{4.55}$$

Remark 4.10. Note that considering the stability properties of the origin of the nominal dynamics means that we consider the stability properties of (4.54a) when the perturbing dynamics has converged. This implies that the cross-track error has

converged, and consequently, the desired yaw angle ψ_d is bounded well away from $\pi/2$ and $-\pi/2$. Hence the elements of diagonal matrices $\boldsymbol{\Lambda}_1$ and $\boldsymbol{\Lambda}_2$ are bounded away from zero and will have clearly defined minimum eigenvalues of λ_{m_1} and λ_{m_2} respectively.

To show that the origin of (4.55) is UGAS we use the Lyapunov function candidate

$$V \triangleq \frac{\delta}{2}\|\boldsymbol{\phi}_2\|^2 + \int_0^{\boldsymbol{\phi}_1} \boldsymbol{P}\boldsymbol{\Lambda}_1\boldsymbol{g}_1(\boldsymbol{y}) \cdot d\boldsymbol{y} \tag{4.56}$$

where $\boldsymbol{P}$ is the positive definite diagonal solution of (4.52) and $\delta > 0$ to be chosen at a later stage. The sector property of g and the fact that $\boldsymbol{P}$ is a positive definite diagonal matrix assure that V is a positive definite function of $\boldsymbol{\phi}_1$ and $\boldsymbol{\phi}_2$. It is straightforward to verify that V is also radially unbounded. Taking the time-derivative of V along the solutions of (4.55) gives

$$\begin{aligned}\dot{V} = &-\tfrac{1}{2}\boldsymbol{g}_1^T(\boldsymbol{\phi}_1)\left[\boldsymbol{\Lambda}_1\boldsymbol{P}\boldsymbol{L}_1\boldsymbol{\Lambda}_1 + \boldsymbol{\Lambda}_1\boldsymbol{L}_1^T\boldsymbol{P}\boldsymbol{\Lambda}_1\right]\boldsymbol{g}_1(\boldsymbol{\phi}_1) \\ &- \delta\boldsymbol{\kappa}^T\boldsymbol{\Lambda}_2\boldsymbol{g}_2(\boldsymbol{\kappa}) - \boldsymbol{g}_1^T(\boldsymbol{\phi}_1)\boldsymbol{\Lambda}_1\boldsymbol{P}\boldsymbol{L}_2\boldsymbol{\Lambda}_2\boldsymbol{g}_2(\boldsymbol{\kappa})\end{aligned} \tag{4.57}$$

If we substitute for $\boldsymbol{Q}$ in (4.57) and take the norm we obtain

$$\dot{V} \leq c\|\boldsymbol{g}_1(\boldsymbol{\phi}_1)\| \cdot \|\boldsymbol{g}_2(\boldsymbol{\kappa})\| - \delta\boldsymbol{\kappa}^T\boldsymbol{\Lambda}_2\boldsymbol{g}_2(\kappa) - \frac{q_m}{2}\|\boldsymbol{g}_1(\boldsymbol{\phi}_1)\|^2$$

with $q_m > 0$ the minimum eigenvalue of $\boldsymbol{\Lambda}_1\boldsymbol{Q}\boldsymbol{\Lambda}_1$ and $c \geq \|\boldsymbol{\Lambda}_1\boldsymbol{P}\boldsymbol{L}_2\boldsymbol{\Lambda}_2\| > 0$. Since g belongs to the sector $[0, \mu]$, with $\mu > 0$, it can be verified that $x/g(x) \geq 1/\mu$, $\forall x \in \mathbb{R}$, and we can bound $\dot{V}$ by

$$\dot{V} \leq c\|\boldsymbol{g}_1(\boldsymbol{\phi}_1)\| \cdot \|\boldsymbol{g}_2(\boldsymbol{\kappa})\| - \frac{\delta\lambda_{m_2}}{\mu}\|\boldsymbol{g}_2(\kappa)\|^2 - \frac{q_m}{2}\|\boldsymbol{g}_1(\boldsymbol{\phi}_1)\|^2$$

Choosing $\delta \geq \mu([c/\sqrt{2q_m}]^2 + \alpha)/\lambda_{m_2}$, where $\alpha > 0$, gives

$$\begin{aligned}\dot{V} &\leq -\left(\frac{c}{\sqrt{2q_m}}\|\boldsymbol{g}_2(\boldsymbol{\kappa})\| - \sqrt{\frac{q_m}{2}}\|\boldsymbol{g}_1(\boldsymbol{\phi}_1)\|\right)^2 - \alpha\|\boldsymbol{g}_2(\boldsymbol{\kappa})\|^2 \\ &\triangleq -W(\boldsymbol{g}_1(\boldsymbol{\phi}_1), \boldsymbol{g}_2(\boldsymbol{\kappa})).\end{aligned} \tag{4.58}$$

The function W is a positive definite function of $\boldsymbol{g}_1(\boldsymbol{\phi}_1)$ and $\boldsymbol{g}_2(\boldsymbol{\kappa}) = \boldsymbol{g}_2(\boldsymbol{M}_3\boldsymbol{\phi}_2)$. Noting that $g(x) = 0$ if and only if $x = 0$ and that matrix $\boldsymbol{M}_3$ has full column rank we can conclude that $W = 0$ if and only if $\boldsymbol{\phi}_1 = 0$ and $\boldsymbol{\phi}_2 = 0$. Hence, W is a positive definite function of $\boldsymbol{\phi}_1$ and $\boldsymbol{\phi}_2$. Consequently the origin of the nominal system (4.55) is GAS and since (4.55) is time-invariant, the origin is UGAS. This result is equivalent to that in Børhaug et al. [31].

Although the Lyapunov function (4.56) has made it possible to prove UGAS for the origin of (4.55), and it satisfies (4.31), it does not satisfy (4.32). However, as shown in Børhaug et al. [31] the function $\tilde{V} \triangleq \ln(V + 1)$ satisfies both (4.31) and (4.32), since

$$\dot{\tilde{V}} \leq -\frac{1}{V(\boldsymbol{\phi}) + 1}W(\boldsymbol{g}_1(\boldsymbol{\phi}_1), \boldsymbol{g}_2(\boldsymbol{M}_3\boldsymbol{\phi}_2)) \tag{4.59a}$$

$$\triangleq -\tilde{W}(\phi) < 0, \tag{4.59b}$$

satisfies (4.31) and

$$\left\| \frac{\partial \tilde{V}}{\partial \boldsymbol{\phi}} \right\| \leq \frac{1}{V+1} \Big(\delta \|\boldsymbol{\phi}_2\| + \|\boldsymbol{g}_1(\boldsymbol{\phi}_1)\| \, \|\boldsymbol{\Lambda}_1\| \, \|\boldsymbol{P}\| \Big) \tag{4.60a}$$

$$\leq \delta \frac{\|\boldsymbol{\phi}_2\|}{\frac{\delta}{2}\|\boldsymbol{\phi}_2\|^2 + 1} + \|\boldsymbol{g}_1(\boldsymbol{\phi})\| \, \|\boldsymbol{\Lambda}_1\| \, \|\boldsymbol{P}\| \tag{4.60b}$$

$$\leq C_1, \quad C_1 > 0, \tag{4.60c}$$

satisfies (4.32), where we used that $\|\boldsymbol{g}_1(\boldsymbol{\phi})\|$ is globally bounded.

4.C Reference Theorems

This appendix presents Theorem 2 and Proposition 2 from [93] which are used in the stability proof of the closed-loop system in Section 4.3.

Theorem 4.5 ([93, Theorem 2]). *Consider system (4.38) under the following conditions:*

1. *Condition 4.2, 4.3, and 4.4 hold;*
2. *there exist α_5, $\alpha_5' \in \mathcal{K}$ such that*

$$\|[L_g V]\| \leq \alpha_5(\|x_1\|)\alpha_5'(\|x_2\|) \tag{4.61}$$

and for each $r > 0$ there exist λ_r, $\eta_r > 0$ such that

$$t \geq 0, \ \|x_1\| \geq \eta_r \implies \alpha_5(\|x_1\|) \leq \lambda_r W(x_1) \tag{4.62}$$

Then, the solutions of (4.38) are uniformly globally bounded.

Proposition 4.1 ([93, Proposition 2]). *Under Condition 4.1 and the conditions of Theorem 4.3 the origin of (4.38) is UGAS.*

Chapter 5

Straight-Line Coordinated Path-Following for Underactuated Underwater Vehicles in the Presence of Ocean Currents

In this chapter coordinated path following for formations of under-actuated agents in three dimensional space is considered. The agents are controlled to follow a straight-line path whilst being affected by an unknown environmental disturbance. The problem is solved using a twofold approach. In particular, the agents are controlled to the desired path using a guidance law that rejects an unknown, but constant, disturbance. Simultaneously, each agent utilises a decentralised nonlinear coordination law to achieve the desired formation. The closed-loop system of path-following and coordination dynamics is analysed using theory for feedback-interconnected systems. In particular, a technique from Loría [93] is used that allows us to analyse a feedback-interconnected systems as a cascaded system. The origin of the closed-loop error dynamics is shown to be globally asymptotically stable.

Each vehicle is guided to a desired straight-line path using integral LOS guidance [43]. The path-following error dynamics can then be placed in cascade with the coordination error dynamics that are used to achieve along-path coordination. However, the combination of the adaptive properties of the integral LOS guidance together with the coordination controller creates a feedback in the cascade formed by the full closed-loop dynamics. Therefore classical cascaded systems theory cannot be applied and it is necessary to 'break the loop' [93]. Using this technique we prove that the origin of the full closed-loop error dynamics is uniformly globally asymptotically stable.

The chapter is organised as follows. The model for the agents and the communication topology are presented in Section 5.1. The controllers and guidance scheme are given in Section 5.2. The closed-loop system is derived in Section 5.3 and stability of the closed-loop system is shown in Section 5.4. Section 5.5 presents the results of a case study using numerical simulations. Section 5.6 contains results

of experiments performed with three AUVs. Section 5.7 presents the conclusions. The material in this chapter is based on Belleter and Pettersen [14] and Belleter et al. [21].

5.1 Modelling

This section recalls the model of the AUVs and the environmental disturbance, the control objectives, and the communication topology for the network of agents. To describe the motion of the AUVs we use the 5-DOF manoeuvring model from Section 2.3. Therefore, the unknown environmental disturbance is modelled as a three dimensional ocean current in this work.

5.1.1 AUV model

The model considered in this chapter is the 5-DOF model for an AUV given in Section 2.3, which describes the motion of the AUV in surge, sway, heave, pitch and yaw. Recall that the state of the vehicle $\boldsymbol{\eta} \triangleq [x, y, z, \theta, \psi]^T$ with respect to the inertial frame i is expressed in three spatial coordinates x, y, and z and two angles θ and ψ which are the pitch and yaw angle respectively. Moreover, recall that the model is derived under the following assumptions for the AUV and the ocean current.

Assumption 5.1. The roll motion is assumed to be passively stabilised by fins or by gravity and can therefore be neglected when modelling the vessel.

Assumption 5.2. The ocean current, $\boldsymbol{V}_c \triangleq [V_x, V_y, V_z]^T$, expressed in the inertial frame i, is assumed to be constant, irrotational and upper-bounded, i.e. $\exists V_{\max} > 0$ such that $\|\boldsymbol{V}_c\| = \sqrt{V_x^2 + V_y^2 + V_z^2} \leq V_{\max}$.

Assumption 5.3. The vehicles are neutrally buoyant and the center of gravity (CG) and the center of buoyancy (CB) are located along the same vertical axis in the body-fixed frame.

Assumption 5.4. The vehicles are assumed to be $x-z$ plane symmetric and have a large length to width ratio.

Assumption 5.5. The surge mode is decoupled from the other degrees of freedom and consider only the dominating interconnections, i.e. the interconnections between sway and yaw and between heave and pitch.

Assumption 5.6. Damping is considered linear.

Remark 5.1. Assumptions 5.1 and 5.3-5.6 are common assumptions in manoeuvring control of slender-body AUVs [60].

Consequently, the model can be expanded into component form as

$$\dot{x} = u_r \cos(\psi)\cos(\theta) - v_r \sin(\psi) + w_r \cos(\psi)\sin(\theta) + V_x \tag{5.1a}$$
$$\dot{y} = u_r \sin(\psi)\cos(\theta) + v_r \cos(\psi) + w_r \sin(\psi)\sin(\theta) + V_y \tag{5.1b}$$
$$\dot{z} = -u_r \sin(\theta) + w_r \cos(\theta) + V_z \tag{5.1c}$$
$$\dot{\theta} = q \tag{5.1d}$$
$$\dot{\psi} = r/\cos(\theta) \tag{5.1e}$$
$$\dot{u}_r = F_{u_r}(v_r, w_r, q, r) - (d_{11}/m_{11})u_r + \tau_u \tag{5.1f}$$
$$\dot{v}_r = X_{v_r}(u_r)q + Y_{v_r}(u_r)v_r \tag{5.1g}$$
$$\dot{w}_r = X_{w_r}(u_r)q + Y_{w_r}(u_r)w_r + Z_{w_r}\sin(\theta) \tag{5.1h}$$
$$\dot{q} = F_q(\theta, u_r, w_r, q) + \tau_q \tag{5.1i}$$
$$\dot{r} = F_r(u_r, v_r, r) + \tau_r \tag{5.1j}$$

The definitions of F_{u_r}, X_{v_r}, Y_{v_r}, X_{w_r}, Y_{w_r}, Z_{w_r}, F_q, and F_r are given in Appendix 5.A.

Assumption 5.7. The function $Y_{v_r}(u_r)$ satisfies

$$Y_{v_r}(u_r) \leq -Y_{v_r}^{\min} < 0,\ \forall u_r \in [-V_{\max}, U_{rd} + a],$$

where a is a parameter of the formation control law to be defined later.

Assumption 5.8. The function $Y_{w_r}(u_r)$ satisfies

$$Y_{w_r}(u_r) \leq -Y_{w_r}^{\min} < 0,\ \forall u_r \in [-V_{\max}, U_{rd} + a],$$

where a is a parameter of the formation control law to be defined later.

Remark 5.2. Assumptions 5.7 and 5.8 are satisfied for commercial vessels by design, since the converse would imply an undamped or nominally unstable vessel in sway and heave respectively.

5.1.2 The control objectives

The goal is coordinating the motion of n AUVs along a straight-line path $\mathcal{P}$ in 3D space to achieve a given formation. Without loss of generality the inertial frame is chosen such that its x-axis is aligned with the desired path, and consequently $\mathcal{P} \triangleq \{(x, y, z) \in \mathbb{R}^3 : y, z = 0\}$. For the jth AUV in the formation the goal can be characterised by the following control objectives

$$\lim_{t\to\infty} y_j(t) - D_{yj} = 0, \tag{5.2a}$$
$$\lim_{t\to\infty} z_j(t) - D_{zj} = 0, \tag{5.2b}$$
$$\lim_{t\to\infty} \psi_j(t) = \psi_{ss}, \quad \psi_{ss} \in (-\tfrac{\pi}{2}, \tfrac{\pi}{2}), \tag{5.2c}$$
$$\lim_{t\to\infty} \theta_j(t) = \theta_{ss}, \quad \theta_{ss} \in (-\tfrac{\pi}{2}, \tfrac{\pi}{2}), \tag{5.2d}$$
$$\lim_{t\to\infty} u_{r_j}(t) - U_{rd} = 0, \tag{5.2e}$$
$$\lim_{t\to\infty} x_j(t) - x_i(t) - d_{ji} = 0. \tag{5.2f}$$

Control objectives (5.2a) and (5.2b) express the path-following control objectives, where D_{yj} and D_{zj} are offsets to the path $\mathcal{P}$ that are given by the desired formation structure. Control objectives (5.2c) and (5.2d) describe the desired side-slipping motion in steady-state, which is necessary for disturbance rejection in the transversal direction of the path despite the absence of actuation in sway and heave. Control objective (5.2e) assures that all vehicles achieve the same desired velocity. Control objective (5.2f) specifies that the inter vehicle distance along the path should converge to a pre-defined value d_{ji} given by the desired formation structure.

5.1.3 Communication topology

To synchronise the along-path distance, communication of the along-path distance between the vehicles is required. This information can then be used in local synchronisation laws resulting in a decentralised approach. Graph theory [98] is used to model the communication.

The communication network is represented by a directed graph or digraph $\mathcal{G}(V, E)$, where V is a set of vertices representing the vessels and E is a set of edges representing the communication flow. The neighbourhood $\mathcal{A}_j$ of v_j is the set of vertices $v_i \in V$ such that there is an edge from v_j to v_i. Hence, when controlling vessel j only the along-path position x_i of the vessels where $i \in \mathcal{A}_j$ may be used. The above allows us to give some definitions, based on Godcil and Royle [68], that are used in the analysis of the formation dynamics. A vertex $v_k \in V$ reachable from vertex $v_i \in V$ if there is a path from v_i to v_k. A vertex is globally reachable if it can be reached from every vertex in $\mathcal{G}(V, E)$, either directly or indirectly. The graph is said to be strongly connected, if all vertices of $\mathcal{G}(V, E)$ are globally reachable.

5.2 Control System

In this section the control system is proposed. In the first subsection the path-following control strategy is introduced. The second subsection describes the controller used to achieve along-path coordination.

5.2.1 Path-following control

Path-following is achieved using integral line-of-sight guidance combined with feedback linearising controllers for the yaw and pitch angle. An illustration of the iLOS in three dimensional space can be seen in Figure 5.1.

Yaw Control

The desired yaw angle is calculated using an integral LOS guidance law, first introduced in Børhaug et al. [30], based on the y distance to the path which results

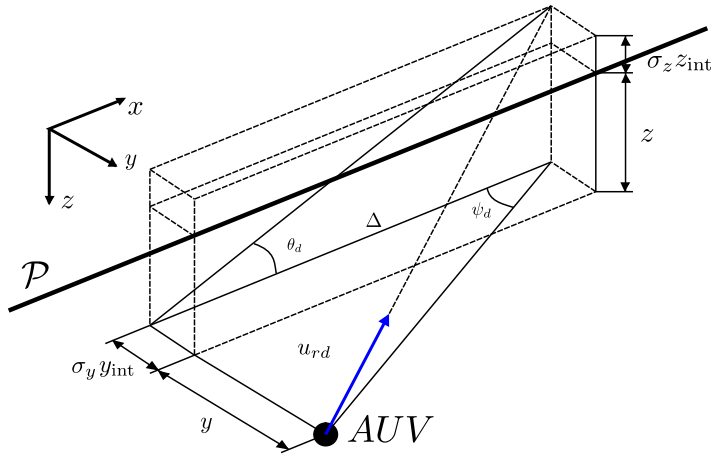

Figure 5.1: Geometry of the 3D-ILOS path-following for $\Delta_y = \Delta_z = \Delta$

in

$$\psi_d \triangleq -\tan^{-1}\left(\frac{(y - D_{yj}) + \sigma_y y_{\text{int}}}{\Delta_y}\right), \quad \Delta_y > 0, \tag{5.3a}$$

$$\dot{y}_{\text{int}} = \frac{\Delta_y (y - D_{yj})}{((y - D_{yj}) + \sigma_y y_{\text{int}})^2 + \Delta_y^2}, \tag{5.3b}$$

with $\sigma_y > 0$ the integral gain, Δ_y the look-ahead distance, and D_{yj} denoting the constant offset from the main path. The desired yaw angle is tracked using the following feedback linearising yaw rate controller

$$\tau_r = -F_r(u_r, v_r, r) - q\sin(\theta)\dot{\psi} + \cos(\theta)\left[\ddot{\psi}_d - k_\psi(\psi - \psi_d) - k_r(\dot{\psi} - \dot{\psi}_d)\right], \tag{5.4}$$

with $k_\psi > 0$ and $k_r > 0$ the proportional and derivative controller gains respectively.

Pitch Control

The desired pitch angle is calculated using an integral LOS guidance based on the z distance to the path, resulting in

$$\theta_d \triangleq \tan^{-1}\left(\frac{(z - D_{zj}) + \sigma_z z_{\text{int}}}{\Delta_z}\right), \quad \Delta_z > 0, \tag{5.5a}$$

$$\dot{z}_{\text{int}} = \frac{\Delta_z (z - D_{zj})}{((z - D_{zj}) + \sigma_z z_{\text{int}})^2 + \Delta_z^2}, \tag{5.5b}$$

with $\sigma_z > 0$ the integral gain, Δ_z the look-ahead distance, and D_{yj} denoting the constant offset from the main path. The desired pitch angle is tracked using the following feedback linearising pitch rate controller

$$\tau_q = -F_q(\theta, u_r, w_r, q) + \ddot{\theta}_d - k_\theta(\theta - \theta_d) - k_q(\dot{\theta} - \dot{\theta}_d), \tag{5.6}$$

with $k_\theta > 0$ and $k_q > 0$ the proportional and derivative controller gains respectively.

5.2.2 Coordination control

The coordination controller consists of a velocity assignment proportional to the coordination error, combined with a feedback linearising surge controller. The velocity assignment is chosen as

$$u_{c_j} \triangleq U_{rd} - g\Big(\sum_{i \in \mathcal{A}_j} (x_j - x_i - d_{ji})\Big), \tag{5.7}$$

with U_{rd} the desired constant relative surge velocity and $g(x)$ proportional to the along-path coordination error. The function $g(x) : \mathbb{R} \to \mathbb{R}$ should be a continuously differentiable saturation-like function satisfying

$$\begin{aligned} -a \leq g(x) \leq a, \quad \forall x \in \mathbb{R}, \quad g(0) = 0, \\ 0 < g'(x) \leq \mu, \forall x \in \mathbb{R}, \quad g'(x) \triangleq \partial g / \partial x \end{aligned} \tag{5.8}$$

where a is the parameter from Assumptions 5.7 and 5.8, and $\mu > 0$ is an arbitrary constant. This also implies that the function $g(x)$ should be a sector function belonging to the sector $[0, \mu]$. A suitable choice for $g(x)$ is for example

$$g\left(x\right) \triangleq \frac{2a}{\pi} \tan^{-1}\left(x\right). \tag{5.9}$$

It was shown in Caharija et al. [43] that in order to overcome the effects of the ocean currents a minimum bound should be placed on the desired velocity. That bound is given in the following assumption adjusted for the case that includes coordination.

Assumption 5.9. The desired relative surge velocity u_c satisfies the following condition:

$$u_c^{\min} > \max\left\{V_{\max} + \frac{5}{2}\left|\frac{Z_{w_r}}{Y_{w_r}(u_c^{\min})}\right|, 2V_{\max} + 2\left|\frac{Z_{w_r}}{Y_{w_r}(u_c^{\min})}\right|\right\}$$

and consequently $U_{rd} > u_c^{\min} + a$ to allow for the necessary velocity manipulation by the coordination law.

Remark 5.3. Note that it is always possible to find values of U_{rd} satisfying Assumption 5.9, since $|Y_{w_r}(u_r)|$ is strictly increasing for $u_r > 0$ [43].

To track u_{c_j} the following feedback linearising P controller is applied to each vessel

$$\tau_u = -F_{u_r}(v_r, r) + \frac{d_{11}}{m_{11}} u_{c_j} + \dot{u}_{c_j} - k_{u_r}(u_r - u_{c_j}), \tag{5.10}$$

with $k_{u_r} > 0$ a constant gain. Note that part of the surge damping is not cancelled to guarantee some robustness w.r.t. model uncertainties.

Using the notation

$$X_\alpha^{\max_j} \triangleq \max_{u_{c_j}\in[U_{\min},U_{\max}]} |X_{\alpha,j}(u_{c_j})| \tag{5.11}$$

$$Y_\alpha^{\min_j} \triangleq \min_{u_{c_j}\in[U_{\min},U_{\max}]} |Y_{\alpha,j}(u_{c_j})| \tag{5.12}$$

with $\alpha \in \{v_r, w_r\}$, $U_{\min} = U_{rd} - a$, and $U_{\max} = U_{rd} + a$ where the main result can then be formulated as follows.

Theorem 5.1. *Consider a formation of n vessels described by (5.1). Suppose that u_d is continuously differentiable, Assumptions 5.2-5.9 are satisfied, and the communication graph contains at least one globally reachable vertex. If the look-ahead distances Δ_y and Δ_z, and the integral gains σ_y and σ_z satisfy the conditions*

$$\Delta_y = \frac{|X_{v_r}^{\max}|}{|Y_{v_r}^{\min}|}\left[\frac{5}{4}\frac{\Gamma_{\max}+V_{\max}+\sigma_y}{\Gamma_{\min}-V_{\max}-\sigma_y}+1\right], \tag{5.13a}$$

$$\Delta_z = \frac{|X_{w_r}^{\max}|}{|Y_{w_r}^{\min}|}\rho(\sigma_z)\left[\frac{5}{4}\frac{\Gamma_{\max}+V_{\max}+\sigma_z}{\Gamma_{\min}-V_{\max}-\sigma_z}+1\right], \tag{5.13b}$$

$$0 < \sigma_y < \Gamma_{\inf} - V_{\max}, \tag{5.13c}$$

$$0 < \sigma_z < U_{\min} - V_{\max} - \frac{5}{2}\left|\frac{Z_{w_r}}{Y_{w_r}^{\min}}\right| \tag{5.13d}$$

with

$$\rho(\sigma_z) \triangleq \frac{U_{\max}-V_{\max}-\sigma_z}{U_{\min}-V_{\max}-\sigma_z-\frac{5}{2}\left|\frac{Z_{w_r}}{Y_{w_r}^{\min}}\right|} \tag{5.14}$$

for $j = 1,\ldots,n$, then the controllers (5.3-5.6), (5.10) guarantee achievement of the control goals (5.2) with $\psi_{ss} = -\tan^{-1}(V_y/\sqrt{\Gamma(s)^2 - V_y^2})$ and $\theta_{ss} = \tan^{-1}(s)$.

Remark 5.4. The constant s and the function $\Gamma(s)$ are defined in the next section when the closed-loop dynamics are derived.

The proof of Theorem 5.1 is given in Section 5.4 which considers the closed-loop stability of the error dynamics.

5.3 Closed-loop System

In this section the closed-loop dynamics are formulated. The closed-loop path-following error and tracking error dynamics are derived first. The coordination error dynamics are derived second and finally the full closed-loop system is presented.

5.3.1 Path-following and tracking error dynamics

In this subsection the tracking and path-following error dynamics are considered. The derivation of these dynamics follow those in Caharija et al. [41] and Caharija

et al. [43], in which the same path-following dynamics are investigated for single vehicles. The tracking errors are analysed by substituting the controllers (5.4), (5.6), and (5.10) into the dynamical system (5.1). For analysis we introduce the vector $\boldsymbol{\xi} \triangleq [\tilde{u}_r, \tilde{\psi}, \tilde{r}, \tilde{\theta}, \tilde{q}]^T$, with tracking errors $\tilde{u}_r \triangleq u_r - u_c$, $\tilde{\psi} \triangleq \psi - \psi_d$, $\tilde{r} \triangleq r - \dot{\psi}_d$, $\tilde{\theta} \triangleq \theta - \theta_d$, and $\tilde{q} \triangleq q - \dot{\theta}_d$. The tracking error dynamics are given by

$$\dot{\boldsymbol{\xi}} = \begin{bmatrix} -k_{u_r} - \frac{d_{11}}{m_{11}} & 0 & 0 & 0 & 0 \\ 0 & 0 & 1 & 0 & 0 \\ 0 & -k_\psi & -k_r & 0 & 0 \\ 0 & 0 & 0 & 0 & 1 \\ 0 & 0 & 0 & -k_\theta & -k_q \end{bmatrix} \boldsymbol{\xi} \triangleq \Sigma \boldsymbol{\xi}. \tag{5.15}$$

The system (5.15) is linear and time-invariant and k_{u_r}, d_{11}/m_{11}, k_ψ, k_θ, k_q, and k_r are all strictly positive. Therefore, Σ is Hurwitz and the origin of the tracking error dynamics (5.15) is uniformly globally exponentially stable (UGES).

The first part of the path-following dynamics consists of the $z - w_r$ subsystem given by

$$\dot{z}_{\text{int}} = \frac{\Delta_z (z - D_{zj})}{((z - D_{zj}) + \sigma_z z_{\text{int}})^2 + \Delta_z^2}, \tag{5.16a}$$

$$\dot{z} = -u_r \sin(\tilde{\theta} + \theta_d) + w_r \cos(\tilde{\theta} + \theta_d) + V_z, \tag{5.16b}$$

$$\dot{w}_r = X_{w_r}(u_r) q + Y_{w_r}(u_r) w_r + Z_{w_r} \sin(\tilde{\theta} + \theta_d). \tag{5.16c}$$

In Caharija et al. [43] it is shown that the equilibrium of (5.16) satisfies

$$z^{\text{eq}} = D_{zj}, \quad w_r^{\text{eq}} = u_c \frac{\sigma_z z_{\text{int}}^{\text{eq}}}{\Delta_z} - V_z \sqrt{\left(\frac{\sigma_z z_{\text{int}}^{\text{eq}}}{\Delta_z} \right)^2 + 1}$$

where $z_{\text{int}}^{\text{eq}}$ is the unique solution of:

$$s\sqrt{s^2 + 1} = \frac{V_z}{u_c} s^2 - \frac{Z_{w_r}}{u_c Y_{w_r}^{u_c}} s + \frac{V_z}{u_c} \tag{5.17}$$

with $s \triangleq \sigma_z z_{\text{int}}^{\text{eq}} / \Delta_z$.

The second part of the path-following dynamics is formed by the $y - v_r$ subsystem given by

$$\dot{y}_{\text{int}} = \frac{\Delta_y (y - D_{yj})}{((y - D_{yj}) + \sigma_y y_{\text{int}})^2 + \Delta_y^2}, \tag{5.18a}$$

$$\begin{aligned} \dot{y} = {} & u_r \sin(\tilde{\psi} + \psi_d) \cos(\tilde{\theta} + \theta_d) + v_r \cos(\tilde{\psi} + \psi_d) \\ & + w_r \sin(\tilde{\psi} + \psi_d) \sin(\tilde{\theta} + \theta_d) + V_y, \end{aligned} \tag{5.18b}$$

$$\dot{v}_r = X_{v_r}(u_r)(\dot{\tilde{\psi}} + \dot{\psi}_d) \cos(\tilde{\theta} + \theta_d) + Y_{v_r}(u_r) v_r, \tag{5.18c}$$

for which it is shown in Caharija et al. [43] that the equilibrium is given by

$$y_{\text{int}}^{\text{eq}} = \frac{\Delta_y}{\sigma_y} \frac{V_y}{\sqrt{\Gamma(s)^2 - V_y^2}}, \quad y^{\text{eq}} = D_{yj}, \quad v_r^{\text{eq}} = 0,$$

with

$$\Gamma(s) \triangleq u_c \frac{1}{\sqrt{s^2+1}} - \frac{Z_{w_r}}{Y_{w_r}^{u_c}} \frac{s^2}{s^2+1}.$$

and

$$\Gamma_{\inf} \triangleq \frac{3}{5}\left[U_{\min} - \left|\frac{Z_{w_r}}{Y_{w_r}^{u_c^{\min}}}\right|\right], \quad \Gamma_{\max} \triangleq U_{\max}. \tag{5.19}$$

The equilibrium point of the (5.16) and (5.18) can be moved to the origin using the introduction of the following error variables

$$e_{z_1} \triangleq z_{\text{int}} - z_{\text{int}}^{\text{eq}},\ e_{z_2} \triangleq (z - D_{zj}) - \sigma_z e_{z_1},\ e_{z_3} \triangleq w_r - w_{\text{int}}^{\text{eq}}$$
$$e_{y_1} \triangleq y_{\text{int}} - y_{\text{int}}^{\text{eq}}, \quad e_{y_2} \triangleq (y - D_{yj}) - \sigma_y e_{y_1},$$

and including the tracking error dynamics (5.15), the system can be written in the cascaded form

$$\begin{aligned} \begin{bmatrix} \dot{e}_{y_1} \\ \dot{e}_{y_2} \\ \dot{v}_r \end{bmatrix} &= \boldsymbol{A}_2(e_{y_2}) \begin{bmatrix} e_{y_1} \\ e_{y_2} \\ v_r \end{bmatrix} + \boldsymbol{B}_2(e_{y_2}) p(e_{y_2}) + \boldsymbol{H_2}\boldsymbol{\chi}, \\ \dot{\boldsymbol{\chi}} &= \begin{bmatrix} \boldsymbol{A}_1(e_{z_2}) & \boldsymbol{H}_1 \\ \boldsymbol{0} & \Sigma \end{bmatrix} \boldsymbol{\chi} + \begin{bmatrix} \boldsymbol{B}_1(e_{z_2}) \\ \boldsymbol{0} \end{bmatrix} f(e_{z_2}) \end{aligned} \tag{5.20}$$

with $\boldsymbol{\chi} \triangleq [e_{z_1}, e_{z_2}, e_{z_3}, \boldsymbol{\xi}^T]^T$. Hence, the tracking errors are placed in cascade with the $z-w_r$ subsystem and this cascade is placed in cascade with the $y-v_r$ subsystem. The matrices $\boldsymbol{A}_1(e_{z_2})$ and $\boldsymbol{A}_2(e_{y_2})$ can be found in (5.50) and (5.51), matrices $\boldsymbol{B}_1(e_{z_2})$, $\boldsymbol{B}_2(e_{y_2})$, $f(e_{z_2})$, and $p(e_{y_2})$ are defined as

$$\boldsymbol{B}_1 \triangleq \left[0, V_z, \frac{\Delta_z^2 X_{w_r}^{u_c} V_z}{(e_{z_2}+\sigma_z z_{\text{int}}^{\text{eq}})^2+\Delta_z^2} - Z_{w_r}\frac{s}{\sqrt{s^2+1}}\right]^T \tag{5.21}$$

$$\boldsymbol{B}_2 \triangleq \left[0, V_y, \frac{-\Delta_y^2 X_{v_r}^{u_c} V_y}{\sqrt{s^2+1}(e_{y_2}+\sigma_y y_{\text{int}}^{\text{eq}})^2+\Delta_y^2}\right]^T \tag{5.22}$$

$$f(e_{z_2}) = 1 - \frac{\sqrt{(\sigma_z z_{\text{int}}^{\text{eq}})^2+\Delta_z^2}}{\sqrt{(e_{z_2}+\sigma_z z_{\text{int}}^{\text{eq}})^2+\Delta_z^2}} \tag{5.23}$$

$$p(e_{y_2}) = 1 - \frac{\sqrt{(\sigma_y y_{\text{int}}^{\text{eq}})^2+\Delta_y^2}}{\sqrt{(e_{y_2}+\sigma_y y_{\text{int}}^{\text{eq}})^2+\Delta_y^2}}. \tag{5.24}$$

The interconnection matrices $\boldsymbol{H}_1(z, z_{\text{int}}, \theta_d, w_r, \boldsymbol{\zeta})$ and $\boldsymbol{H_2}(y, y_{\text{int}}, \theta_d, \psi_d, v_r, \boldsymbol{\chi})$ contain the terms perturbing terms for the cascade from control tracking errors to the $z-w_r$ subsystem and the perturbing terms van $z-w_r$ to the $y-v_r$ subsystem respectively. The interconnection term $\boldsymbol{H}_1\boldsymbol{\xi}$ goes to zero when $\boldsymbol{\xi}$ goes to zero and $\boldsymbol{H_2}\boldsymbol{\chi}$ goes to zero when $\boldsymbol{\chi}$ goes to zero. The interconnection matrices are given by

$$\boldsymbol{H}_1 \triangleq \begin{bmatrix} 0 & 0 \\ 1 & 0 \\ \frac{\Delta_z X_{w_r}(\tilde{u}_r+u_c)}{(e_{z_2}+\sigma_z z_{\text{int}}^{\text{eq}})^2+\Delta_z^2} & 1 \end{bmatrix} \begin{bmatrix} \boldsymbol{h}_z^T \\ \boldsymbol{h}_{w_r}^T \end{bmatrix} \tag{5.25}$$

$$\boldsymbol{H}_2 \triangleq \begin{bmatrix} 0 & 0 \\ 1 & 0 \\ -\frac{\Delta_y X_{v_r}(\tilde{u}_r+u_c)\cos(\tilde{\theta}+\theta_d)}{(e_{y_2}+\sigma_y y_{\text{int}}^{\text{eq}})^2+\Delta_y^2} & 1 \end{bmatrix} \begin{bmatrix} \boldsymbol{h}_y^T \\ \boldsymbol{h}_{v_r}^T \end{bmatrix} \tag{5.26}$$

where the expressions for $\boldsymbol{h}_z^T$, $\boldsymbol{h}_{w_r}^T$, $\boldsymbol{h}_y^T$, and $\boldsymbol{h}_{v_r}^T$ can be found in Appendix 5.A.

In Caharija et al. [43] it is shown that the path-following cascaded system (5.20) has a UGAS and ULES equilibrium at the origin for a constant velocity satisfying Assumption 5.9 and constants satisfying (5.13).

Remark 5.5. Note that for the case of a constant velocity u_c we have $U_{\max} \equiv U_{\min} \equiv u_c$, $X^{\max} \equiv X^{\min} \equiv X^{u_c}$, and $Y^{\max} \equiv Y^{\min} \equiv Y^{u_c}$ for the constants in (5.13).

Remark 5.6. Note that the proof in Caharija et al. [43] applies for a constant velocity u_c. However in the case considered here the velocity is not constant, and therefore the proof cannot be directly applied to the coordinated path-following scenario. However it will be shown that when analysing the closed-loop system in Section 5.4 we can still utilise this proof to guarantee an equilibrium on the path when the velocity satisfies $u_c \in [U_{rd} - a, U_{rd} + a]$ as defined in (5.7).

Remark 5.7. Despite the singularity in θ in the open-loop system (2.11), this singularity does not appear in the closed-loop path-following error dynamics (5.20). Therefore, global results can be achieved for the path-following error.

5.3.2 Coordination error dynamics

The coordination error dynamics are expressed in the x-direction of the inertial frame and therefore we consider (5.1a)

$$\begin{aligned}\dot{x} &= (u_c + \tilde{u}_r)\cos(\tilde{\psi} + \psi_d)\cos(\tilde{\theta} + \theta_d) - v_r \sin(\tilde{\psi} + \psi_d) \\ &\quad + w_r \cos(\tilde{\psi} + \psi_d)\sin(\tilde{\theta} + \theta_d) + V_x \\ &= \Gamma(s)\cos(\psi_d) + g(x)\cos(\psi_{ss})\cos(\theta_{ss}) + V_x + \boldsymbol{h}_x^T \boldsymbol{\zeta}\end{aligned} \tag{5.27}$$

where $\boldsymbol{h}_x^T \boldsymbol{\zeta}$ is the interconnection term between the coordination error dynamics and path-following error dynamics with $\boldsymbol{\zeta} = [e_{y_1}, e_{y_2}, v_r, \boldsymbol{\chi}]^T$. The elements of $\boldsymbol{h}_x^T$ are given by

$$\begin{aligned}
h_{x1} &= h_{x4} = h_{x9} = h_{x11} = 0 \\
h_{x2} &= g(x)\cos(\theta_{ss})\left[\frac{\cos(\psi_t) - 1}{e_{y2}}\cos(\psi_{ss}) + \frac{\sin(\psi_t)}{e_{y2}}\sin(\psi_{ss})\right] \\
h_{x3} &= -\sin(\tilde{\psi} + \psi_d) \\
h_{x5} &= u_c \cos(\psi_d)\left[\frac{\cos(\theta_t) - 1}{e_{z2}}\cos(\theta_{ss}) + \frac{\sin(\theta_t)}{e_{z2}}\sin(\theta_{ss})\right] \\
&\quad + w_r^{\text{eq}} \cos(\psi_d)\left[\frac{\sin(\theta_t)}{e_{z2}}\cos(\theta_{ss}) + \frac{\cos(\theta_t) - 1}{e_{z2}}\sin(\theta_{ss})\right] \\
h_{x6} &= \cos(\tilde{\psi} + \psi_d)\sin(\tilde{\theta} + \theta_d) \\
h_{x7} &= \cos(\tilde{\psi} + \psi_d)\cos(\tilde{\theta} + \theta_d) \\
h_{x8} &= \left[w_r^{\text{eq}} \sin(\tilde{\theta} + \theta_d) + u_c \cos(\tilde{\theta} + \theta_d)\right]\left[\frac{\cos(\tilde{\psi}) - 1}{\tilde{\psi}}\cos(\psi_d) - \frac{\sin(\tilde{\psi})}{\tilde{\psi}}\sin(\psi_d)\right] \\
h_{x10} &= \left[w_r^{\text{eq}} \cos(\psi_d) + u_c \cos(\psi_d)\right]\left[\frac{\sin(\tilde{\theta})}{\tilde{\theta}}\cos(\theta_d) + \frac{\cos(\tilde{\theta}) - 1}{\tilde{\theta}}\sin(\theta_d)\right].
\end{aligned} \tag{5.28}$$

The contribution to the along-path velocity of the surge velocity and the current is given by $U_x \triangleq \Gamma(s)\cos(\psi_{ss}) + V_x$. Using this, we can introduce the change of coordinates $\vartheta_j \triangleq x_j - d_j - \int_{t_0}^{t} U_x ds$ for $j = 1, \ldots, n$ where d_j is such that $d_j - d_i = d_{ji}$. The path-following dynamics (5.27) can be transformed into the coordination error dynamics using this changes of coordinates

$$\dot{\vartheta}_j = -g\left(\sum_{i\in\mathcal{A}_j}(\vartheta_j - \vartheta_i)\right)\cos(\psi_{ss})\cos(\theta_{ss}) + \boldsymbol{h}_x^T\boldsymbol{\zeta}. \tag{5.29}$$

Remark 5.8. Note that $\vartheta_j - \vartheta_i = 0, \forall i, j = 1, \ldots, n$ implies that (5.2f) is satisfied and along-path coordination is achieved. Moreover, since $\tilde{u}_r$ converges exponentially to zero satisfaction of (5.2f) also implies that (5.2e) is satisfied.

To consider all vessels we write the system in vector form by defining $\boldsymbol{\vartheta} \triangleq [\vartheta_1, \ldots, \vartheta_n]^T$, $\boldsymbol{g}(\boldsymbol{\vartheta}) \triangleq [g(\vartheta_1), \ldots, g(\vartheta_n)]^T$, $\boldsymbol{\Lambda} \triangleq [\mathbf{diag}\{\cos(\psi_{ss_1})\cos(\theta_{ss_1}), \ldots, \cos(\psi_{ss_n})\cos(\theta_{ss_n})\}]$, $\boldsymbol{\zeta} \triangleq [\boldsymbol{\zeta}_1^T, \ldots, \boldsymbol{\zeta}_n^T]^T$, and $\boldsymbol{H}_x \triangleq [\boldsymbol{h}_{x_1}, \ldots, \boldsymbol{h}_{x_n}]^T$, such that (5.29) can be written as

$$\dot{\boldsymbol{\vartheta}} = -\boldsymbol{\Lambda}\boldsymbol{g}(\boldsymbol{L}\boldsymbol{\vartheta}) + \boldsymbol{H}_x(\boldsymbol{\zeta}, \boldsymbol{\vartheta})\boldsymbol{\zeta} \tag{5.30}$$

where $\boldsymbol{L}$ is the Laplacian matrix of the graph $\mathcal{G}$ with elements:

$$l_{ji} \triangleq \begin{cases} \delta_j & \text{if } j = i \\ -1, & \text{if } j \neq i \ \wedge \ (j,i) \in E, \ j, i = 1, \ldots, n \\ 0, & \text{otherwise} \end{cases} \tag{5.31}$$

with δ_j the number of outgoing edges from v_j. By definition the Laplacian has one or more eigenvalues at zero with the vector of all ones as eigenvector. If the graph is strongly connected, i.e. it has n globally reachable vertices, then the zero eigenvalue is simple and $\boldsymbol{L}$ is symmetric and positive semi-definite (see [68, 98]).

As stated in Børhaug et al. [31] the consensus properties of the coordination-error dynamics cannot be determined by simply analysing its stability properties, since it can have multiple equilibria depending on the network topology. Therefore, a coordinate transform is proposed in Børhaug et al. [31, Lemma 2] which can also be derived for system equation (5.30).

Lemma 5.2 ([31, Lemma 2])**.** *Consider system (5.30). Under the condition of Theorem 5.1 there exists a coordinate transformation $\boldsymbol{\phi} \triangleq \boldsymbol{T}\boldsymbol{\vartheta}$, $\boldsymbol{T} \in \mathbb{R}^{(n-1)\times n}$, such that the following holds:*

1. *$\boldsymbol{\phi} = \mathbf{0}$ implies that $\vartheta_1 = \ldots = \vartheta_n$;*
2. *the dynamics of $\boldsymbol{\phi}$ are of the form*

$$\dot{\boldsymbol{\phi}} = \boldsymbol{f}(\boldsymbol{\phi}) + \boldsymbol{G}(\boldsymbol{\zeta}, \boldsymbol{\phi})\boldsymbol{\zeta} \tag{5.32}$$

   with $\boldsymbol{G}(\boldsymbol{\zeta}, \boldsymbol{\phi})$ globally bounded, uniformly in $\boldsymbol{\zeta}$ and $\boldsymbol{\phi}$;
3. *$\dot{\boldsymbol{\phi}} = \boldsymbol{f}(\boldsymbol{\phi})$ is UGAS with positive definite and radially unbounded Lyapunov function $V = V(\boldsymbol{\phi})$ satisfying*

$$\frac{\partial V}{\partial \boldsymbol{\phi}}(\boldsymbol{\phi})\boldsymbol{f}(\boldsymbol{\phi}) \leq -W(\boldsymbol{\phi}) < 0,\ \forall \boldsymbol{\phi} \in \mathbb{R}^{n-1} \setminus \{\mathbf{0}\} \tag{5.33}$$

$$\left\| \frac{\partial V}{\partial \boldsymbol{\phi}}(\boldsymbol{\phi}) \right\| \leq C_1,\ \forall \boldsymbol{\phi} \in \mathbb{R}^{n-1}. \tag{5.34}$$

The proof of this lemma is given in Appendix 5.B.

The total closed-loop system can now be formulated as:

$$\dot{\boldsymbol{\phi}} = \boldsymbol{f}(\boldsymbol{\phi}) + \boldsymbol{G}(\boldsymbol{\zeta}, \boldsymbol{\phi})\boldsymbol{\zeta} \tag{5.35a}$$

$$\dot{\boldsymbol{\zeta}} = \left[\begin{array}{c|cc} \boldsymbol{A}_2(e_{y_2}) & \multicolumn{2}{c}{\boldsymbol{H}_2} \\ \hline \mathbf{0} & \boldsymbol{A}_1(e_{z_2}) & \boldsymbol{H}_1 \\ & \mathbf{0} & \Sigma \end{array}\right] \boldsymbol{\zeta} + \begin{bmatrix} \boldsymbol{B}_2(e_{y_2})p(e_{y_2}) \\ \boldsymbol{B}_1(e_{z_2})f(e_{z_2}) \\ \mathbf{0} \end{bmatrix} \tag{5.35b}$$

By splitting u_c in the constant desired velocity U_{rd} and the adaptive part $g(x)$ the coupling between the coordination dynamics and path-following error dynamics becomes evident

$$\dot{\boldsymbol{\phi}} = \boldsymbol{f}(\boldsymbol{\phi}) + \boldsymbol{G}(\boldsymbol{\zeta}, \boldsymbol{\phi})\boldsymbol{\zeta} \tag{5.36a}$$

$$\begin{aligned} \dot{\boldsymbol{\zeta}} = &\left[\begin{array}{c|cc} \boldsymbol{A}_2(e_{y_2}, U_{rd}) & \multicolumn{2}{c}{\boldsymbol{H}_2} \\ \hline \mathbf{0} & \boldsymbol{A}_1(e_{z_2}, U_{rd}) & \boldsymbol{H}_1 \\ & \mathbf{0} & \Sigma \end{array}\right] \boldsymbol{\zeta} \\ &+ \begin{bmatrix} \boldsymbol{B}_2(e_{y_2})p(e_{y_2}) \\ \boldsymbol{B}_1(e_{z_2})f(e_{z_2}) \\ \mathbf{0} \end{bmatrix} + \begin{bmatrix} \boldsymbol{C}_2(e_{y_2}) \\ \boldsymbol{C}_1(e_{z_2}) \\ \mathbf{0} \end{bmatrix} g(x) \end{aligned} \tag{5.36b}$$

with

$$\boldsymbol{C}_1(e_{z_2}) \triangleq \left[0, -\frac{\sigma_z z_{\text{int}}^{\text{eq}}}{\left(e_{z_2}+\sigma z_{\text{int}}^{\text{eq}}\right)^2+\Delta_z^2}, \frac{\Delta_z X_{w_r}^{u_c} \sigma_z z_{\text{int}}^{\text{eq}}}{\left(\left(e_{z_2}+\sigma_z z_{\text{int}}^{\text{eq}}\right)^2+\Delta_z^2\right)^{3/2}}\right]^T$$

$$\boldsymbol{C}_2(e_{y_2}) \triangleq \left[0, \frac{\sigma_y y_{\text{int}}^{\text{eq}}}{\left(e_{y_2}+\sigma_y y_{\text{int}}^{\text{eq}}\right)^2+\Delta_y^2} \frac{\Delta_z}{\left(e_{z_2}+\sigma_z z_{\text{int}}^{\text{eq}}\right)^2+\Delta_z^2}, \frac{1}{\sqrt{s^2+1}} \frac{\Delta_y X_{w_r}^{u_c}}{\left(\left(e_{y_2}+\sigma_y y_{\text{int}}^{\text{eq}}\right)^2+\Delta_y^2\right)^{3/2}}\right]^T$$

where $\boldsymbol{C}(e_{y_2}, e_{z_2})g(x)$ is the feedback from coordination dynamics in path-following dynamics.

5.4 Closed-loop Stability

In this section we investigate the closed-loop stability properties. The proof for stability will follow along the lines of that in Section 4.4. First note that, as in Chapter 4, the coupling term seen in (5.36b) is a result of the combination of having a multi-agent system and having disturbance rejection. With only one of these, the system would be in a cascaded form. Now instead the system has a feedback-interconnected form. However, feedback-interconnected systems can be analysed as cascade-interconnected system using a technique called 'breaking the loop', as introduced in Loría [93]. In Loría [93] it is shown how a system of the form:

$$\dot{x}_1 = f_1(t, x_1) + g(t, x_1, x_2) \tag{5.37a}$$

$$\dot{x}_2 = f_2(t, x_1, x_2) \tag{5.37b}$$

can be analysed as a cascaded system of the form

$$\dot{\xi}_1 = f_1(t, \xi_1) + g(t, \xi_1, \xi_2)\xi_2 \tag{5.38a}$$

$$\dot{\xi}_2 = f_2(t, x_1(t), \xi_2) = \tilde{f}_2(t, \xi_2) \tag{5.38b}$$

where $f_2(t, x_1(t), \xi_2)$ depends on the *parameter* x_1, with $x_1(t)$ denoting solutions of (5.37a), under the conditions that

1. $x_1 = 0$ is a UGAS equilibrium for $\dot{x}_1 = f_1(t, x_1)$.
2. The solutions of (5.37) are uniformly globally bounded.

In Loría [93] it is shown that if these conditions are satisfied in the manner presented in the remainder of this section, then the solutions of the system (5.38) will coincide with that of (5.37) for an appropriate choice of initial conditions.

Condition 1) translates to the closed-loop system (5.35) satisfying the following condition:

Condition 5.1. *(1) $\boldsymbol{\phi} = 0$ is a UGAS equilibrium for $\dot{\boldsymbol{\phi}} = \boldsymbol{f}(\boldsymbol{\phi})$.*

Condition 5.1 is verified by claim 3) from Lemma 5.2, which establishes stability of the nominal coordination dynamics.

Verifying condition 2) requires satisfying the following three subconditions 2a), 2b), and 2c).

Condition 5.2. *(2a) There exists a $\mathcal{C}^1$ positive definite radially unbounded function $\tilde{V} : \mathbb{R} \times \mathbb{R}^{n_1} \to \mathbb{R}_{\geq 0}, \alpha_1 \in \mathcal{K}_\infty$ and continuous non-decreasing functions $\alpha_4, \alpha_4' : \mathbb{R}_{\geq 0} \times \mathbb{R} \to \mathbb{R}_{\geq 0}$ such that*

$$\tilde{V}(t, x_1) \geq \alpha_1(\|x_1\|) \tag{5.39}$$

and that,

$$\dot{\tilde{V}}_{(5.35a)}(t, x_1) \leq \alpha_4(\|x_1\|)\alpha_4'(\|x_2\|); \tag{5.40}$$

$$\int_a^\infty \frac{\mathrm{d}\tilde{v}}{\alpha_4(\alpha_1^{-1}(\tilde{v}))} = \infty \tag{5.41}$$

This condition is used to verify that (5.35a) has no finite escape times uniform in $\boldsymbol{\zeta}$. We define $\alpha_1(\|x_1\|)$ as the lower bound of the radially unbounded Lyapunov function from Appendix 5.B. More specifically, $\alpha_1(\|\boldsymbol{\phi}\|) \triangleq \ln(V + 1)$ where V is given in (5.57). Now using Lemma 5.2 and its proof in Appendix 5.B we have

$$\begin{aligned}
\dot{\tilde{V}}_{(5.35a)}(t, x_1) &\leq -W(\boldsymbol{\phi}) + \left\| \frac{\partial V}{\partial \boldsymbol{\phi}}(\boldsymbol{\phi}) \right\| \|\boldsymbol{G}(\boldsymbol{\zeta}, \boldsymbol{\phi})\| \|\boldsymbol{\zeta}\| \\
&\leq \left[\frac{\delta \|\boldsymbol{\phi}_2\|}{\frac{\delta}{2}\|\boldsymbol{\phi}_2\|^2 + 1} + \|\boldsymbol{g}_1(\boldsymbol{\phi})\| \, \|\boldsymbol{\Lambda}_1\| \, \|\boldsymbol{P}\| \right] C_2 \|\boldsymbol{\zeta}\| \\
&\leq \left[\frac{\delta \|\boldsymbol{\phi}_2\|}{\frac{\delta}{2}\|\boldsymbol{\phi}_2\| + 1} + \|\boldsymbol{g}_1(\boldsymbol{\phi})\| \, \|\boldsymbol{\Lambda}_1\| \, \|\boldsymbol{P}\| \right] C_2 \|\boldsymbol{\zeta}\|
\end{aligned} \tag{5.42}$$

where the existence of the constant $C_2 > 0$ above is a consequence of $\boldsymbol{G}(\boldsymbol{\zeta}, \boldsymbol{\phi})$ being bounded in its arguments. Moreover, it should be noted from the definition of $g(\cdot)$ in (5.8) that $g(\cdot)$ is upper bounded by a constant a and that the growth of $g(\cdot)$ in its argument is upper-bounded by μ and lower-bounded by zero. This implies that $g(\cdot)$ has its maximal growth around the origin, outside the origin it keeps growing at a smaller rate as it approaches the upper-bound. Therefore, any function $g(\|\boldsymbol{\phi}\|)$ can be bounded by a function of the form $\beta\|\boldsymbol{\phi}\|/(\|\boldsymbol{\phi}\| + \gamma)$ for which there exists constants $\beta > 0$ sufficiently larger than a and $\gamma > 0$ sufficiently small to dominate the growth of $g(\cdot)$. Consequently, we can bound (5.42) as

$$\begin{aligned} \dot{\tilde{V}}_{(5.35a)}(t, x_1) &\leq \left[\frac{\delta\|\boldsymbol{\phi}_2\|}{\frac{\delta}{2}\|\boldsymbol{\phi}_2\| + 1} + \|\boldsymbol{g}_1(\boldsymbol{\phi})\| \, \|\boldsymbol{\Lambda}_1\| \, \|\boldsymbol{P}\| \right] C_2\|\boldsymbol{\zeta}\| \\ &\leq \frac{\varepsilon\|\boldsymbol{\phi}\|}{\|\boldsymbol{\phi}\| + \kappa} C_2\|\boldsymbol{\zeta}\| \end{aligned} \tag{5.43}$$

where $\varepsilon > 0$ is sufficiently large and $\kappa > 0$ is sufficiently small. From the above we can satisfy (5.40) by choosing $\alpha_4(\|\boldsymbol{\phi}\|) \triangleq \|\boldsymbol{\phi}\|/(\|\boldsymbol{\phi}\| + \kappa)$ and $\alpha_4'(\|\boldsymbol{\zeta}\|) \triangleq \varepsilon C_2\|\boldsymbol{\zeta}\|$. Computation of the inverse of $\alpha_1(\|\boldsymbol{\phi}\|)$ is not an easy tasks and results in a complicated function. However, to verify (5.41) we do not need to calculate $\alpha_1^{-1}(\|\boldsymbol{\phi}\|)$ if we note that $\alpha_1(\|\boldsymbol{\phi}\|)$ is a function in class $\mathcal{K}_\infty$ and from Khalil [82, Lemma 4.2] (see Lemma A.1), we know that it holds that $\alpha_1^{-1}(\|\boldsymbol{\phi}\|)$ is defined on $[0, \infty)$ and belongs to class $\mathcal{K}_\infty$. With the definition for $\alpha_4(\|\boldsymbol{\phi}\|)$ above, for (5.41) we have

$$\begin{aligned} \int_a^\infty \frac{\mathrm{d}\tilde{v}}{\alpha_4(\alpha_1^{-1}(\tilde{v}))} &= \int_a^\infty \frac{\alpha_1^{-1}(\tilde{v}) + \kappa}{\alpha_1^{-1}(\tilde{v})} \mathrm{d}\tilde{v} \\ &= \int_a^\infty 1 \, \mathrm{d}\tilde{v} + \int_a^\infty \frac{\kappa}{\alpha_1^{-1}(\tilde{v})} \mathrm{d}\tilde{v} = \infty \end{aligned} \tag{5.44}$$

since the integral from a to ∞ of 1 is equal to infinity and the integral of $\kappa/\alpha_1^{-1}(\tilde{v}) \geq 0$ because $\alpha_1^{-1}(\tilde{v}) \in \mathcal{K}_\infty$. Consequently, (5.41) is satisfied. Therefore, Condition 5.2 is satisfied.

Remark 5.9. The fact that (5.35a) has no finite escape times uniform in $\boldsymbol{\zeta}$ can also be verified by the following observations on the growth rate of $\boldsymbol{\phi}$. It can be seen from (5.55a) that the nominal dynamics $\boldsymbol{f}(\boldsymbol{\phi})$ have a growth rate dependent on $g(\boldsymbol{L}\boldsymbol{\phi})$, which has at most linear growth and is bounded by constants according to the definitions in (5.8). From (5.28) we can see that same holds for the perturbing term $\boldsymbol{G}(\boldsymbol{\zeta}, \boldsymbol{\phi})\boldsymbol{\zeta}$. Consequently, the growth rate of (5.35a) is less then linear everywhere, which implies no finite escape times uniform in $\boldsymbol{\zeta}$.

Condition 5.3. *(2b) We dispose of a $\mathcal{C}^1$ function $V : \mathbb{R} \times \mathbb{R}^{n_1} \to \mathbb{R}_{\geq 0}$, $\alpha_1, \alpha_2 \in \mathcal{K}_\infty$, and a positive semidefinite function W such that*

$$\alpha_1(\|x_1\|) \leq V(t, x_1) \leq \alpha_2(\|x_1\|) \tag{5.45}$$

$$\frac{\partial V}{\partial t} + \frac{\partial V}{\partial x_1} f_1(t, x_1) \leq -W(x_1) \tag{5.46}$$

for all $t \in [t_o, t_{\max})$ and all $x_1 \in \mathbb{R}^{n_1}$.

Condition 5.3 holds as a direct consequence of Condition 5.1 being satisfied with $t_{\max} = \infty$ by the proof of Lemma 5.2.

Condition 5.4. *(2c) There exists $\beta \in \mathcal{KL}$ such that the solutions $x_2(t, t_o, x_{2o}, x_1)$ of $\dot{x}_2 = \tilde{f}_2(t, x_2)$ satisfy*

$$\|x_2(t, t_o, x_{2o}, x_1)\| \leq \beta(\|x_{2o}\|, t - t_o) \quad \forall t \in [t_o, t_{\max}). \tag{5.47}$$

It should be noted that $\|x_2(t, t_o, x_{2o}, x_1)\|$ represents the solutions of (5.37b) for fixed values of the parameter x_1, i.e. solutions of the path-following error dynamics (5.35b) for fixed values of the coordination error $\boldsymbol{\phi}$ and hence fixed values of the velocity. Consequently, Condition 5.4 implies that the solutions of x_2, i.e. subsystem (5.35b), are required to asymptotically decreasing to zero for all possible values of the parameter x_1. For (5.35) it then suffices to show that (5.35b) is UGAS for all fixed velocities $u_c \in [U_{rd} - a, U_{rd} + a]$. Hence, for all possible states of the synchronisation error (5.35a) the adaptation function $g(\cdot)$ that appears in the (5.35b) takes values in the range $[-a, a]$.

Consequently, a proof that the error dynamics of the integral line-of-sight path-following strategy is UGAS is sufficient to proof Condition 5.4. This proof is available from the work in Caharija et al. [43] and Caharija [39], where it is shown that the error dynamics of the integral line-of-sight path following is in fact UGAS and ULES for constant velocities. In fact, if we choose the look-ahead distances Δ_y and Δ_z, and the integral gains σ_y and σ_z as in Theorem 5.1, then the conditions of the proof in Caharija et al. [40] are satisfied for all $u_c \in [U_{rd} - a, U_{rd} + a]$. Therefore, we can show that there is a stable equilibrium on the path for each value of the coordination function.

Condition 2) is now verified with the following theorem:

Theorem 5.3. *The solutions of (5.35) are uniformly globally bounded.*

Proof. The proof of this theorem follows from Loría [93, Theorem 2], which is given as Theorem 5.5 in Appendix 5.C. In the case presented here, it is straightforward to verify that item 2) of Theorem 5.5 holds. In particular, in this case

$$\|[L_g V]\| = \left\| \frac{\partial V(x_1)}{\partial x_1} g(t, x_1, x_2) \right\| \tag{5.48a}$$

$$\leq \left\| \frac{\partial V}{\partial \boldsymbol{\phi}}(\boldsymbol{\phi}) \right\| \|\boldsymbol{G}(\boldsymbol{\zeta}, \boldsymbol{\phi})\| \|\boldsymbol{\zeta}\| \tag{5.48b}$$

$$\leq \left[\frac{\delta \|\boldsymbol{\phi}_2\|}{\frac{\delta}{2}\|\boldsymbol{\phi}_2\|^2 + 1} + \|\boldsymbol{g}_1(\boldsymbol{\phi})\| \, \|\boldsymbol{\Lambda}_1\| \, \|\boldsymbol{P}\| \right] C_2 \|\boldsymbol{\zeta}\| \tag{5.48c}$$

$$\leq \frac{\varepsilon \|\boldsymbol{\phi}\|}{\|\boldsymbol{\phi}\| + \kappa} C_2 \|\boldsymbol{\zeta}\| \leq C_1 C_2 \|\boldsymbol{\zeta}\| \tag{5.48d}$$

where C_1 is the constant from (5.34) and note that we have used the results from the verification of Condition 5.2. From (5.48d) it can be seen that to bound $\|[L_g V]\|$, we can choose $\alpha_5(\|\boldsymbol{\phi}\|) \in \mathcal{K}$ as a function of the form $\|\boldsymbol{\phi}\|/(\|\boldsymbol{\phi}\| + \kappa)$ for an appropriate choice of $\kappa > 0$. Having chosen a suitable family of functions for $\alpha_5(\|\boldsymbol{\phi}\|)$, we then

note that forward completeness of (5.35a) is implied by the fulfilment of Condition 5.2 and Condition 5.3 [93]. Therefore, the solutions of the cascade (5.35) exist for all time. Moreover, we know that according to Condition 5.4, $\|\boldsymbol{\zeta}\|$ decreases for all values of $\boldsymbol{\phi}$ since there is always an equilibrium on the path. Therefore, after a certain time, $W(\boldsymbol{\phi})$ dominates $\|[L_g V]\| \leq C_1 C_2 \|\boldsymbol{\zeta}\|$. More specifically, there exists a certain time after which it holds that $\alpha_5'(\|\boldsymbol{\zeta}\|) \triangleq \varepsilon C_2 \|\boldsymbol{\zeta}\| \leq \lambda_r$, such that $\alpha_5(\|\boldsymbol{\phi}\|) \leq \lambda_r W(\boldsymbol{\phi})$. Consequently, item 2) of Theorem 5.5 is satisfied. Moreover, since it is shown that Condition 5.2, 5.3, and 5.4 hold, Theorem 5.5 holds and consequently Theorem 5.3 holds. □

Theorem 5.4. *The origin of (5.35) is UGAS if Condition 5.1 and the conditions of Theorem 5.3 hold.*

Proof. It is shown that both Condition 5.1 and Theorem 5.3 hold and hence we can invoke [93, Proposition 2], given as Proposition 5.1 in Appendix 5.C, for system (5.35). □

This implies that all the control goals (5.2) are achieved and thus the proof of Theorem 5.1 is complete.

5.5 Case Study

This case study considers three AUVs moving in three dimensional space affected by a constant three dimensional ocean current. The parameters for the model (5.1) are obtained from da Silva et al. [45] and are given in Section C.2. The simulation parameters to describe the formation, the ocean current, the tuning of the integral line-of-sight guidance, and the formation control strategy are given in Table 5.1. The parameters in Table 5.1 are chosen such that they satisfy all conditions of Theorem 5.1. The initial position for the AUVs is given by

$$\begin{bmatrix} x_{1o} \\ y_{1o} \\ z_{1o} \\ \theta_{1o} \\ \psi_{1o} \end{bmatrix} = \begin{bmatrix} 0 \\ -100 \\ -50 \\ 0 \\ \pi \end{bmatrix}, \quad \begin{bmatrix} x_{2o} \\ y_{2o} \\ z_{2o} \\ \theta_{2o} \\ \psi_{2o} \end{bmatrix} = \begin{bmatrix} 0 \\ 50 \\ -50 \\ 0 \\ \pi/2 \end{bmatrix}, \quad \begin{bmatrix} x_{3o} \\ y_{3o} \\ z_{3o} \\ \theta_{3o} \\ \psi_{3o} \end{bmatrix} = \begin{bmatrix} 0 \\ -50 \\ -50 \\ 0 \\ -\pi/2 \end{bmatrix}.$$

The motion of the vehicles in three dimensional space can be seen in Figure 5.2. From Figure 5.2 it can be seen that the vehicles converge to their assigned path. This is confirmed by the error plots in Figures 5.3-5.5. From which is it can be seen that the y- and z-direction path-following errors converge to zero in Figure 5.3 and 5.4 respectively. Finally Figure 5.5 show that the along-path formation error go to zero and the desired formation is achieved.

5.6 Experimental Verification

This section presents the results of an experimental verification tests performed using three light autonomous underwater vehicles (LAUVs) from the University of Porto.

Table 5.1: Simulation parameters.

Variable	Value	Unit	Variable	Value	Unit
Δ_y	10	m	σ_y	0.2	-
Δ_z	20	m	σ_z	0.2	-
V_x	-0.11028	m/s	V_y	0.08854	m/s
V_z	-0.05	m/s	D_{z_1}	-20	m
D_{z_2},D_{z_3}	-10	m	D_{y_1}	0	m
D_{y_2}	-50	m	D_{y_3}	50	m
d_{12}	50	m	d_{13}	50	m
U_{rd}	2	m/s	a	0.2	m/s

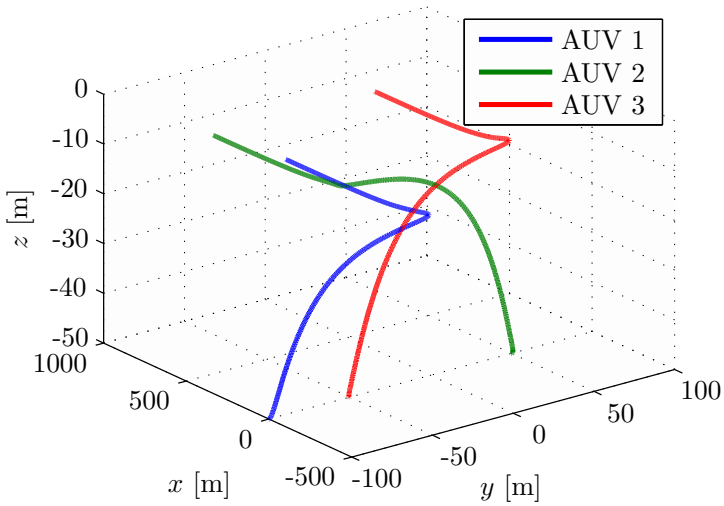

Figure 5.2: AUV trajectories in 3-D space

5.6.1 Vehicle description and capabilities

A picture of one of the LAUVs can be seen in Figure 5.6. The LAUVs are approximately 110 [cm] long depending on the configuration and have a diameter of 15 [cm]. The vehicles are designed to be light-weight and to be portable by one person. Therefore, their weight is between $15 - 20$ [kg] depending on the configuration. The vehicles are rated for a maximum depth of 100 [m]. For propulsion the vehicle uses a DC motor coupled to a three-blade propeller. The propulsion system allows the LAUV to reach speeds of approximately 2 [m/s]. To steer the LAUV is equipped with four fins. The vertically placed fins are used as rudders to control the yaw rotation. The horizontally placed fins are used as control surfaces to control the pitch rotation that is used to control the depth. The vehicles are equipped with GPS so that they can get position measurements when at the surface. For underwater navigation the vehicles are equipped with acoustic modems, long baseline (LBL) navigation, ultra-short baseline (USBL) navigation, a Doppler velocity

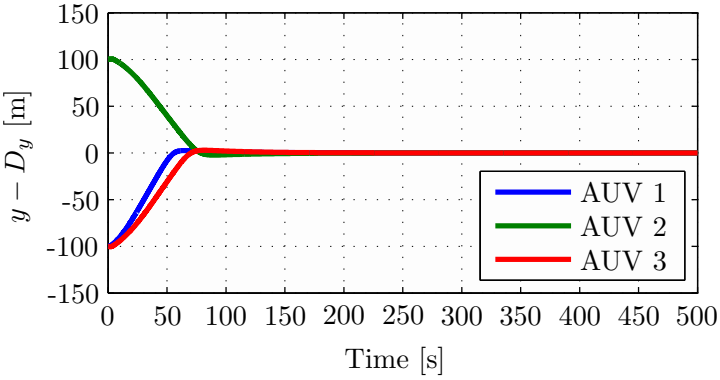

Figure 5.3: y-path-following error

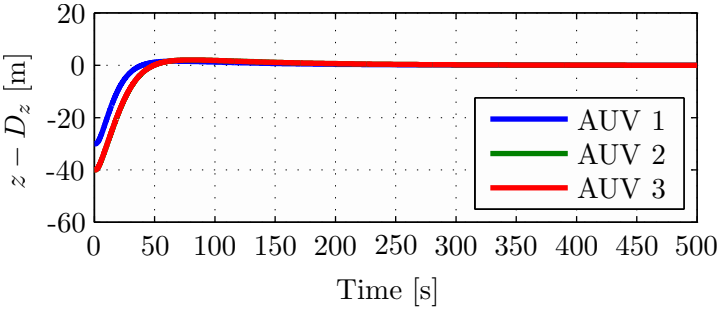

Figure 5.4: z-path-following error

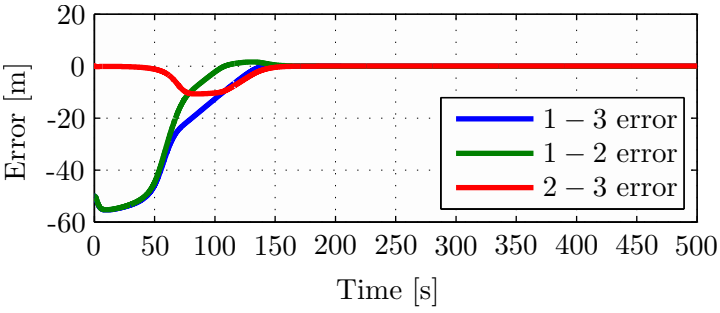

Figure 5.5: Along-path formation errors

Figure 5.6: Image of one of the LAUVs used during the experiments.

log (DVL), and a forward looking sonar for obstacle avoidance. For communication purposes the vehicles are equipped with an antenna that allows communication through WiFi and GSM/HSDPA.

5.6.2 Software toolchain

The vehicles are operated using the open-source toolchain developed at the Underwater Systems and Technology Laboratory (LSTS) at the University of Porto. This toolchain consists, among others, of the unified navigation environment DUNE, the inter-module communication protocol (IMC), and Neptus which is the command and control software. DUNE is the on-board software running on the vehicles and communication gateways. The software is responsible for interactions with sensors, payload, and actuators and also takes care of anything related to communications, navigation, control, manoeuvring, plan execution and vehicle supervision. To extend the functionality of the vehicles, source code can be added to the DUNE code repository. This is usually done as separate tasks that can interact with all other aspects on DUNE by exchanging data through the message bus system. For this communication, both on-board the vehicles and between vehicles, IMC is used. IMC consists of a set of messages common to all entities in the system, e.g. vehicles and communication nodes, and allows data exchange and communication. Hence, each entity of the network runs DUNE tasks to function, while IMC provides data-exchange and communication capabilities between vehicles and between different processes on the vehicles. The command and control software Neptus can be used during all different phases of a typical mission life cycle: planning, simulation, execution and post-mission analysis. It provides a graphical user interface with profiles of the available vehicles that include the sensory and manoeuvring capabilities of vehicles. Moreover, it provides different types of geographical maps. All of this can be used to plan and simulate missions considering all aspects of the mission including battery life, available sensors, etc. During execution Neptus can be used to visualise incoming real-time data from the operation, allows for tele-operation of vehicles, and can be used to send new manoeuvring commands to the vehicles. In the review and analysis phase Neptus can be used to process and visualise all the data stored through IMC messages of each vehicle. This allows the

user to visualise and analyse the data.

5.6.3 Mission description and implementation

The mission considers the coordination of three LAUVs that are required to coordinate their motion to a line formation on parallel straight-line paths. The test is performed in the harbour of Porto. To contain the motion of the LAUVs they are assigned rectangular shape paths. The motion pattern can be seen in Figure 5.7. From Figure 5.7 it can be seen that the lenght of the path is not the same for each AUV. The paths are placed this way to avoid collisions between the AUVs during cornering. However, this has the adverse effect that the path of the orange AUV on the inside is shorter than the path of the green AUV on the outside trajectory. In fact, the length of the corner section for the green AUV is 30 [m] longer than that of the yellow AUV and 60 [m] longer than that of the orange AUV. This means that each time a corner is taken, coordination is lost and the metric for the relative along-path distance does not make sense in the corner section. Therefore, the goal is to only achieve coordination on the straight-line sections of 200 [m] length depicted in Figure 5.7, which are sections of common length to each vehicle. The corner sections will be traversed in a way that aims to keep the formation error as small as possible before reaching the next straight-line section. This is done by normalising each corner section such that to the AUVs they appear to have the same length. This normalised distance is then scaled to artificially increase path-following errors on the normalised section. This will result in the outside AUV speeding up in the corner and the inside AUV slowing down to reduce the distance between the AUVs as much as possible before the next straight-line section is reached. To achieve coordination, communication of the along-path distances between the vehicles is necessary. For the purposes of this experiment, the AUVs are at the surface and communicate using their WiFi antennas. The communication is not done directly but is routed through a Manta communication gateway set up at the dock side. The communication gateway makes a local communication network for the vehicles to send their messages through. Each vehicle communicates its position to only one other vehicle and receives a position from the third vehicle.

The AUVs are given a nominal speed of $u_{rd} = 1.25$ [m/s] and can adjust their speed by 0.25 [m/s] either way. Since each AUV communicates its messages to only one other vehicle and the desired formation is a line, the argument of the synchronisation function $g(\cdot)$ will simply be the along-path distances of each vehicle subtracted. Consequently, the velocity assignment is made by taking.

$$u_{c_j}(t) = 1.25 - \frac{2 \cdot 0.25}{\pi} \text{atan}(x_j - x_i). \tag{5.49}$$

The look-ahead distance for the vehicles is set to $\Delta = 4$ [m] and the integral gain is set to $\sigma = 0.5$ [m/s]. To be able to communicate through the WiFi network, the vehicles should be at the surface. Therefore, the depth controller of the vehicle is used to keep the vehicles on the surface.

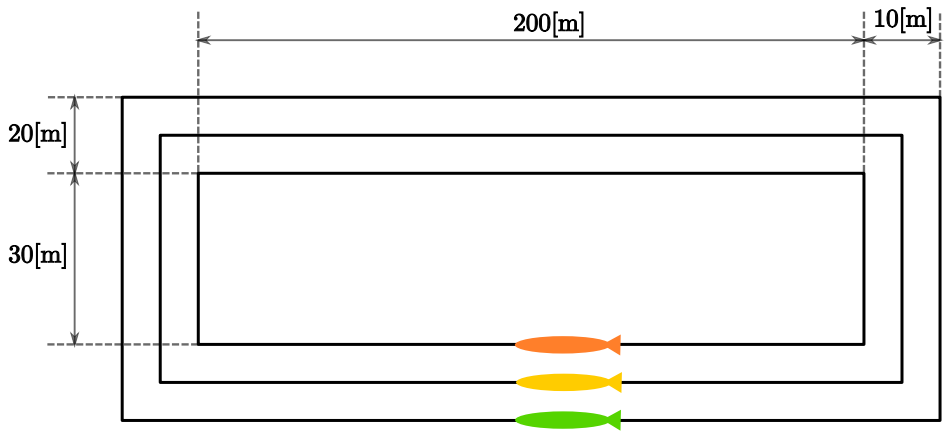

Figure 5.7: LAUV paths with dimensions

5.6.4 Simulation benchmark

To evaluate the experimental data gathered during the mission described above, we first perform a simulation which can be used as a benchmark. These simulations were performed using DUNE, which provides high-accuracy hardware simulations of the vehicles to test code implementations. To simulate an environmental disturbance, a constant ocean current is added with a component in north and east direction. The ocean current has a velocity of 0.2 [m/s] from the east direction and -0.1 [m/s] from north direction. The vehicle paths generated by the simulations can be seen in Figure 5.8, from which we see that the paths accurately resemble the pattern suggested in Figure 5.7. The desired velocity assignments can be seen in Figure 5.9, from which it can be seen that the desired velocity assignment is as expected. Especially during the corner sections it can be seen that the red vehicle is waiting for the other vehicles by lowering its speed, and we see the blue vehicle changing its velocity once it synchronises with the red vehicle. On the straight-line sections the velocity does not converge precisely to the nominal value but oscillates around it. These same oscillations can be seen in the plot for the synchronisation errors given in Figure 5.10. The error does not go to zero but oscillates around it. This can be expected for the hardware simulations presented here, which have discrete communication. This causes the vehicles to overshoot their desired positions to achieve synchronisation. Moreover, this discretisation causes transients in the velocity controllers at every step which also prevent the vehicles from following tracking their desired inputs, which is something that in the theory and numerical simulations is guaranteed by the feedback linearising controllers.

5.6.5 Experimental results

The trajectories for the vehicles performing the mission described in Subsection 5.6.3 can be seen in Figure 5.11. From Figure 5.11 it can be seen that the vehicles converge to the prescribed patterns. However, the trajectories are less smooth in

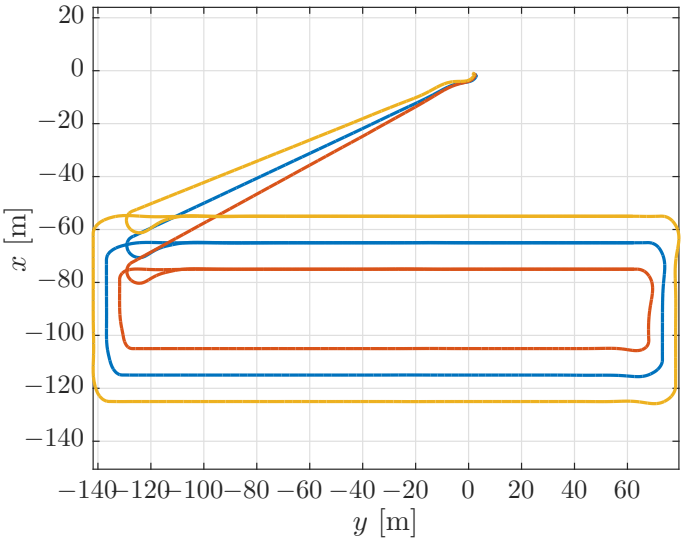

Figure 5.8: On-board estimates of the paths of the vehicles.

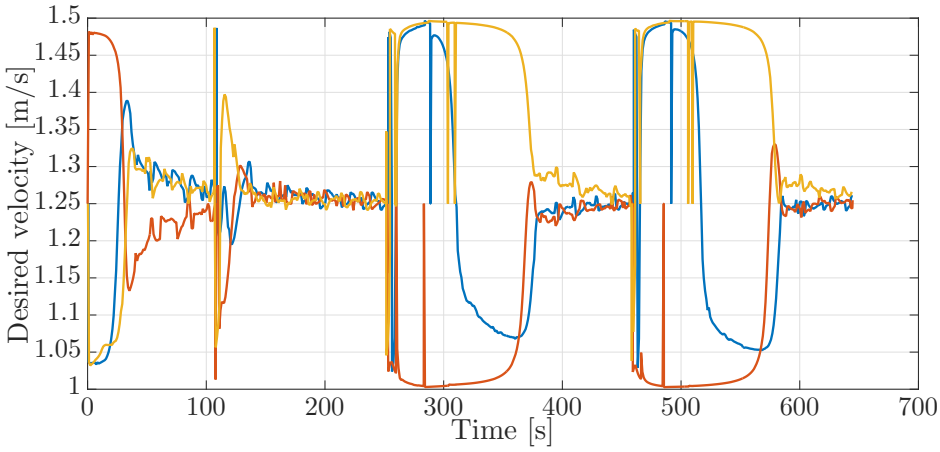

Figure 5.9: Desired velocity assignment for the vehicles in simulation.

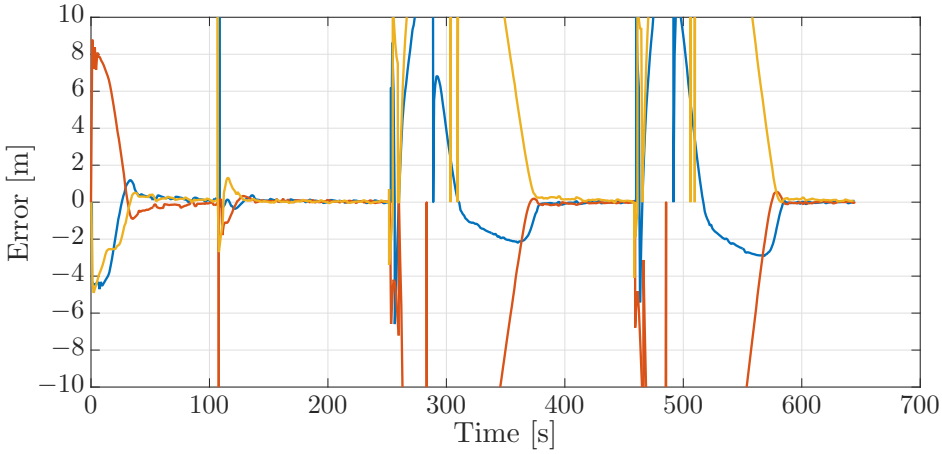

Figure 5.10: Synchronisation errors between the vehicles in simulation. The blue line is the synchronisation error of the blue vehicle with measurements from the red vehicle. The red line is the synchronisation error of the red vehicle with measurements from the yellow vehicle. The yellow line is the synchronisation error of the yellow vehicle with measurements from the blue vehicle.

open water than in simulation. This can be seen by comparing Figure 5.8 and Figure 5.11. This is a performance degradation that is to be expected by the added uncertainties in the experiments, especially at the surface where the vehicles are also exposed to waves. Note that in Figure 5.11, the distances between the rectangles may not be accurate as depicted, since the placement depends on the first global estimate of the position and are interpolated from there. However, the overall shape of the path suggests the geometric task of path following is achieved satisfactorily for the circumstances under consideration. The desired velocity assignment can be seen in Figure 5.12. It can be seen that the pattern of the relative velocity assignments resemble those of the simulation results in Figure 5.9. However, like for the motion patterns the added uncertainty reduces the performance. In particular, the oscillations on the straight-line sections are larger and the signal is less smooth in general. Despite the oscillations it can be seen that the velocity assignment is done as desired by making the vehicles that are ahead wait while the vehicles that are behind speed up until a steady-state is reached. The same difference with respect to the simulations can be seen from the plots of the synchronisation errors, which are given in Figure 5.13. The synchronisation errors in Figure 5.13 show larger oscillations on the straight-line sections and are less smooth in general than the synchronisation errors from the simulations in Figure 5.10. From Figure 5.13 it can be seen that after a transient period in which the vehicles converge to the desired paths and get in formation, they reach a steady-state until they arrive at the next waypoint. The steady-state has oscillations of the synchronisation errors with an amplitude of up to 2 [m]. However, it should be noted that the oscillations are much smaller on the second straight-line section. This suggests that the difference in environmental circumstances between the two sides of the rectangle might

play an important roll in the amplitude of the oscillations. The amplitude of the oscillations should preferably be lowered in future experiments. In the remainder of this subsection we will discuss measures to achieve this. Before going into these measures, we note the fact that the communication only attains a low bandwidth of about 1 [Hz]. Consequently, the desired velocity can only be updated every second which causes vehicles to overshoot the desired formation. Although a similar bandwidth is utilised in the simulations of Subsection 5.6.4, the bandwidth is attained uniformly over the whole path in the simulations, while in the experiments communication is more intermittent and the attained bandwidth differs between the vehicles.

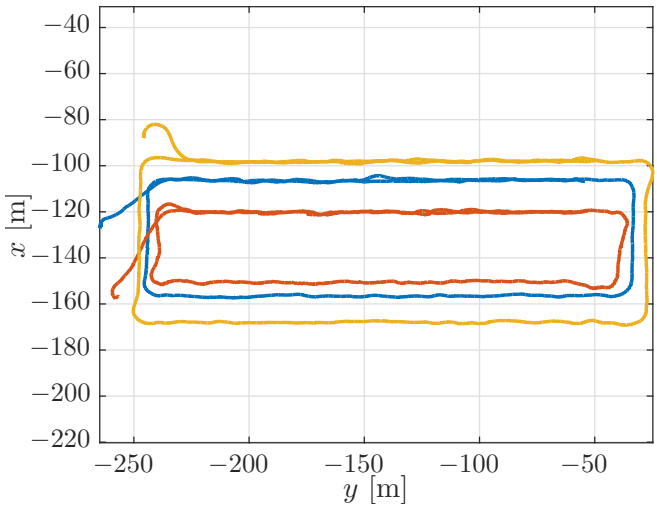

Figure 5.11: On board estimates of the paths of the vehicles in the experiments.

The oscillations on the straight-line sections can be attributed to several factors. The most important is the low bandwidth of communication which causes delays in the changes of the desired velocity that are required to achieve the formation. Moreover, a transient in the velocity controller is induced every time the velocity is changed. These changes in the velocity are much less smooth in this case than it would be if the communication bandwidth was higher. This is already the case for the hardware simulations in Subsection 5.6.4 and is exacerbated by the more intermittent communication in the experiments. Added to that, there is more delay in the communication, which requires interpolation to compare incoming along-path distance measurements to stored along-path distances of the vehicle itself, such that the timestamps of those measurements match. Consequently, the calculated errors become less accurate due to the interpolation, and the control action is applied with a delay since the error is 'old' at the time the control action is computed and applied. Besides increasing the bandwidth, over which direct control might not be available, several other measures can be taken. One measure could be to change the synchronisation function. More specifically, the slope of the arctangent around

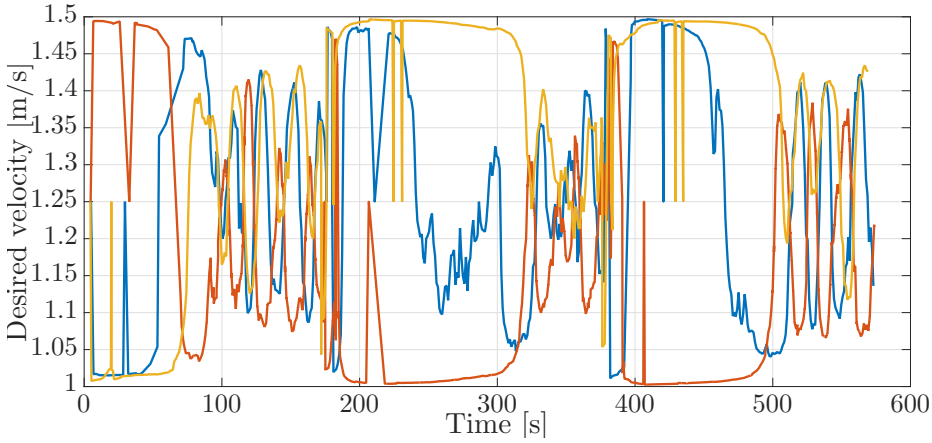

Figure 5.12: Desired velocity assignment for the vehicles in the experiments.

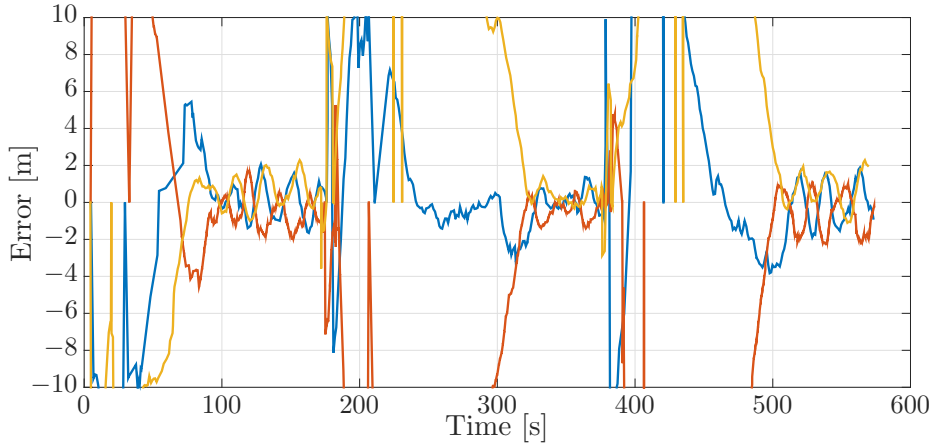

Figure 5.13: Synchronisation errors between the vehicles in the experiments. The blue line is the synchronisation error of the blue vehicle with measurements from the red vehicle. The red line is the synchronisation error of the red vehicle with measurements from the yellow vehicle. The yellow line is the synchronisation error of the yellow vehicle with measurements from the blue vehicle.

the origin can be decreased. This has the effect that changes in the velocity will be smoother, and if the vehicles overshoot the desired position, then the resulting change in velocity is less severe. This might be combined with an increase of the look-ahead vehicles, which will make the guidance of the vehicles less reactive to changes in the velocity and the transients in the controller. The negative effect of changing the slope of the arctangent is that it will take longer for the vehicles to converge to the formation. Therefore, the choice will be a trade-off between convergence speed and desired steady-state behaviour. For the case considered here, speed of convergence plays an important role due to the transients introduced in each corner. For future implementations this requirement can be removed by letting vehicles have the same corners and interweaving trajectories as suggested in Figure 5.14. The implementation in Figure 5.14 makes the cornering distance identical for each vehicle and should maintain formation when coming to the next straight-line section. Therefore, the necessity of fast transients is removed. Another measure to remove the oscillations is a change in the communication topology. In the implementation presented here the graph is cyclic. This has an advantage that all the vehicles wait for vehicles that are left behind. This assures again that the steady-state is reached faster. However, it also implies that all the vehicles should synchronise at the same time. More specifically, partial synchronisation between two of the vehicles is disturbed by one of the vehicles is waiting for the third while the other vehicle desired to maintain the nominal velocity. This can be solved by implementing the communication graph in a leader-follower like structure where two of the vehicles synchronise only to the leader, which allows for synchronisation between two of the vehicles while the third vehicle still converges. Another option could be that each vehicle sends its information to both of the others. However, this is more complicated from an implementation perspective since interpolation will have to be applied to match all the time-stamps of incoming messages, which will also introduce some additional errors. Despite the difficulties mentioned here, the experimental results illustrate the effectiveness of the proposed coordinated path-following strategy.

5.7 Conclusions

In this chapter a control strategy for straight-line coordinated path-following of under-actuated vehicles moving in three dimensional space has been presented. It has been shown that using integral LOS guidance the vehicles are able to reject an unknown, but constant, environmental disturbance, whilst simultaneously coordinating their motion along a desired path with a nonlinear decentralised coordination law to achieve a desired formation. The origin of the combined coordination and path-following error dynamics is shown to be UGAS by showing that our feedback-interconnected system can be analysed as a cascaded system and satisfies the conditions to prove UGAS. Simulation results have been presented that validate the theoretical results. Moreover, experiments with actual AUVs are included to validate the control strategy in a practical situation.

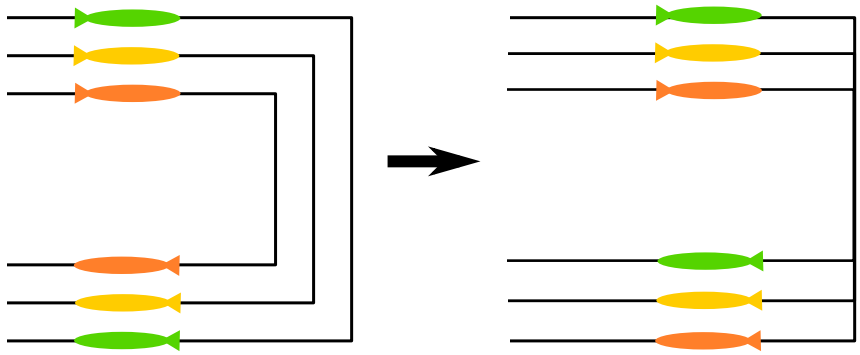

Figure 5.14: Current implementation of cornering (left) and suggested alternative implementation (right).

5.A Function Definitions

$$
\begin{aligned}
F_{u_r}(v_r, w_r, r, q) &\triangleq \frac{1}{m_{11}}[(m_{22}v_r + m_{25}r)r - (m_{33}w_r + m_{34}q)q], \\
X_{v_r}(u_r) &\triangleq \frac{m_{25}^2 - m_{11}m_{55}}{m_{22}m_{55} - m_{25}^2}u_r + \frac{d_{55}m_{25} - d_{25}m_{55}}{m_{22}m_{55} - m_{25}^2}, \\
Y_{v_r}(u_r) &\triangleq \frac{(m_{22} - m_{11})m_{25}}{m_{22}m_{55} - m_{25}^2}u_r - \frac{d_{22}m_{55} - d_{52}m_{25}}{m_{22}m_{55} - m_{25}^2}, \\
X_{w_r}(u_r) &\triangleq \frac{-m_{34}^2 + m_{11}m_{44}}{m_{33}m_{44} - m_{34}^2}u_r + \frac{d_{44}m_{34} - d_{34}m_{44}}{m_{33}m_{44} - m_{34}^2}, \\
Y_{w_r}(u_r) &\triangleq \frac{(m_{11} - m_{33})m_{34}}{m_{33}m_{44} - m_{34}^2}u_r - \frac{d_{33}m_{44} - d_{43}m_{34}}{m_{33}m_{44} - m_{34}^2}, \\
Z_{w_r} &\triangleq \frac{BG_zWm_{34}}{m_{33}m_{44} - m_{34}^2}, \\
F_q(\theta, u_r, w_r, q) &\triangleq \frac{m_{34}d_{33} - m_{33}(d_{43} - (m_{33} - m_{11})u_r)}{m_{33}m_{44} - m_{34}^2}w_r \\
&\quad + \frac{m_{34}(d_{34} - m_{11}u_r) - m_{33}(d_{44} - m_{34}u_r)}{m_{33}m_{44} - m_{34}^2}q \\
&\quad - \frac{BG_zWm_{33}}{m_{33}m_{44} - m_{34}^2}\sin(\theta), \\
F_r(u_r, v_r, r) &\triangleq \frac{m_{25}d_{22} - m_{22}(d_{53} + (m_{22} - m_{11})u_r)}{m_{22}m_{55} - m_{25}^2}v_r \\
&\quad + \frac{m_{25}(d_{25} + m_{11}u_r) - m_{22}(d_{55} + m_{25}u_r)}{m_{22}m_{55} - m_{25}^2}r.
\end{aligned}
$$

Vectors $\boldsymbol{h}_z \triangleq [h_{z1}, h_{z2}, h_{z3}, h_{z4}, h_{z5}]^T$ and $\boldsymbol{h}_{w_r} \triangleq [h_{w_r1}, h_{w_r2}, h_{w_r3}, h_{w_r4}, h_{w_r5}]^T$ are defined as:

$$
\begin{aligned}
h_{z1} &= -\sin(\tilde{\theta} + \theta_d); \quad h_{z2} = h_{z3} = h_{z5} = 0 \\
h_{z4} &= w_r \left[\frac{\cos(\tilde{\theta}) - 1}{\tilde{\theta}} \cos(\theta_d) - \frac{\sin(\tilde{\theta})}{\tilde{\theta}} \sin(\theta_d) \right] \\
&\quad - u_c \left[\frac{\sin(\tilde{\theta})}{\tilde{\theta}} \cos(\theta_d) + \frac{\cos(\tilde{\theta}) - 1}{\tilde{\theta}} \sin(\theta_d) \right] \\
h_{w_r1} &= \frac{X_{w_r}(\tilde{u}_r + u_c) - X^{u_c}_{w_r}}{\tilde{u}_r} \gamma_{w_r}(z_{\text{int}}, z, w_r) \\
&\quad + w_r \frac{Y_{w_r}(\tilde{u}_r + u_c) - Y^{u_c}_{w_r}}{\tilde{u}_r}, \\
h_{w_r4} &= Z_{w_r} \left[\frac{\sin(\tilde{\theta})}{\tilde{\theta}} \cos(\theta_d) + \frac{\cos(\tilde{\theta} - 1)}{\tilde{\theta}} \sin(\theta_d) \right], \\
h_{w_r5} &= X_{w_r}(\tilde{u}_r + u_c); \quad h_{w_r2} = h_{w_r3} = 0.
\end{aligned}
$$

The vectors $\boldsymbol{h}_y$ and $\boldsymbol{h}_{v_r}$ are defined as:

$$
\begin{aligned}
\boldsymbol{h}_y &\triangleq [h_{y1}, h_{y2}, h_{y3}, h_{y4}, h_{y5}, h_{y6}, h_{y7}, h_{y8}]^T, \quad \text{where,} \\
h_{y2} &= \frac{u_c}{e_{z2}} \left[\frac{\Delta_z}{\sqrt{(e_{z_2} + \sigma_z z^{\text{eq}}_{\text{int}})^2 + \Delta_z^2}} - \frac{1}{\sqrt{s^2 + 1}} \right] \\
&\quad - \frac{s}{\sqrt{s^2 + 1}} \frac{Z_{w_r}}{Y^{u_c}_{w_r}} \frac{1}{e_z} \left[\frac{e_{z_2} + \sigma_z z^{\text{eq}}_{\text{int}}}{\sqrt{(e_{z_2} + \sigma_z z^{\text{eq}}_{\text{int}})^2 + \Delta_z^2}} - \frac{s}{\sqrt{s^2 + 1}} \right], \\
h_{y3} &= \sin(\tilde{\theta} + \theta_d) \sin(\tilde{\psi} + \psi_d), \; h_{y4} = \cos(\tilde{\theta} + \theta_d) \sin(\tilde{\psi} + \psi_d) \\
h_{y5} &= \left[u_c \cos(\tilde{\theta} + \theta_d) - \frac{s}{\sqrt{s^2 + 1}} \frac{Z_{w_r}}{Y^{u_c}_{w_r}} \sin(\tilde{\theta} + \theta_d) \right] \\
&\quad \cdot \left[\frac{\sin(\tilde{\psi})}{\tilde{\psi}} \cos(\psi_d) + \frac{\cos(\tilde{\psi} - 1)}{\tilde{\psi}} \sin(\psi_d) \right] \\
&\quad + v_r \left[\frac{\cos(\tilde{\psi}) - 1}{\tilde{\psi}} \cos(\psi_d) - \frac{\sin(\tilde{\psi})}{\tilde{\psi}} \sin(\psi_d) \right], \\
h_{y7} &= u_c \sin(\psi_d) \left[\frac{\cos(\tilde{\theta}) - 1}{\tilde{\theta}} \cos(\theta_d) - \frac{\sin(\tilde{\theta})}{\tilde{\theta}} \sin(\theta_d) \right] \\
&\quad - \frac{s}{\sqrt{s^2 + 1}} \frac{Z_{w_r}}{Y^{u_c}_{w_r}} \sin(\psi_d) \left[\frac{\sin(\tilde{\theta})}{\tilde{\theta}} \cos(\theta_d) + \frac{\cos(\tilde{\theta}) - 1}{\tilde{\theta}} \sin(\theta_d) \right] \\
h_{y1} &= h_{y6} = h_{y8} = 0, \\
\boldsymbol{h}_{v_r} &\triangleq [h_{v_r1}, h_{v_r2}, h_{v_r3}, \; h_{v_r4}, h_{v_r5}, h_{v_r6}, h_{v_r7}, h_{v_r8}]^T \quad \text{where,} \\
h_{v_r2} &= \frac{X^{u_c}_{v_r}}{e_{z_2}} \left[\frac{\Delta_z}{\sqrt{(e_{z_2} + \sigma_z z^{\text{eq}}_{\text{int}})^2 + \Delta_z^2}} - \frac{1}{\sqrt{s^2 + 1}} \right] \gamma_{v_r}(y_{\text{int}}, y, v_r),
\end{aligned}
$$

$$
\begin{aligned}
h_{v_r 4} &= \frac{X_{v_r}(\tilde{u}_r + u_c) - X_{v_r}^{u_c}}{\tilde{u}_r} \cos(\tilde{\theta} + \theta_d) \gamma_{v_r}(y_{\text{int}}, y, v_r) \\
&\quad + v_r \frac{Y_{v_r}(\tilde{u}_r + u_c) - Y_{v_r}^{u_c}}{\tilde{u}_r}, \\
h_{v_r 6} &= X_{v_r}(\tilde{u}_r + u_c) \cos(\tilde{\theta} + \theta_d), \; h_{v_r 1} = h_{v_r 3} = h_{v_r 5} = h_{v_r 8} = 0 \\
h_{v_r 7} &= \left[\frac{\cos(\tilde{\theta}) - 1}{\tilde{\theta}} \cos(\theta_d) - \frac{\sin(\tilde{\theta})}{\tilde{\theta}} \sin(\theta_d) \right] X_{v_r}^{u_c} \gamma_{v_r}(y_{\text{int}}, y, v_r).
\end{aligned}
$$

Functions $\gamma_{w_r}(z_{\text{int}}, z, w_r)$ and $\gamma_{v_r}(y_{\text{int}}, y, v_r)$ are defined as

$$
\begin{aligned}
\gamma_{w_r} &\triangleq \frac{\Delta_z u_c (z + \sigma_z z_{\text{int}}}{((z + \sigma_z z_{\text{int}}^{\text{eq}})^2 + \Delta_z^2)^{3/2}} + \frac{\Delta_z^2}{((z + \sigma_z z_{\text{int}}^{\text{eq}})^2 + \Delta_z^2)^{3/2}} w_r \\
&\quad + \frac{\sigma_z \Delta_z^2}{((z + \sigma_z z_{\text{int}}^{\text{eq}})^2 + \Delta_z^2)^2} z + \frac{\Delta_z V_z}{(z + \sigma_z z_{\text{int}}^{\text{eq}})^2 + \Delta_z^2)}, \\
\gamma_{v_r} &\triangleq \frac{\Delta_y \Gamma(s)(y + \sigma_y y_{\text{int}}}{((y + \sigma_y y_{\text{int}}^{\text{eq}})^2 + \Delta_y^2)^{3/2}} - \frac{\Delta_y^2}{((y + \sigma_y y_{\text{int}}^{\text{eq}})^2 + \Delta_y^2)^{3/2}} v_r \\
&\quad - \frac{\sigma_y \Delta_y^2}{((y + \sigma_y y_{\text{int}}^{\text{eq}})^2 + \Delta_y^2)^2} y - \frac{\Delta_y V_y}{(y + \sigma_y y_{\text{int}}^{\text{eq}})^2 + \Delta_y^2)}.
\end{aligned}
$$

$$
\boldsymbol{A}_1 \triangleq \begin{bmatrix} \frac{-\sigma_z \Delta_z}{(e_{z_2}+\sigma_z z_{\text{int}}^{\text{eq}})^2+\Delta_z^2} & \frac{\Delta_z}{(e_{z_2}+\sigma_z z_{\text{int}}^{\text{eq}})^2+\Delta_z^2} & 0 \\ \frac{-\sigma_z^2 \Delta_z}{(e_{z_2}+\sigma_z z_{\text{int}}^{\text{eq}})^2+\Delta_z^2} & \left(\frac{\sigma_z \Delta_z}{(e_{z_2}+\sigma_z z_{\text{int}}^{\text{eq}})^2+\Delta_z^2} - \frac{u_c}{\sqrt{(e_{z_2}+\sigma_z z_{\text{int}}^{\text{eq}})^2+\Delta_z^2}} \right) & \frac{\Delta_z}{\sqrt{(e_{z_2}+\sigma_z z_{\text{int}}^{\text{eq}})^2+\Delta_z^2}} \\ \frac{-\sigma_z^2 \Delta_z^2 X_{w_r}^{u_c}}{((e_{z_2}+\sigma_z z_{\text{int}}^{\text{eq}})^2+\Delta_z^2)^2} & \left(\frac{\sigma_z \Delta_z^2 X_{w_r}^{u_c}}{((e_{z_2}+\sigma_z z_{\text{int}}^{\text{eq}})^2+\Delta_z^2)^2} + \frac{Z_{w_r}}{\sqrt{(e_{z_2}+\sigma_z z_{\text{int}}^{\text{eq}})^2+\Delta_z^2}} - \frac{u_c \Delta_z X_{w_r}^{u_c}}{((e_{z_2}+\sigma_z z_{\text{int}}^{\text{eq}})^2+\Delta_z^2)^{3/2}} \right) & \left(Y_{w_r}^{u_c} - \frac{\Delta_z^2 X_{w_r}^{u_c}}{((e_{z_2}+\sigma_z z_{\text{int}}^{\text{eq}})^2+\Delta_z^2)^{3/2}} \right) \end{bmatrix} \tag{5.50}
$$

$$
\boldsymbol{A}_2 \triangleq \begin{bmatrix} -\frac{\sigma_y \Delta_y}{(e_{y_2}+\sigma_y y_{\text{int}}^{\text{eq}})^2+\Delta_y^2} & \frac{\Delta_y}{(e_{y_2}+\sigma_y y_{\text{int}}^{\text{eq}})^2+\Delta_y^2} & 0 \\ -\frac{\sigma_y^2 \Delta_y}{(e_{y_2}+\sigma_y y_{\text{int}}^{\text{eq}})^2+\Delta_y^2} & \left(\frac{\sigma_y \Delta_y}{(e_{y_2}+\sigma_y y_{\text{int}}^{\text{eq}})^2+\Delta_y^2} - \frac{\Gamma(s)}{\sqrt{(e_{y_2}+\sigma_y y_{\text{int}}^{\text{eq}})^2+\Delta_y^2}} \right) & \frac{\Delta_y}{\sqrt{(e_{y_2}+\sigma_y y_{\text{int}}^{\text{eq}})^2+\Delta_y^2}} \\ \frac{1}{\sqrt{s^2+1}} \frac{\sigma_y^2 \Delta_y^2 X_{w_r}^{u_c}}{((e_{y_2}+\sigma_y y_{\text{int}}^{\text{eq}})^2+\Delta_y^2)^2} & \frac{1}{\sqrt{s^2+1}} \left(\frac{\Gamma(s) \Delta_y X_{w_r}^{u_c}}{((e_{y_2}+\sigma_y y_{\text{int}}^{\text{eq}})^2+\Delta_y^2)^{3/2}} - \frac{\sigma_y \Delta_y^2 X_{w_r}^{u_c}}{((e_{y_2}+\sigma_y y_{\text{int}}^{\text{eq}})^2+\Delta_y^2)^2} \right) & \left(Y_{w_r}^{u_c} - \frac{\Delta_y^2 X_{w_r}^{u_c}}{\sqrt{s^2+1}((e_{y_2}+\sigma_y y_{\text{int}}^{\text{eq}})^2+\Delta_y^2)^{3/2}} \right) \end{bmatrix} \tag{5.51}
$$

5.B Proof of Lemma 5.2

The proof for Lemma 5.2 follows along the lines of the proof given in [31]. However, we now have to account for the matrix $\boldsymbol{\Lambda}$ in the dynamics (in addition to the interconnection term $\boldsymbol{H}_x\boldsymbol{\zeta}$ being different). According to Assumption 5.9 the communication graph $\mathcal{G}$ has at least one globally reachable vertex. Therefore in this proof we assume that $\mathcal{G}$ has $1 \leq r < n$ globally reachable vertices. This allows us, without loss of generality, to partition $\boldsymbol{L}$ as

$$\boldsymbol{L} = \begin{bmatrix} \boldsymbol{L}_1 & \boldsymbol{L}_2 \\ \boldsymbol{0} & \boldsymbol{L}_3 \end{bmatrix} \tag{5.52}$$

where $\boldsymbol{L}_1 \in \mathbb{R}^{(n-r)\times(n-r)}$ is anti-Hurwitz, i.e., $-\boldsymbol{L}_1$ is Hurwitz, and satisfies

$$\boldsymbol{P}\boldsymbol{L}_1 + \boldsymbol{L}_1^T\boldsymbol{P} = \boldsymbol{Q}, \qquad \boldsymbol{Q} = \boldsymbol{Q}^T > 0 \tag{5.53}$$

for some positive definite diagonal matrix $\boldsymbol{P}$ [91]. The sub-graph corresponding to $\boldsymbol{L}_3 \in \mathbb{R}^{r\times r}$, i.e. $\mathcal{G}(\boldsymbol{L}_3)$, is strongly connected. Hence $\boldsymbol{L}_3$ is positive semi-definite, with zero as a simple eigenvalue and a corresponding eigenvector $\mathbf{1}_r = [1, ..., 1]^T \in \mathbb{R}^r$. Consequently, $\boldsymbol{L}_3$ can be decomposed into $\boldsymbol{L}_3 = \boldsymbol{M}_3\boldsymbol{M}_3^T$, where $\boldsymbol{M}_3 \in \mathbb{R}^{r\times(r-1)}$ has full column rank. A coordinate transform is then given by

$$\boldsymbol{\phi} \triangleq \begin{bmatrix} \boldsymbol{L}_1 & \boldsymbol{L}_2 \\ \boldsymbol{0} & \boldsymbol{M}_3^T \end{bmatrix} \boldsymbol{\vartheta} \triangleq \boldsymbol{T}\boldsymbol{\vartheta}. \tag{5.54}$$

We can now verify the claims of Lemma 5.2.

Claim 1):

$$\boldsymbol{\phi} = \boldsymbol{0} \;\Rightarrow\; \begin{bmatrix} \boldsymbol{I} & \boldsymbol{0} \\ \boldsymbol{0} & \boldsymbol{M}_3 \end{bmatrix} \boldsymbol{\phi} = \boldsymbol{L}\boldsymbol{\vartheta} = \boldsymbol{0} \;\Rightarrow\; \boldsymbol{\vartheta} = \alpha\mathbf{1}_n,\ \alpha \in \mathbb{R}.$$

Consequently, $\boldsymbol{\phi} = \boldsymbol{0}$ implies that $\vartheta_j = \vartheta_i$, $j, i = 1, ..., n$.

Claim 2): Differentiating (5.54) w.r.t time we obtain

$$\dot{\boldsymbol{\phi}} = \begin{bmatrix} -\boldsymbol{L}_1\boldsymbol{\Lambda}_1\boldsymbol{g}_1(\boldsymbol{\phi}_1) - \boldsymbol{L}_2\boldsymbol{\Lambda}_2\boldsymbol{g}_2(\boldsymbol{\kappa}) \\ -\boldsymbol{M}_3^T\boldsymbol{\Lambda}_2\boldsymbol{g}_2(\boldsymbol{\kappa}) \end{bmatrix} + \boldsymbol{T}\boldsymbol{H}_x(\boldsymbol{\zeta}, \boldsymbol{\vartheta})\boldsymbol{\zeta} \tag{5.55a}$$

$$\triangleq \boldsymbol{f}(\boldsymbol{\phi}) + \boldsymbol{G}(\boldsymbol{\zeta}, \boldsymbol{\phi})\boldsymbol{\zeta} \tag{5.55b}$$

where $\boldsymbol{\phi} = [\boldsymbol{\phi}_1^T, \boldsymbol{\phi}_2^T]^T$, with $\boldsymbol{\phi}_1 \in \mathbb{R}^{n-r}$ and $\boldsymbol{\phi}_2 \in \mathbb{R}^r$, and we defined $\boldsymbol{\kappa} \triangleq \boldsymbol{M}_3\boldsymbol{\phi}_2$ to simplify notation. Moreover, using (5.28) it is straightforward to verify that $\boldsymbol{G}(\boldsymbol{\zeta}, \boldsymbol{\phi}) \triangleq \boldsymbol{T}\boldsymbol{H}_x(\boldsymbol{\zeta}, \boldsymbol{\vartheta})$ is globally bounded in its arguments.

Claim 3): Consider the stability properties of the nominal system

$$\begin{bmatrix} \dot{\boldsymbol{\phi}}_1 \\ \dot{\boldsymbol{\phi}}_2 \end{bmatrix} = \begin{bmatrix} -\boldsymbol{L}_1\boldsymbol{\Lambda}_1\boldsymbol{g}_1(\boldsymbol{\phi}_1) - \boldsymbol{L}_2\boldsymbol{\Lambda}_2\boldsymbol{g}_2(\boldsymbol{\kappa}) \\ -\boldsymbol{M}_3^T\boldsymbol{\Lambda}_2\boldsymbol{g}_2(\boldsymbol{\kappa}) \end{bmatrix} = \boldsymbol{f}(\boldsymbol{\phi}). \tag{5.56}$$

Remark 5.10. Note that considering the stability properties of the origin of the nominal dynamics means that we consider the stability properties of (5.55a) when the perturbing dynamics has converged. This implies that the cross-track errors

have converged, and consequently, the desired yaw angle ψ_d and pitch angle θ_d are bounded well away from $\pi/2$ and $-\pi/2$. Hence the elements of diagonal matrices $\boldsymbol{\Lambda}_1$ and $\boldsymbol{\Lambda}_2$ are bounded away from zero and will have clearly defined minimum eigenvalues of λ_{m_1} and λ_{m_2} respectively.

To show that the origin of (5.56) is UGAS we use the Lyapunov function candidate

$$V \triangleq \frac{\delta}{2}\|\boldsymbol{\phi}_2\|^2 + \int_0^{\boldsymbol{\phi}_1} \boldsymbol{P}\boldsymbol{\Lambda}_1\boldsymbol{g}_1(\boldsymbol{y}) \cdot d\boldsymbol{y} \tag{5.57}$$

where $\boldsymbol{P}$ is the positive definite diagonal solution of (5.53) and $\delta > 0$ to be chosen at a later stage. The sector property of g and the fact that $\boldsymbol{P}$ is a positive definite diagonal matrix assure that V is a positive definite function of $\boldsymbol{\phi}_1$ and $\boldsymbol{\phi}_2$. It is straightforward to verify that V is also radially unbounded. Taking the time-derivative of V along the solutions of (5.56) gives

$$\begin{aligned}\dot{V} = &-\tfrac{1}{2}\boldsymbol{g}_1^T(\boldsymbol{\phi}_1)\left[\boldsymbol{\Lambda}_1\boldsymbol{P}\boldsymbol{L}_1\boldsymbol{\Lambda}_1 + \boldsymbol{\Lambda}_1\boldsymbol{L}_1^T\boldsymbol{P}\boldsymbol{\Lambda}_1\right]\boldsymbol{g}_1(\boldsymbol{\phi}_1) \\ &- \delta\boldsymbol{\kappa}^T\boldsymbol{\Lambda}_2\boldsymbol{g}_2(\boldsymbol{\kappa}) - \boldsymbol{g}_1^T(\boldsymbol{\phi}_1)\boldsymbol{\Lambda}_1\boldsymbol{P}\boldsymbol{L}_2\boldsymbol{\Lambda}_2\boldsymbol{g}_2(\boldsymbol{\kappa})\end{aligned} \tag{5.58}$$

If we substitute for $\boldsymbol{Q}$ in (5.58) and take the norm we obtain

$$\dot{V} \leq c\|\boldsymbol{g}_1(\boldsymbol{\phi}_1)\| \cdot \|\boldsymbol{g}_2(\boldsymbol{\kappa})\| - \delta\boldsymbol{\kappa}^T\boldsymbol{\Lambda}_2\boldsymbol{g}_2(\kappa) - \frac{q_m}{2}\|\boldsymbol{g}_1(\boldsymbol{\phi}_1)\|^2$$

with $q_m > 0$ the minimum eigenvalue of $\boldsymbol{\Lambda}_1\boldsymbol{Q}\boldsymbol{\Lambda}_1$ and $c \geq \|\boldsymbol{\Lambda}_1\boldsymbol{P}\boldsymbol{L}_2\boldsymbol{\Lambda}_2\| > 0$. Since g belongs to the sector $[0, \mu]$, with $\mu > 0$, it can be verified that $x/g(x) \geq 1/\mu$, $\forall x \in \mathbb{R}$, and we can bound $\dot{V}$ by

$$\dot{V} \leq c\|\boldsymbol{g}_1(\boldsymbol{\phi}_1)\| \cdot \|\boldsymbol{g}_2(\boldsymbol{\kappa})\| - \frac{\delta\lambda_{m_2}}{\mu}\|\boldsymbol{g}_2(\kappa)\|^2 - \frac{q_m}{2}\|\boldsymbol{g}_1(\boldsymbol{\phi}_1)\|^2$$

Choosing $\delta \geq \mu([c/\sqrt{2q_m}]^2 + \alpha)/\lambda_{m_2}$, where $\alpha > 0$, gives

$$\begin{aligned}\dot{V} &\leq -\left(\frac{c}{\sqrt{2q_m}}\|\boldsymbol{g}_2(\boldsymbol{\kappa})\| - \sqrt{\frac{q_m}{2}}\|\boldsymbol{g}_1(\boldsymbol{\phi}_1)\|\right)^2 - \alpha\|\boldsymbol{g}_2(\boldsymbol{\kappa})\|^2 \\ &\triangleq -W(\boldsymbol{g}_1(\boldsymbol{\phi}_1), \boldsymbol{g}_2(\boldsymbol{\kappa})).\end{aligned} \tag{5.59}$$

The function W is a positive definite function of $\boldsymbol{g}_1(\boldsymbol{\phi}_1)$ and $\boldsymbol{g}_2(\boldsymbol{\kappa}) = \boldsymbol{g}_2(\boldsymbol{M}_3\boldsymbol{\phi}_2)$. Noting that $g(x) = 0$ if and only if $x = 0$ and that matrix $\boldsymbol{M}_3$ has full column rank we can conclude that $W = 0$ if and only if $\boldsymbol{\phi}_1 = 0$ and $\boldsymbol{\phi}_2 = 0$. Hence, W is a positive definite function of $\boldsymbol{\phi}_1$ and $\boldsymbol{\phi}_2$. Consequently the origin of the nominal system (5.56) is GAS and since (5.56) is time-invariant, the origin is UGAS. This result is equivalent to that in [31].

Although the Lyapunov function (5.57) has made it possible to prove UGAS for the origin of (5.56), and it satisfies (5.33), it does not satisfy (5.34). However, as shown in [31] the function $\tilde{V} \triangleq \ln(V + 1)$ satisfies both (5.33) and (5.34), since

$$\dot{\tilde{V}} \leq -\frac{1}{V(\boldsymbol{\phi}) + 1}W(\boldsymbol{g}_1(\boldsymbol{\phi}_1), \boldsymbol{g}_2(\boldsymbol{M}_3\boldsymbol{\phi}_2)) \tag{5.60a}$$

$$\triangleq -\tilde{W}(\boldsymbol{\phi}) < 0, \tag{5.60b}$$

satisfies (5.33) and

$$\left\| \frac{\partial \tilde{V}}{\partial \boldsymbol{\phi}} \right\| \leq \frac{1}{V+1} \Big(\delta \|\boldsymbol{\phi}_2\| + \|\boldsymbol{g}_1(\boldsymbol{\phi}_1)\| \, \|\boldsymbol{\Lambda}_1\| \, \|\boldsymbol{P}\| \Big) \tag{5.61a}$$

$$\leq \delta \frac{\|\boldsymbol{\phi}_2\|}{\frac{\delta}{2}\|\boldsymbol{\phi}_2\|^2 + 1} + \|\boldsymbol{g}_1(\boldsymbol{\phi})\| \, \|\boldsymbol{\Lambda}_1\| \, \|\boldsymbol{P}\| \tag{5.61b}$$

$$\leq C_1, \quad C_1 > 0, \tag{5.61c}$$

satisfies (5.34), where we used that $\|\boldsymbol{g}_1(\boldsymbol{\phi})\|$ is globally bounded.

5.C Reference Theorems

This appendix presents Theorem 2 and Proposition 2 from [93] which are used in the stability proof of the closed-loop system in Section 5.4.

Theorem 5.5 ([93, Theorem 2]). *Consider system (5.37) under the following conditions:*

1. *Condition 5.2, 5.3, and 5.4 hold;*
2. *there exist α_5, $\alpha_5' \in \mathcal{K}$ such that*

$$\|[L_g V]\| \leq \alpha_5(\|x_1\|)\alpha_5'(\|x_2\|) \tag{5.62}$$

and for each $r > 0$ there exist λ_r, $\eta_r > 0$ such that

$$t \geq 0, \ \|x_1\| \geq \eta_r \implies \alpha_5(\|x_1\|) \leq \lambda_r W(x_1) \tag{5.63}$$

Then, the solutions of (5.37) are uniformly globally bounded.

Proposition 5.1 ([93, Proposition 2]). *Under Condition 5.1 and the conditions of Theorem 5.3 the origin of (5.37) is UGAS.*

Chapter 6

Leader-Follower Synchronisation for Underactuated Marine Vessels on Curved Trajectories

This chapter considers leader-follower synchronisation for inhomogeneous multi-agent systems with underactuated agents. In particular, we consider synchronisation of underactuated marine vessels on straight-line trajectories and curved paths. The leader can be a vehicle with arbitrary dynamics as long as it moves in the same space as the follower(s). The follower can be any type of marine vehicle described by the nonlinear manoeuvring model that is introduced in Section 2.2. For formation control purposes, each follower can again be the leader of other followers, or all followers can have the same leader. Examples of possible configurations are ASVs following an AUV as communication nodes during AUV search and survey operations, or a fleet of ASVs manoeuvring by following a leader. Since we consider an underactuated system, we need to take into account the full dynamic model in the control design and analysis. In particular, since the system is underactuated it is not possible to consider a purely kinematic model since then the internal sway dynamics cannot be analysed. Moreover, for the case considered here it is not possible to perform feedback linearisation of the full dynamics. The leader dynamics and the leader trajectories are assumed to be unknown. The leader is free to move as it wants independently of the follower, while the follower has access to measurements of the leader's position and velocity in the inertial frame for use in its guidance law. If the follower uses controllers with acceleration feedforward, the leader's acceleration and jerk also need to be measured. This includes cases where there is communication between the leader and follower, but also when the follower reads AIS measurements of the leader Kyrkjebø [84].

It should be noted that the leader-follower synchronisation scheme in this work has its dual problem in trajectory tracking. Hence, the input signal of the leader could easily be replaced by a virtual leader. This is true for most, if not all, leader-follower type synchronisation schemes since the leader can always be represented as a virtual vehicle with known trajectory and properties. However, when performing trajectory tracking in most cases it is preferable to use information about the

dynamics of the vehicle since then perfect tracking can be achieved for all types of motions. When the leader dynamics and desired trajectory are not known a priori, the followers' internal dynamics might be perturbed by the chosen leader motion. Moreover when the strategy is applied in a chained form, i.e. followers become leaders to other vehicles, the duality is lost. The stability properties derived in this work will still hold with respect to each leader.

Preliminary results for this problem have been presented in Belleter and Pettersen [16], where the followers' yaw rate was used as a parameter to limit the motion of the follower to reduce the synchronisation error. However, in this work the effect of the internal dynamics was not considered in the analysis of the guidance. In this chapter we generalize the results of Belleter and Pettersen [16] by analysing the complete closed-loop system including the fully actuated closed-loop dynamics, the underactuated sway dynamics in addition to the synchronisation error kinematics. We discuss the conditions to achieve synchronisation and the physical meaning of these conditions. In particular, we show that the synchronisation error kinematics become integral input-to-state stable (iISS) with respect to changes in the velocity when coupled with the underactuated dynamics, i.e. perfect synchronisation is not possible on trajectories that excite the underactuated dynamics. Moreover, we also prove that the constant bearing guidance from Breivik et al. [37] gives uniformly semiglobally exponentially stable (USGES) synchronisation error kinematics with an explicit bound on the solutions, rather then only showing uniformly global asymptotically stability and uniformly locally exponential stability through linearisation around the origin as proved in previous work.

The work is organised as follows. In Section 6.1 the dynamic model for the follower and the constant bearing guidance algorithm are introduced. The closed-loop behaviour is investigated in Section 6.2. Section 6.3 presents simulations considering different scenarios. Finally Section 6.4 gives the conclusions of the work.

6.1 The Follower: Modelling and Control

This section presents the model for the follower and the guidance law for the follower that is used to synchronise its motion to that of the leader. The leader-follower synchronisation scheme is developed for a class of systems described by a 3-DOF manoeuvring model. This class of systems includes underactuated ASVs and AUVs moving in the horizontal plane. However, it should be noted that the leader-follower scheme and analysis can be extended to different classes of systems with similar properties such as unmanned aerial vehicles by considering the appropriate dynamic model, control/guidance scheme, and appropriate disturbances.

6.1.1 The Vessel Model

In this section we consider the model for a surface vessel moving given in Chapter 2. This model can be used to describe an autonomous surface vessel or an autonomous underwater vehicle moving in a plane. Recall, that the model can be represented

in component form as

$$\dot{x} = u_r \cos(\psi) - v_r \sin(\psi) + V_x, \tag{6.1a}$$
$$\dot{y} = u_r \sin(\psi) + v_r \cos(\psi) + V_y, \tag{6.1b}$$
$$\dot{\psi} = r, \tag{6.1c}$$
$$\dot{u}_r = F_{u_r}(v_r, r) + \tau_u, \tag{6.1d}$$
$$\dot{v}_r = X(u_r)r + Y(u_r)v_r, \tag{6.1e}$$
$$\dot{r} = F_r(u_r, v_r, r) + \tau_r, \tag{6.1f}$$

which is clearly underactuated in sway. Therefore, tracking has to be achieved by a suitable velocity and heading assignment that takes into account the underactuation. For this purpose constant bearing guidance is used. The definitions of F_{u_r}, $X(u_r)$, $Y(u_r)$, and F_r are given by

$$F_{u_r} \triangleq \frac{1}{m_{11}}(m_{22}v_r + m_{23}r)r - \frac{d_{11}}{m_{11}}u_r, \tag{6.2}$$
$$X(u_r) \triangleq \frac{m_{23}^2 - m_{11}m_{33}}{m_{22}m_{33} - m_{23}^2}u_r + \frac{d_{33}m_{23} - d_{23}m_{33}}{m_{22}m_{33} - m_{23}^2}, \tag{6.3}$$
$$Y(u_r) \triangleq \frac{(m_{22} - m_{11})m_{23}}{m_{22}m_{33} - m_{23}^2}u_r - \frac{d_{22}m_{33} - d_{32}m_{23}}{m_{22}m_{33} - m_{23}^2}, \tag{6.4}$$
$$\begin{aligned} F_r(u_r, v_r, r) \triangleq & \frac{m_{23}d_{22} - m_{22}(d_{32} + (m_{22} - m_{11})u_r)}{m_{22}m_{33} - m_{23}^2}v_r \\ & + \frac{m_{23}(d_{23} + m_{11}u_r) - m_{22}(d_{33} + m_{23}u_r)}{m_{22}m_{33} - m_{23}^2}r. \end{aligned} \tag{6.5}$$

Note that $X(u_r)$ and $Y(u_r)$ are bounded for bounded arguments and $Y(u_r)$ satisfies the following assumption.

Assumption 6.1. It is assumed that $Y(u_r)$ satisfies

$$Y(u_r) \leq -Y^{\min} < 0, \, \forall u_r \in [-V_{\max}, U_{\max}].$$

with $U_{\max}$ the maximal surge speed of the follower.

Remark 6.1. This assumption is satisfied for commercial vessels by design, since $Y(u_r) \geq 0$ would imply an undamped or nominally unstable vessel in sway direction.

The ocean current is assumed to satisfy the following assumption.

Assumption 6.2. The ocean current is assumed to be constant and irrotational w.r.t. n, i.e., $\boldsymbol{V_c} \triangleq [V_x, V_y, 0]^T$. Furthermore, it is bounded by $V_{\max} > 0$ such that $\|V_c\| = \sqrt{V_x^2 + V_y^2} \leq V_{max}$.

6.1.2 Constant Bearing Guidance

This subsection briefly describes constant bearing guidance (CB) as presented in Fossen [60] and Breivik and Fossen [35]. CB guidance assigns a desired velocity

based on two different components expressed in the earth-fixed frame. The first component is the velocity of the leader $\boldsymbol{v}_l^n = [\dot{x}_l, \dot{y}_l]^T$ which needs to be matched. The second component is the follower-leader approach velocity $\boldsymbol{v}_a^n$ which is proportional, but upper-bounded by a maximum, to the relative position in the earth-fixed frame between the follower and the leader $\tilde{\boldsymbol{p}}^n = [\tilde{x}^n, \tilde{y}^n]^T$ and is aligned along the line-of-sight (LOS) vector. The superscript n denotes that the variable is expressed in the earth-fixed frame. An illustration of the constant bearing guidance can be seen in Figure 6.1. The desired velocity assignment for constant bearing guidance is given by

$$\boldsymbol{v}_d^n = \boldsymbol{v}_l^n + \boldsymbol{v}_a^n, \tag{6.6}$$

$$\boldsymbol{v}_a^n = -\kappa \frac{\tilde{\boldsymbol{p}}^n}{\|\tilde{\boldsymbol{p}}^n\|}, \tag{6.7}$$

with $\boldsymbol{v}_l^n$ the leader velocity, $\boldsymbol{v}_a^n$ the approach velocity, and

$$\tilde{\boldsymbol{p}}^n \triangleq \boldsymbol{p}^n - \boldsymbol{p}_l^n, \tag{6.8}$$

is the LOS vector between the follower and the leader, where $\|\tilde{\boldsymbol{p}}^n\| \geq 0$ is the euclidean length of this vector and

$$\kappa = U_a^{\max} \frac{\|\tilde{\boldsymbol{p}}^n\|}{\sqrt{(\tilde{\boldsymbol{p}}^n)^T \tilde{\boldsymbol{p}}^n + \Delta_{\tilde{p}}^2}}, \tag{6.9}$$

with $U_a^{\max}$ the maximum approach speed and $\Delta_{\tilde{p}}$ a tuning parameter to affect the transient leader-follower rendezvous behaviour, which results in the synchronisation error kinematics

$$\dot{\tilde{\boldsymbol{p}}}^n = \boldsymbol{v}_d^n - \boldsymbol{v}_l^n = -U_a^{\max} \frac{\tilde{\boldsymbol{p}}^n}{\sqrt{(\tilde{\boldsymbol{p}}^n)^T \tilde{\boldsymbol{p}}^n + \Delta_{\tilde{p}}^2}}. \tag{6.10}$$

From (6.7) and (6.9) it can be seen that as $\tilde{\boldsymbol{p}}^n \to 0$ the approach speed goes to zero and the velocity of the follower approaches the leader velocity. Conversely when $\tilde{\boldsymbol{p}}^n \to \infty$ the approach velocity approaches $U_a^{\max}$ and the guidance commands the maximum allowed velocity to close the gap.

Assumption 6.3. To assure that the problem is feasible we assume that the sum of the magnitude of the leader velocity, the maximum approach speed, and ocean current is smaller than the maximum feasible surge velocity of the follower U_{feas}, i.e.

$$\|\boldsymbol{v}_l^n\| + U_a^{\max} + \|\boldsymbol{V}_c\| \leq U_{\text{feas}} \tag{6.11}$$

for all $t > 0$. Moreover, the desired speed is required to be positive, and we therefore need to assume that

$$\|\boldsymbol{v}_l^n\| - U_a^{\max} - \|\boldsymbol{V}_c\| > 0 \tag{6.12}$$

for all $t > 0$.

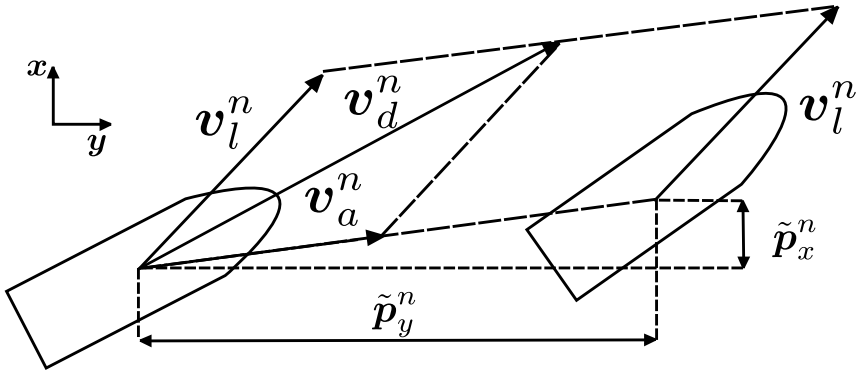

Figure 6.1: Constant bearing guidance velocity assignments and position error.

Remark 6.2. Note that in order to converge to a point that is at a desired off-set w.r.t the leader $\boldsymbol{p}_r$, the position of the leader should be included in (6.8) as $\boldsymbol{p}_l^n \triangleq \boldsymbol{p}_{l,\text{true}}^n + \boldsymbol{R}(\psi_l)\boldsymbol{p}_r$ where $\boldsymbol{R}(\psi_l)$ is a rotation matrix describing the orientation of the leader. For curved paths the velocity $\boldsymbol{v}_l^n$ should then also be calculated in the off-set point to track the curvature with minimal error which requires the leader's yaw rate.

As shown in Fossen [60] the stability and convergence of the CB guidance scheme, i.e., (6.6)–(6.7) and (6.9), can be investigated using the positive definite, radially unbounded Lyapunov function candidate (LFC)

$$V = \frac{1}{2}(\tilde{\boldsymbol{p}}^n)^T\tilde{\boldsymbol{p}}^n. \tag{6.13}$$

Time differentiation of (6.13) along the trajectories of $\tilde{\boldsymbol{p}}^n$ gives

$$\dot{V} = (\tilde{\boldsymbol{p}}^n)^T(\boldsymbol{v}_d^n - \boldsymbol{v}_l^n) = -\kappa\frac{(\tilde{\boldsymbol{p}}^n)^T\tilde{\boldsymbol{p}}^n}{\|\tilde{\boldsymbol{p}}^n\|} \tag{6.14a}$$

$$= -U_{a,\max}\frac{(\tilde{\boldsymbol{p}}^n)^T\tilde{\boldsymbol{p}}^n}{\sqrt{(\tilde{\boldsymbol{p}}^n)^T\tilde{\boldsymbol{p}}^n + \Delta_{\tilde{p}}^2}} < 0, \quad \forall\,\tilde{\boldsymbol{p}}^n \neq 0 \tag{6.14b}$$

with $\boldsymbol{v}_d^n - \boldsymbol{v}_l^n = \boldsymbol{v}_a^n$ by definition. Hence, the origin $\tilde{\boldsymbol{p}}^n = 0$ is UGAS, which is the result given in Fossen [60].

Note however that by defining

$$\phi^*(t, \tilde{\boldsymbol{p}}^n) \triangleq \frac{U_a^{\max}}{\sqrt{(\tilde{\boldsymbol{p}}^n)^T\tilde{\boldsymbol{p}}^n + \Delta_{\tilde{p}}^2}} \tag{6.15}$$

which for each $r > 0$ and $|\tilde{\boldsymbol{p}}^n(t)| \leq r$ gives

$$\phi^*(t, \tilde{\boldsymbol{p}}^n) \leq \frac{U_a^{\max}}{\sqrt{r^2 + \Delta_{\tilde{p}}^2}} \triangleq c^*(r) \tag{6.16}$$

which substituted in (6.14) gives

$$\dot{V} \leq -2c^*(r)V(t, \tilde{\boldsymbol{p}}^n) \tag{6.17}$$

for all $|\tilde{\boldsymbol{p}}^n(t_0)| \leq r$ and any $r > 0$. The solutions of a linear system of the form $\dot{x} = -2c^*(r)x$ are given by

$$x(t) = e^{-2c^*(r)(t-t_0)}x(t_0) \tag{6.18}$$

so by applying the comparison lemma Khalil [82, Lemma 3.4] we have

$$V(t, \tilde{\boldsymbol{p}}^n) \leq e^{-2c^*(r)(t-t_0)}V(t_0, \tilde{\boldsymbol{p}}^n(t_0)) \tag{6.19}$$

and consequently

$$\|\tilde{\boldsymbol{p}}^n(t)\| \leq \|\tilde{\boldsymbol{p}}^n(t_0)\|e^{-c^*(r)(t-t_0)} \tag{6.20}$$

for all $t > t_0$, $|\tilde{\boldsymbol{p}}^n(t_0)| \leq r$, and any $r > 0$. Therefore, we can conclude that (6.10) is a USGES system according to Loría and Panteley [95, Definition 2.7], a result which has not previously been shown in Fossen [60].

Theorem 6.1. *Using the constant bearing guidance scheme, i.e.* (6.6)-(6.7) *and* (6.9)*, the origin of the synchronisation error kinematics* (6.10) *is uniformly semi-globally exponentially stable.*

The desired heading ψ_d and its derivative, the desired yaw rate r_d, are calculated by extracting heading information from the inner and outer products of the desired velocity $\boldsymbol{v}_d^n$ and the actual velocity $\boldsymbol{v}^n$ [37]. This assures that $\boldsymbol{v}^n$ is aligned with $\boldsymbol{v}_d^n$. Moreover, since it provides us with course, and equivalently heading, information it allows for compensation of the environmental disturbance. More details about constant bearing guidance can be found in Fossen [60] and the references therein.

6.1.3 The Controller

The control goals are

$$\lim_{t\to\infty} \tilde{\boldsymbol{p}}^n = \boldsymbol{0}, \tag{6.21}$$

$$\lim_{t\to\infty} \tilde{\boldsymbol{v}}^n \triangleq \boldsymbol{v}^n - \boldsymbol{v}_d^n = 0, \tag{6.22}$$

which corresponds to synchronisation with the leader, i.e., that the follower vessel follows the leader, with a constant desired relative position and the same inertial frame velocity. Note that the body frame velocity may be different due to differences in actuation topology etc. In this section, we present feedback linearising controllers using the desired velocity and heading angle from 6.1.2, in order to achieve these control goals. In the following section it will be shown that the feasibility of these goals depends on the type of motion the leader executes.

Since the follower is underactuated we can not directly control the velocity in the earth-fixed coordinates, but rather the forward velocity and yaw rate in body-fixed coordinates. Therefore, we transform the velocity error in the earth-fixed

frame to an error in the body-fixed frame using the coordinate transformation

$$\begin{bmatrix} \tilde{\psi} \\ \tilde{u}_r \\ \tilde{v}_r \end{bmatrix} = \begin{bmatrix} 1 & 0 & 0 \\ 0 & \cos(\tilde{\psi}+\psi_d) & \sin(\tilde{\psi}+\psi_d) \\ 0 & -\sin(\tilde{\psi}+\psi_d) & \cos(\tilde{\psi}+\psi_d) \end{bmatrix} \begin{bmatrix} \tilde{\psi} \\ \tilde{\boldsymbol{v}}^n \end{bmatrix}. \tag{6.23}$$

It is straightforward to show that the Jacobian of this transformation is given by

$$\frac{\partial T}{\partial(\tilde{\psi}, \tilde{\boldsymbol{v}}^n)} = \begin{bmatrix} 1 & 0 & 0 \\ -\tilde{v}_x^n \mathrm{s}(\cdot) + \tilde{v}_y^n \mathrm{c}(\cdot) & \mathrm{c}(\cdot) & \mathrm{s}(\cdot) \\ -\tilde{v}_x^n \mathrm{c}(\cdot) - \tilde{v}_y^n \mathrm{s}(\cdot) & -\mathrm{s}(\cdot) & \mathrm{c}(\cdot) \end{bmatrix} \tag{6.24}$$

with $\mathrm{s}(\cdot) = \sin(\tilde{\psi}+\psi_d)$ and $\mathrm{c}(\cdot) = \cos(\tilde{\psi}+\psi_d)$. The Jacobian (6.24) can easily be verified to be non-singular. Consequently, T is a global diffeomorphism. A physical interpretation of this is that when $\tilde{\psi}$ is driven to zero, i.e., $\boldsymbol{v}^n$ is aligned with $\boldsymbol{v}_d^n$ by the CB guidance algorithm, the relative surge velocity error can be used to control $\boldsymbol{v}^n$ to $\boldsymbol{v}_d^n$. Note that perturbation of the underactuated sway motion will disturb this balance which will be shown in the analysis of the next section.

Remark 6.3. For the underactuated model considered here only $\tilde{u}_r = u_r - u_d$ can be used for control purposes, while for the fully actuated case $\tilde{v}_r = v_r - v_d$ could be used to control the sway velocity and the perturbation problem does not exist. For the underactuated case the heading controller needs to assure that $\boldsymbol{v}^n$ is aligned with $\boldsymbol{v}_d^n$ and the control action can be prescribed solely by the surge actuator, something which prevents the magnitude from being matched on curved trajectories and in the presence of accelerations.

Remark 6.4. Note that the coupling between the heading and velocity control is what allows for disturbance rejection. Since if a larger (or smaller) velocity is needed to compensate for the effect of the current, the heading controller will assure that the vessel is rotated such that $\boldsymbol{v}^n$ and $\boldsymbol{v}_d^n$ are aligned and hence the vessel keeps the correct course.

We will use the following feedback linearising P controller for the surge velocity:

$$\tau_u = -F_{u_r}(v_r, r) + \dot{u}_d - k_{u_r}(u_r - u_d), \tag{6.25}$$

with $k_{u_r} > 0$ a constant controller gain.

Using (6.25) we can control u_r towards u_d provided that we have the acceleration of the leader available to calculate $\dot{u}_d$, but we cannot directly control v_r. Along the lines of Breivik et al. [37] we aim to control v_r indirectly by using a proper yaw rate controller. Following Breivik et al. [37] we have for $\tilde{\chi} = \chi - \chi_d$:

$$\sin(\tilde{\chi}) = \frac{\boldsymbol{v}_d^n \times \boldsymbol{v}^n}{\|\boldsymbol{v}_d^n\| \|\boldsymbol{v}^n\|} = \frac{\dot{y} v_{d,x}^n - \dot{x} v_{d,y}^n}{\sqrt{\left((v_{d,x}^n)^2 + (v_{d,y}^n)^2\right)(\dot{x}^2 + \dot{y}^2)}} \tag{6.26a}$$

$$\cos(\tilde{\chi}) = \frac{(\boldsymbol{v}_d^n)^T \boldsymbol{v}^n}{\|\boldsymbol{v}_d^n\| \|\boldsymbol{v}^n\|} = \frac{\dot{x} v_{d,x}^n + \dot{y} v_{d,y}^n}{\sqrt{\left((v_{d,x}^n)^2 + (v_{d,y}^n)^2\right)(\dot{x}^2 + \dot{y}^2)}} \tag{6.26b}$$

$$\tan(\tilde{\chi}) = \frac{\boldsymbol{v}_d^n \times \boldsymbol{v}^n}{(\boldsymbol{v}_d^n)^T \boldsymbol{v}^n} = \frac{\dot{y} v_{d,x}^n - \dot{x} v_{d,y}^n}{\dot{x} v_{d,x}^n + \dot{y} v_{d,y}^n} \Rightarrow \tilde{\chi} = -\text{atan2}(\dot{y} v_{d,x}^n - \dot{x} v_{d,y}^n, \dot{x} v_{d,x}^n + \dot{y} v_{d,y}^n) \tag{6.26c}$$

where $\tilde{\chi} \triangleq \psi - \psi_d + \beta - \beta_d \triangleq \tilde{\psi} + \tilde{\beta}$ with $\tilde{\beta}$ the difference in side-slip angle between different orientations. We can thus define

$$\psi_d - \tilde{\beta} = \psi - \text{atan2}(\dot{y} v_{d,x}^n - \dot{x} v_{d,y}^n, \dot{x} v_{d,x}^n + \dot{y} v_{d,y}^n) \tag{6.27}$$

Note that from (6.26) we also have

$$\dot{\tilde{\chi}} = \frac{\dot{x}\ddot{y} - \dot{y}\ddot{x}}{\dot{x}^2 + \dot{y}^2} + \frac{v_{d,y}^n \dot{v}_{d,x}^n - v_{d,x}^n \dot{v}_{d,y}^n}{(v_{d,x}^n)^2 + (v_{d,y}^n)^2} \tag{6.28}$$

so we can write

$$r_d - \dot{\tilde{\beta}} = r - \frac{\dot{x}\ddot{y} - \dot{y}\ddot{x}}{\dot{x}^2 + \dot{y}^2} - \frac{v_{d,y}^n \dot{v}_{d,x}^n - v_{d,x}^n \dot{v}_{d,y}^n}{(v_{d,x}^n)^2 + (v_{d,y}^n)^2} \tag{6.29a}$$

$$\triangleq r - R_1(u_r, v_r, \dot{x}, \dot{y}, \boldsymbol{v}_d^n) r - R_2(\boldsymbol{v}_d^n, \dot{\boldsymbol{v}}_d^n) - R_3(u_r, v_r, \dot{x}, \dot{y}, \boldsymbol{v}_d^n, \dot{\boldsymbol{v}}_d^n) \tag{6.29b}$$

where $v_{c,u}^b \triangleq V_x \cos(\psi) + V_y \sin(\psi)$ and $v_{c,v}^b \triangleq V_x \sin(\psi) - V_y \cos(\psi)$ are the components of the current expressed in the body frame axis and

$$\begin{aligned}
R_1(\cdot) &\triangleq \frac{u_r^2 + v_r^2 + V_x^2 + X(u_r)(u_r + v_{c,u}^b) - v_r v_{c,v}^b + u_r v_{c,u}^b - v_{d,x}^n (V_x - v_r \sin(\psi))}{u_r^2 + v_r^2 + 2(u_r v_{c,x}^b + v_r v_{c,y}^b) + V_x^2 + V_y^2} \\
&\quad + \frac{-(v_{d,y}^n (v_r - v_{c,v}^b) - v_{d,x}^n v_{c,u}^b)\cos(\psi) + \cos^2(\psi)(V_y^2 - V_x^2)}{u_r^2 + v_r^2 + 2(u_r v_{c,x}^b + v_r v_{c,y}^b) + V_x^2 + V_y^2} \leq C_{R_1}^{\max} \\
R_2(\cdot) &\triangleq \frac{v_{d,y}^n \dot{v}_{d,x}^n - v_{d,x}^n \dot{v}_{d,y}^n}{(v_{d,x}^n)^2 + (v_{d,y}^n)^2} \\
R_3(\cdot) &\triangleq \frac{Y(u_r) v_r (u_r + v_{c,u}^b) + k_{u_r}(u_r - u_d)(v_r - v_{c,v}^b)}{u_r^2 + v_r^2 + 2(u_r v_{c,x}^b + v_r v_{c,y}^b) + V_x^2 + V_y^2} \\
&\quad + \frac{\dot{v}_{d,x}^n (v_{c,u}^b - v_r)\cos(\psi) + \dot{v}_{d,y}^n (V_x - v_r \sin(\psi) - v_{c,u}^b \cos(\psi))}{u_r^2 + v_r^2 + 2(u_r v_{c,x}^b + v_r v_{c,y}^b) + V_x^2 + V_y^2} \leq C_{R_3}
\end{aligned}$$

Note that R_1 can be bounded by the constant $C_{R_1}^{\max}$ since R_1 has the same growth rate in v_r and u_r for the denominator and numerator while the ocean current components are bounded (in body frame) and constant (in inertial frame). The term R_3 can be bounded by the constant C_{R_3} since the denominator and numerator grow at the same rate with respect to v_r and u_r and the current is bounded. Note that the denominator of R_1, R_2, and R_3 are larger than zero for nonzero $\|\boldsymbol{v}^n\|$ and $\|\boldsymbol{v}_d^n\|$ which is verified by Assumption 6.3. Boundedness of R_2 will be considered later since its numerator grows linearly with v_r and its denominator does not grow with v_r.

Since the inertial frame velocities, i.e. $\dot{x}$ and $\dot{y}$, are measured V_x and V_y can be substituted in expression (6.29) using the model equations (6.1a) and (6.1b)

respectively for implementation purposes. Alternatively a kinematic ocean current observer as in Aguiar and Pascoal [2] can be used to estimate $\dot{x}$, $\dot{y}$, V_x, and V_y based on measurements of the positions and relative velocities. Hence, all the variables in (6.29) are known and can thus be substituted in the yaw rate controller. A further derivative of (6.29) can be taken to obtain $\ddot{\psi}_d - \ddot{\tilde{\beta}}$ as an acceleration feedforward. Note that this will also require knowledge of the jerk of the leader motion since it contains $\dot{R}_2(\boldsymbol{v}_d^n, \dot{\boldsymbol{v}}_d^n)$ and $\dot{R}_3(u_r, v_r, \dot{x}, \dot{y}, \boldsymbol{v}_d^n, \dot{\boldsymbol{v}}_d^n)$.

To control the yaw rate we use the following controller:

$$\begin{aligned}\tau_r = &-F_r(u_r, v_r, r) + \frac{1}{R_1(u_r, v_r, \dot{x}, \dot{y}, \boldsymbol{v}_d^n)}\Big(- \dot{R}_1(u_r, v_r, \dot{x}, \dot{y}, \boldsymbol{v}_d^n)r - \dot{R}_2(\boldsymbol{v}_d^n, \dot{\boldsymbol{v}}_d^n) \\ &- \dot{R}_3(u_r, v_r, \dot{x}, \dot{y}, \boldsymbol{v}_d^n, \dot{\boldsymbol{v}}_d^n) - k_\psi(\psi - \psi_d + \tilde{\beta}) - k_r(\dot{\psi} - \dot{\psi}_d + \dot{\tilde{\beta}})\Big) \qquad (6.30a)\end{aligned}$$

$$\begin{aligned}= &-F_r(u_r, v_r, r) + \frac{1}{R_1(u_r, v_r, \dot{x}, \dot{y}, \boldsymbol{v}_d^n)}\Big(- \dot{R}_1(u_r, v_r, \dot{x}, \dot{y}, \boldsymbol{v}_d^n)r - \dot{R}_2(\boldsymbol{v}_d^n, \dot{\boldsymbol{v}}_d^n) \\ &- \dot{R}_3(u_r, v_r, \dot{x}, \dot{y}, \boldsymbol{v}_d^n, \dot{\boldsymbol{v}}_d^n) - k_\psi\tilde{\chi} - k_r\dot{\tilde{\chi}}\Big) \qquad (6.30b)\end{aligned}$$

with $k_\psi > 0$ and $k_r > 0$ constant controller gains. This control action is well defined if $R_1(u_r, v_r, \dot{x}, \dot{y}, \boldsymbol{v}_d^n)$ satisfies certain conditions, which is something discussed in the following when considering the boundedness of r. We introduce the vector $\boldsymbol{\xi} \triangleq [\tilde{u}_r, \tilde{\chi}, \dot{\tilde{\chi}}]^T$, with the tracking errors $\tilde{u}_r \triangleq u_r - u_d$, $\tilde{\chi} \triangleq \tilde{\psi} + \tilde{\beta}$, and $\dot{\tilde{\chi}} \triangleq \dot{\tilde{\psi}} - \dot{\tilde{\beta}}$. The dynamics of $\boldsymbol{\xi}$ can be found by applying the controllers (6.25) and (6.30) to the dynamical system (6.1) resulting in:

$$\dot{\boldsymbol{\xi}} = \begin{bmatrix} -k_{u_r} & 0 & 0 \\ 0 & 0 & 1 \\ 0 & -k_\psi & -k_r \end{bmatrix} \boldsymbol{\xi} \triangleq \Sigma\boldsymbol{\xi}. \qquad (6.31)$$

The system (6.31) is linear and time-invariant and k_{u_r}, k_ψ, and k_r are strictly positive. Consequently, Σ is Hurwitz and the origin of (6.31) is uniformly globally exponentially stable and hence the controllers guarantee exponential tracking of the desired surge velocity and course.

Note that through the assignment of (6.30) we use the heading controller to perform course control, i.e. we force the direction of $\boldsymbol{v}_d^n$ and $\boldsymbol{v}^n$ to be equal. To investigate how the course controller affects r we start by rewriting (6.29) to obtain

$$r = \frac{1}{R_1(u_r, v_r, \dot{x}, \dot{y}, \boldsymbol{v}_d^n)}\left(\dot{\tilde{\chi}} - R_2(\boldsymbol{v}_d^n, \dot{\boldsymbol{v}}_d^n) - R_3(u_r, v_r, \dot{x}, \dot{y}, \boldsymbol{v}_d^n, \dot{\boldsymbol{v}}_d^n)\right) \qquad (6.32)$$

This function is well defined if the numerator of R_1 given in (6.29) is larger than zero. This condition is satisfied if u_d is sufficiently large at all time and if u_r starts sufficiently close to u_d The term $\dot{\tilde{\chi}}/R_1$ will be bounded since $\dot{\tilde{\chi}}$ is bounded and R_1 is bounded by constant C_{R_1} as shown earlier. The same holds for the term R_3/R_1. The term R_2/R_1 however grows linearly in v_r since $\dot{v}_{d,x}^n$ and $\dot{v}_{d,y}^n$ depend linearly on v_r since the derivative of the approach speed $\boldsymbol{v}_a^n$ depends on $\dot{x}$ and $\dot{y}$. When

(6.32) is substituted in (6.1e) the linear growth will assure that there is no finite escape time for v_r but some conditions have to be satisfied to show boundedness. Summarizing the above we have that the course controller results in a well defined yaw rate if the following condition is satisfied.

Condition 6.1. *If the numerator of R_1 is strictly larger than zero, then the yaw rate equation (6.32) is well defined and bounded. In particular, besides being upper-bounded there also exists a lower bound for R_1 such that $0 < C_{R_1}^{\min} \leq R_1(u_r, v_r, \dot{x}, \dot{y})$.*

Remark 6.5. Condition 6.1 is satisfied for a sufficiently large desired surge velocity u_d if u_r starts in a neighbourhood of u_d. Further analysis has to be performed to find the precise physical meaning of the bound, but it appears to be that inertial frame velocity vector has to have a positive magnitude for all time. This can be satisfied by keeping the surge velocity u_r sufficiently large to be able to dominate the effects of the ocean current and the sway velocity v_r. In particular, if the inertial frame velocity vector would have a zero crossing, the rotation would change instantaneously and when the magnitude of the inertial frame velocity vector is zero then the desired rotation is undefined.

Remark 6.6. Note that Condition 6.1 is a condition that plays a role in the initial behaviour when the difference between the initial orientation of the follower and the leader is large, e.g. if they point in opposite directions. In this case u_d obtained from (6.23) needs to be saturated to a lower bound such that it stays positive and well defined. As soon as the follower is oriented in the same direction as the leader Condition 6.1 is easily satisfied for physically sensible motions of the leader and u_d can simply be obtained from (6.23).

The term R_2 can be interpreted as dependent on the desired curvature of the motion. In particular it can be rewritten as $R_2 = \|\boldsymbol{v}_d^n\|\kappa$ where κ denotes the curvature of the desired trajectory. This term grows linearly with the inertial frame velocities of the follower since it depends on $\dot{\boldsymbol{v}}_a^n$

$$R_2(\boldsymbol{v}_d^n, \dot{\boldsymbol{v}}_d^n) = \frac{v_{d,y}^n \dot{v}_{d,x}^n - v_{d,x}^n \dot{v}_{d,y}^n}{(v_{d,x}^n)^2 + (v_{d,y}^n)^2} = \frac{v_{d,y}^n \dot{v}_{l,x}^n - v_{d,x}^n \dot{v}_{l,y}^n}{(v_{d,x}^n)^2 + (v_{d,y}^n)^2} + \frac{v_{d,y}^n \dot{v}_{a,x}^n - v_{d,x}^n \dot{v}_{a,y}^n}{(v_{d,x}^n)^2 + (v_{d,y}^n)^2} \quad (6.33)$$

which using the transformation (6.23) can be bounded by

$$\begin{aligned} R_2 &\leq \frac{U_a^{\max} \tilde{v}_r}{(v_{d,x}^n)^2 + (v_{d,y}^n)^2} \left(\frac{v_{d,y}^n + v_{d,x}^n}{\sqrt{\tilde{x}^2 + \tilde{y}^2 + \Delta_{\tilde{p}}^2}} + \frac{v_{d,y}^n(\tilde{x}^2 + \tilde{x}\tilde{y}) + v_{d,x}^n(\tilde{y}^2 + \tilde{x}\tilde{y})}{(\tilde{x}^2 + \tilde{y}^2 + \Delta_{\tilde{p}}^2)^{3/2}} \right) + C_{R_2} \\ &\triangleq R_2' \tilde{v}_r + C_{R_2} \end{aligned} \quad (6.34)$$

where C_{R_2} is some constant which magnitude will depend on the leader's velocity and acceleration. Note that the term R_2' is uniformly bounded for desired velocities greater than zero and that it decreases as the positional error grows. Moreover, it contains two parameters that can be tuned, i.e. the maximum approach speed $U_{a,\max}$ and the interaction tuning parameter $\Delta_{\tilde{p}}$. Hence, these tuning parameters can be used to influence the interaction behaviour between r and v_r.

6.2 Closed-Loop Analysis

In this section the closed-loop system, i.e. the fully actuated closed-loop dynamics, the underactuated sway dynamics, and the synchronisation error kinematics, are investigated. In particular, the closed-loop path-following error kinematics and dynamics for (6.1) with the proposed leader-follower synchronisation scheme is given by:

$$\dot{\tilde{\boldsymbol{p}}}^n = -\frac{U_a^{\max}\tilde{\boldsymbol{p}}^n}{\sqrt{(\tilde{\boldsymbol{p}}^n)^T\tilde{\boldsymbol{p}}^n + \Delta_{\tilde{p}}^2}} + \begin{bmatrix} \tilde{u}_r\cos(\tilde{\chi}-\tilde{\beta}+\psi_d) - \tilde{v}_r\sin(\tilde{\chi}-\tilde{\beta}+\psi_d) \\ \tilde{u}_r\sin(\tilde{\chi}-\tilde{\beta}+\psi_d) + \tilde{v}_r\cos(\tilde{\chi}-\tilde{\beta}+\psi_d) \end{bmatrix} \tag{6.35a}$$

$$\dot{\tilde{v}}_r = Y(u_r)\tilde{v}_r + X(u_r)r - \dot{v}_d - Y(u_r)v_d \tag{6.35b}$$

$$\dot{\boldsymbol{\xi}} = \Sigma\boldsymbol{\xi} \tag{6.35c}$$

where v_d and $\dot{v}_d$ can be verified to be given by:

$$v_d = (V_x - v_{d,x}^n)\sin(\psi) - (V_y - v_{d,y}^n)\cos(\psi) \tag{6.36}$$

$$\begin{aligned}\dot{v}_d &= -\dot{v}_{d,x}^n\sin(\psi) + (V_x - v_{d,x}^n)r\cos(\psi) + \dot{v}_{d,y}^n\cos(\psi) + (V_y - v_{d,y}^n)r\sin(\psi) \\ &= -(\dot{v}_{d,x}^n + \dot{v}_{a,x}^n + (V_y - v_{d,y}^n)r)\sin(\psi) + (\dot{v}_{l,y}^n + \dot{v}_{a,y}^n + (V_x - v_{d,x}^n)r)\cos(\psi)\end{aligned} \tag{6.37}$$

with v_d bounded for a bounded leader velocity. The equation for $\dot{v}_d$ depends on $\dot{v}_{a,x}^n$, $\dot{v}_{a,y}^n$, and r which will depend on $\tilde{v}_r$. However as in (6.34) we can derive a bound for $\dot{v}_d$

$$\dot{v}_d \leq \left(\frac{\|\boldsymbol{V}_c - \boldsymbol{v}_d^n\|^2 R_2'}{C_{R_1}^{\min}} + \frac{U_a^{\max}}{\sqrt{\tilde{x}^2+\tilde{y}^2+\Delta_{\tilde{p}}^2}}\left(1 + \frac{(\tilde{x}+\tilde{y})^2}{\tilde{x}^2+\tilde{y}^2+\Delta_{\tilde{p}}^2}\right)\right)\tilde{v}_r + C_2 \tag{6.38a}$$

$$\leq C_3\tilde{v}_r + C_2 \tag{6.38b}$$

where C_2 is a constant which will depend on the leader's maximum velocity and acceleration and on the magnitude of the ocean current. The magnitude of the constant C_3 can again be adjusted by tuning $U_a^{\max}$ and $\Delta_{\tilde{p}}$.

Please note that the terms perturbing the CB path-following error system in (6.35a) compared to (6.10) arise since we here do not only consider the kinematic model, but instead take into account the (underactuated) dynamics given in (6.35b)-(6.35c). We thus take into account that the desired inertial frame velocity may not be matched since part of the error in the inertial frame velocity error is transferred to the sway direction as seen in (6.23).

In order to not violate Condition 6.1 we analyse the system (6.35) under the following assumption.

Assumption 6.4. The desired relative surge velocity is saturated to a sufficiently large lower bound $u_{d,\min}$ such that Condition 6.1 is not violated. It is assumed that there exists such a lower bound that satisfies $u_{d,\min} < \|\boldsymbol{v}_d^n\|$, i.e. that the leader velocity can be matched without violating Condition 6.1.

Since $u_r = u_d$ is a stable equilibrium point the surge velocity dynamics, for any $\delta > 0$ there exists a positively invariant neighbourhood of the equilibrium point such that all solutions originating in this neighbourhood satisfy $|u_r - u_d| < \delta$. Therefore in the remainder we only consider solutions starting in the neighbourhood of $u_r = u_d$ such that Condition 6.1 is not violated and there are no finite escape times.

Since substituting (6.32) in (6.35b) shows that there is no finite escape time for v_r and the tracking dynamics (6.35c) are UGES, it suffices to investigate local boundedness of v_r near the set where $u_r - u_d \leq \delta$ such that r is well defined. Therefore we consider the system

$$\dot{\tilde{v}}_r = Y(u_r)\tilde{v}_r + X(u_r)r - \dot{v}_d - Y(u_r)v_d \tag{6.39}$$

We substitute (6.32) and we obtain

$$\begin{aligned}\dot{\tilde{v}}_r = Y(u_r)\tilde{v}_r + \frac{X(u_r)}{R_1(u_r, v_r, \dot{x}, \dot{y}, \boldsymbol{v}_d^n)} \left(\dot{\tilde{\chi}} - R_2(\boldsymbol{v}_d^n, \dot{\boldsymbol{v}}_d^n) - R_3(u_r, v_r, \dot{x}, \dot{y}, \boldsymbol{v}_d^n, \dot{\boldsymbol{v}}_d^n)\right) \\ - \dot{v}_d - Y(u_r)v_d\end{aligned} \tag{6.40}$$

Using the following Lyapunov function we show boundedness for all solutions starting in the neighbourhood of $u_r = u_d$ by considering the Lyapunov function

$$V(\tilde{v}_r) = \frac{1}{2}\tilde{v}_r^2 \tag{6.41}$$

The derivative of (6.41) along the solutions of (6.39) is given by

$$\begin{aligned}\dot{V}(\tilde{v}_r) &= Y(u_r)\tilde{v}_r^2 + \frac{X(u_r)\left(\dot{\tilde{\chi}} - R_2(\boldsymbol{v}_d^n, \dot{\boldsymbol{v}}_d^n) - R_3(u_r, v_r, \dot{x}, \dot{y}, \boldsymbol{v}_d^n, \dot{\boldsymbol{v}}_d^n)\right)}{R_1(u_r, v_r, \dot{x}, \dot{y}, \boldsymbol{v}_d^n)}\tilde{v}_r \\ &\quad + \left(\dot{v}_d - Y(u_r)v_d\right)\tilde{v}_r \qquad (6.42a) \\ &\leq -\left(|Y^{\min}| - \frac{|X^{\max}|R_2'}{C_{R_1}^{\min}} - C_3\right)\tilde{v}_r^2 + \frac{|X^{\max}|\left(|\dot{\tilde{\chi}}| + C_{R_2} + C_{R_3}\right)}{C_{R_1}^{\min}}\tilde{v}_r \\ &\quad + (C_2 + |Y^{\max}|v_d)\tilde{v}_r \qquad (6.42b)\end{aligned}$$

where $Y^{\min}$, $Y^{\max}$, and $X^{\max}$ are the minimum and maximum values over the interval of velocities considered and will exist for sufficiently small δ. From which we can conclude boundedness if

$$\frac{|Y^{\min}|}{|X^{\max}|} > \frac{|R_2'|}{C_{R_1}^{\min}} + \frac{C_3}{|X^{\max}|} \tag{6.43}$$

which is a bound that depends on the leader motion, the environmental disturbance, and parameters $U_a^{\max}$ and $\Delta_{\tilde{p}}$. From (6.34) and (6.38) we can see that the term R_2' can be tuned using the parameters $U_a^{\max}$ and $\Delta_{\tilde{p}}$. In particular, if we increase $\Delta_{\tilde{p}}$, i.e. choose a smoother leader-follower rendez-vous behaviour, then the terms R_2' and C_3 will be reduced. Hence, condition (6.43) can be guaranteed to hold by appropriate tuning of the constant bearing guidance algorithm and all solutions of (6.35b) originating in a neighbourhood of $u_r = u_d$ are uniformly bounded.

Remark 6.7. Note that increasing $\Delta_{\tilde{p}}$ has an effect on the dissipating term in (6.35a). In particular, it lowers the 'gain' of the synchronisation around the origin, i.e. the turning manoeuvre required will be less severe which has a positive effect on (6.43), but the synchronisation error increases since the follower takes a smoother trajectory.

We can now investigate the interconnection between (6.35a) and (6.35b). In particular, we show that the synchronisation error kinematics are integral input-to-state stable with respect to the output of (6.35b) and (6.35c). If we lump the perturbations into a new input $\nu(t) \triangleq [\nu_1(t), \nu_2(t)]^T$ we can rewrite (6.35a) as

$$\dot{\tilde{\boldsymbol{p}}}^n = -\frac{U_a^{\max}}{\sqrt{(\tilde{\boldsymbol{p}}^n)^T\tilde{\boldsymbol{p}}^n + \Delta_{\tilde{p}}^2}}\tilde{\boldsymbol{p}}^n + \nu(t) \tag{6.44}$$

If we consider the Lyapunov function

$$V(\tilde{\boldsymbol{p}}^n) = \frac{(\tilde{\boldsymbol{p}}^n)^T\tilde{\boldsymbol{p}}^n}{\sqrt{(\tilde{\boldsymbol{p}}^n)^T\tilde{\boldsymbol{p}}^n + \Delta^2}} \tag{6.45}$$

we obtain

$$\dot{V}(\tilde{\boldsymbol{p}}^n) = \frac{2(\tilde{\boldsymbol{p}}^n)^T\dot{\tilde{\boldsymbol{p}}}^n}{\sqrt{(\tilde{\boldsymbol{p}}^n)^T\tilde{\boldsymbol{p}}^n + \Delta_{\tilde{p}}^2}} - \frac{\left((\tilde{\boldsymbol{p}}^n)^T\dot{\tilde{\boldsymbol{p}}}^n\right)\left((\tilde{\boldsymbol{p}}^n)^T\tilde{\boldsymbol{p}}^n\right)}{2\left((\tilde{\boldsymbol{p}}^n)^T\tilde{\boldsymbol{p}}^n + \Delta_{\tilde{p}}^2\right)^{3/2}} \tag{6.46a}$$

$$\leq -\frac{2U_a^{\max}(\tilde{\boldsymbol{p}}^n)^T\tilde{\boldsymbol{p}}^n}{(\tilde{\boldsymbol{p}}^n)^T\tilde{\boldsymbol{p}}^n + \Delta_{\tilde{p}}^2} - \frac{U_a^{\max}\left((\tilde{\boldsymbol{p}}^n)^T\tilde{\boldsymbol{p}}^n\right)}{\left((\tilde{\boldsymbol{p}}^n)^T\tilde{\boldsymbol{p}}^n + \Delta_{\tilde{p}}^2\right)^2} + \frac{3}{2}\|\nu(t)\| \tag{6.46b}$$

$$\leq -\frac{2U_a^{\max}(\tilde{\boldsymbol{p}}^n)^T\tilde{\boldsymbol{p}}^n}{(\tilde{\boldsymbol{p}}^n)^T\tilde{\boldsymbol{p}}^n + \Delta_{\tilde{p}}^2} - \frac{U_a^{\max}\left((\tilde{\boldsymbol{p}}^n)^T\tilde{\boldsymbol{p}}^n\right)}{\left((\tilde{\boldsymbol{p}}^n)^T\tilde{\boldsymbol{p}}^n + \Delta_{\tilde{p}}^2\right)^2} + \frac{3\sqrt{2}}{2}\|[\tilde{u_r}, \tilde{v}_r]^T\| \tag{6.46c}$$

The first two terms are clearly negative definite and the third term is a class $\mathcal{K}$ function of the input. Consequently, (6.45) is an iISS Lyapunov function for (6.35a) [6] (see Definition A.6) and the system (6.35a) is iISS (see Definition A.5) with respect to $\tilde{u}_r$ and $\tilde{v}_r$. The results of this section can be summarised in the following theorem.

Theorem 6.2. *Consider the system* (6.35). *Under Assumptions 6.2-6.4 all the solutions of* (6.35) *starting in a neighbourhood of* $u_r = u_d$ *are bounded if the CB guidance algorithm is tuned such that it holds that*

$$\frac{|Y^{\min}|}{|X^{\max}|} > \frac{|R_2'|}{C_{R_1}^{\min}} + \frac{C_3}{|X^{\max}|} \tag{6.47}$$

for the given leader motion. Moreover, the synchronisation error kinematics (6.35a) *are integral input-to-state stable with respect to the output of* (6.35b)-(6.35c).

Table 6.1: Simulation parameters.

Variable	Value	Unit	Variable	Value	Unit
$U_{a,\max}$	2	m/s	k_ψ	0.04	-
$\Delta_{\tilde{p}}$	500	m	k_r	0.9	-
V_x	-1.1028	m/s	k_{u_r}	0.1	-
V_y	0.8854	m/s			

Corollary 6.3. *If the leader trajectory is a straight-line with constant velocity then, under the conditions of Theorem 6.2, the synchronisation error converges to zero.*

Proof. In this case the course of the leader and its inertial frame velocity are constant. Therefore, as the follower synchronizes with the leader its course will converge to the leader's course. Since $\tilde{v}_r$ is not directly controllable the only stable configuration the follower can be regulated to, to keep a constant course, will be when $r \to 0$ and $v_r \to 0$. Consequently, both $\tilde{v}_r$ and $\tilde{u}_r$ go to zero and we arrive at the unperturbed version of (6.35a), i.e. (6.10), which has a USGES equilibrium according to Theorem 6.1. □

6.3 Simulations

In this section two scenarios are used as case studies to validate the control strategy

1. the leader moves along a straight-line path that is at an angle with respect to the earth-fixed frame.
2. the leader moves along a sinusoidal path.

In both cases the follower ship is affected by a constant ocean current. The leader is represented by a point moving in the horizontal plane that is to be followed. This allows for a very straightforward implementation of the desired path and illustrates that the leader dynamics are not needed for the control strategy. Some parameters for the simulations are given in Table 6.1. This includes the parameters for the controllers and guidance law, and the magnitude of the ocean current. The follower vessel in the simulation is described by the ship model from Fredriksen and Pettersen [63], which is given in Section C.1.

6.3.1 Straight-line Path Following

The motion of the leader and the follower in the horizontal plane can be seen in Figure 6.2. From Figure 6.2 it can be seen that the follower converges to the trajectory of the leader and compensates for the current by side-slipping to maintain the desired path. The side-slipping is a desired result of the control strategy and is necessary to remain on the straight-line path in the presence of ocean currents. In particular, since the vessel is underactuated in sway, a side-slip angle w.r.t. the path is necessary to compensate for the force pushing the vessel in the transverse direction of the path. Since the desired heading angle is calculated from the inner

and outer products of the desired and actual velocity, the desired angle is the angle for which the velocity error is zero, which is the necessary side-slip angle.

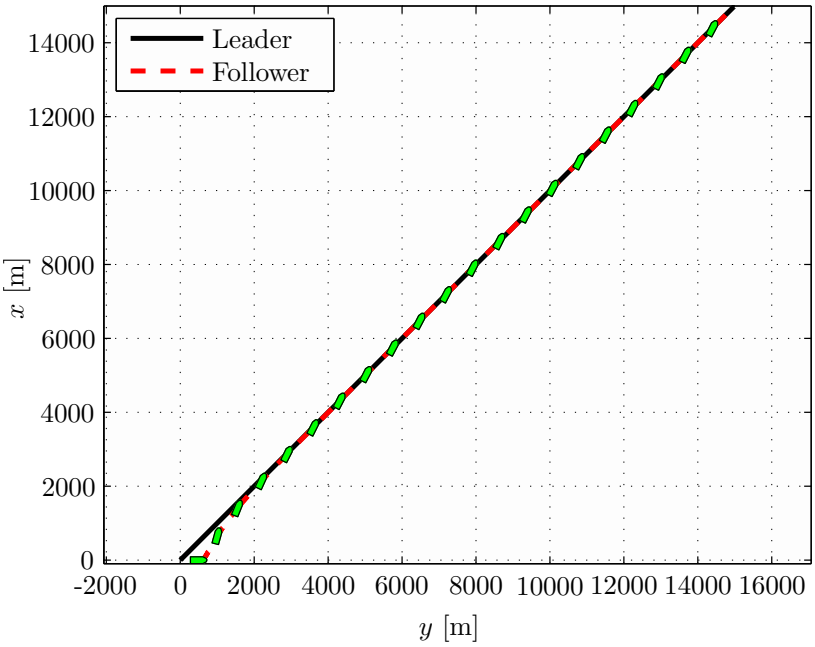

Figure 6.2: Motion in the horizontal plane.

The synchronisation error in x and y can be seen in Figure 6.3. Figure 6.3 clearly shows that $\tilde{x}^n$ and $\tilde{y}^n$ converge to zero. Hence, target tracking or leader-follower synchronisation with zero synchronisation error is attained for straight-line motions with $r_d \to 0$ which is in-line with our analysis of Section 6.2.

6.3.2 Sinusoidal Path Following

In the second case study the leader generates a sinusoidal reference for the follower which demands a constantly changing desired yaw rate. Hence, the synchronisation error kinematics are perturbed.

The trajectory of the leader and the follower for tracking of a sinusoidal path can be seen in Figure 6.4. From Figure 6.4 it can be seen that the follower gets close to the trajectory of the leader and compensates for the current to maintain the desired path. Figure 6.5 shows the position synchronisation error in the x and y direction. From Figure 6.5 it can be seen that the synchronisation error in x decreases to below an amplitude of about 1.5 meters, while the error in y direction, which is the direction transversal to the propagation of the sinusoid and most prone to drift, decreases to below 2.5 meter. Note that the error plots are asymmetric due to the vessel changing its direction with respect to the current which causes different behaviour.

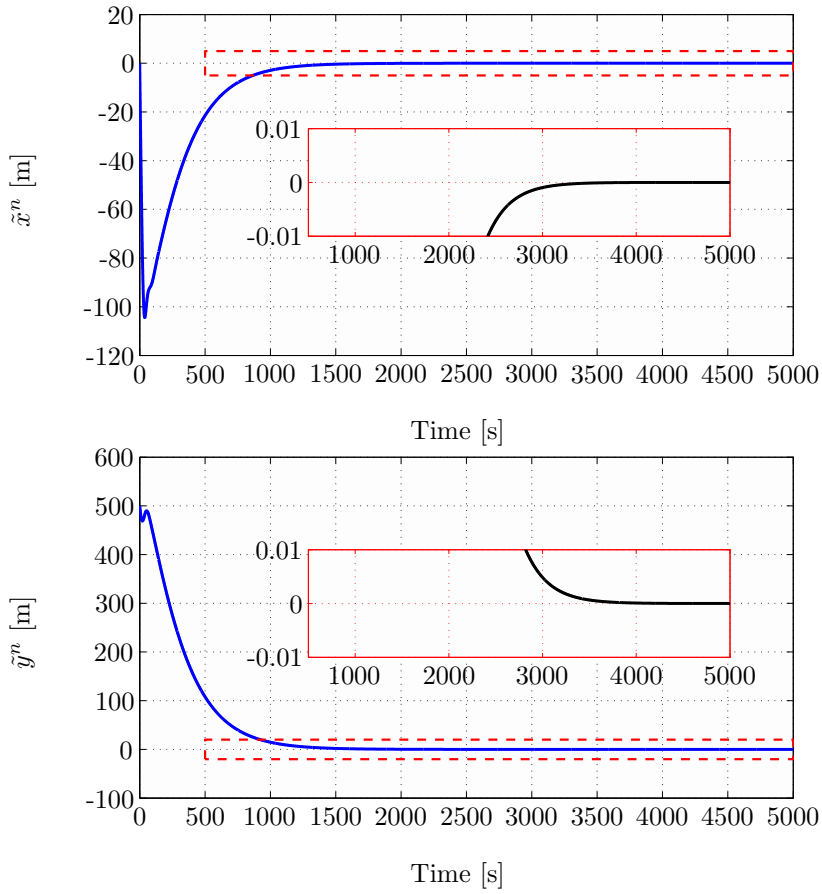

Figure 6.3: x (top) and y (bottom) synchronisation error.

The behaviour in the test-case is in-line with the analysis of Section 6.2 since we have convergence from large initial errors, the follower converges towards the trajectory of the leader. When the follower is close to the leader the follower exhibits integral input-to-state stable behaviour and stays in a neighbourhood of the leader dependent on the size of the desired yaw rate to track this motion.

6.4 Conclusions

This chapter has presented and analysed a control scheme for leader-follower synchronisation for inhomogeneous multi-agent systems consisting of an underactuated follower and a leader vessel with unknown dynamics. The developed leader-follower scheme can be applied to multi-agent systems with underactuated follower agents that are subjected to environmental disturbances. The dynamics of the leader is unknown, and the leader may be fully actuated or underactuated. Position and velocity measurements of the leader are available to the follower for use in the

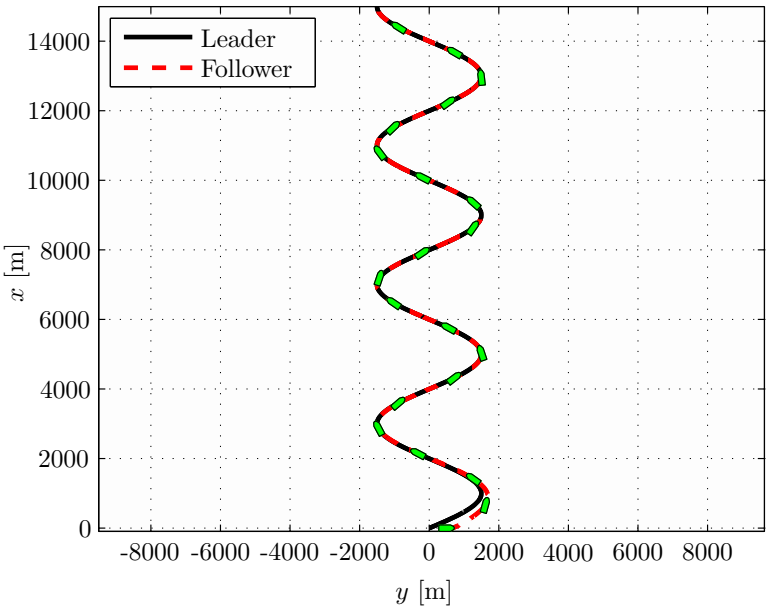

Figure 6.4: Motion in the horizontal plane.

guidance law. If the follower uses controllers with acceleration feedforward, acceleration and jerk measurements of the leader also need to be available to the follower. The leader is free to move as it wants independently of the follower(s), and can for instance be manually controlled. The follower thus has no information about the future motion of the leader. The follower uses a constant bearing guidance algorithm to track the leader. The constant bearing guidance algorithm is shown to provide USGES synchronisation error kinematics with an explicit bound on the solutions. The constant bearing guidance algorithm is then coupled to controllers designed for the underactuated follower vehicle. This results in a closed-loop system consisting of the fully actuated controlled dynamics, underactuated dynamics, and synchronisation error kinematics. The solutions of the underactuated and the fully actuated dynamics, have been shown to be bounded under certain conditions. Furthermore, the synchronisation error kinematics has been shown to be integral input-to-state stable with respect to changes in the unactuated sway velocity. Moreover, it has been shown that synchronisation can be achieved when the leader moves along a straight-line since in this case the perturbation of the underactuated dynamics to the synchronisation error kinematics vanishes. The validity of the control scheme has been shown in a case study.

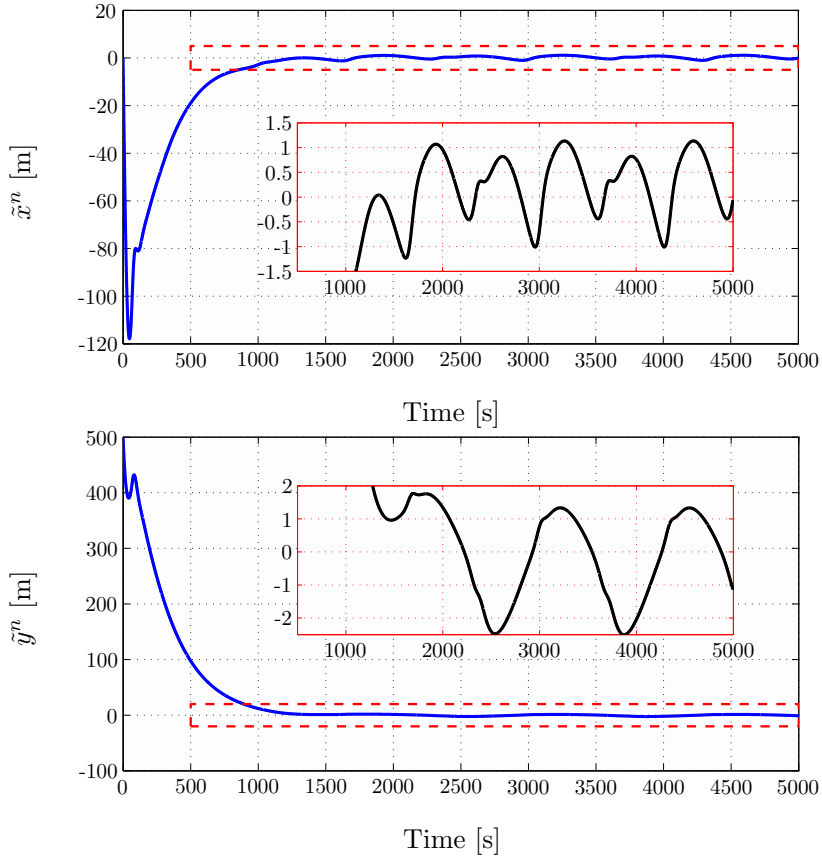

Figure 6.5: x (top) and y (bottom) synchronisation error.

Part III

Curved Path Following for Underactuated Marine Vessels

Chapter 7

Observer Based Path Following for Underactuated Marine Vessels in the Presence of Ocean Currents: A Local Approach

In this chapter a solution to the problem of following a curved path in the presence of a constant ocean current disturbance is presented. The path is parametrised by a path variable that is used to propagate a path-tangential reference frame. The update law for the path variable is chosen such that the motion of the path-tangential frame ensures that the vessel remains on the normal of the path-tangential reference frame. As shown in the seminal work [124] such a parametrisation is only possible locally. A tube is defined in which the aforementioned parametrisation is valid and the path-following problem is solved within this tube. The size of the tube is proportional to the size of the curvature of the path. The locality of this approach is a disadvantage. The advantage of this local parametrisation that keeps the vessel on the normal is that the path-following error is always defined as the shortest distance to the path.

To achieve path following we use a line-of-sight guidance law that is combined with an observer to estimate the unknown ocean current. The closed-loop system of the vessel with the observer and controller is investigated by first showing boundedness of the sway velocity and then showing global asymptotic stability of the path-following errors within the tube. Since the current is unknown the vessel cannot be guaranteed to stay within the tube for an arbitrary current and an arbitrary curvature of the path. Hence, the initial estimation error for the current might cause a transient that takes the vessel out of the tube if the actual curvature of the path is close to the maximally feasible curvature for the vessel. This maximally feasible curvature is dependent on the parameters of the ship and the desired path-following velocity.

The outline of the chapter is as follows. In the Section 7.1 the vessel model from Section 2.2 is recalled. The path-following problem and the chosen path parametrisation are introduced in Section 7.2. Section 7.3 presents the ocean current observer

that is used together with the guidance law and controllers. The closed-loop system is then formulated and analysed in Section 7.4. A simulation case study is presented in Section 7.5 and conclusions are given in Section 7.6. The material in this chapter is based on Maghenem et al. [96].

7.1 Vessel Model

In this section we consider the model for a surface vessel given in Chapter 2. This model can be used to describe an autonomous surface vessel or an autonomous underwater vehicle moving in a plane. Recall, that the model can be represented in component form as

$$\dot{x} = u_r \cos(\psi) - v_r \sin(\psi) + V_x, \tag{7.1a}$$
$$\dot{y} = u_r \sin(\psi) + v_r \cos(\psi) + V_y, \tag{7.1b}$$
$$\dot{\psi} = r, \tag{7.1c}$$
$$\dot{u}_r = F_{u_r}(v_r, r) - \tfrac{d_{11}}{m_{11}} u_r + \tau_u, \tag{7.1d}$$
$$\dot{v}_r = X(u_r) r + Y(u_r) v_r, \tag{7.1e}$$
$$\dot{r} = F_r(u_r, v_r, r) + \tau_r, \tag{7.1f}$$

The functions $X(u_r)$, $Y(u_r)$, F_u, and F_r are given by

$$F_{u_r}(v_r, r) \triangleq \frac{1}{m_{11}}(m_{22} v_r + m_{23} r) r, \tag{7.2a}$$
$$X(u_r) \triangleq \frac{m_{23}^2 - m_{11} m_{33}}{m_{22} m_{33} - m_{23}^2} u_r + \frac{d_{33} m_{23} - d_{23} m_{33}}{m_{22} m_{33} - m_{23}^2}, \tag{7.2b}$$
$$Y(u_r) \triangleq \frac{(m_{22} - m_{11}) m_{23}}{m_{22} m_{33} - m_{23}^2} u_r - \frac{d_{22} m_{33} - d_{32} m_{23}}{m_{22} m_{33} - m_{23}^2}, \tag{7.2c}$$
$$\begin{aligned} F_r(u_r, v_r, r) \triangleq{}& \frac{m_{23} d_{22} - m_{22}(d_{32} + (m_{22} - m_{11}) u_r)}{m_{22} m_{33} - m_{23}^2} v_r \\ &+ \frac{m_{23}(d_{23} + m_{11} u_r) - m_{22}(d_{33} + m_{23} u_r)}{m_{22} m_{33} - m_{23}^2} r. \end{aligned} \tag{7.2d}$$

Note that the functions $X(u_r)$ and $Y(u_r)$ are linear functions of the velocity. The kinematic variables are illustrated in Figure 7.1. As specified in Chapter 2, the ocean current satisfies the following assumption.

Assumption 7.1. The ocean current is assumed to be constant and irrotational with respect to the inertial frame, i.e. $\boldsymbol{V}_c \triangleq [V_x, V_y, 0]^T$. Furthermore, it is bounded by $V_{\max} > 0$ such that $\|\boldsymbol{V}_c\| = \sqrt{V_x^2 + V_y^2} \leq V_{\max}$.

Moreover, for the considered range of values of the desired surge velocity u_{rd} the following assumption holds.

Assumption 7.2. It is assumed that $Y(u_r)$ satisfies

$$Y(u_r) \leq -Y_{\min} < 0, \, \forall u_r \in [-V_{\max}, u_{rd}],$$

i.e. $Y(u_r)$ is negative for the range of desired velocities considered.

Remark 7.1. Assumptions 7.2 is satisfied for commercial vessels by design, since the converse would imply an undamped or nominally unstable vessel in sway.

Additionally we assume that the following assumption holds

Assumption 7.3. It is assumed that $2V_{\max} < u_{rd}(t)\ \forall t$, i.e. the desired relative velocity of the vessel is larger than the maximum value of the ocean current.

Assumption 7.3 assures that the vessel has enough propulsion power to overcome the ocean current affecting it. The factor two in Assumption 7.3 adds some extra conservativeness to bound the solutions of the ocean current observer, this is discussed further in Section 7.3.

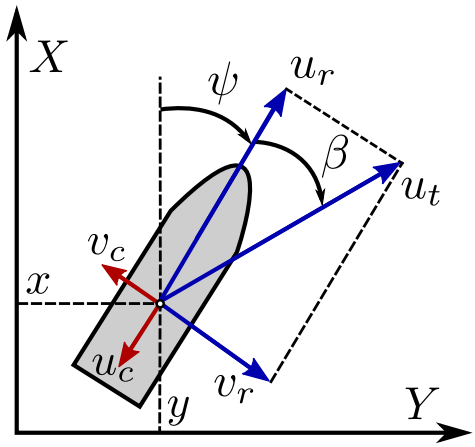

Figure 7.1: Definition of the ship's kinematic variables.

7.2 Problem definition

The goal is to follow a smooth path P, parametrised by a path variable θ, by appropriately controlling the ship's surge velocity and yaw rate. For an underactuated vessel, path following can be achieved by positioning the vessel on the path with the total velocity $u_t \triangleq \sqrt{u_r^2 + v_r^2}$ (see Figure 7.1) tangential to the path. To express the path-following error we propagate a path-tangential frame along P such that the vessel will be on the normal of the path-tangential frame at all time. This is illustrated in Figure 7.2. The preceding implies that the progression of the path-tangential frame is controlled such that the path-following error takes the form:

$$\begin{bmatrix} x_{b/p} \\ y_{b/p} \end{bmatrix} = \begin{bmatrix} \cos(\gamma_p(\theta)) & \sin(\gamma_p(\theta)) \\ -\sin(\gamma_p(\theta)) & \cos(\gamma_p(\theta)) \end{bmatrix} \begin{bmatrix} x - x_P(\theta) \\ y - y_P(\theta) \end{bmatrix} \tag{7.3a}$$

$$= \begin{bmatrix} 0 \\ y_{b/p} \end{bmatrix}, \tag{7.3b}$$

where $\gamma(\theta)$ is the angle of the path with respect to the X-axis, $x_{b/p}$ is the deviation from the normal in tangential direction, and $y_{b/p}$ is the deviation from the tangent in normal direction. The time derivative of the angle $\gamma(\theta)$ is given by $\dot{\gamma}(\theta) = \kappa(\theta)\dot{\theta}$ where $\kappa(\theta)$ is the curvature of P at θ. The goal is to regulate $x_{b/p}$ and $y_{b/p}$ to zero.

7.2.1 Locally valid parametrisation

The error in the tangential direction $x_{b/p}$ will be kept at zero by the choice of the update law for the path variable θ, i.e. the vehicle is kept on the normal. It is well known that such a parametrisation will only be unique locally [124]. In particular, such a unique expression exists when the vehicle is closer to the path than the inverse of the maximum curvature of the path, i.e. when $y_{b/p} < 1/\kappa_{\max}$ where $\kappa_{\max}$ is the maximum curvature of the path. Note that this is equivalent to being closer than the radius of the smallest inscribed circle of the path. To design such a parametrisation we first consider the error dynamics of the vessel with respect to the path frame, which is given by:

$$\dot{x}_{b/p} = -\dot{\theta}(1 - \kappa(\theta)y_{b/p}) + u_t \cos(\chi - \gamma_p(\theta)) + V_T, \tag{7.4a}$$

$$\dot{y}_{b/p} = u_t \sin(\chi - \gamma_p(\theta)) + V_N - \kappa(\theta)\dot{\theta}x_{b/p}, \tag{7.4b}$$

where $\chi \triangleq \psi + \beta$ is the course angle (see Figure 7.1) and $V_T \triangleq V_x \cos(\gamma_p(\theta)) + V_y \sin(\gamma_p(\theta))$ and $V_N \triangleq V_y \cos(\gamma_p(\theta)) - V_x \sin(\gamma_p(\theta))$ are the ocean current component in the tangential direction and normal direction of the path-tangential reference frame, respectively. Consequently, if the path variable θ is updated according to

$$\dot{\theta} = \frac{u_t \cos(\chi - \gamma_p(\theta)) + V_T}{1 - \kappa(\theta)y_{b/p}}, \tag{7.5}$$

the vessel stays on the normal when it starts on the normal. In particular, substitution of (7.5) in (7.4a) results in $\dot{x}_{b/p} = 0$. To make sure that the update law (7.5) is well defined the following condition should be satisfied

Condition 7.1. *To have a well defined update law for the path variable θ it should hold that*

$$1 - \kappa(\theta)y_{b/p} \neq 0 \tag{7.6}$$

for all time.

Note that Condition 7.1 implies that the update law is well defined within the tube of radius $y_{b/p} < 1/\kappa_{\max}$ which results in the parametrisation being only locally valid.

The update law (7.5) depends on the current component V_T. However, since the current is assumed unknown we have to replace V_T by its estimate $\hat{V}_T \triangleq \hat{V}_x \cos(\gamma(\theta)) + \hat{V}_y \sin(\gamma(\theta))$. Consequently, (7.3b) does not hold until the current is estimated correctly. Therefore, (7.3) takes the form

$$\begin{bmatrix} x_{b/p} \\ y_{b/p} \end{bmatrix} = \begin{bmatrix} \cos(\gamma(\theta)) & \sin(\gamma(\theta)) \\ -\sin(\gamma(\theta)) & \cos(\gamma(\theta)) \end{bmatrix} \begin{bmatrix} x - x_P(\theta) \\ y - y_P(\theta) \end{bmatrix}. \tag{7.7}$$

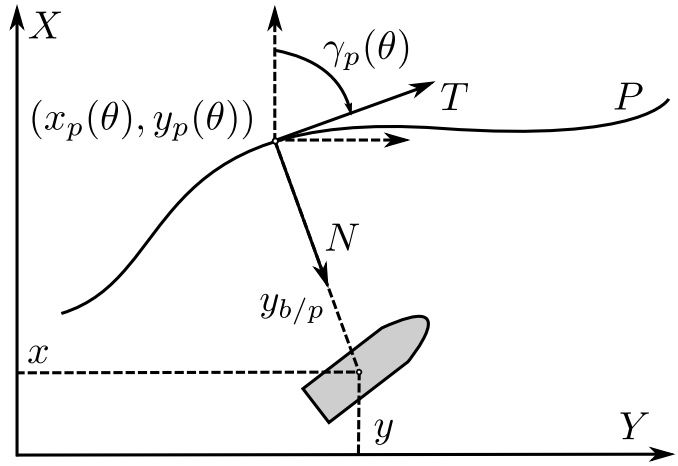

Figure 7.2: Definition of the path.

To force (7.7) to become equal to (7.3) once the ocean current is estimated correctly we augment (7.5) to be

$$\dot{\theta} = \frac{u_t \cos(\chi - \gamma_p(\theta)) + \hat{V}_T + k_\delta x_{b/p}}{1 - \kappa(\theta) y_{b/p}}, \tag{7.8}$$

such that the path-tangential reference frame propagates based on an estimate of the ocean current and has a restoring term to drive $x_{b/p}$ to zero. Hence, substituting (7.8) in (7.4a) gives

$$\dot{x}_{b/p} = -k_\delta x_{b/p} + \tilde{V}_T, \tag{7.9}$$

which shows that if the estimate of the current has converged the restoring term $k_\delta x_{b/p}$ remains to drive $x_{b/p}$ to zero after which the vessel remains on the normal of the path-tangential frame.

The dynamics of the error along the normal are given by

$$\dot{y}_{b/p} = u_t \sin(\chi - \gamma_p(\theta)) + V_N - x_{b/p}\kappa(\theta)\dot{\theta}. \tag{7.10}$$

In the next section a guidance law is chosen to stabilise the origin of the dynamics (7.9)-(7.10) and achieve the goal of path following.

Note that since the path parametrisation is only local, we can only utilise it within a tube around the path with radius $1/\kappa_{\max}$. To achieve global results this tube needs to be made attractive and invariant, such that the vehicle first converges to the tube after which the unique parametrisation to achieve path-following can be used. The disadvantage of this is that a two-step approach is needed to solve the path-following problem, which complicates the analysis. There is, however, also a big advantage to this approach, since extra design freedom is available when making the tube attractive. This allows one to design the approach behaviour and convergence when far from the path, while for a global one-step approach this is in general not possible to do independently of the behaviour close to the path. Hence,

for the one-step approach the global behaviour will be a compromise between the desired behaviour far away from the path and the desired behaviour close to the path. For the two-step approach, the behaviour far away from the path and close to the path can be optimised independently. This, for instance, allows strategies where the vehicle moves along the normal of the path to reach the path as fast as possible. Moreover, in cluttered environments this allows the vessel to converge to the path along a clearly defined approach path, after which it can switch to the guidance strategy that allows it to follow the desired path P.

7.3 Controller, Observer, and Guidance

In this section we design the two control laws τ_u and τ_r, and the ocean current estimator that are used to achieve path-following. In the first subsection we present the velocity control law τ_u. The second subsection presents the ocean current estimator. The third subsection presents the guidance to be used within the tube.

7.3.1 Surge velocity control

The velocity control law is a feedback-linearising P-controller that is used to drive the relative surge velocity to a desired u_{rd} and is given by

$$\tau_u = -F_{u_r}(v_r, r) + \dot{u}_{rd} + \frac{d_{11}}{m_{11}} u_{rd} - k_u(u_r - u_{rd}), \tag{7.11}$$

where $k_u > 0$ is a constant controller gain. It is straightforward to verify that (7.11) ensures global exponential tracking of the desired velocity. In particular, when (7.11) is substituted in (7.1d) we obtain

$$\dot{\tilde{u}}_r = -k_u(u_r - u_{rd}) = -k_u \tilde{u}_r, \tag{7.12}$$

where $\tilde{u}_r \triangleq u_r - u_{rd}$. Consequently, the velocity error dynamics are described by a stable linear systems, which assures exponential tracking of the desired velocity u_{rd}.

7.3.2 Ocean current estimator

This subsection presents the ocean current estimator introduced in [2]. This observer provides the estimate of the ocean current needed to implement (7.8) and the guidance law developed in the next subsection. Rather than estimating the time-varying current components in the path frame V_T and V_N the observer is used to estimate the constant ocean current components in the inertial frame V_x and V_y. The observer from [2] is based on the kinematic equations of the vehicle, i.e. (7.1a) and (7.1b), and requires measurements of the vehicle's x and y position

in the inertial frame. The observer is formulated as

$$\dot{\hat{x}} = u_r \cos(\psi) - v_r \sin(\psi) + \hat{V}_x + k_{x_1}\tilde{x} \tag{7.13a}$$

$$\dot{\hat{y}} = u_r \sin(\psi) + v_r \cos(\psi) + \hat{V}_y + k_{y_1}\tilde{y} \tag{7.13b}$$

$$\dot{\hat{V}}_x = k_{x_2}\tilde{x} \tag{7.13c}$$

$$\dot{\hat{V}}_y = k_{y_2}\tilde{y} \tag{7.13d}$$

where $\tilde{x} \triangleq x - \hat{x}$ and $\tilde{y} = y - \hat{y}$ are the positional errors and k_{x_1}, k_{x_2}, k_{y_1}, and k_{y_2} are constant positive gains. Consequently, the estimation error dynamics are given by

$$\dot{\tilde{x}} = \tilde{V}_x - k_{x_1}\tilde{x} \tag{7.14a}$$

$$\dot{\tilde{y}} = \tilde{V}_y - k_{y_1}\tilde{y} \tag{7.14b}$$

$$\dot{\tilde{V}}_x = -k_{x_2}\tilde{x} \tag{7.14c}$$

$$\dot{\tilde{V}}_y = -k_{y_2}\tilde{y} \tag{7.14d}$$

which can be written in vector form as

$$\begin{bmatrix} \dot{\tilde{x}} \\ \dot{\tilde{y}} \\ \dot{\tilde{V}}_x \\ \dot{\tilde{V}}_y \end{bmatrix} = \begin{bmatrix} -k_{x_1} & 0 & 1 & 0 \\ 0 & -k_{y_1} & 0 & 1 \\ -k_{x_2} & 0 & 0 & 0 \\ 0 & -k_{y_2} & 0 & 0 \end{bmatrix} \begin{bmatrix} \tilde{x} \\ \tilde{y} \\ \tilde{V}_x \\ \tilde{V}_y \end{bmatrix}. \tag{7.15}$$

which is a linear system with negative eigenvalues. Hence, the observer error dynamics are globally exponentially stable at the origin. Note that this implies that also $\hat{V}_T$ and $\hat{V}_N$ go to V_T and V_N respectively with exponential convergence since it holds that

$$\hat{V}_T = \hat{V}_x \cos(\gamma(\theta)) + \hat{V}_y \sin(\gamma(\theta)), \tag{7.16a}$$

$$\hat{V}_N = -\hat{V}_x \sin(\gamma(\theta)) + \hat{V}_y \cos(\gamma(\theta)). \tag{7.16b}$$

For implementation of the controllers it is desired that $\|\hat{V}_N(t)\| < u_{rd}(t)\ \forall t$. To achieve this we first choose the initial conditions of the estimator as

$$[\hat{x}(t_0), \hat{y}(t_0), \hat{V}_x(t_0), \hat{V}_y(t_0)]^T = [x(t_0), y(t_0), 0, 0]^T. \tag{7.17}$$

Consequently, the initial estimation error is given by

$$[\tilde{x}(t_0), \tilde{y}(t_0), \tilde{V}_x(t_0), \tilde{V}_y(t_0)]^T = [0, 0, V_x, V_y]^T, \tag{7.18}$$

which has a norm smaller than or equal to $V_{\max}$ according to Assumption 7.1. Now consider the function

$$W(t) = \tilde{x}^2 + \tilde{y}^2 + \frac{1}{k_{x_2}}\tilde{V}_x^2 + \frac{1}{k_{y_2}}\tilde{V}_y^2, \tag{7.19}$$

which has the following time derivative

$$\begin{aligned}\dot{W}(t) &= 2\tilde{x}\dot{\tilde{x}} + 2\tilde{y}\dot{\tilde{y}} + \frac{2}{k_{x_2}}\tilde{V}_x\dot{\tilde{V}}_x + \frac{2}{k_{y_2}}\tilde{V}_y\dot{\tilde{V}}_y \\ &= 2\tilde{x}(\tilde{V}_x - k_{x_1}\tilde{x}) + 2\tilde{y}(\tilde{V}_y - k_{y_1}\tilde{y}) - 2\tilde{V}_y\tilde{y} - 2\tilde{V}_x\tilde{x} \\ &= -2k_{x_1}\tilde{x}^2 - 2k_{y_1}\tilde{y}^2 \leq 0.\end{aligned} \tag{7.20}$$

This implies that $W(t) \leq \|W(t_0)\|$. From our choice of initial conditions we know that

$$\|W(t_0)\| = \frac{1}{k_{x_2}}V_x^2 + \frac{1}{k_{y_2}}V_y^2 \leq \frac{1}{\min(k_{x_2}, k_{y_2})}V_{\max}^2. \tag{7.21}$$

Moreover, it is straightforward to verify

$$\frac{1}{\max(k_{x_2}, k_{y_2})}\|\tilde{\boldsymbol{V}}_c(t)\|^2 \leq W(t). \tag{7.22}$$

Combining the observations given above we obtain

$$\frac{1}{\max(k_{x_2}, k_{y_2})}\|\tilde{\boldsymbol{V}}_c(t)\|^2 \leq \frac{1}{\min(k_{x_2}, k_{y_2})}V_{\max}^2. \tag{7.23}$$

Consequently, we obtain

$$\|\tilde{\boldsymbol{V}}_c(t)\| \leq \sqrt{\frac{\max(k_{x_2}, k_{y_2})}{\min(k_{x_2}, k_{y_2})}}V_{\max} < \sqrt{\frac{\max(k_{x_2}, k_{y_2})}{\min(k_{x_2}, k_{y_2})}}u_{rd}(t),\ \forall t, \tag{7.24}$$

which implies that if the gains are chosen as $k_{x_2} = k_{y_2}$ we have

$$\|\hat{V}_N\| \leq 2V_{\max} \leq u_{rd}(t),\ \forall t. \tag{7.25}$$

Hence, $\|\hat{V}_N\| < u_{rd}(t),\ \forall t$ if $2V_{\max} < u_{rd}(t),\ \forall t$.

Remark 7.2. The bound $2V_{\max} < u_{rd},\ \forall t$, is only required when deriving the bound on the solutions of the observer. In particular, it is required to guarantee that $\|\hat{V}_N\| < u_{rd}(t),\ \forall t$. For the rest of the analysis it suffices that $V_{\max} < u_{rd},\ \forall t$. Therefore, if the more conservative bound $2V_{\max} < u_{rd},\ \forall t$, is not satisfied the observer can be changed to an observer that allows explicit bounds on the estimate $\hat{V}_N$, e.g. the observer developed Narendra and Annaswamy [103], rather than an observer that only provides a bound on the error $\tilde{\boldsymbol{V}}_c$ as is the case here. For practical purposes the estimate can also be saturated such that $\|\hat{V}_N\| < u_{rd},\ \forall t$, which is the approach taken in Moe et al. [100]. However, in the theoretical analysis of the yaw controller we use derivatives of $\hat{V}_N$ which will be discontinuous when saturation is applied.

7.3.3 Guidance

This subsection presents the guidance that is used in combination with the local parametrisation. Since, the chosen parametrisation is only valid in a tube around

the path, the proposed guidance is designed for operation in the tube. Inside the tube we propose the following guidance law

$$\psi_d = \gamma(\theta) - \operatorname{atan}\left(\frac{v_r}{u_{rd}}\right) - \operatorname{atan}\left(\frac{y_{b/p}+g}{\Delta}\right). \tag{7.26}$$

The guidance law consists of three terms. The first term is a feedforward of the angle of the path with respect to the inertial frame. The second part is the desired side-slip angle, i.e. the angle between the surge velocity and the total speed when $u_r \equiv u_{rd}$. This side-slip angle is used to make the vehicle's total speed tangential to the path when the sway velocity is non-zero. The third term is a line-of-sight (LOS) term that is intended to steer the vessel to the path, where g is a term dependent on the ocean current. The choice of g provides extra design freedom to compensate for the component of the ocean current along the normal axis V_N. To analyse the effect of this guidance law and to design g we consider the error dynamics along the normal (7.10). To do this we substitute (7.26) in (7.10) and obtain

$$\dot{y}_{b/p} = u_{td}\sin\Big(\psi_d + \tilde{\psi} + \beta_d - \gamma_p(\theta)\Big) + V_N - x_{b/p}\kappa(\theta)\dot{\theta} + \tilde{u}_r\sin(\psi - \gamma_p(\theta)) \tag{7.27a}$$

$$= -u_{td}\frac{y_{b/p}+g}{\sqrt{(y_{b/p}+g)^2+\Delta^2}} + V_N + G_1(\tilde{\psi}, \tilde{u}_r, x_{b/p}, \psi_d, y_{b/p}, u_{td}, \dot{\gamma}_p(\theta)) \tag{7.27b}$$

where $G_1(\cdot)$ is a perturbing term given by

$$\begin{aligned} G_1(\cdot) = {} & u_{td}\Big[1-\cos(\tilde{\psi})\Big]\sin\left(\arctan\left(\frac{y_{b/p}+g}{\Delta}\right)\right) + \tilde{u}_r\sin(\psi-\gamma_p(\theta)) \\ & + u_{td}\cos\left(\arctan\left(\frac{y_{b/p}+g}{\Delta}\right)\right)\sin(\tilde{\psi}) - x_{b/p}\dot{\gamma}_p(\theta) \end{aligned} \tag{7.28}$$

and $u_{td} \triangleq \sqrt{u_{rd}^2 + v_r^2}$ is the desired total velocity. Note that $G_1(\cdot)$ satisfies

$$G_1(0,0,0,\psi_d, y_{b/p}, u_{td}, \dot{\gamma}_p(\theta)) = 0 \tag{7.29a}$$

$$\|G_1(\tilde{\psi}, \tilde{u}_r, x_{b/p}, \psi_d, y_{b/p}, u_{td}, \dot{\gamma}_p(\theta))\| \leq \zeta(\dot{\gamma}_p(\theta), u_{td})\|(\tilde{\psi}, \tilde{u}, x_{b/p})\|, \tag{7.29b}$$

where $\zeta(\dot{\gamma}_p(\theta), u_{td}) > 0$, which shows that $G_1(\cdot)$ is zero when the perturbing variables are zero and that it has maximal linear growth in the perturbing variables.

To compensate for the ocean current component V_N the variable g is now chosen to satisfy the equality

$$u_{td}\frac{g}{\sqrt{\Delta^2 + (y_{b/p}+g)^2}} = \hat{V}_N. \tag{7.30}$$

which is a choice inspired by [100]. In order for g to satisfy the equality above, g should be the solution of the following second order equality

$$\underbrace{(u_{td}^2 - \hat{V}_N^2)}_{-a}\left(\frac{g}{\hat{V}_N}\right)^2 = \underbrace{\Delta^2 + y_{b/p}^2}_{c} + 2\underbrace{y_{b/p}\hat{V}_N}_{b}\left(\frac{g}{\hat{V}_N}\right), \tag{7.31}$$

hence we choose g to be

$$g = \hat{V}_N \frac{b + \sqrt{b^2 - ac}}{-a}, \tag{7.32}$$

which has the same sign as $\hat{V}_N$ and is well defined for $(u_{rd}^2 - \hat{V}_N^2) > 0$. Moreover, since

$$\sqrt{b^2 - ac} = \sqrt{\Delta^2(u_{td}^2 - \hat{V}_N^2) + y_{b/p}^2 u_{td}^2} \tag{7.33}$$

solutions are real for $(u_{rd}^2 - \hat{V}_N^2) > 0$.

Consequently if we substitute this choice for g in (7.27) we obtain

$$\dot{y}_{b/p} = -u_{td} \frac{y_{b/p}}{\sqrt{(y_{b/p} + g)^2 + \Delta^2}} + \tilde{V}_N + G_1(\tilde{\psi}, \tilde{u}, x_{b/p}, \psi_d, y_{b/p}, u_{td}, \dot{\gamma}_p(\theta)). \tag{7.34}$$

The desired yaw rate can be found by taking the time derivative of (7.26) resulting in

$$\dot{\psi}_d = \kappa(\theta)\dot{\theta} + \frac{\dot{v}_r u_{rd} - \dot{u}_{rd} v_r}{u_{rd}^2 + v_r^2} + \frac{\Delta(\dot{y}_{b/p} + \dot{g})}{\Delta^2 + (y_{b/p} + g)^2}, \tag{7.35}$$

where $\dot{v}_r$ as given in (7.1e), $\dot{y}_{b/p}$ in (7.34), and $\dot{g}$ is given by

$$\dot{g} = \dot{\hat{V}}_N \frac{b + \sqrt{b^2 - ac}}{-a} + \frac{\partial g}{\partial a}\dot{a} + \frac{\partial g}{\partial b}\dot{b} + \frac{\partial g}{\partial c}\dot{c}, \tag{7.36}$$

where

$$\frac{\partial g}{\partial a} = \hat{V}_N \frac{c}{2a\sqrt{b^2 - ac}} + \hat{V}_N \frac{b + \sqrt{b^2 - ac}}{a^2}, \tag{7.37a}$$

$$\dot{a} = 2\hat{V}_N \dot{\hat{V}}_N - 2u_{rd}\dot{u}_{rd} - 2v_r \left[X(u_r)r + Y(u_r)v_r\right], \tag{7.37b}$$

$$\frac{\partial g}{\partial b} = \hat{V}_N \frac{b + \sqrt{b^2 - ac}}{a\sqrt{b^2 - ac}}, \tag{7.37c}$$

$$\dot{b} = 2\hat{V}_N \dot{y}_{b/p} + 2\dot{\hat{V}}_N y_{b/p}, \qquad \frac{\partial g}{\partial c} = \hat{V}_N \frac{1}{2\sqrt{b^2 - ac}}, \qquad \dot{c} = 2y_{b/p}\dot{y}_{b/p}. \tag{7.37d}$$

Note that $\dot{y}_{b/p}$ appears a number of times in the expression for $\dot{\psi}_d$ and that $\dot{y}_{b/p}$ depends on $\tilde{V}_N$. Consequently, $\dot{\psi}_d$ depends on an unknown variable and cannot be used to control the yaw rate. This was not considered in [100] where the proposed controller contained both $\dot{\psi}_d$ and $\ddot{\psi}_d$.

Moreover, since $\dot{\psi}_d$ contains $\dot{v}_r$, which depends on $r = \dot{\psi}$, the yaw rate error $\dot{\tilde{\psi}} \triangleq \dot{\psi} - \dot{\psi}_d$ grows with $\dot{\psi}$ which leads to a necessary condition for a well defined

yaw rate error. The yaw rate error dynamics are given by

$$\begin{aligned}\dot{\tilde{\psi}} = r &\left[1 + \frac{X(u_r)u_{rd}}{u_{rd}^2 + v_r^2} - \frac{\Delta}{\Delta^2 + \left(y_{b/p} + g\right)^2}\frac{\partial g}{\partial a}\left(2v_r X(u_r)\right)\right] \\ &- \kappa(\theta)\dot{\theta} + \frac{Y(u_r)v_r u_{rd} - \dot{u}_{rd}v_r}{u_{rd}^2 + v_r^2} \\ &+ \frac{\Delta}{\Delta^2 + \left(y_{b/p} + g\right)^2}\dot{\hat{V}}_N \frac{b + \sqrt{b^2 - ac}}{-a} \\ &+ \frac{\Delta}{\Delta^2 + \left(y_{b/p} + g\right)^2}\frac{\partial g}{\partial a}\left(2\hat{V}_N\dot{\hat{V}}_N - 2u_{rd}\dot{u}_{rd} - 2v_r Y(u_r)v_r\right) \\ &+ \frac{\Delta}{\Delta^2 + \left(y_{b/p} + g\right)^2}\frac{\partial g}{\partial b}\left(2\dot{\hat{V}}_N y_{b/p}\right) \\ &+ \left[1 + \frac{\partial g}{\partial c}2y_{b/p} + \frac{\partial g}{\partial b}\left(2\hat{V}_N\right)\right]\frac{\Delta\dot{y}_{b/p}}{\Delta^2 + \left(y_{b/p} + g\right)^2}\end{aligned} \tag{7.38}$$

which leads to the following necessary condition for a well defined yaw rate, i.e. existence of the yaw controller,

Condition 7.2. *To have a well defined yaw controller it should hold that*

$$C_r \triangleq 1 + \frac{X(u_r)u_{rd}}{u_{rd}^2 + v_r^2} - \frac{\partial g}{\partial a}\frac{2v_r X(u_r)\Delta}{\Delta^2 + \left(y_{b/p} + g\right)^2} \neq 0. \tag{7.39}$$

for all time after entering the tube.

Remark 7.3. The condition above can be verified for any positive velocity, for the vehicles considered in this thesis. Note that for most vessels this condition is verifiable since standard ship design practices will result in similar properties of the function $X(u_r)$. Besides having a lower bound greater then zero C_r is also upper-bounded since the term between brackets can be verified to be bounded in its arguments.

Since $\dot{\psi}_d$ depends on the unknown signal $\tilde{V}_N$ we cannot take $\dot{\psi}_d = r_d$. To define an expression for r_d without requiring the knowledge of $\tilde{V}_N$ we use (7.38) to define

$$\begin{aligned}r_d \triangleq -\frac{1}{C_r}&\left[\kappa(\theta)\left(\frac{u_t\cos(\psi + \beta - \gamma_p(\theta)) + k_\delta x_{b/p} + \hat{V}_T}{1 - \kappa(\theta)y_{b/p}}\right)\right. \\ &+ \frac{Y(u_r)v_r u_{rd} - \dot{u}_{rd}v_r}{u_{rd}^2 + v_r^2} + \frac{\Delta}{\Delta^2 + \left(y_{b/p} + g\right)^2}\left[\dot{\hat{V}}_N\frac{b + \sqrt{b^2 - ac}}{-a}\right. \\ &+ \frac{\partial g}{\partial a}\left(2\hat{V}_N\dot{\hat{V}}_N - 2u_{rd}\dot{u}_{rd} - 2v_r Y(u_r)v_r\right) + \frac{\partial g}{\partial b}\left(2\dot{\hat{V}}_N y_{b/p}\right) \\ &\left.\left.+ \left[1 + \frac{\partial g}{\partial c}2y_{b/p} + \frac{\partial g}{\partial b}2\hat{V}_N\right]\left(\frac{-u_{td}y_{b/p}}{\sqrt{\Delta^2 + (y_{b/p} + g)^2}} + G_1(\cdot)\right)\right]\right]\end{aligned} \tag{7.40}$$

which results in the following yaw angle error dynamics

$$\dot{\tilde{\psi}} = C_r\tilde{r} + \left[1 + \frac{\partial g}{\partial c}2y_{b/p} + \frac{\partial g}{\partial b}\left(2\hat{V}_N\right)\right]\frac{\Delta\tilde{V}_N}{\Delta^2 + \left(y_{b/p}+g\right)^2} \tag{7.41}$$

where $\tilde{r} \triangleq r - r_d$ is the yaw rate error. From (7.41) it can be seen that choosing r_d as in (7.40) results in yaw angle error dynamics that have a term dependent on the yaw rate error $\tilde{r}$ and a perturbing term that vanishes when the estimation error $\tilde{V}_N$ goes to zero.

To add acceleration feedforward to the yaw rate controller, the derivative of r_d needs to be calculated. However, when we analyse the dependencies of r_d we obtain

$$r_d = r_d(h, y_{b/p}, x_{b/p}, \tilde{\psi}, \tilde{x}, \tilde{y}), \tag{7.42}$$

where $h = [\theta, v_r, u_r, u_{rd}, \dot{u}_{rd}, \hat{V}_T, \hat{V}_N]^T$ is introduced for the sake of brevity and represents all the variables whose derivatives do not contain $\tilde{V}_N$ or $\tilde{V}_T$. Consequently, the acceleration feedforward cannot be taken as $\dot{r}_d$ since using (7.42), (7.9), and (7.10) it is straightforward to verify this signal contains the unknowns $\tilde{V}_T$ and $\tilde{V}_N$. Therefore we define the yaw rate controller in terms of only known signals as:

$$\begin{aligned}\tau_r = &- F(u_r, v_r, r) + \frac{\partial r_d}{\partial h^T}\dot{h} + \frac{\partial r_d}{\partial y_{b/p}}\left(-u_{td}\frac{y_{b/p}}{\sqrt{\Delta^2 + (y_{b/p}+g)^2}} + G_1(\cdot)\right) \\ &+ \frac{\partial r_d}{\partial x_{b/p}}\left(-k_\delta x_{b/p}\right) + \frac{\partial r_d}{\partial \tilde{\psi}}C_r\tilde{r} - \frac{\partial r_d}{\partial \tilde{x}}k_x\tilde{x} - \frac{\partial r_d}{\partial \tilde{y}}k_y\tilde{y} - k_1\tilde{r} - k_2\tilde{\psi}\end{aligned} \tag{7.43}$$

Using (7.43) in (7.1f) we then obtain the yaw rate error dynamics

$$\begin{aligned}\dot{\tilde{r}} = &- k_1\tilde{r} - k_2C_r\tilde{\psi} - \frac{\partial r_d}{\partial \tilde{\psi}}\left[1 + \frac{\partial g}{\partial c}2y_{b/p} + \frac{\partial g}{\partial b}\left(2\hat{V}_N\right)\right]\frac{\Delta\tilde{V}_N}{\Delta^2 + \left(y_{b/p}+g\right)^2} \\ &- \frac{\partial r_d}{\partial y_{b/p}}\tilde{V}_N - \frac{\partial r_d}{\partial x_{b/p}}\tilde{V}_T + \frac{\partial r_d}{\partial \tilde{x}}\tilde{V}_x + \frac{\partial r_d}{\partial \tilde{y}}\tilde{V}_y\end{aligned} \tag{7.44}$$

which has a term depending on the yaw angle error, a term depending on the yaw rate error, and perturbing terms depending on the unknown ocean current estimation error.

Remark 7.4. It is straightforward to verify that all the terms in (7.35) are smooth fractionals that are bounded with respect to ($y_{b/p}$, $x_{b/p}$, $\tilde{x}$, $\tilde{y}$, $\tilde{\psi}$) or are periodic functions with linear arguments and consequently the partial derivatives (7.43) and (7.44) are all bounded. This is something that is used when showing closed-loop stability in the next section.

7.4 Closed-Loop Analysis

In this section we analyse the closed-loop system of the model (7.1) with controllers (7.11) and (7.43) and observer (7.13) when the frame propagates with (7.8) along

the path P. To show that path following is achieved we have to show that the following error dynamics converge to zero

$$\dot{x}_{b/p} = -k_\delta x_{b/p} + \tilde{V}_T \tag{7.45a}$$

$$\dot{y}_{b/p} = -u_{td}\frac{y_{b/p}}{\sqrt{\Delta^2 + (y_{b/p}+g)^2}} + G_1(\cdot) + \tilde{V}_N \tag{7.45b}$$

$$\dot{\tilde{\psi}} = C_r\tilde{r} + \left[1 + \frac{\partial g}{\partial c}2y_{b/p} + \frac{\partial g}{\partial b}\left(2\hat{V}_N\right)\right]\frac{\Delta\tilde{V}_N}{\Delta^2 + \left(y_{b/p}+g\right)^2} \tag{7.45c}$$

$$\begin{aligned}\dot{\tilde{r}} = &-k_1\tilde{r} - k_2C_r\tilde{\psi} - \frac{\partial r_d}{\partial y_{b/p}}\tilde{V}_N - \frac{\partial r_d}{\partial x_{b/p}}\tilde{V}_T + \frac{\partial r_d}{\partial \tilde{x}}\tilde{V}_x + \frac{\partial r_d}{\partial \tilde{y}}\tilde{V}_y \\ &- \frac{\partial r_d}{\partial \tilde{\psi}}\left[1 + \frac{\partial g}{\partial c}2y_{b/p} + \frac{\partial g}{\partial b}\left(2\hat{V}_N\right)\right]\frac{\Delta\tilde{V}_N}{\Delta^2 + \left(y_{b/p}+g\right)^2}\end{aligned} \tag{7.45d}$$

$$\dot{\tilde{u}} = -\left(k_u + \frac{d_{11}}{m_{11}}\right)\tilde{u} \tag{7.45e}$$

The system (7.45) has the following perturbed form:

$$\dot{\tilde{X}} \triangleq \begin{bmatrix}\dot{x}_{b/p}\\ \dot{y}_{b/p}\\ \dot{\tilde{\psi}}\\ \dot{\tilde{r}}\\ \dot{\tilde{u}}\end{bmatrix} = \begin{bmatrix}-k_\delta x_{b/p}\\ -u_{td}\frac{y_{b/p}}{\sqrt{\Delta^2+(y_{b/p}+g)^2}} + G_1(\cdot)\\ C_r\tilde{r}\\ -k_1\tilde{r} - k_2C_r\tilde{\psi}\\ -k_3\tilde{u}\end{bmatrix} + \begin{bmatrix}\tilde{V}_T\\ \tilde{V}_N\\ \left[1 + \frac{\partial g}{\partial c}2y_{b/p} + \frac{\partial g}{\partial b}\left(2\hat{V}_N\right)\right]\frac{\Delta\tilde{V}_N}{\Delta^2+\left(y_{b/p}+g\right)^2}\\ -\frac{\partial r_d}{\partial \boldsymbol{p}_{b/p}}\begin{bmatrix}\tilde{V}_T\\ \tilde{V}_N\end{bmatrix} - \frac{\partial r_d}{\partial \tilde{\psi}}\left[1 + \frac{\partial g}{\partial c}2y_{b/p} + \frac{\partial g}{\partial b}2\hat{V}_N\right]\frac{\Delta\tilde{V}_N}{\Delta^2+\left(y_{b/p}+g\right)^2} - \frac{\partial r_d}{\partial \boldsymbol{p}_{\tilde{b}/p}}\tilde{\boldsymbol{V}}_c\\ 0\end{bmatrix} \tag{7.46}$$

where $\boldsymbol{p}_{b/p} \triangleq [x_{b/p}, y_{b/p}]^T$ and all the perturbing terms disappear as the current estimates converge to zero. In particular, we cannot apply our desired control action whilst the current estimates have not converged yet, since the current cannot be compensated for until it is estimated correctly.

The full closed-loop system of the model (7.1) with controllers (7.11) and (7.43) and observer (7.13) is given by

$$\dot{\tilde{X}}_1 \triangleq \begin{bmatrix}\dot{y}_{b/p}\\ \dot{\tilde{\psi}}\\ \dot{\tilde{r}}\end{bmatrix} = \begin{bmatrix}-u_{td}\frac{y_{b/p}}{\sqrt{\Delta^2+(y_{b/p}+g)^2}} + G_1(\cdot)\\ C_r\tilde{r}\\ -k_1\tilde{r} - k_2C_r\tilde{\psi}\end{bmatrix} +$$

$$\begin{bmatrix} \tilde{V}_N \\ \left[1+\frac{\partial g}{\partial c}2y_{b/p}+\frac{\partial g}{\partial b}\left(2\hat{V}_N\right)\right]\frac{\Delta\tilde{V}_N}{\Delta^2+\left(y_{b/p}+g\right)^2} \\ -\frac{\partial r_d}{\partial \boldsymbol{p}_{b/p}}\begin{bmatrix}\tilde{V}_T\\ \tilde{V}_N\end{bmatrix}-\frac{\partial r_d}{\partial \psi}\left[1+\frac{\partial g}{\partial c}2y_{b/p}+\frac{\partial g}{\partial b}2\hat{V}_N\right]\frac{\Delta\tilde{V}_N}{\Delta^2+\left(y_{b/p}+g\right)^2}-\frac{\partial r_d}{\partial \bar{\boldsymbol{p}}}\tilde{\boldsymbol{V}}_c \end{bmatrix} \tag{7.47a}$$

$$\dot{\tilde{X}}_2 \triangleq \begin{bmatrix} \dot{x}_{b/p} \\ \dot{\tilde{x}} \\ \dot{\tilde{y}} \\ \dot{\tilde{V}}_x \\ \dot{\tilde{V}}_y \\ \dot{\tilde{u}} \end{bmatrix} = \begin{bmatrix} -k_\delta x_{b/p}+\tilde{V}_T \\ -k_x\tilde{x}-\tilde{V}_x \\ -k_y\tilde{y}-\tilde{V}_y \\ -k_{x1}\tilde{x} \\ -k_{y1}\tilde{y} \\ -k_u\tilde{u} \end{bmatrix} \tag{7.47b}$$

$$\dot{v}_r = X(u_{rd}+\tilde{u})r_d(h, y_{b/p}, x_{b/p}, \tilde{\psi}, \tilde{x}, \tilde{y}) + X(u_{rd}+\tilde{u})\tilde{r} + Y(u_{rd}+\tilde{u})v_r \tag{7.47c}$$

Before starting with the stability analysis of (7.47), we first establish GES of (7.47b) by using the following lemma.

Lemma 7.1. *The system* (7.47b) *is GES.*

Proof. Note that (7.47b) is a cascaded system of the form

$$\dot{x}_{b/p} = -k_\delta x_{b/p} + \tilde{V}_T, \tag{7.48a}$$

$$\begin{bmatrix} \dot{\tilde{x}} \\ \dot{\tilde{y}} \\ \dot{\tilde{V}}_x \\ \dot{\tilde{V}}_y \\ \dot{\tilde{u}} \end{bmatrix} = \begin{bmatrix} -k_x\tilde{x}-\tilde{V}_x \\ -k_y\tilde{y}-\tilde{V}_y \\ -k_{x1}\tilde{x} \\ -k_{y1}\tilde{y} \\ -k_u\tilde{u} \end{bmatrix}. \tag{7.48b}$$

The nominal dynamics of (7.48) are given by $\dot{x}_{b/p} = -k_\delta x_{b/p}$ from (7.48a), which is a stable linear system and thus GES. The perturbing dynamics are given by (7.48b) and where shown to be GES in Section 7.3. The interconnection term is the term $\tilde{V}_T$ from (7.48a). The growth of the interconnection term can be bounded by $\|\tilde{V}_T\| \leq \|[\tilde{V}_x, \tilde{V}_y]^T\|$, which satisfies the condition for the interconnection term from Theorem A.3. Note that it is trivial to shown the nominal dynamics admit the quadratic Lyapunov function $V_{x_{b/p}} = 1/2x_{b/p}^2$. Consequently, all the conditions of Theorem A.3 and Proposition A.1 are satisfied. Therefore, the cascaded system (7.48) is GES, which implies that (7.47b) is GES. □

Note that although we show that the system (7.47b) is GES, the dynamics of $x_{b/p}$ are only defined in the tube to avoid the singularity in the parametrisation. Hence, the stability result is only valid in the tube.

The first step in the stability analysis of (7.47) is to assure that the closed-loop system is forward complete and that the sway velocity v_r remains bounded. Therefore, under the assumption that Condition 7.1-7.2 are satisfied, i.e. $1-\kappa(\theta)y_{b/p} \neq 0$ and $C_r \neq 0$, we take the following three steps:

1. First, we prove that the trajectories of the closed-loop system are forward complete.

2. Then, we derive a necessary condition such that v_r is locally bounded with respect to $(\tilde{X}_1, \tilde{X}_2)$.

3. Finally, we establish that for a sufficiently big value of Δ, v_r is locally bounded only with respect to $\tilde{X}_2$.

The above three steps are taken by formulation and proving three lemmas. For the sake of brevity in the main body of this chapter the proofs of the following lemmas are replaced by a sketch of each proof in the main body. The full proofs can be found in the Appendices 7.A-7.C.

Lemma 7.2 (Forward completeness)**.** *The trajectories of the global closed-loop system* (7.47) *are forward complete.*

The proof of this lemma is given in Appendix 7.A. The general idea is as follows. Forward completeness for (7.47b) is evident since this part of the closed-loop system consists of GES error dynamics. Using the forward completeness and in fact boundedness of (7.47b) we can show forward completeness of (7.47c), $\dot{\tilde{\psi}}$, and $\dot{\tilde{r}}$. Hence, forward completeness of (7.47) depends on forward completeness of $\dot{y}_{b/p}$. To show forward completeness of $\dot{y}_{b/p}$, we consider the $y_{b/p}$ dynamics with $\tilde{X}_2$, $\tilde{\psi}$, $\tilde{r}$, and v_r as input, which allows us to claim forward completeness of $\dot{y}_{b/p}$ according to Theorem A.6. Consequently, all the states of the closed-loop system are forward complete and hence the closed-loop system (7.47) is forward complete

Lemma 7.3 (Boundedness near $(\tilde{X}_1, \tilde{X}_2) = 0$)**.** *The system* (7.47c) *is bounded near* $(\tilde{X}_1, \tilde{X}_2) = 0$ *if and only if the curvature of* P *satisfies the following condition:*

$$\kappa_{\max} \triangleq \max_{\theta \in P} |\kappa(\theta)| < \frac{Y_{\min}}{X_{\max}}. \tag{7.49}$$

The proof of this lemma is given in Appendix 7.B. A sketch of the proof is as follows. The sway velocity dynamics (7.47c) are analysed using a quadratic Lyapunov function $V = 1/2 v_r^2$. It can be shown that the derivative of this Lyapunov function satisfies the conditions for boundedness when the solutions are on or close to the manifold where $(\tilde{X}_1, \tilde{X}_2) = 0$. Consequently, (7.47c) satisfies the conditions of boundedness near $(\tilde{X}_1, \tilde{X}_2) = 0$ as long as (7.49) is satisfied.

In Lemma 7.3 we show boundedness of v_r for small values of $(\tilde{X}_1, \tilde{X}_2)$ to derive the bound on the curvature. However, locality with respect to $\tilde{X}_1$, i.e. the path-following errors and yaw angle and yaw rate errors, is not desired and in the next lemma boundedness independent of $\tilde{X}_1$ is shown under an extra condition on the look-ahead distance Δ.

Lemma 7.4 (Boundedness near $\tilde{X}_2 = 0$)**.** *If the following additional assumption is satisfied:*

$$\exists\ \sigma > 0 \text{ s.t. } \quad 1 - \kappa(\theta) y_{b/p} \geq \sigma > 0 \quad \wedge \quad \left[Y_{\min} - X_{\max} \kappa_{\max} \frac{1}{\sigma} \right] > 0 \tag{7.50}$$

the system (7.47c) *is bounded only near* $\tilde{X}_2 = 0$ *if we have*

$$\Delta > \frac{4X_{\max}}{\left[Y_{\min} - X_{\max}\kappa_{\max}\frac{1}{\sigma}\right]} \tag{7.51}$$

$$\kappa_{\max} < \sigma\frac{Y_{\min}}{X_{\max}} \tag{7.52}$$

Remark 7.5. The size of σ can be calculated by using the following tuning procedure.

1. Start by calculating the absolute bound on the curvature from Lemma 7.3. This is a bound that is necessary for feasibility of the trajectories.
2. Now choose a positive Δ and using the maximum curvature of the path, solve (7.51) to obtain a possible value for σ.
3. Using the value for σ obtained in the previous step and the maximum value of the curvature we can use the inequality $1 - \kappa(\theta)y_{b/p} \geq \sigma$ from (7.50) to calculate the size of the tube as

$$y_{b/p}^{\text{tube}} = \frac{1-\sigma}{\kappa_{\max}}. \tag{7.53}$$

If initial conditions are within the tube $y_{b/p}^{\text{tube}}$, and are chosen such that the transient caused by the unknown current does not force the vessel out of the tube. Then the sway velocity is bounded for all time. Note that the choice of Δ in step two given above determines how large the tube will be. More specifically, a larger choice for Δ will result in a smaller value for σ which will lead to a larger tube in step three. However, due to the nature of the guidance a larger Δ will mean slower steering and consequently slower convergence to the path.

The proof of Lemma 7.4 is given in Appendix 7.C, the general idea is given as follows. The proof follows along the same lines of that of Lemma 7.3 but solutions are considered close to the manifold $\tilde{X}_2 = 0$ rather than $(\tilde{X}_1, \tilde{X}_2) = 0$. It is shown that boundedness can still be shown if (7.51) is satisfied additionally to the conditions of Lemma 7.3.

Theorem 7.5. *Consider a* θ*-parametrised path denoted by* $P(\theta) \triangleq (x_p(\theta), y_p(\theta))$. *Then under Conditions 7.1-7.2 and the conditions of Lemma 7.2-7.4, the system* (7.1) *with control laws* (7.11) *and* (7.43) *and observer* (7.13) *follows the path* P, *while maintaining* v_r, τ_r *and* τ_u *bounded. In particular, the origin of the system* (7.47a)-(7.47b) *is exponentially stable in the tube.*

Proof. From the fact that the origin of (7.47b) is GES, the fact that the closed-loop system (7.47) is forward complete according to Lemma 7.2, and the fact that solutions of (7.47c) are locally bounded near $\tilde{X}_2 = 0$ according to Lemma 7.4, we can conclude that there is a finite time $T > t$ after which solutions of (7.47b) will be sufficiently close to $\tilde{X}_2 = 0$ to guarantee boundedness of v_r.

Having established that v_r is bounded we first analyse the cascade

$$\begin{bmatrix} \dot{\tilde{\psi}} \\ \dot{\tilde{r}} \end{bmatrix} = \begin{bmatrix} C_r \tilde{r} \\ -k_1 \tilde{r} - k_2 C_r \tilde{\psi} \end{bmatrix} + \begin{bmatrix} G_2(\cdot) \\ -\frac{\partial r_d}{\partial \tilde{\psi}} G_2(\cdot) - \frac{\partial r_d}{\partial \boldsymbol{p}_{b/p}} [\tilde{V}_T, \tilde{V}_N]^T + \frac{\partial r_d}{\partial [\tilde{x}, \tilde{y}]^T} \tilde{\boldsymbol{V}}_c \end{bmatrix} \tag{7.54a}$$

$$\begin{bmatrix} \dot{x}_{b/p} \\ \dot{\tilde{x}} \\ \dot{\tilde{y}} \\ \dot{\tilde{V}}_x \\ \dot{\tilde{V}}_y \\ \dot{\tilde{u}} \end{bmatrix} = \begin{bmatrix} -k_\delta x_{b/p} + \tilde{V}_T \\ -k_x \tilde{x} - \tilde{V}_x \\ -k_y \tilde{y} - \tilde{V}_y \\ -k_{x1} \tilde{x} \\ -k_{y1} \tilde{y} \\ -k_u \tilde{u} \end{bmatrix} \tag{7.54b}$$

The perturbing system (7.54b) is GES as shown in Lemma 7.1. The interconnection term, i.e. the second and third term in (7.54a), satisfies the linear growth criteria from Theorem A.3. More specifically, it does not grow with the $\tilde{\psi}$ and $\tilde{r}$ since all the partial derivatives of r_d and g can be bounded by constants. The nominal dynamics, i.e. the first matrix in (7.54a), can be analysed with the following quadratic Lyapunov function

$$V_{(\tilde{r},\tilde{\psi})} = \frac{1}{2}\tilde{r}^2 + \frac{1}{2}k_2\tilde{\psi}^2 \tag{7.55}$$

whose derivative along the solutions of the nominal system is given by

$$\dot{V}_{(\tilde{r},\tilde{\psi})} = -k_1\tilde{r}^2 - k_2 C_r \tilde{\psi}\tilde{r} + k_2 C_r \tilde{r}\tilde{\psi} = -k_2\tilde{r}^2 \leq 0 \tag{7.56}$$

which implies that $\tilde{r}$ and $\tilde{\psi}$ are bounded. The derivative of (7.56) is given by

$$\ddot{V}_{(\tilde{r},\tilde{\psi})} = -2k_1^2\tilde{r}^2 - 2k_1 k_2 C_r \tilde{\psi}\tilde{r} \tag{7.57}$$

which is bounded since $\tilde{r}$ and $\tilde{\psi}$ are bounded. This implies that (7.56) is a uniformly continuous function. Consequently, by applying Barbalat's lemma (see Lemma A.7) we have that

$$\lim_{t\to\infty} \dot{V}_{(\tilde{r},\tilde{\psi})} = \lim_{t\to\infty} -k_1\tilde{r}^2 = 0 \;\Rightarrow\; \lim_{t\to\infty} \tilde{r} = 0. \tag{7.58}$$

Since C_r is persistently exciting, which follows from the fact that C_r is upper bounded and lower bounded by a constant larger then zero, it follows from the expression of the nominal dynamics that

$$\lim_{t\to\infty} \tilde{r} = 0 \;\Rightarrow\; \lim_{t\to\infty} \tilde{\psi} = 0. \tag{7.59}$$

This implies that the system is globally asymptotically stable according to Definition A.3 and since the nominal dynamics are linear it follows that the nominal dynamics are globally exponentially stable. Consequently, from the above it follows that the cascade (7.54) is GES using Theorem A.3 and Proposition A.1.

We now consider the following dynamics

$$\dot{y}_{b/p} = -u_{td}\frac{y_{b/p}}{\sqrt{\Delta^2 + (y_{b/p} + g)^2}} + \tilde{V}_N + G_1(\cdot). \tag{7.60}$$

Note that we can view the systems (7.54) and (7.60) as a cascaded system where the nominal dynamics are formed by the first term of (7.60), the interconnection term is given by second matrix of (7.60), and the perturbing dynamics are given by (7.54). As we have just shown the perturbing dynamics are GES. Using the bound on $G_1(\cdot)$ from (7.29) it is straightforward to verify that the interconnection term satisfies the conditions of Theorem A.3. We now consider the following Lyapunov function for the nominal system

$$V_{y_{b/p}} = \frac{1}{2} y_{b/p}^2. \tag{7.61}$$

whose derivative along the solutions of the nominal system is given by

$$\dot{V}_{y_{b/p}} = -u_{td} \frac{y_{b/p}^2}{\sqrt{\Delta^2 + (y_{b/p} + g)^2}} \leq 0, \tag{7.62}$$

which implies that the nominal system is GAS. Moreover, since it is straightforward to verify that $\dot{V}_{y_{b/p}} \leq \alpha V_{y_{b/p}}$ for some constant α dependent on initial conditions, it follows from the comparison lemma (Lemma A.5) that the nominal dynamics are also LES. Consequently, the cascaded system satisfies the conditions of Theorem A.3 and Lemma A.4, and therefore the cascaded system is GAS and LES. This implies that the origin of the error dynamics, i.e. $(\tilde{X}_1, \tilde{X}_2) = (0, 0)$, is globally asymptotically stable and locally exponentially stable. However, since the parametrisation is only valid locally we can only claim exponential stability in the tube. □

7.5 Case Study

This section presents a case study to verify the theoretical results presented in this chapter. The case study under consideration is following of a circular path using the model of an underactuated surface vessel from Fredriksen and Pettersen [63], the parameters of which are given in Section C.1. The ocean current components are given by $V_x = -1$ [m/s] and $V_y = 1.2$ [m/s] and consequently $V_{\max} \approx 1.562$ [m/s]. The desired relative surge velocity is chosen to be constant and set to $u_{rd} = 5$ [m/s] such that Assumption 7.3 is verified. Using the ship's model parameters from Section C.1 and the expressions (7.2c) and (7.2d) it is straightforward to see that the curvature bound from Lemma 7.3 is given by $\kappa_{\max} < (Y_{\min})/(X_{\max}) \approx 0.1333$. The observer is initialised as suggested in Subsection 7.3.2 and the observer gains are selected as $k_{x_1} = k_{y_1} = 1$ and $k_{x_1} = k_{y_1} = 0.1$. The controller gains are selected as $k_{u_r} = 0.1$ for the surge velocity controller and $k_1 = 1000$ and $k_2 = 400$ for the yaw rate controller.

In this case study the vessel is required to follow a circle with a radius of 400 [m] that is centred around the origin. Consequently, the curvature of the path is given by $\kappa_p = 1/400 = 0.0025$. To choose the parameters of the guidance law we will now follow the tuning procedure lined out in Remark 7.5. In the first step we verify that the feasibility constraint on the curvature is satisfied for the path under consideration, which is clearly the case since $\kappa_p < (Y_{\min})/(X_{\max}) \approx 0.133$. In the second step we fix our Δ as $\Delta = 40$ [m], which results in $\sigma \approx 0.0268$. In

the third step we use the value for σ to calculate the size of the tube as $y_{b/p}^{\text{tube}} \approx 369.983$ [m]. Note that this is only slightly smaller then the size of the tube where the parametrisation is valid, i.e. 400 [m]. To stay within this tube we choose the initial conditions as

$$[u_r(t_0), v_r(t_0), r(t_0), x(t_0), y(t_0), \psi(t_0)]^T = [0, 0, 0, 700, 10, \pi/2]^T. \tag{7.63}$$

The resulting trajectory for the vessel can be seen in Figure 7.3. The blue dashed line is the trajectory of the vessel and the red circle is the reference path. The yellow vessels represent the orientation of the vessel at certain instances. From the plot in Figure 7.3 it can be seen that the vessel converges to the circle and starts to follow the path. Moreover, it can be seen from the yellow vessels that the orientation of the ship is not tangential to the circle which is necessary to compensate for the ocean current.

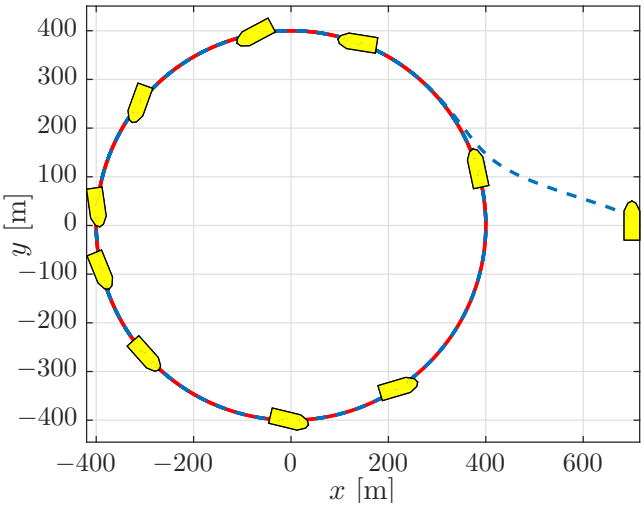

Figure 7.3: Path of the vessel in the $x - y$-plane. The dashed blue line is the trajectory of the path and the red line is the reference. The yellow ships denote the orientation of the vessel at certain times.

The path-following errors can be seen in the top plot of Figure 7.4 which confirm that the path-following errors converge to zero. A detail of the steady-state is given to show the reduction of the error. Moreover, note that because of the choice of parametrisation the error in tangential direction $x_{b/p}$ is zero throughout the motion except from a very small transient at the beginning caused by the transient of the observer. The estimates obtained from the ocean current observer can be seen in the second plot from the top in Figure 7.4. From this plot it can be seen that the estimates converge exponentially with no overshoot. This underlines the conservativeness of the bound from Assumption 7.3 that is required for the error bound for the observer as explained in Subsection 7.3.2. The third plot in Figure

7.4 depicts the yaw rate and the sway velocity induced by the motion. It can be seen that these do not converge to zero but converge to a periodic motion. Note that for circular motion in the absence of current the yaw rate would converge to zero. However, when current is present the vessel needs to change its turning rate depending on if it goes with or against the current. The relative surge velocity is given in the fourth plot from the top in Figure 7.4 and shows that the surge velocity converges exponentially to the desired value. This plot is especially interesting in combination with the plot of the magnitude of C_r given at the bottom of Figure 7.4. From this plot it can clearly be seen that Condition 7.2 is verified both in steady-state and during the transient of the velocity controller.

7.6 Conclusion

This chapter considered curved-path following for underactuated marine vessels in the presence of constant ocean currents. In this approach the path is parametrised by a path variable with a update law that is designed to keep the vessel on the normal of a path-tangential reference frame. This assures the path-following error is defined as the shortest distance to the path. However, the disadvantage is that this type of update law has a singularity which only allows for local results. The vessel is steered using a line-of-sight guidance law, which to compensate for the unknown ocean currents is aided by an ocean current observer. The closed-loop system with the controllers and observer was analysed. This was done by first showing boundedness of the underactuated sway velocity dynamics under certain conditions. It was then shown that if these conditions are satisfied and the sway velocity is bounded the path-following errors are exponentially stable within the tube. Due to the singularity the feasibility of this problem depends on the initial conditions, the curvature of the path, and the magnitude of the ocean current. More specifically, the size of the tube in which the parametrisation is well defined was shown to be a function of the maximal curvature of the path. This implies that the combination of curvature and ocean current should be such that a suitable set of initial conditions exists for which the transient of the ocean current observer does not take the vessel out of the tube.

7.A Proof of Lemma 7.2

Consider the following part of the global closed-loop system:

$$\begin{bmatrix} \dot{\tilde{\psi}} \\ \dot{\tilde{r}} \end{bmatrix} = \begin{bmatrix} C_r \tilde{r} \\ -k_1 \tilde{r} - k_2 C_r \tilde{\psi} \end{bmatrix} + \underbrace{\begin{bmatrix} \left[1 + \frac{\partial g}{\partial c} 2 y_{b/p} + \frac{\partial g}{\partial b}\left(2\hat{V}_N\right)\right] \frac{\Delta \tilde{V}_N}{\Delta^2 + \left(y_{b/p}+g\right)^2} \\ -\frac{\partial r_d}{\partial \boldsymbol{p}_{b/p}} \begin{bmatrix} \tilde{V}_T \\ \tilde{V}_N \end{bmatrix} - \frac{\partial r_d}{\partial \tilde{\psi}} \left[1 + \frac{\partial g}{\partial c} 2 y_{b/p} + \frac{\partial g}{\partial b} 2\hat{V}_N\right] \frac{\Delta \tilde{V}_N}{\Delta^2 + \left(y_{b/p}+g\right)^2} - \frac{\partial r_d}{\partial \tilde{\boldsymbol{p}}_{b/p}} \tilde{\boldsymbol{V}}_c \end{bmatrix}}_{R(h, y_{b/p}, x_{b/p}, \tilde{\psi}, \tilde{x}, \tilde{y})} \tag{7.64a}$$

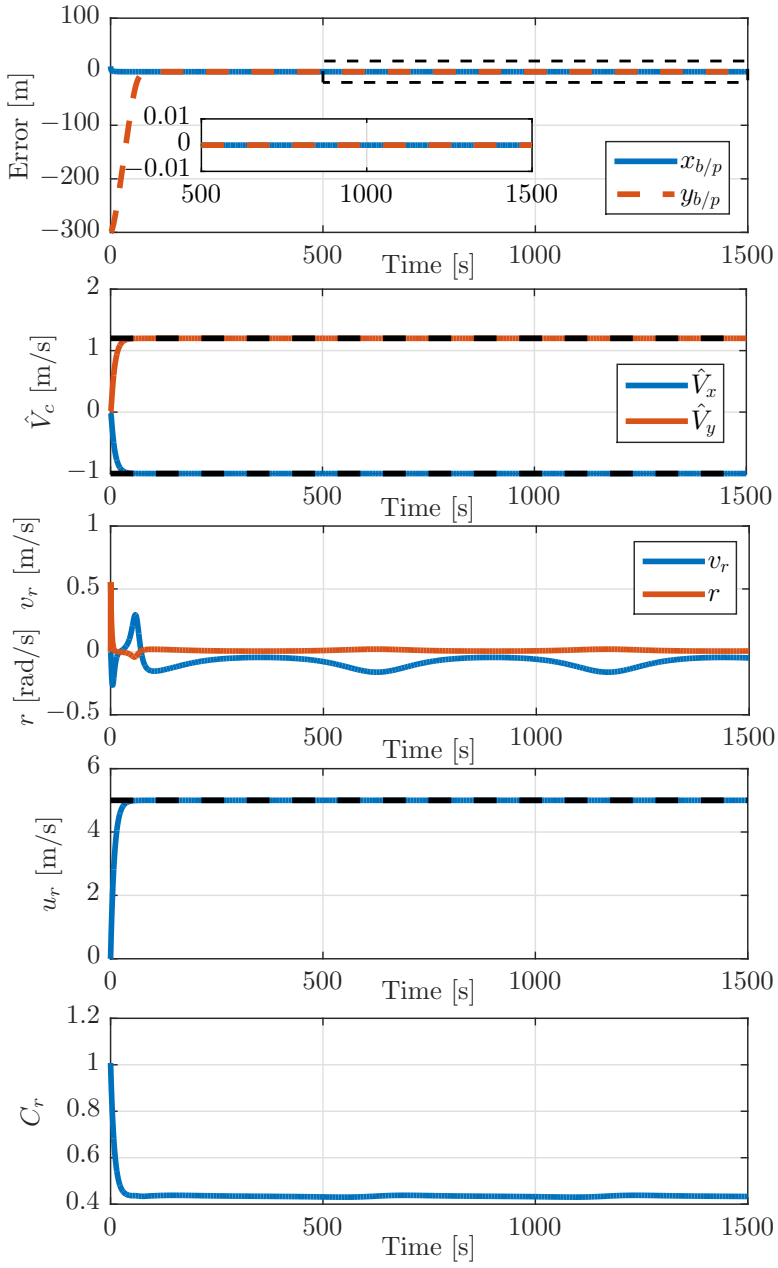

Figure 7.4: Path following errros plotted agains time (top), current estimates against time (second), sway velocity and yaw rate against time (third), surge velocity against time (fourth), and size of C_r over time (bottom).

$$\dot{v}_r = X(u_{rd}+\tilde{u})r_d(h, y_{b/p}, x_{b/p}, \tilde{\psi}, \tilde{x}, \tilde{y}) + X(u_{rd}+\tilde{u})\tilde{r} + Y(u_{rd}+\tilde{u})v_r \quad (7.64b)$$

From the boundedness of the vector $[\tilde{X}_2^T, \kappa(\theta), u_{rd}, \dot{u}_{rd}, V_T, V_N]^T$ we know that $\left\|[\tilde{X}_2^T, \kappa(\theta), u_{rd}, \dot{u}_{rd}, V_T, V_N]^T\right\| \leq \beta_0$, and from (7.40) we can conclude the existence of positive functions $a_{r_d}(\cdot)$, $b_{r_d}(\cdot)$, $a_R(\cdot)$, and $b_R(\cdot)$ which are all continuous in their arguments and are such that such the following inequalities hold:

$$|r_d(\cdot)| \leq a_{r_d}(\Delta, \beta_0)\,|v_r| + b_{r_d}(\Delta, \beta_0) \quad (7.65)$$

and,

$$\|R(\cdot)\| \leq a_R(\Delta, \beta_0)\,|v_r| + b_R(\Delta, \beta_0) \quad (7.66)$$

Then taking the following Lyapunov function candidate:

$$V_1(\tilde{\psi}, \tilde{r}, v_r) = \frac{1}{2}\left(k_2\tilde{\psi}^2 + \tilde{r}^2 + v_r^2\right) \quad (7.67)$$

whose time derivative along the solutions of (7.64) is

$$\begin{aligned}\dot{V}_1(\cdot) = {} & k_2 C_r \tilde{r}\tilde{\psi} - k_1\tilde{r}^2 - k_2 C_r \tilde{r}\tilde{\psi} + [\tilde{\psi} \;\; \tilde{r}]R(\cdot) + Y(u_{rd}+\tilde{u})v_r^2 \\ & + X(u_{rd}+\tilde{u})\tilde{r}v_r + X(u_{rd}+\tilde{u})r_d(\cdot)v_r\end{aligned} \quad (7.68)$$

Using Young's inequality we note that

$$\begin{aligned}\dot{V}_1(\cdot) \leq {} & k_1\tilde{r}^2 + \tilde{\psi}^2 + \tilde{r}^2 + R^2(\cdot) + Y(u_{rd}+\tilde{u})v_r^2 \\ & + |X(u_{rd}+\beta_0)|\left(\tilde{r}^2 + v_r^2\right) + |X(u_{rd}+\beta_0)|\left(r_d^2(\cdot) + v_r^2\right) \\ \leq {} & \alpha V + \beta,\ \alpha \geq 0,\ \beta \geq 0\end{aligned} \quad (7.69)$$

Note that since the differential inequality (7.69) is scaler we can invoke the comparison lemma Khalil [82, Lemma 3.4] given as Lemma A.5 in Appendix A. From Lemma A.5 we know that the solutions of differential inequality (7.69) are bounded by the solutions of the linear system:

$$\dot{x} = \alpha x + \beta \quad (7.70)$$

which has solutions

$$x(t) = \frac{\|x(t_0)\|\alpha + \beta}{\alpha}e^{\alpha(t-t_0)} - \frac{\beta}{\alpha} \quad (7.71)$$

Hence, from Lemma A.5 we have that

$$V_1(\cdot) \leq \frac{\|V_1(t_0)\|\alpha + \beta}{\alpha}e^{\alpha(t-t_0)} - \frac{\beta}{\alpha} \quad (7.72)$$

which shows the solutions of $V_1(\cdot)$ are defined up to $t_{\max} = \infty$ and consequently from (7.67) it follows that the solutions of $\tilde{\psi}$, $\tilde{r}$, and v_r must be defined up to $t_{\max} = \infty$. Hence, the solutions of (7.64) satisfy Definition A.7 and we can conclude forward completeness of trajectories of (7.64).

The forward completeness of trajectories of the global closed-loop system now depends on forward completeness of $\dot{y}_{b/p}$ from (7.47a). We can conclude forward completeness of $\dot{y}_{b/p}$ by considering the Lyapunov function

$$V_2 = \frac{1}{2} y_{b/p}^2. \tag{7.73}$$

The time derivative of (7.73) is given by

$$\begin{aligned} \dot{V}_2 &= y_{b/p} \dot{y}_{b/p} \\ &\leq -u_{td} \frac{y_{b/p}}{\sqrt{\Delta^2 + (y_{b/p} + g)^2}} + (G_1(\cdot) + \tilde{V}_N) y_{b/p} \\ &\leq (G_1(\cdot) + \tilde{V}_N) y_{b/p} \end{aligned} \tag{7.74}$$

where using the bound on $G_1(\cdot)$ from (7.29) and Young's inequality we obtain

$$\dot{V}_2 \leq V_2 + \frac{1}{2} \left(\zeta^2(\dot{\gamma}_p(\theta), u_{td}) \| [\tilde{\psi}, \tilde{r}, x_{b/p}]^T \|^2 + \tilde{V}_N^2 \right) \tag{7.75}$$

$$\leq V_2 + \sigma_2(v_r, \tilde{\psi}, \tilde{r}, \tilde{V}_N, \tilde{V}_T, x_{b/p}) \tag{7.76}$$

with $\sigma_2(\cdot) \in \mathcal{K}_\infty$. Consequently, if we view the arguments of $\sigma_2(\cdot)$ as input to the $y_{b/p}$ dynamics, then (7.75) satisfies Theorem A.6 and hence $\dot{x}_{b/p}$ and $\dot{y}_{b/p}$ are forward complete. Note that the arguments of $\sigma_2(\cdot)$ are all forward complete and therefore fit the definition of an input signal given in Definition A.7. We have now shown forward completeness of (7.47a) and (7.47c) and since (7.47b) is GES is is trivially forward complete. We can therefore claim forward completeness of the entire closed-loop system (7.47) and the proof of Lemma 7.2 is complete.

7.B Proof of Lemma 7.3

Recall the sway velocity dynamics (7.47c):

$$\dot{v}_r = X(\tilde{u} + u_{rd})(r_d + \tilde{r}) + Y(u_{rd} + \tilde{u}) v_r, \quad Y(u_{rd}) < 0$$

Consider the following Lyapunov function candidate:

$$V_3(v_r) = \frac{1}{2} v_r^2 \tag{7.77}$$

The derivative of (7.77) along the solutions of (7.47c) is given by

$$\begin{aligned} \dot{V}_3 &= v_r \dot{v}_r = v_r X(u_{rd} + \tilde{u}) r_d + X(u_{rd} + \tilde{u}) v_r \tilde{r} + Y(u_{rd} + \tilde{u}) v_r^2 \\ &\leq X(u_{rd}) r_d v_r + a_x \tilde{u} r_d v_r + X(u_{rd}) v_r \tilde{r} + a_x \tilde{u} v_r \tilde{r} + a_y \tilde{u} v_r^2 + Y(u_{rd}) v_r^2 \end{aligned} \tag{7.78}$$

where we used the fact that:

$$Y(u_r) = a_y u_r + b_y \tag{7.79}$$

$$X(u_r) = a_x u_r + b_x \tag{7.80}$$

The term $r_d v_r$ can be bounded as a function of v_r as follows

$$\begin{aligned} r_d v_r = &- \frac{v_r}{C_r}\left[\kappa(\theta)\left(\frac{u_t\cos(\psi+\beta-\gamma_p(\theta))+k_\delta x_{b/p}+\hat{V}_T}{1-\kappa(\theta)y_{b/p}}\right)\right. \\ &+ \frac{Y(u_r)v_r u_{rd}-\dot{u}_{rd}v_r}{u_{rd}^2+v_r^2}+\frac{\Delta}{\Delta^2+\left(y_{b/p}+g\right)^2}\left[\dot{\hat{V}}_N\frac{b+\sqrt{b^2-ac}}{-a}\right. \\ &+ \frac{\partial g}{\partial a}\left(2\hat{V}_N\dot{\hat{V}}_N-2u_{rd}\dot{u}_{rd}-2v_rY(u_r)v_r\right)+\frac{\partial g}{\partial b}\left(2\dot{\hat{V}}_N y_{b/p}\right) \\ &\left.\left.+\left[1+\frac{\partial g}{\partial c}2y_{b/p}+\frac{\partial g}{\partial b}2\hat{V}_N\right]\left(\frac{-u_{td}y_{b/p}}{\sqrt{\Delta^2+(y_{b/p}+g)^2}}+G_1(\cdot)\right)\right]\right] \\ \leq &\frac{1}{C_r}\left|\kappa(\theta)\right|v_r^2\frac{1}{1-\kappa(\theta)y_{b/p}}+F_2(\tilde{X}_1,\tilde{X}_2,\Delta,V_T,V_N,u_{rd})v_r^2 \\ &+F_1(\tilde{X}_1,\tilde{X}_2,\Delta,V_T,V_N,u_{rd})v_r \\ &-\frac{1}{C_r}\left(\frac{u_{rd}}{u_{rd}^2+v_r^2}-\frac{2\Delta v_r}{\Delta^2+(y_{b/p}+g)^2}\frac{\partial g}{\partial a}\right)Y(u_r)v_r^2 \end{aligned} \tag{7.81}$$

where $F_{1,2}(\cdot)$ are continuous functions in their arguments with:

$$F_2(0,0,\Delta,V_T,V_N,u_{rd})=0. \tag{7.82}$$

When substituting (7.81) in (7.78) we obtain

$$\begin{aligned} \dot{V}_3 \leq\ & X(u_{rd})F_2(\tilde{X}_1,\tilde{X}_2,\Delta,V_T,V_N,u_{rd})v_r^2+\left|\tfrac{C_r^*-C_r}{C_rC_r^*}\right|\left(\left|X(u_{rd})\kappa(\theta)\right|-\left|Y(u_{rd})\right|\right)v_r^2 \\ &+\frac{1}{C_r^*}\left[\left|X(u_{rd})\right|\left|\kappa(\theta)\right|\left(1+\frac{y_{b/p}}{1-\kappa(\theta)y_{b/p}}\right)-\left|Y(u_{rd})\right|+a_y\tilde{u}\right]v_r^2 \\ &+\left(X(u_{rd})F_1(\tilde{X}_1,\tilde{X}_2,\Delta,V_T,V_N,u_{rd})+a_x\tilde{u}(r_d+\tilde{r})+X(u_{rd})\tilde{r}\right)v_r \end{aligned} \tag{7.83}$$

where $C_r^*(v_r,y_{b/p},\Delta,V_N,u_{rd})=C_r(v_r,y_{b/p},\Delta,\hat{V}_N=V_N,u_r=u_{rd})$. When substituting (7.81) in (7.78) we have used the fact that

$$\frac{1}{C_r}\left(\frac{u_{rd}}{u_{rd}^2+v_r^2}-\frac{2\Delta v_r}{\Delta^2+(y_{b/p}+g)^2}\frac{\partial g}{\partial a}\right)X(u_r)Y(u_r)v_r^2=\frac{C_r-1}{C_r}Y(u_r)v_r^2. \tag{7.84}$$

Remark 7.6. Note that $C_r^*(v_r,y_{b/p},\Delta,V_N,u_{rd})$ can be found independently of $y_{b/p}$ and $x_{b/p}$ since the terms in C_r are bounded with respect to these variables.

Consequently, on the manifold where $(\tilde{X}_1,\tilde{X}_2)=0$ we have

$$\dot{V}_3\leq\frac{1}{C_r^*}\left(X_{\max}\left|\kappa(\theta)\right|-Y_{\min}\right)v_r^2+X(u_{rd})F_1(0,0,\Delta,V_T,V_N,u_{rd})|v_r| \tag{7.85}$$

which is bounded as long as

$$X_{\max}\left|\kappa(\theta)\right|-Y_{\min}<0. \tag{7.86}$$

Hence, satisfaction of (7.86) renders the quadratic term in (7.85) negative and since the quadratic term is dominant for sufficiently large v_r, (7.85) is negative definite for sufficiently large v_r. If $\dot{V}_3$ is negative for sufficiently large v_r this implies that V_3 decreases for sufficiently large v_r. Since $V_3 = 1/2v_r^2$, a decrease in V_3 implies a decrease in v_r^2 and by extension in v_r. Therefore, v_r cannot increase above a certain value and v_r is bounded near the manifold where $(\tilde{X}_1, \tilde{X}_2) = 0$.

Consequently, close to the manifold where $(\tilde{X}_1, \tilde{X}_2) = 0$ the sufficient and necessary condition for local boundedness of (7.47c) is the following:

$$X_{\max} |\kappa(\theta)| - Y_{\min} < 0. \tag{7.87}$$

which is satisfied if and only if the condition in Lemma 7.3 is satisfied.

7.C Proof of Lemma 7.4

Recall the sway velocity dynamics (7.47c):

$$\dot{v}_r = X(\tilde{u} + u_{rd})(r_d + \tilde{r}) + Y(u_{rd} + \tilde{u})v_r, \quad Y(u_{rd}) < 0$$

Consider the following Lyapunov function candidate:

$$V_3(v_r) = \frac{1}{2}v_r^2 \tag{7.88}$$

The derivative of (7.88) along the solutions of (7.47c) is given by

$$\begin{aligned} \dot{V}_3 = v_r\dot{v}_r &= v_r X(u_{rd} + \tilde{u})r_d + X(u_{rd} + \tilde{u})v_r\tilde{r} + Y(u_{rd} + \tilde{u})v_r^2 \\ &\leq X(u_{rd})r_d v_r + a_x\tilde{u}r_d v_r + X(u_{rd})v_r\tilde{r} + a_x\tilde{u}v_r\tilde{r} + a_y\tilde{u}v_r^2 + Y(u_{rd})v_r^2 \end{aligned} \tag{7.89}$$

where we used the fact that:

$$Y(u_r) = a_y u_r + b_y \tag{7.90}$$
$$X(u_r) = a_x u_r + b_x \tag{7.91}$$

The term $r_d v_r$ is given by:

$$
\begin{aligned}
r_d v_r = &- \frac{1}{C_r} v_r \Bigg[\kappa(\theta) \frac{u_t \cos(\psi + \beta - \gamma_p(\theta))}{1 - \kappa(\theta) y_{b/p}} + \kappa(\theta) \frac{k_\delta x_{b/p} + \hat{V}_T}{1 - \kappa(\theta) y_{b/p}} \\
&+ \frac{\Delta \left(b + \sqrt{b^2 - ac} \right)}{a\Delta^2 + a \left(y_{b/p} + g \right)^2} \left(-k_{x_1} \tilde{x} \sin(\gamma_p(\theta)) + k_{y_1} \tilde{y} \cos(\gamma_p(\theta)) \right) \\
&+ \frac{\Delta \kappa(\theta) \hat{V}_T \left(b + \sqrt{b^2 - ac} \right)}{a\Delta^2 + a \left(y_{b/p} + g \right)^2} \left(\frac{u_t \cos(\psi + \beta - \gamma_p(\theta))}{1 - \kappa(\theta) y_{b/p}} + \frac{k_\delta x_{b/p} - \hat{V}_T}{1 - \kappa(\theta) y_{b/p}} \right) \\
&+ \frac{\Delta \frac{\partial g}{\partial a} 2 \hat{V}_N}{\Delta^2 + \left(y_{b/p} + g \right)^2} \left(k_{x_1} \tilde{x} \sin(\gamma_p(\theta)) - k_{y_1} \tilde{y} \cos(\gamma_p(\theta)) \right) \\
&- \frac{\Delta \kappa(\theta) \frac{\partial g}{\partial a} 2 \hat{V}_N \hat{V}_T}{\Delta^2 + \left(y_{b/p} + g \right)^2} \left(\frac{u_t \cos(\psi + \beta - \gamma_p(\theta))}{1 - \kappa(\theta) y_{b/p}} + \frac{k_\delta x_{b/p} + \hat{V}_T}{1 - \kappa(\theta) y_{b/p}} \right) \\
&- \frac{\Delta \frac{\partial g}{\partial a}}{\Delta^2 + \left(y_{b/p} + g \right)^2} \left(2 u_{rd} \dot{u}_{rd} - 2 v_r Y(u_r) v_r \right) + \frac{Y(u_r) v_r u_{rd} - \dot{u}_{rd} v_r}{u_{rd}^2 + v_r^2} \\
&+ \frac{\Delta \frac{\partial g}{\partial b} 2 y_{b/p}}{\Delta^2 + \left(y_{b/p} + g \right)^2} \left(k_{x_1} \tilde{x} \sin(\gamma_p(\theta)) - k_{y_1} \tilde{y} \cos(\gamma_p(\theta)) \right) \\
&- \frac{\Delta \kappa(\theta) \frac{\partial g}{\partial b} 2 y_{b/p} \hat{V}_T}{\Delta^2 + \left(y_{b/p} + g \right)^2} \left(\frac{u_t \cos(\psi + \beta - \gamma_p(\theta))}{1 - \kappa(\theta) y_{b/p}} + \frac{k_\delta x_{b/p} + \hat{V}_T}{1 - \kappa(\theta) y_{b/p}} \right) \\
&- \phi(\cdot) u_{td} \frac{y_{b/p}}{\sqrt{\Delta^2 + (y_{b/p} + g)^2}} + \phi(\cdot) \tilde{u} \sin(\psi - \gamma_p) \\
&+ \phi(\cdot) \left[1 - \cos(\tilde{\psi}) \right] u_{td} \sin \left(\arctan \left(\frac{y_{b/p} + g}{\Delta} \right) \right) \\
&+ \phi(\cdot) \cos \left(\arctan \left(\frac{y_{b/p} + g}{\Delta} \right) \right) \sin(\tilde{\psi}) u_{td} \\
&- 2 \phi(\cdot) x_{b/p} \kappa(\theta) \left(\frac{u_t \cos(\psi + \beta - \gamma_p(\theta))}{1 - \kappa(\theta) y_{b/p}} + \frac{k_\delta x_{b/p} + \hat{V}_T}{1 - \kappa(\theta) y_{b/p}} \right) \Bigg]
\end{aligned}
\tag{7.92}
$$

where the function $\phi(y_{b/p}, v_r, u_{rd}, \hat{V}_N, \Delta)$ is bounded by a constant with respect to v_r and defined as

$$
\phi(\cdot) \triangleq \underbrace{\frac{2\Delta y_{b/p}}{\Delta^2 + \left(y_{b/p} + g \right)^2} \frac{\partial g}{\partial c}}_{\phi_1(\cdot)} + \underbrace{\frac{\Delta}{\Delta^2 + \left(y_{b/p} + g \right)^2}}_{\phi_2(\cdot)} + \underbrace{\frac{2\Delta \hat{V}_N}{\Delta^2 + \left(y_{b/p} + g \right)^2} \frac{\partial g}{\partial b}}_{\phi_3(\cdot)} \tag{7.93}
$$

We can rewrite $r_d v_r$ to obtain

$$\begin{aligned} r_d v_r = &- \frac{1}{C_r} v_r \Bigg[\kappa(\theta) \frac{u_t \cos(\psi + \beta - \gamma_p(\theta))}{1 - \kappa(\theta) y_{b/p}} \\ &- \phi_2(\cdot) u_{td} \frac{y_{b/p} + g}{\sqrt{\Delta^2 + (y_{b/p} + g)^2}} + \phi_2(\cdot) \hat{V}_N \\ &+ \phi_2(\cdot) \left[1 - \cos(\tilde{\psi})\right] u_{td} \sin\left(\arctan\left(\frac{y_{b/p} + g}{\Delta}\right)\right) \\ &+ \phi_2(\cdot) \cos\left(\arctan\left(\frac{y_{b/p} + g}{\Delta}\right)\right) \sin(\tilde{\psi}) u_{td} \Bigg] - \frac{1}{C_r} v_r \Phi_1(\cdot) \\ &- \frac{1}{C_r} \left(\frac{u_{rd}}{u_{rd}^2 + v_r^2} - \frac{2\Delta v_r}{\Delta^2 + (y_{b/p} + g)^2} \frac{\partial g}{\partial a} \right) Y(u_r) v_r^2 \end{aligned} \tag{7.94}$$

where $\Phi_1(\cdot)$ collects terms that are bounded with respect to v_r and terms that grow linearly with v_r but vanish when $\tilde{X}_2 = 0$. The function $\Phi_1(\cdot)$ is defined as

$$\begin{aligned} \Phi_1(\cdot) \triangleq\ & \kappa(\theta) \frac{k_\delta x_{b/p} - \hat{V}_T}{1 - \kappa(\theta) y_{b/p}} - \frac{\dot{u}_{rd} v_r}{u_{rd}^2 + v_r^2} + \frac{2 u_{rd} \dot{u}_{rd} \Delta}{\Delta^2 + \left(y_{b/p} + g\right)^2} \frac{\partial g}{\partial a} \\ &+ \frac{\Delta \left(b + \sqrt{b^2 - ac}\right)}{a\Delta^2 + a\left(y_{b/p} + g\right)^2} \left(-k_{x_1} \tilde{x} \sin(\gamma_p(\theta)) + k_{y_1} \tilde{y} \cos(\gamma_p(\theta))\right) \\ &+ \frac{\Delta \kappa(\theta) \hat{V}_T \left(b + \sqrt{b^2 - ac}\right)}{a\Delta^2 + a\left(y_{b/p} + g\right)^2} \left(\frac{u_t \cos(\psi + \beta - \gamma_p(\theta))}{1 - \kappa(\theta) y_{b/p}} + \frac{k_\delta x_{b/p} + \hat{V}_T}{1 - \kappa(\theta) y_{b/p}} \right) \\ &+ \frac{\Delta \frac{\partial g}{\partial a} 2 \hat{V}_N}{\Delta^2 + \left(y_{b/p} + g\right)^2} \left(k_{x_1} \tilde{x} \sin(\gamma_p(\theta)) - k_{y_1} \tilde{y} \cos(\gamma_p(\theta))\right) \\ &- \frac{\Delta \frac{\partial g}{\partial a} 2 \kappa(\theta) \hat{V}_N \hat{V}_T}{\Delta^2 + \left(y_{b/p} + g\right)^2} \left(\frac{u_t \cos(\psi + \beta - \gamma_p(\theta))}{1 - \kappa(\theta) y_{b/p}} + \frac{k_\delta x_{b/p} + \hat{V}_T}{1 - \kappa(\theta) y_{b/p}} \right) \\ &+ \frac{\Delta \frac{\partial g}{\partial b} 2 y_{b/p}}{\Delta^2 + \left(y_{b/p} + g\right)^2} \left(k_{x_1} \tilde{x} \sin(\gamma_p(\theta)) - k_{y_1} \tilde{y} \cos(\gamma_p(\theta))\right) \\ &- \frac{\Delta \frac{\partial g}{\partial b} 2 y_{b/p} \kappa(\theta) \hat{V}_T}{\Delta^2 + \left(y_{b/p} + g\right)^2} \left(\frac{u_t \cos(\psi + \beta - \gamma_p(\theta))}{1 - \kappa(\theta) y_{b/p}} + \frac{k_\delta x_{b/p} + \hat{V}_T}{1 - \kappa(\theta) y_{b/p}} \right) \\ &- \left(\phi_1(\cdot) + \phi_3(\cdot)\right) u_{td} \frac{y_{b/p}}{\sqrt{\Delta^2 + (y_{b/p} + g)^2}} + \phi(\cdot) \tilde{u} \sin(\psi - \gamma_p) \\ &+ \left(\phi_1(\cdot) + \phi_3(\cdot)\right) \left[1 - \cos(\tilde{\psi})\right] u_{td} \sin\left(\arctan\left(\frac{y_{b/p} + g}{\Delta}\right)\right) \\ &+ \left(\phi_1(\cdot) + \phi_3(\cdot)\right) \cos\left(\arctan\left(\frac{y_{b/p} + g}{\Delta}\right)\right) \sin(\tilde{\psi}) u_{td} \\ &- 2\phi(\cdot) x_{b/p} \kappa(\theta) \left(\frac{u_t \cos(\psi + \beta - \gamma_p(\theta))}{1 - \kappa(\theta) y_{b/p}} + \frac{k_\delta x_{b/p} + \hat{V}_T}{1 - \kappa(\theta) y_{b/p}} \right) \end{aligned} \tag{7.95}$$

We now introduce $C_r^*(\cdot)$ as defined in the proof of Lemma 7.3, so we can rewrite $r_d v_r$ to obtain:

$$\begin{aligned} r_d v_r = &- \frac{1}{C_r^*} v_r \left[\frac{\kappa(\theta) u_t \cos(\psi + \beta - \gamma_p(\theta))}{1 - \kappa(\theta) y_{b/p}} - \right. \\ &\phi_2(\cdot) u_{td} \frac{y_{b/p} + g}{\sqrt{\Delta^2 + (y_{b/p} + g)^2}} + \\ &\phi_2(\cdot) \left[1 - \cos(\tilde{\psi}) \right] u_{td} \sin\left(\arctan\left(\frac{y_{b/p} + g}{\Delta} \right) \right) + \\ &\left. \phi_2(\cdot) \cos\left(\arctan\left(\frac{y_{b/p} + g}{\Delta} \right) \right) \sin(\tilde{\psi}) u_{td} \right] - \frac{1}{C_r} v_r \Phi_2(\cdot) \\ &- \frac{1}{C_r} \left(\frac{u_{rd}}{u_{rd}^2 + v_r^2} - \frac{2\Delta v_r}{\Delta^2 + (y_{b/p} + g)^2} \frac{\partial g}{\partial a} \right) Y(u_r) v_r^2 \end{aligned} \tag{7.96}$$

where $\Phi_2(\cdot)$ collects terms that are bounded with respect to v_r and terms that grow linearly with v_r but vanish when $\tilde{X}_2 = 0$. The function $\Phi_2(\cdot)$ is defined as

$$\begin{aligned} \Phi_2(\cdot) \triangleq \Phi_1(\cdot) &+ \frac{C_r^* - C_r}{C_r^*} \left[\phi_2(\cdot) \left[1 - \cos(\tilde{\psi}) \right] u_{td} \sin\left(\arctan\left(\frac{y_{b/p} + g}{\Delta} \right) \right) \right. \\ &+ \frac{\kappa(\theta) u_t \cos(\psi + \beta - \gamma_p(\theta))}{1 - \kappa(\theta) y_{b/p}} - \frac{\phi_2(\cdot) u_{td} \left(y_{b/p} + g \right)}{\sqrt{\Delta^2 + (y_{b/p} + g)^2}} \\ &+ \phi_2(\cdot) \cos\left(\arctan\left(\frac{y_{b/p} + g}{\Delta} \right) \right) \sin(\tilde{\psi}) u_{td} \\ &\left. - \left(\frac{u_{rd}}{u_{rd}^2 + v_r^2} - \frac{2\Delta v_r}{\Delta^2 + (y_{b/p} + g)^2} \frac{\partial g}{\partial a} \right) Y(u_r) v_r \right] + \phi_2(\cdot) \hat{V}_N \end{aligned} \tag{7.97}$$

Considering the above we derive the following upper bound for $r_d v_r$:

$$r_d v_r \leq \left| \frac{1}{C_r^*} v_r \right| \left[\frac{|\kappa(\theta)| \, u_t}{1 - \kappa(\theta) y_{b/p}} + 4 \left| \phi_2(\cdot) \right| u_{td} \right] - \frac{1}{C_r} v_r \Phi_2(\cdot) \tag{7.98}$$

$$- \frac{1}{C_r} \left(\frac{u_{rd}}{u_{rd}^2 + v_r^2} - \frac{2\Delta v_r}{\Delta^2 + (y_{b/p} + g)^2} \frac{\partial g}{\partial a} \right) Y(u_r) v_r^2 \tag{7.99}$$

Using the fact that: $u_t \leq |u_r| + |v_r|$, we obtain:

$$\begin{aligned} r_d v_r &\leq \left| \frac{v_r}{C_r^*} \right| \left[\frac{|\kappa(\theta)| \left(|u_r| + |v_r| \right)}{1 - \kappa(\theta) y_{b/p}} + 4 \left| \phi_2(\cdot) \right| |u_{rd}| + 4 \left| \phi_2(\cdot) \right| |v_r| \right] - \frac{v_r}{C_r} \Phi_2(\cdot) \\ &\quad - \frac{1}{C_r} \left(\frac{u_{rd}}{u_{rd}^2 + v_r^2} - \frac{2\Delta v_r}{\Delta^2 + (y_{b/p} + g)^2} \frac{\partial g}{\partial a} \right) Y(u_r) v_r^2 \\ &\leq \left| \frac{1}{C_r^*} \right| \frac{|\kappa(\theta)| \, v_r^2}{1 - \kappa(\theta) y_{b/p}} + 4 \left| \frac{1}{C_r^*} \right| \left| \phi_2(\cdot) \right| v_r^2 + \Phi_3(\cdot) \\ &\quad - \frac{1}{C_r} \left(\frac{u_{rd}}{u_{rd}^2 + v_r^2} - \frac{2\Delta v_r}{\Delta^2 + (y_{b/p} + g)^2} \frac{\partial g}{\partial a} \right) Y(u_r) v_r^2 \end{aligned} \tag{7.100}$$

where Φ_3 collects the terms that grow linear in v_r and terms that grow quadratically in v_r but vanish when $\tilde{X}_2 = 0$. The function Φ_3 is defined as

$$\Phi_3(\cdot) \triangleq \left|\frac{1}{C_r^*}\right| \frac{|\kappa(\theta)|\,|v_r u_r|}{1-\kappa(\theta) y_{b/p}} + \left|\frac{1}{C_r^*}\right| |v_r u_{rd}|\,|\phi_2(\cdot)| - \frac{1}{C_r} v_r \Phi_2(\cdot) \tag{7.101}$$

Observing the definition of $\Phi_3(\cdot)$ one can easily conclude the existence of three continuous positive functions $F_{0,2}(\tilde{X}_1, \tilde{X}_2, u_{rd}, \dot{u}_{rd}, V_T, V_N, \Delta)$ which are bounded since the vector $[\tilde{X}_2^T, u_{rd}, \dot{u}_{rd}, V_T, V_N, \Delta]^T$ is bounded, and where

$$F_2(\tilde{X}_1, \tilde{X}_2 = 0, u_{rd}, \dot{u}_{rd}, V_T, V_N, \Delta) = 0,$$

such that:

$$\Phi_3(\cdot) \leq F_2(\cdot) v_r^2 + F_1(\cdot) v_r + F_0(\cdot) \tag{7.102}$$

Consequently, when we substitute (7.100) in (7.89) obtain:

$$\begin{aligned}
\dot{V}_3 = v_r \dot{v}_r \leq & |X(u_{rd})| \left[\left|\frac{1}{C_r^*}\right| \frac{|\kappa(\theta)|\, v_r^2}{1-\kappa(\theta) y_{b/p}} + 4 \left|\frac{1}{C_r^*}\right| |\phi_2(\cdot)|\, v_r^2 + \Phi_3(\cdot) \right] \\
& + a_x \tilde{u} \dot{r}_d v_r + X(u_{rd}) v_r \tilde{r} + a_x \tilde{u} v_r \tilde{r} + a_y \tilde{u} v_r^2 + Y(u_{rd}) v_r^2 \\
& - \frac{1}{C_r} \left(\frac{u_{rd}}{u_{rd}^2 + v_r^2} - \frac{2\Delta v_r}{\Delta^2 + (y_{b/p} + g)^2} \frac{\partial g}{\partial a} \right) X(u_{rd} Y(u_{rd}) v_r^2 \\
\leq & \left|\frac{1}{C_r^*}\right| \left[\frac{X_{\max} \kappa_{\max}}{1-\kappa(\theta) y_{b/p}} + 4 X_{\max} |\phi_2(\cdot)| - Y_{\min} \right] v_r^2 \\
& + |X(u_{rd})|\,|\Phi_3(\cdot)| + a_x \tilde{u} \dot{r}_d v_r + X(u_{rd}) v_r \tilde{r} + a_x \tilde{u} v_r \tilde{r} + a_y \tilde{u} v_r^2
\end{aligned} \tag{7.103}$$

To have boundedness of v_r for small values of $\tilde{X}_2$ we have to satisfy the following inequality:

$$\frac{X_{\max} \kappa_{\max}}{1-\kappa(\theta) y_{b/p}} + 4 X_{\max} |\phi_2(\cdot)| - Y_{\min} < 0 \tag{7.104}$$

such that the quadratic term in (7.103) is negative. Using (7.50) we need to choose Δ, such that:

$$|\phi_2(\cdot)| < \frac{\left[Y_{\min} - X_{\max} \kappa_{\max} \frac{1}{\sigma} \right]}{4 X_{\max}} > 0, \tag{7.105}$$

since $|\phi_2(\cdot)| \leq \frac{1}{\Delta}$, we can take $\Delta > \frac{4 X_{\max}}{\left[Y_{\min} - X_{\max} \kappa_{\max} \frac{1}{\sigma} \right]}$ such that (7.104) holds. Consequently, near the manifold $\tilde{X}_2 = 0$ it holds that (7.103) is negative definite for sufficiently large v_r. If $\dot{V}_3$ is negative for sufficiently large v_r this implies that V_3 decreases for sufficiently large v_r. Since $V_3 = 1/2 v_r^2$, a decrease in V_3 implies a decrease in v_r^2 and by extension in v_r. Consequently, v_r cannot increase above a certain value and v_r is bounded near $\tilde{X}_2 = 0$.

Chapter 8

Observer Based Path Following for Underactuated Marine Vessels in the Presence of Ocean Currents: A Global Approach

This chapter presents another approach to investigate the problem of following a curved path in the presence of a constant ocean current disturbance. In this chapter the path is parametrised in a different way such that the parametrisation is globally valid. This is done by releasing the requirement in place in Chapter 7 that the vehicle had to be on the normal. This leaves extra freedom to derive the update law of the parametrisation and means that the singularity in the parametrisation in Chapter 7 can be avoided. This is an approach first suggested in Lapierre et al. [87]. Note that this strategy has the disadvantage that the path-following error is no longer defined as the shortest distance to the path, which is the case when the vehicle is on the normal as in the local parametrisation. Note that even though in this case we track a point on the path rather then simply reduce the shortest distance to the path this still qualifies as a path-following approach. More specifically, there are no pre-defined time constraints as to where the vehicle needs to be and it is therefore not a trajectory tracking problem. Moreover, as will be shown the parametrisation that is applied propagates based on the velocity and motion of the vehicle and not vice-versa as it would in a manoeuvring problem.

When the path is parametrised according to the global parametrisation we can solve the path-following problem using a combination of an ocean current observer and a controller based on a *line-of-sight-like* guidance. The guidance for this case is said to be line-of-sight-like since it adopts a time-varying look-ahead distance depending on the path-following error. It is shown that this dependency on the path-following errors is necessary to show boundedness of the sway velocity. The closed-loop system of the vessel with the observer and controller is investigated by first showing boundedness of the sway velocity and then showing global asymptotic stability of the path-following errors.

The outline of the chapter is as follows. In the Section 8.1 the vessel model from

Section 2.2 is recalled. The path-following problem and the chosen path parametrisation are introduced in Section 8.2. Section 8.3 presents the ocean current observer that is used together with the guidance law and controllers. The closed-loop system is then formulated and analysed in Section 8.4. A simulation case study is presented in Section 8.5 and conclusions are given in Section 8.6. The material in this chapter is based on Belleter et al. [22].

8.1 Vessel Model

In this section we consider the model for a surface vessel given in Chapter 2. This model can be used to describe an autonomous surface vessel or an autonomous underwater vehicle moving in a plane. Recall, that the model can be represented in component form as

$$\dot{x} = u_r \cos(\psi) - v_r \sin(\psi) + V_x, \tag{8.1a}$$
$$\dot{y} = u_r \sin(\psi) + v_r \cos(\psi) + V_y, \tag{8.1b}$$
$$\dot{\psi} = r, \tag{8.1c}$$
$$\dot{u}_r = F_{u_r}(v_r, r) - \tfrac{d_{11}}{m_{11}} u_r + \tau_u, \tag{8.1d}$$
$$\dot{v}_r = X(u_r) r + Y(u_r) v_r, \tag{8.1e}$$
$$\dot{r} = F_r(u_r, v_r, r) + \tau_r, \tag{8.1f}$$

The functions $X(u_r)$, $Y(u_r)$, F_u, and F_r are given by

$$F_{u_r}(v_r, r) \triangleq \frac{1}{m_{11}}(m_{22} v_r + m_{23} r) r, \tag{8.2a}$$
$$X(u_r) \triangleq \frac{m_{23}^2 - m_{11} m_{33}}{m_{22} m_{33} - m_{23}^2} u_r + \frac{d_{33} m_{23} - d_{23} m_{33}}{m_{22} m_{33} - m_{23}^2}, \tag{8.2b}$$
$$Y(u_r) \triangleq \frac{(m_{22} - m_{11}) m_{23}}{m_{22} m_{33} - m_{23}^2} u_r - \frac{d_{22} m_{33} - d_{32} m_{23}}{m_{22} m_{33} - m_{23}^2}, \tag{8.2c}$$
$$\begin{aligned} F_r(u_r, v_r, r) \triangleq{}& \frac{m_{23} d_{22} - m_{22}(d_{32} + (m_{22} - m_{11}) u_r)}{m_{22} m_{33} - m_{23}^2} v_r \\ &+ \frac{m_{23}(d_{23} + m_{11} u_r) - m_{22}(d_{33} + m_{23} u_r)}{m_{22} m_{33} - m_{23}^2} r. \end{aligned} \tag{8.2d}$$

Note that the functions $X(u_r)$ and $Y(u_r)$ are linear functions of the velocity. The kinematic variables are illustrated in Figure 8.1. As specified in Chapter 2, the ocean current satisfies the following assumption.

Assumption 8.1. The ocean current is assumed to be constant and irrotational with respect to the inertial frame, i.e. $\boldsymbol{V_c} \triangleq [V_x, V_y, 0]^T$. Furthermore, it is bounded by $V_{\max} > 0$ such that $\|V_c\| = \sqrt{V_x^2 + V_y^2} \leq V_{\max}$.

Moreover, for the considered range of values of the desired surge velocity u_{rd} the following assumption holds.

Assumption 8.2. It is assumed that $Y(u_r)$ satisfies

$$Y(u_r) \leq -Y_{\min} < 0, \, \forall u_r \in [-V_{\max}, u_{rd}],$$

i.e. $Y(u_r)$ is negative for the range of desired velocities considered.

Remark 8.1. Assumptions 8.2 is satisfied for commercial vessels by design, since the converse would imply an undamped or nominally unstable vessel in sway.

Additionally we assume that the following assumption holds

Assumption 8.3. It is assumed that $2V_{\max} < u_{rd}(t) \; \forall t$, i.e. the desired relative velocity of the vessel is larger than the maximum value of the ocean current.

Assumption 8.3 assures that the vessel has enough propulsion power to overcome the ocean current affecting it. The factor two in Assumption 8.3 adds some extra conservativeness to bound the solutions of the ocean current observer, this is discussed further in Section 8.3.

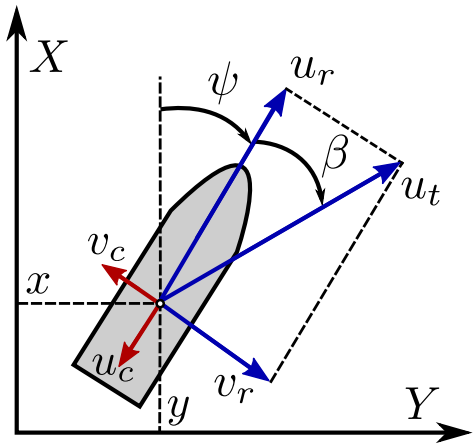

Figure 8.1: Definition of the ship's kinematic variables.

8.2 Problem definition

The goal is to follow a smooth path P, parametrised by a path variable θ, by appropriately controlling the ship's surge velocity and yaw rate. For an underactuated vessel path following can be achieved by positioning the vessel on the path with the total velocity $u_t \triangleq \sqrt{u_r^2 + v_r^2}$ (see Figure 8.1) tangential to the path. To express the path-following errors we propagate a path-tangential frame along P. This is illustrated in Figure 8.2. The path-following errors, $\boldsymbol{p}_{b/p}$, take the following form:

$$\boldsymbol{p}_{b/p} \triangleq \begin{bmatrix} x_{b/p} \\ y_{b/p} \end{bmatrix} = \begin{bmatrix} \cos(\gamma_p(\theta)) & \sin(\gamma_p(\theta)) \\ -\sin(\gamma_p(\theta)) & \cos(\gamma_p(\theta)) \end{bmatrix} \begin{bmatrix} x - x_P(\theta) \\ y - y_P(\theta) \end{bmatrix} \tag{8.3}$$

where $\gamma(\theta)$ is the angle of the path with respect to the X-axis. The time derivative of the angle $\gamma(\theta)$ is given by $\dot{\gamma}(\theta) = \kappa(\theta)\dot{\theta}$ where $\kappa(\theta)$ is the curvature of P at θ. The path-following error is expressed in $x_{b/p}$ and $y_{b/p}$ which are the relative positions between the path frame and body frame expressed along the axes of the path frame. Hence, $x_{b/p}$ is the position of the vehicle along the path-frame tangential axis and $y_{b/f}$ is the position of the vehicle along the path-frame normal axis. The goal is to regulate both $x_{b/p}$ and $y_{b/p}$ to zero.

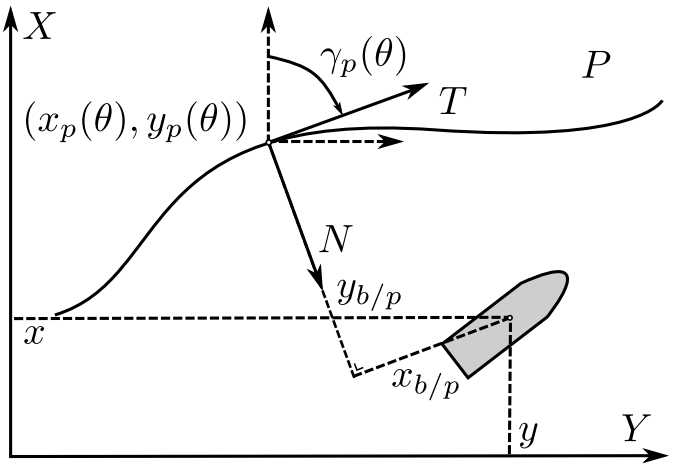

Figure 8.2: Definition of the path.

The error dynamics of a vessel with respect to the path frame are given by:

$$\dot{x}_{b/p} = -\dot{\theta}(1 - \kappa(\theta)y_{b/p}) + u_t \cos(\chi - \gamma_p(\theta)) + V_T \tag{8.4a}$$

$$\dot{y}_{b/p} = u_t \sin(\chi - \gamma_p(\theta)) + V_N - \kappa(\theta)\dot{\theta}x_{b/p} \tag{8.4b}$$

where $\chi \triangleq \psi + \beta$ is the course angle (see Figure 8.1) and $V_T \triangleq V_x \cos(\gamma_p(\theta)) + V_y \sin(\gamma_p(\theta))$ and $V_N \triangleq V_y \cos(\gamma_p(\theta)) - V_x \sin(\gamma_p(\theta))$ are the ocean current component in the tangential direction and normal direction of the path-tangential reference frame respectively.

To avoid the singularity in the parametrisation of Chapter 7 we no longer require the vessel to remain on the normal. Therefore, as proposed in [86] we can use the update law as an extra degree of freedom in the controller design. In particular, the propagation speed of the frame is used to get the desired behaviour of the $x_{b/p}$ dynamics. This is achieved by setting

$$\dot{\theta} = u_t \cos(\chi - \gamma_p(\theta)) + k_x f_\theta(x_{b/p}, y_{b/p}) + V_T \tag{8.5}$$

where $k_x > 0$ is a control gain for the convergence of $x_{b/p}$ and $f_\theta(x_{b/p}, y_{b/p})$ is a function to be designed later satisfying $f_\theta(x_{b/p}, y_{b/p})x_{b/p} > 0$. Consequently, when substituting (8.5) in (8.4a) we obtain

$$\dot{x}_{b/p} = -k_x f_\theta(x_{b/p}, y_{b/p}) + \dot{\theta}\kappa(\theta)y_{b/p} \tag{8.6}$$

For the case where the current is unknown we need to replace V_T by its estimate $\hat{V}_T$, and the update law becomes

$$\dot{\theta} = u_t \cos(\chi - \gamma(\theta)) + k_x f_\theta(x_{b/p}, y_{b/p}) + \hat{V}_T \tag{8.7}$$

Substituting this revised update law into (8.4) results in

$$\dot{x}_{b/p} = -k_x f_\theta(x_{b/p}, y_{b/p}) + \dot{\theta}\kappa(\theta) y_{b/p} + \tilde{V}_T \tag{8.8}$$

$$\dot{y}_{b/p} = u_t \sin(\chi - \gamma_p(\theta)) + V_N - x_{b/p}\kappa(\theta)\dot{\theta}. \tag{8.9}$$

Note that although the parametrisation (8.7) does not contain a singularity as it did in Chapter 7 it also does not decouple (8.8) from (8.9) as it did in Chapter 7. Consequently, since (8.8) depends on $y_{b/p}$ the $x_{b/p}$ no longer converge independently from those of $y_{b/p}$ and both $x_{b/p}$ and $y_{b/p}$ will have to be regulated to zero using the surge and yaw rate controllers. Moreover, note that although this parametrisation has the advantage that the update law can be well defined on the entire state space the path-following error is no longer defined as the shortest distance to the path since the vessel is not on the normal.

8.3 Controllers, Observer, and Guidance

In this section we design the two control laws τ_u and τ_r, and the ocean current estimator that are used to achieve path-following. In the first subsection we present the velocity control law τ_u. The second subsection presents the ocean current observer. The third subsection presents the guidance to be used.

8.3.1 Surge velocity control

The velocity control law is a feedback-linearising P-controller that is used to drive the relative surge velocity to a desired u_{rd} and is given by

$$\tau_u = -F_{u_r}(v_r, r) + \dot{u}_{rd} + \frac{d_{11}}{m_{11}} u_{rd} - k_u(u_r - u_{rd}) \tag{8.10}$$

where $k_u > 0$ is a constant controller gain. It is straightforward to verify that (8.10) ensures global exponential tracking of the desired velocity. In particular, when (8.10) is substituted in (8.1d) we obtain

$$\dot{\tilde{u}}_r = -k_u(u_r - u_{rd}) = -k_u \tilde{u}_r \tag{8.11}$$

where $\tilde{u}_r \triangleq u_r - u_{rd}$. Consequently, the velocity error dynamics are described by a stable linear systems, which assures exponential tracking of the desired velocity u_{rd}.

8.3.2 Ocean current estimator

This subsection presents the ocean current estimator introduced in [2]. This observer provides the estimate of the ocean current needed to implement (8.7) and

the guidance law developed in the next subsection. Rather then estimating the time-varying current components in the path frame V_T and V_N the observer is used to estimate the constant ocean current components in the inertial frame V_x and V_y. The observer from [2] is based on the kinematic equations of the vehicle, i.e. (8.1a) and (8.1b), and requires measurements of the vehicle's x and y position in the inertial frame. The observer is formulated as

$$\dot{\hat{x}} = u_r \cos(\psi) - v_r \sin(\psi) + \hat{V}_x + k_{x_1}\tilde{x} \tag{8.12a}$$

$$\dot{\hat{y}} = u_r \sin(\psi) + v_r \cos(\psi) + \hat{V}_y + k_{y_1}\tilde{y} \tag{8.12b}$$

$$\dot{\hat{V}}_x = k_{x_2}\tilde{x} \tag{8.12c}$$

$$\dot{\hat{V}}_y = k_{y_2}\tilde{y} \tag{8.12d}$$

where $\tilde{x} \triangleq x - \hat{x}$ and $\tilde{y} = y - \hat{y}$ are the positional errors and k_{x_1}, k_{x_2}, k_{y_1}, and k_{y_2} are constant positive gains. Consequently, the estimation error dynamics are given by

$$\dot{\tilde{x}} = \tilde{V}_x - k_{x_1}\tilde{x} \tag{8.13a}$$

$$\dot{\tilde{y}} = \tilde{V}_y - k_{y_1}\tilde{y} \tag{8.13b}$$

$$\dot{\tilde{V}}_x = -k_{x_2}\tilde{x} \tag{8.13c}$$

$$\dot{\tilde{V}}_y = -k_{y_2}\tilde{y} \tag{8.13d}$$

which can be written in vector form as

$$\begin{bmatrix} \dot{\tilde{x}} \\ \dot{\tilde{y}} \\ \dot{\tilde{V}}_x \\ \dot{\tilde{V}}_y \end{bmatrix} = \begin{bmatrix} -k_{x_1} & 0 & 1 & 0 \\ 0 & -k_{y_1} & 0 & 1 \\ -k_{x_2} & 0 & 0 & 0 \\ 0 & -k_{y_2} & 0 & 0 \end{bmatrix} \begin{bmatrix} \tilde{x} \\ \tilde{y} \\ \tilde{V}_x \\ \tilde{V}_y \end{bmatrix} \tag{8.14}$$

which is a linear system with negative eigenvalues. Hence, the observer error dynamics are globally exponentially stable at the origin. Note that this implies that also $\hat{V}_T$ and $\hat{V}_N$ go to V_T and V_N respectively with exponential convergence since it holds that

$$\hat{V}_T = \hat{V}_x \cos(\gamma(\theta)) + \hat{V}_y \sin(\gamma(\theta)) \tag{8.15a}$$

$$\hat{V}_N = -\hat{V}_x \sin(\gamma(\theta)) + \hat{V}_y \cos(\gamma(\theta)) \tag{8.15b}$$

For implementation of the controllers it is desired that $\|\hat{V}_N(t)\| < u_{rd}(t)\ \forall t$. To achieve this we first choose the initial conditions of the estimator as

$$[\hat{x}(t_0), \hat{y}(t_0), \hat{V}_x(t_0), \hat{V}_y(t_0)]^T = [x(t_0), y(t_0), 0, 0]^T. \tag{8.16}$$

Consequently, the initial estimation error is given by

$$[\tilde{x}(t_0), \tilde{y}(t_0), \tilde{V}_x(t_0), \tilde{V}_y(t_0)]^T = [0, 0, V_x, V_y]^T \tag{8.17}$$

which has a norm smaller than or equal to $V_{\max}$ according to Assumption 8.1. Now consider the function

$$W(t) = \tilde{x}^2 + \tilde{y}^2 + \frac{1}{k_{x_2}}\tilde{V}_x^2 + \frac{1}{k_{y_2}}\tilde{V}_y^2 \tag{8.18}$$

which has the following time derivative

$$\begin{aligned}\dot{W}(t) &= 2\tilde{x}\dot{\tilde{x}} + 2\tilde{y}\dot{\tilde{y}} + \frac{2}{k_{x_2}}\tilde{V}_x\dot{\tilde{V}}_x + \frac{2}{k_{y_2}}\tilde{V}_y\dot{\tilde{V}}_y \\ &= 2\tilde{x}(\tilde{V}_x - k_{x_1}\tilde{x}) + 2\tilde{y}(\tilde{V}_y - k_{y_1}\tilde{y}) - 2\tilde{V}_y\tilde{y} - 2\tilde{V}_x\tilde{x} \\ &= -2k_{x_1}\tilde{x}^2 - 2k_{y_1}\tilde{y}^2 \leq 0.\end{aligned} \tag{8.19}$$

This implies that $W(t) \leq \|W(t_0)\|$. From our choice of initial conditions we know that

$$\|W(t_0)\| = \frac{1}{k_{x_2}}V_x^2 + \frac{1}{k_{y_2}}V_y^2 \leq \frac{1}{\min(k_{x_2}, k_{y_2})}V_{\max}^2. \tag{8.20}$$

Moreover, it is straightforward to verify

$$\frac{1}{\max(k_{x_2}, k_{y_2})}\|\tilde{\boldsymbol{V}}_c(t)\|^2 \leq W(t). \tag{8.21}$$

Combining the observations given above we obtain

$$\frac{1}{\max(k_{x_2}, k_{y_2})}\|\tilde{\boldsymbol{V}}_c(t)\|^2 \leq \frac{1}{\min(k_{x_2}, k_{y_2})}V_{\max}^2. \tag{8.22}$$

Consequently, we obtain

$$\|\tilde{\boldsymbol{V}}_c(t)\| \leq \sqrt{\frac{\max(k_{x_2}, k_{y_2})}{\min(k_{x_2}, k_{y_2})}}V_{\max} < \sqrt{\frac{\max(k_{x_2}, k_{y_2})}{\min(k_{x_2}, k_{y_2})}}u_{rd}(t),\ \forall t, \tag{8.23}$$

which implies that if the gains are chosen as $k_{x_2} = k_{y_2}$ we have

$$\|\hat{V}_N\| \leq 2V_{\max} \leq u_{rd}(t),\ \forall t. \tag{8.24}$$

Hence, $\|\hat{V}_N\| < u_{rd}(t),\ \forall t$ if $2V_{\max} < u_{rd}(t),\ \forall t$.

Remark 8.2. The bound $2V_{\max} < u_{rd},\ \forall t$, is only required when deriving the bound on the solutions of the observer. In particular, it is required to guarantee that $\|\hat{V}_N\| < u_{rd}(t),\ \forall t$. For the rest of the analysis it suffices that $V_{\max} < u_{rd},\ \forall t$. Therefore, if the more conservative bound $2V_{\max} < u_{rd},\ \forall t$, is not satisfied the observer can be changed to an observer that allows explicit bounds on the estimate $\hat{V}_N$, e.g. the observer developed Narendra and Annaswamy [103], rather than an observer that only provides a bound on the error $\tilde{\boldsymbol{V}}_c$ as is the case here. For practical purposes the estimate can also be saturated such that $\|\hat{V}_N\| < u_{rd},\ \forall t$, which is the approach taken in Moe et al. [100]. However, in the theoretical analysis of the yaw controller we use derivatives of $\hat{V}_N$ which will be discontinuous when saturation is applied.

8.3.3 Guidance for global parametrisation

When using the global parametrisation we can define one guidance law that can be used everywhere. As in Chapter 7 and Moe et al. [100] we choose a guidance law of the form:

$$\psi_d = \gamma(\theta) - \text{atan}\left(\frac{v_r}{u_{rd}}\right) - \text{atan}\left(\frac{y_{b/p} + g}{\Delta(x_{b/p}, y_{b/p})}\right) \tag{8.25}$$

The guidance law consists of three terms. The first term is a feedforward of the angle of the path with respect to the inertial frame. The second part is the desired side-slip angle, i.e. the angle between the surge velocity and the total speed when $u_r \equiv u_{rd}$. This side-slip angle is used to make the vehicle's total speed tangential to the path when the sway velocity is non-zero. The third term is a line-of-sight (LOS) term that is intended to steer the vessel to the path, where g is a term dependent on the ocean current. The choice of g provides extra design freedom to compensate for the component of the ocean current along the normal axis V_N.

Note that the guidance law (8.25) is very similar to the local guidance law in Chapter 7. However, in (8.25) the look-ahead distance Δ is not constant as in Chapter 7 but is a function of $x_{b/p}$ and $y_{b/p}$ to be specified later.

Remark 8.3. The guidance law (8.25) with the choice $\Delta(x_{b/p}, y_{b/p}) = \sqrt{\mu^2 + x_{b/p}^2}$ was utilised in Moe et al. [100]. However, as will be shown this leads to a desired yaw rate that goes to infinity as $y_{b/p}$ goes to infinity. Consequently, no finite value of the constant μ can be found that stabilises the system globally, i.e. for any $y_{b/p}$.

When we substitute (8.25) in (8.9) we obtain

$$\dot{y}_{b/p} = u_{td} \sin\Big(\psi_d + \tilde{\psi} + \beta_d - \gamma_p(\theta)\Big) + V_N - x_{b/p}\kappa(\theta)\dot{\theta} + \tilde{u}_r \sin(\psi - \gamma_p(\theta)) \tag{8.26a}$$

$$= -\frac{u_{td}(y_{b/p} + g)}{\sqrt{(y_{b/p} + g)^2 + \Delta^2}} - x_{b/p}\dot{\gamma}_p(\theta) + V_N + G_1(\tilde{\psi}, \tilde{u}_r, g, \psi_d, y_{b/p}, u_{td}) \tag{8.26b}$$

where $G_1(\cdot)$ is a perturbing term given by

$$\begin{aligned} G_1(\cdot) = u_{td}\Big[1 - \cos(\tilde{\psi})\Big] \sin\left(\text{arctan}\left(\frac{y_{b/p} + g}{\Delta}\right)\right) + \tilde{u}_r \sin(\psi - \gamma_p(\theta)) \\ + u_{td} \cos\left(\text{arctan}\left(\frac{y_{b/p} + g}{\Delta}\right)\right) \sin(\tilde{\psi}) \end{aligned} \tag{8.27}$$

Note that $G_1(\cdot)$ satisfies

$$G_1(0, 0, g, \psi_d, y_{b/p}, u_{td}) = 0 \tag{8.28a}$$

$$\|G_1(\tilde{\psi}, \tilde{u}_r, \psi_d, y_{b/p}, u_{td})\| \leq \zeta(u_{td}) \|[\tilde{\psi}, \tilde{u}_r]^T\|, \ \zeta(u_{td}) > 0 \tag{8.28b}$$

where $\zeta(u_{td}) > 0$, which shows that $G_1(\cdot)$ is zero when the perturbing variables are zero and that it has maximal linear growth in the perturbing variables.

To compensate for the ocean current component V_N the variable g is now chosen to satisfy the equality

$$u_{td}\frac{g}{\sqrt{\Delta^2+(y_{b/p}+g)^2}}=\hat{V}_N. \tag{8.29}$$

which is a choice inspired by [100]. In order for g to satisfy the equality above, it should be the solution of the following second order equality

$$\underbrace{(u_{td}^2-\hat{V}_N^2)}_{-a}\left(\frac{g}{\hat{V}_N}\right)^2=\underbrace{\Delta^2+y_{b/p}^2}_{c}+2\underbrace{y_{b/p}\hat{V}_N}_{b}\left(\frac{g}{\hat{V}_N}\right) \tag{8.30}$$

hence we choose g to be

$$g=\hat{V}_N\frac{b+\sqrt{b^2-ac}}{-a} \tag{8.31}$$

which has the same sign as $\hat{V}_N$ and is well defined for $(u_{rd}^2-\hat{V}_N^2)=-a>0$. Substituting this in (8.26) gives

$$\dot{y}_{b/p}=-u_{td}\frac{y_{b/p}}{\sqrt{(y_{b/p}+g)^2+\Delta^2}}-x_{b/p}\dot{\gamma}_p(\theta)+\tilde{V}_N+G_1(\tilde{\psi},\tilde{u},\psi_d,y_{b/p},u_{td}) \tag{8.32}$$

Recall that the error in tangential direction is given by :

$$\dot{x}_{b/p}=-\dot{\theta}+\dot{\theta}\kappa(\theta)y_{b/p}+\sqrt{u_r^2+v_r^2}\cos(\psi+\beta-\gamma_p(\theta))+V_T \tag{8.33}$$

where $\kappa(\theta)$ is the curvature of the path at the point $(x_p(\theta),y_p(\theta))$. We now choose $\dot{\theta}$ to be:

$$\dot{\theta}=\sqrt{u_r^2+v_r^2}\cos(\psi+\beta-\gamma_p(\theta))+k_\delta\frac{x_{b/p}}{\sqrt{1+x_{b/p}^2}}+\hat{V}_T \tag{8.34}$$

such that we obtain:

$$\dot{x}_{b/p}=-k_\delta\frac{x_{b/p}}{\sqrt{1+x_{b/p}^2}}+\dot{\theta}\kappa(\theta)y_{b/p}+\tilde{V}_T. \tag{8.35}$$

where $k_\delta>0$. In this way we introduce a stabilising term to the tangential error dynamics by appropriately controlling the propagation of our path-tangential frame.

The derivative of (8.25) is given by

$$\begin{aligned}\dot{\psi}_d=\kappa(\theta)\dot{\theta}-\frac{\dot{v}_r u_{rd}-\dot{u}_{rd}v_r}{u_{rd}^2+v_r^2}-\frac{\Delta(\dot{y}_{b/p}+\dot{g})}{\Delta^2+(y_{b/f}+g)^2}\\+\frac{y_{b/p}+g}{\Delta^2+(y_{b/p}+g)^2}\left[\frac{\partial\Delta}{\partial x_{b/p}}\dot{x}_{b/p}+\frac{\partial\Delta}{\partial y_{b/p}}\dot{y}_{b/p}\right]\end{aligned} \tag{8.36}$$

with

$$\dot{g}=\dot{\hat{V}}_N\frac{b+\sqrt{b^2-ac}}{-a}+\frac{\partial g}{\partial a}\dot{a}+\frac{\partial g}{\partial b}\dot{b}+\frac{\partial g}{\partial c}\dot{c} \tag{8.37}$$

where

$$\frac{\partial g}{\partial a} = \hat{V}_N \frac{c}{2a\sqrt{b^2-ac}} + \hat{V}_N \frac{b+\sqrt{b^2-ac}}{a^2} \tag{8.38a}$$

$$\frac{\partial g}{\partial b} = \hat{V}_N \frac{b+\sqrt{b^2-ac}}{a\sqrt{b^2-ac}} \tag{8.38b}$$

$$\frac{\partial g}{\partial c} = \hat{V}_N \frac{1}{2\sqrt{b^2-ac}} \tag{8.38c}$$

$$\dot{a} = 2\hat{V}_N\dot{\hat{V}}_N - 2u_{rd}\dot{u}_{rd} - 2v_r\left[X(u_r)r + Y(u_r)v_r\right] \tag{8.38d}$$

$$\dot{b} = \hat{V}_N\dot{y}_{b/p} + \dot{\hat{V}}_N y_{b/p} \tag{8.38e}$$

$$\dot{c} = 2y_{b/p}\dot{y}_{b/p} + 2\Delta(x_{b/p}, y_{b/p})\left[\frac{\partial \Delta}{\partial x_{b/p}}\dot{x}_{b/p} + \frac{\partial \Delta}{\partial y_{b/p}}\dot{y}_{b/p}\right] \tag{8.38f}$$

The expression for $\dot{\psi}_d$ contains terms depending on $\dot{y}_{b/p}$ and $\dot{x}_{b/p}$ which depend on $\tilde{V}_N$ and $\tilde{V}_T$ respectively. Consequently, $\dot{\psi}_d$ depends on unknown variables and cannot be used to control the yaw rate. This was not considered in [100] where the proposed controller contained both $\dot{\psi}_d$ and $\ddot{\psi}_d$.

Moreover, from (8.25) we see that $\dot{\psi}_d$ contains $\dot{v}_r$, which depends on $r = \dot{\psi}$. Therefore, the yaw rate error $\dot{\tilde{\psi}} \triangleq \dot{\psi} - \dot{\psi}_d$ grows with $\dot{\psi}$ which leads to a necessary condition for a well defined yaw rate error. The yaw rate error dynamics are given by

$$\begin{aligned}
\dot{\tilde{\psi}} = {} & r\left[1 + \frac{X(u_r)u_{rd}}{u_{rd}^2+v_r^2} - \frac{\Delta}{\Delta^2 + \left(y_{b/p}+g\right)^2}\frac{\partial g}{\partial a}\left(2v_r X(u_r)\right)\right] \\
& - \kappa(\theta)\dot{\theta} + \frac{Y(u_r)v_r u_{rd} - \dot{u}_{rd}v_r}{u_{rd}^2+v_r^2} \\
& + \frac{\Delta}{\Delta^2 + \left(y_{b/p}+g\right)^2}\left[\dot{\hat{V}}_N\frac{b+\sqrt{b^2-ac}}{-a} + \frac{\partial g}{\partial b}\left(2\dot{\hat{V}}_N y_{b/p}\right)\right. \\
& + \frac{\partial g}{\partial a}\left(2\hat{V}_N\dot{\hat{V}}_N - 2u_{rd}\dot{u}_{rd} - 2v_r Y(u_r)v_r\right) \\
& + \left[1 + \frac{\partial g}{\partial c}2y_{b/p} + \frac{\partial g}{\partial b}\left(2\hat{V}_N\right)\right]\dot{y}_e \\
& \left. + \frac{\partial g}{\partial c}2\Delta\left[\frac{\partial \Delta}{\partial x_{b/p}}\dot{x}_{b/p} + \frac{\partial \Delta}{\partial y_{b/p}}\dot{y}_{p/f}\right]\right] \\
& - \frac{y_{b/p}+g}{\Delta^2+(y_{b/p}+g)^2}\left[\frac{\partial \Delta}{\partial x_{b/p}}\dot{x}_{b/p} + \frac{\partial \Delta}{\partial y_{b/p}}\dot{y}_{b/p}\right]
\end{aligned} \tag{8.39}$$

which shows we have the following necessary condition for the existence of our controller:

Condition 8.1. *If it holds that*

$$C_r \triangleq 1 + \left[\frac{u_{rd}}{u_{rd}^2+v_r^2} - \frac{2v_r\Delta}{\Delta^2+\left(y_{b/p}+g\right)^2}\frac{\partial g}{\partial a}\right]X(u_r) > 0. \tag{8.40}$$

then the yaw rate controller is well defined for all time.

Remark 8.4. The condition above can be verified for any positive velocity, for the vehicles considered in this thesis. Note that for most vessels this condition is verifiable since standard ship design practices will result in similar properties of the function $X(u_r)$. Besides having a lower bound greater then zero C_r is also upper-bounded since the term between brackets can be verified to be bounded in its arguments.

Since $\dot{\psi}_d$ depends on the unknown signal $\tilde{V}_N$ we cannot take $\dot{\psi}_d = r_d$. To define an expression for r_d without requiring the knowledge of $\tilde{V}_N$ we use (8.40) to define

$$\begin{aligned}
r_d = &-\frac{1}{C_r}\left[\kappa(\theta)\left(u_t\cos(\psi+\beta-\gamma_p(\theta)) + k_\delta\frac{x_{b/p}}{\sqrt{1+x_{b/p}^2}} + \hat{V}_T\right)\right. \\
&+ \frac{Y(u_r)v_r u_{rd} - \dot{u}_{rd}v_r}{u_{rd}^2+v_r^2} + \frac{\Delta}{\Delta^2+\left(y_{b/p}+g\right)^2}\left[\dot{\hat{V}}_N\frac{b+\sqrt{b^2-ac}}{-a}\right. \\
&+ \frac{\partial g}{\partial b}\left(2\dot{\hat{V}}_N y_{b/p}\right) + \frac{\partial g}{\partial a}\left(2\hat{V}_N\dot{\hat{V}}_N - 2u_{rd}\dot{u}_{rd} - 2v_r Y(u_r)v_r\right) \\
&+ \left[1+\frac{\partial g}{\partial c}2y_{b/p} + \frac{\partial g}{\partial b}2\hat{V}_N\right]\left(\frac{-u_{td}y_{b/p}}{\sqrt{\Delta^2+(y_{b/p}+g)^2}} + G_1(\cdot) - x_{b/p}\kappa(\theta)\dot{\theta}\right) \\
&+ \frac{\partial g}{\partial c}2\Delta\left[\frac{\partial\Delta}{\partial x_{b/p}}\left(-k_\delta\frac{x_{b/p}}{\sqrt{1+x_{b/p}^2}} + y_{b/p}\kappa(\theta)\dot{\theta}\right)\right. \\
&\left.\left.+ \frac{\partial\Delta}{\partial y_{b/p}}\left(-u_{td}\frac{y_{b/p}}{\sqrt{\Delta^2+(y_{b/p}+g)^2}} + G_1(\cdot) - x_{b/p}\kappa(\theta)\dot{\theta}\right)\right]\right] \\
&- \frac{y_{b/p}+g}{\Delta^2+(y_{b/p}+g)^2}\left[\frac{\partial\Delta}{\partial x_{b/p}}\left(-k_\delta\frac{x_{b/p}}{\sqrt{1+x_{b/p}^2}} + y_{b/p}\kappa(\theta)\dot{\theta}\right)\right. \\
&\left.\left.+ \frac{\partial\Delta}{\partial y_{b/p}}\left(-u_{td}\frac{y_{b/p}}{\sqrt{\Delta^2+(y_{b/p}+g)^2}} + G_1(\cdot) - x_{b/p}\kappa(\theta)\dot{\theta}\right)\right]\right]
\end{aligned} \tag{8.41}$$

with,

$$\begin{aligned}
\dot{\hat{V}}_N = &-\dot{\hat{V}}_x\sin(\gamma_p(\theta)) + \dot{\hat{V}}_y\cos(\gamma_p(\theta)) \\
&-\kappa(\theta)\left(u_t\cos(\psi+\beta-\gamma_p(\theta)) + \frac{k_\delta x_{b/p}}{\sqrt{1+x_{b/p}^2}} - \hat{V}_T\right)\hat{V}_T
\end{aligned} \tag{8.42}$$

Notice that (8.41) is equivalent to (8.36), but without the terms depending on the unknowns $\tilde{V}_x$ and $\tilde{V}_y$ that cannot be used in the input functions. If we substitute

(8.41) in (8.39) and use $\tilde{r} \triangleq r - r_d$ we obtain

$$\begin{aligned}\dot{\tilde{\psi}} = C_r\tilde{r} &+ \frac{\Delta}{\Delta^2 + \left(y_{b/p}+g\right)^2}\left[1 + \frac{\partial g}{\partial c}2y_{b/p} + \frac{\partial g}{\partial b}2\hat{V}_N\right]\tilde{V}_N \\ &+ \left(\frac{2\Delta^2}{\Delta^2 + \left(y_{b/p}+g\right)^2}\frac{\partial g}{\partial c} - \frac{y_{b/p}+g}{\Delta^2 + (y_{b/p}+g)^2}\right)\frac{\partial \Delta}{\partial \boldsymbol{p}_{b/p}}\left[\tilde{V}_T, \tilde{V}_N\right]^T\end{aligned} \tag{8.43}$$

Note that we have used the notation

$$\frac{\partial \Delta}{\partial \boldsymbol{p}_{b/p}}\left[\tilde{V}_T, \tilde{V}_N\right]^T = \frac{\partial \Delta}{\partial x_{b/p}}\tilde{V}_T + \frac{\partial \Delta}{\partial y_{b/p}}\tilde{V}_N. \tag{8.44}$$

From (8.43) it can be seen that choosing r_d as in (8.41) results in yaw angle error dynamics that have a term dependent on the yaw rate error $\tilde{r}$ and a perturbing term that vanishes when the estimation errors $\tilde{V}_T$ and $\tilde{V}_N$ go to zero. To add acceleration feedforward to the yaw rate controller, the derivative of r_d should be calculated. Using the expression of r_d in (8.41) with (8.12), (8.13) and (8.15) it can be seen that r_d has the following dependencies

$$r_d = r_d(h^T, y_{b/p}, x_{b/p}, \tilde{\psi}, \tilde{x}, \tilde{y}), \quad h \triangleq [\theta, v_r, u_r, u_{rd}, \dot{u}_{rd}, \hat{V}_T, \hat{V}_N]^T. \tag{8.45}$$

where h is a vector that contains all the variable whose time derivative do not depend on $\tilde{V}_N$ and $\tilde{V}_T$. However, the other dependencies of r_d do introduce new terms depending on $\tilde{V}_N$ and $\tilde{V}_T$ when the acceleration feedforward is calculated. Consequently, we define our yaw rate controller instead with an acceleration feedforward that contains only the known terms from $\dot{r}_d$

$$\begin{aligned}\tau_r = &- F(u_r, v_r, r) + \frac{\partial r_d}{\partial h^T}\dot{h} + \frac{\partial r_d}{\partial x_{b/p}}\left(-k_\delta \frac{x_{b/p}}{\sqrt{1+x_{b/p}^2}} + y_{b/p}\kappa(\theta)\dot{\theta}\right) \\ &+ \frac{\partial r_d}{\partial \tilde{\psi}}C_r\tilde{r} - \frac{\partial r_d}{\partial \tilde{x}}k_x\tilde{x} - \frac{\partial r_d}{\partial \tilde{y}}k_y\tilde{y} - k_1\tilde{r} - k_2C_r\tilde{\psi} \\ &+ \frac{\partial r_d}{\partial y_{b/p}}\left(-u_{td}\frac{y_{b/p}}{\sqrt{\Delta^2 + (y_{b/p}+g)^2}} + G_1(\cdot) - x_{b/p}\kappa(\theta)\dot{\theta}\right).\end{aligned} \tag{8.46}$$

where $k_1 > 0$ and $k_2 > 0$ are constant controller gains.

Using the controller (8.46) in (8.1f) the yaw rate error dynamics become

$$\begin{aligned}\dot{\tilde{r}} = &- k_1\tilde{r} - k_2C_r\tilde{\psi} - \frac{\partial r_d}{\partial y_{b/p}}\tilde{V}_N - \frac{\partial r_d}{\partial x_{b/p}}\tilde{V}_T + \frac{\partial r_d}{\partial \tilde{x}}\tilde{V}_x + \frac{\partial r_d}{\partial \tilde{y}}\tilde{V}_y \\ &- \frac{\partial r_d}{\partial \tilde{\psi}}\left[\frac{\Delta}{\Delta^2 + \left(y_{b/p}+g\right)^2}\left[1 + \frac{\partial g}{\partial c}2y_{b/p} + \frac{\partial g}{\partial b}2\hat{V}_N\right]\tilde{V}_N\right. \\ &\left.+ \left(\frac{2\Delta^2}{\Delta^2 + \left(y_{b/p}+g\right)^2}\frac{\partial g}{\partial c} - \frac{y_{b/p}+g}{\Delta^2 + (y_{b/p}+g)^2}\right)\frac{\partial \Delta}{\partial \boldsymbol{p}_{b/p}}\left[\tilde{V}_T, \tilde{V}_N\right]^T\right]\end{aligned} \tag{8.47}$$

which contains two stabilising terms $-k_1\tilde{r}$ and $-k_2C_r\tilde{\psi}$, and perturbing terms depending on $\tilde{V}_T$ and $\tilde{V}_N$ that cannot be cancelled by the controller.

Remark 8.5. It is straightforward to verify that all the terms in (8.36) are smooth fractionals that are bounded with respect to ($y_{b/p}$, $x_{b/p}$, $\tilde{x}$, $\tilde{y}$, $\tilde{\psi}$) or are periodic functions with linear arguments and consequently the partial derivatives in (8.46) and (8.47) are all bounded. This is something that is used when showing closed-loop stability in the next section.

8.4 Closed-Loop Analysis

In this section we analyse the closed-loop system of the model (8.1) with controllers (8.10) and (8.46) and observer (8.12), when the frame propagates along the path P with update law (8.7). To show that path following is achieved we have to show that the following error dynamics converge to zero

$$\dot{y}_{b/p} = -u_{td}\frac{y_{b/p}}{\sqrt{\Delta^2+(y_{b/p}+g)^2}} + G_1(\cdot) - x_{b/p}\kappa(\theta)\dot{\theta} + \tilde{V}_N \tag{8.48a}$$

$$\dot{x}_{b/p} = -k_\delta\frac{x_{b/p}}{\sqrt{1+x_{b/p}^2}} + y_{b/p}\kappa(\theta)\dot{\theta} + \tilde{V}_T \tag{8.48b}$$

$$\begin{aligned}\dot{\tilde{\psi}} = {} & C_r\tilde{r} + \frac{\Delta}{\Delta^2+\left(y_{b/p}+g\right)^2}\left[1+\frac{\partial g}{\partial c}2y_{b/p}+\frac{\partial g}{\partial b}2\hat{V}_N\right]\tilde{V}_N \\ & + \left(\frac{2\Delta^2}{\Delta^2+\left(y_{b/p}+g\right)^2}\frac{\partial g}{\partial c} - \frac{y_{b/p}+g}{\Delta^2+(y_{b/p}+g)^2}\right)\frac{\partial \Delta}{\partial \boldsymbol{p}_{b/p}}\left[\tilde{V}_T,\tilde{V}_N\right]^T\end{aligned} \tag{8.48c}$$

$$\begin{aligned}\dot{\tilde{r}} = {} & -k_1\tilde{r} - k_2C_r\tilde{\psi} - \frac{\partial r_d}{\partial y_{b/p}}\tilde{V}_N - \frac{\partial r_d}{\partial x_{b/p}}\tilde{V}_T + \frac{\partial r_d}{\partial \tilde{x}}\tilde{V}_x + \frac{\partial r_d}{\partial \tilde{y}}\tilde{V}_y \\ & - \frac{\partial r_d}{\partial \tilde{\psi}}\left[\frac{\Delta}{\Delta^2+\left(y_{b/p}+g\right)^2}\left[1+\frac{\partial g}{\partial c}2y_{b/p}+\frac{\partial g}{\partial b}2\hat{V}_N\right]\tilde{V}_N\right. \\ & \left. + \left(\frac{2\Delta^2}{\Delta^2+\left(y_{b/p}+g\right)^2}\frac{\partial g}{\partial c} - \frac{y_{b/p}+g}{\Delta^2+(y_{b/p}+g)^2}\right)\frac{\partial \Delta}{\partial \boldsymbol{p}_{b/p}}\left[\tilde{V}_T,\tilde{V}_N\right]^T\right]\end{aligned} \tag{8.48d}$$

$$\dot{\tilde{u}} = -k_u\tilde{u} \tag{8.48e}$$

To show that the error variables in (8.48) converge to zero, we formulate the following total closed-loop system that also contains all variables that converge to zero independently of the variables in (8.48)

$$\begin{aligned}\dot{\tilde{X}}_1 = \begin{bmatrix}\dot{y}_{b/p}\\ \dot{x}_{b/p}\\ \dot{\tilde{\psi}}\\ \dot{\tilde{r}}\end{bmatrix} = {} & \begin{bmatrix}-u_{td}\frac{y_{b/p}}{\sqrt{\Delta^2+(y_{b/p}+g)^2}} - x_{b/p}\kappa(\theta)\dot{\theta} + G_1(\cdot)\\ -k_\delta\frac{x_{b/p}}{\sqrt{1+x_{b/p}^2}} + y_{b/p}\kappa(\theta)\dot{\theta}\\ C_r\tilde{r}\\ -k_1\tilde{r} - k_2C_r\tilde{\psi}\end{bmatrix} \\ & + \begin{bmatrix}\tilde{V}_N\\ \tilde{V}_T\\ G_2(\Delta, y_{b/p}, x_{b/p}, g, \hat{V}_N, \hat{V}_T, \tilde{V}_N, \tilde{V}_T)\\ -\frac{\partial r_d}{\partial \tilde{\psi}}G_2(\cdot) - \frac{\partial r_d}{\partial y_{b/p}}\tilde{V}_N - \frac{\partial r_d}{\partial x_{b/p}}\tilde{V}_T + \frac{\partial r_d}{\partial \tilde{x}}\tilde{V}_x + \frac{\partial r_d}{\partial \tilde{y}}\tilde{V}_y\end{bmatrix}\end{aligned} \tag{8.49a}$$

$$\dot{\tilde{X}}_2 = \begin{bmatrix} \dot{\tilde{x}} \\ \dot{\tilde{y}} \\ \dot{\tilde{V}}_x \\ \dot{\tilde{V}}_y \\ \dot{\tilde{u}} \end{bmatrix} = \begin{bmatrix} -k_{x_1}\tilde{x} - \tilde{V}_x \\ -k_{y_1}\tilde{y} - \tilde{V}_y \\ -k_{x_2}\tilde{x} \\ -k_{y_2}\tilde{y} \\ -k_u\tilde{u} \end{bmatrix} \tag{8.49b}$$

$$\dot{v}_r = X(u_{rd}+\tilde{u})r_d(h, y_{b/p}, x_{b/p}, \tilde{\psi}, \tilde{x}, \tilde{y}) + X(u_{rd}+\tilde{u})\tilde{r} + Y(u_{rd}+\tilde{u})v_r \tag{8.49c}$$

where

$$\begin{aligned} G_2(\cdot) = {} & \frac{\Delta}{\Delta^2 + \left(y_{b/p}+g\right)^2}\left[1 + \frac{\partial g}{\partial c}2y_{b/p} + \frac{\partial g}{\partial b}2\hat{V}_N\right]\tilde{V}_N \\ & + \left(\frac{2\Delta^2}{\Delta^2 + \left(y_{b/p}+g\right)^2}\frac{\partial g}{\partial c} - \frac{y_{b/p}+g}{\Delta^2 + (y_{b/p}+g)^2}\right)\frac{\partial \Delta}{\partial \boldsymbol{p}_{b/p}}\left[\tilde{V}_T, \tilde{V}_N\right]^T \end{aligned} \tag{8.50}$$

Note that $G_2(\Delta, y_{b/p}, x_{b/p}, g, \hat{V}_N, \hat{V}_T, \tilde{V}_N, \tilde{V}_T)$ satisfies

$$G_2(\Delta, y_{b/p}, x_{b/p}, g, \hat{V}_N, \hat{V}_T, 0, 0) = 0 \tag{8.51}$$

$$\|G_2(\Delta, y_{b/p}, x_{b/p}, g, \hat{V}_N, \hat{V}_T, \tilde{V}_N, \tilde{V}_T)\| \leq \zeta_2(\Delta)\|[\tilde{V}_T, \tilde{V}_N]\|, \tag{8.52}$$

where $\zeta_2(\Delta) > 0$, which shows that $G_2(\cdot)$ is zero when the perturbing variables, i.e. $\tilde{V}_T$ and $\tilde{V}_N$, are zero and that it has at most linear growth in the perturbing variables. Note that by an appropriate choice of Δ we will assure that $\zeta_2(\Delta) > 0$ is a constant independent of $x_{b/p}$ and $y_{b/p}$.

The first step in the stability analysis of (8.49) is to assure that the closed-loop system is forward complete and that the sway velocity v_r remains bounded. Therefore, under the assumption that Condition 8.1 is satisfied, i.e. $C_r > 0$, we take the following three steps:

1. First, we prove that the trajectories of the closed-loop system are forward complete.
2. Then, we derive a necessary condition such that v_r is locally bounded with respect to $(\tilde{X}_1, \tilde{X}_2)$.
3. Finally, we establish that for a sufficiently big value of Δ, v_r is locally bounded only with respect to $\tilde{X}_2$, i.e. independently of $\tilde{X}_1$.

Furthermore we design the time-varying look-ahead distance as

$$\Delta(x_{b/p}, y_{b/p}) = \sqrt{\mu + x_{b/p}^2 + y_{b/p}^2}, \tag{8.53}$$

where $\mu > 0$ is a constant. The choice of (8.53) depending on $x_{b/p}$ and $y_{b/p}$ is necessary to find a bounded value of μ to assure local boundedness of v_r with respect to $\tilde{X}_2$ independently of $\tilde{X}_1$.

The above three steps are taken by formulating and proving three lemmas. For the sake of brevity in the main body of this chapter, the proofs of the following lemmas are replaced by a sketch of each proof in the main body. The full proofs can be found in the Appendices 8.A-8.C.

Remark 8.6. In the proof of Lemma 8.2 it is shown that by choosing (8.53) the skew symmetric terms $-x_{b/p}\kappa(\theta)\dot{\theta}$ and $y_{b/p}\kappa(\theta)\dot{\theta}$ do not affect the boundedness of the sway velocity. Choosing Δ to be a constant, independent of $x_{b/p}$ and $y_{b/p}$, as we did in the local case considered in Chapter 7, is impossible since we no longer use $\dot{\theta}$ to cancel all terms in the $x_{b/p}$ dynamics and we can no longer view $x_{b/p}$ as a perturbation to the $y_{b/f}$ dynamics. The choice of Δ proposed in Moe et al. [100], i.e. $\Delta(x_{b/p}) = \sqrt{\mu + x_{b/p}^2}$ is also impossible since the terms that cancel due to skew-symmetry in the case presented here will not vanish. The terms that remain have no upper bound independent of $y_{b/p}$ and g, and therefore a lower bound on μ necessary for boundedness of v_r independent on $x_{b/p}$ and $y_{b/p}$ cannot be found.

Lemma 8.1 (Forward completeness)**.** *The trajectories of the closed-loop system* (8.49) *are forward complete.*

The proof of this lemma is given in Appendix 8.A. The general idea is as follows. Forward completeness for (8.49b) is evident since this part of the closed-loop system consists of GES error dynamics. Using the forward completeness and in fact boundedness of (8.49b) we can show forward completeness of (8.49c), $\dot{\tilde{\psi}}$, and $\dot{\tilde{r}}$. Hence, forward completeness of (8.49) depends on forward completeness of $\dot{x}_{b/p}$ and $\dot{y}_{b/p}$. To show forward completeness of $\dot{x}_{b/p}$ and $\dot{y}_{b/p}$, we consider the $x_{b/p}$ and $y_{b/p}$ dynamics with $\tilde{X}_2$, $\tilde{\psi}$, $\tilde{r}$, and v_r as input which allows us to claim forward completeness of $\dot{x}_{b/p}$ and $\dot{y}_{b/p}$ according to Theorem A.6. Consequently, all the states of the closed-loop system are forward complete and hence the closed-loop system (8.49) is forward complete

Lemma 8.2 (Boundedness near $(\tilde{X}_1, \tilde{X}_2) = 0$)**.** *The system* (8.49c) *is bounded near* $(\tilde{X}_1, \tilde{X}_2) = 0$ *if and only if the curvature of* P *satisfies the following condition:*

$$\kappa_{\max} \triangleq \max_{\theta \in P} |\kappa(\theta)| < \frac{Y_{\min}}{2X_{\max}}. \tag{8.54}$$

The proof of this lemma is given in Appendix 8.B. A sketch of the proof is as follows. The sway velocity dynamics (8.49c) are analysed using a quadratic Lyapunov function $V = 1/2v_r^2$. It can be shown that the derivative of this Lyapunov function satisfies the conditions for boundedness when the solutions are on or close to the manifold where $(\tilde{X}_1, \tilde{X}_2) = 0$. Consequently, (8.49c) satisfies the conditions of boundedness near $(\tilde{X}_1, \tilde{X}_2) = 0$ as long as (8.54) is satisfied.

In Lemma 8.2 we show boundedness of v_r for small values of $(\tilde{X}_1, \tilde{X}_2)$ to derive the bound on the curvature. However, locality with respect to $\tilde{X}_1$, i.e. the path-following errors and yaw angle and yaw rate errors, is not desirable and in the next lemma boundedness independent of $\tilde{X}_1$ is shown under an extra condition on the constant μ from the definition (8.53) of the look-ahead distance Δ.

Lemma 8.3 (Boundedness near $\tilde{X}_2 = 0$)**.** *The system* (8.49c) *is bounded near* $\tilde{X}_2 = 0$*, independent of* $\tilde{X}_1$*, if we choose*

$$\mu > \frac{8X_{\max}}{Y_{\min} - 2X_{\max}\kappa_{\max}}. \tag{8.55}$$

The proof of this lemma is given in Appendix 8.C. The general idea is given as follows. The proof follows along the same lines of that of Lemma 8.2 but solutions are considered close to the manifold $\tilde{X}_2 = 0$ rather than $(\tilde{X}_1, \tilde{X}_2) = 0$. It is shown that boundedness can still be shown if (8.55) is satisfied additionally to the conditions of Lemma 8.2.

Theorem 8.4. *Consider a θ-parametrised path denoted by $P(\theta) \triangleq (x_p(\theta), y_p(\theta))$. Then under Condition 8.1 and the conditions of Lemma 8.1-8.3, the system* (8.1) *with control laws* (8.10) *and* (8.46) *and observer* (8.12) *follows the path P, while maintaining v_r, τ_r and τ_u bounded. In particular, the origin of the system* (8.49a)-(8.49b) *is GAS and LES.*

Proof. From the fact that the origin of (8.49b) is GES, the fact that the closed-loop system (8.49) is forward complete according to Lemma 8.1, and the fact that solutions of (8.49c) are locally bounded near $\tilde{X}_2 = 0$ according to Lemma 8.3, we can conclude that there is a finite time $T > t$ after which solutions of (8.49b) will be sufficiently close to $\tilde{X}_2 = 0$ to guarantee boundedness of v_r.

Having established that v_r is bounded we first analyse the cascade

$$\begin{bmatrix} \dot{\tilde{\psi}} \\ \dot{\tilde{r}} \end{bmatrix} = \begin{bmatrix} C_r \tilde{r} \\ -k_1 \tilde{r} - k_2 C_r \tilde{\psi} \end{bmatrix} + \begin{bmatrix} G_2(\cdot) \\ -\frac{\partial r_d}{\partial \tilde{\psi}} G_2(\cdot) - \frac{\partial r_d}{\partial \boldsymbol{p}_{b/p}} [\tilde{V}_T, \tilde{V}_N]^T + \frac{\partial r_d}{\partial [\tilde{x}, \tilde{y}]^T} \tilde{\boldsymbol{V}}_c \end{bmatrix} \tag{8.56a}$$

$$\begin{bmatrix} \dot{\tilde{x}} \\ \dot{\tilde{y}} \\ \dot{\tilde{V}}_x \\ \dot{\tilde{V}}_y \\ \dot{\tilde{u}} \end{bmatrix} = \begin{bmatrix} -k_{x_1} \tilde{x} - \tilde{V}_x \\ -k_{y_1} \tilde{y} - \tilde{V}_y \\ -k_{x_2} \tilde{x} \\ -k_{y_2} \tilde{y} \\ -k_u \tilde{u} \end{bmatrix} \tag{8.56b}$$

The perturbing system (8.56b) is GES as shown in Section 8.3. The interconnection term, i.e. the second matrix in (8.56a), satisfies the linear growth criteria from Theorem A.3. More specifically, it does not grow with the $\tilde{\psi}$ and $\tilde{r}$ since all the partial derivatives of r_d and $G_2(\cdot)$ can respectively be bounded by constants and linear functions of $\tilde{V}_x$ and $\tilde{V}_y$. The nominal dynamics, i.e. the first matrix in (8.56a), can be analysed with the following quadratic Lyapunov function

$$V_{(\tilde{r},\tilde{\psi})} = \frac{1}{2}\tilde{r}^2 + \frac{1}{2}k_2\tilde{\psi}^2 \tag{8.57}$$

whose derivative along the solutions of the nominal system is given by

$$\dot{V}_{(\tilde{r},\tilde{\psi})} = -k_1\tilde{r}^2 - k_2 C_r \tilde{\psi}\tilde{r} + k_2 C_r \tilde{r}\tilde{\psi} = -k_2\tilde{r}^2 \leq 0 \tag{8.58}$$

which implies that $\tilde{r}$ and $\tilde{\psi}$ are bounded. The derivative of (8.58) is given by

$$\ddot{V}_{(\tilde{r},\tilde{\psi})} = -2k_1^2\tilde{r}^2 - 2k_1 k_2 C_r \tilde{\psi}\tilde{r} \tag{8.59}$$

which is bounded since $\tilde{r}$ and $\tilde{\psi}$ are bounded. This implies that (8.58) is a uniformly continuous function. Consequently, by applying Barbalat's lemma (see Lemma A.7) we have that

$$\lim_{t\to\infty} \dot{V}_{(\tilde{r},\tilde{\psi})} = \lim_{t\to\infty} -k_1\tilde{r}^2 = 0 \;\Rightarrow\; \lim_{t\to\infty} \tilde{r} = 0. \tag{8.60}$$

Since C_r is persistently exciting, which follows from the fact that C_r is upper bounded and lower bounded by a constant larger then zero, it follows from the expression of the nominal dynamics that

$$\lim_{t\to\infty} \tilde{r} = 0 \;\Rightarrow\; \lim_{t\to\infty} \tilde{\psi} = 0. \tag{8.61}$$

This implies that the system is globally asymptotically stable according to Definition A.3 and since the nominal dynamics are linear it follows that the nominal dynamics are globally exponentially stable. Consequently, from the above it follows that the cascade (8.56) is GES using Theorem A.3 and Proposition A.1.

We now consider the following dynamics

$$\begin{bmatrix} \dot{y}_{b/p} \\ \dot{x}_{b/p} \end{bmatrix} = \begin{bmatrix} -u_{td}\frac{y_{b/p}}{\sqrt{\Delta^2+(y_{b/p}+g)^2}} - x_{b/p}\kappa(\theta)\dot{\theta} \\ -k_\delta \frac{x_{b/p}}{\sqrt{1+x_{b/p}^2}} + y_{b/p}\kappa(\theta)\dot{\theta} \end{bmatrix} + \begin{bmatrix} \tilde{V}_N + G_1(\cdot) \\ \tilde{V}_T \end{bmatrix}. \tag{8.62}$$

Note that we can view the systems (8.56) and (8.62) as a cascaded system where the nominal dynamics are formed by the first matrix of (8.62), the interconnection term is given by second matrix of (8.62), and the perturbing dynamics are given by (8.56). As we have just shown the perturbing dynamics are GES. Using (8.28) it is straightforward to verify that the interconnection term satisfies the conditions of Theorem A.3. We now consider the following Lyapunov function for the nominal system

$$V_{(x_{b/p},y_{b/p})} = \frac{1}{2}x_{b/p}^2 + \frac{1}{2}y_{b/p}^2. \tag{8.63}$$

whose derivative along the solutions of the nominal system is given by

$$\dot{V}_{(x_{b/p},y_{b/p})} = -u_{td}\frac{y_{b/p}^2}{\sqrt{\Delta^2+(y_{b/p}+g)^2}} - k_\delta \frac{x_{b/p}^2}{\sqrt{1+x_{b/p}^2}} \leq 0, \tag{8.64}$$

which implies that the nominal system is GAS. Moreover, since it is straightforward to verify that $\dot{V}_{(x_{b/p},y_{b/p})} \leq \alpha V_{(x_{b/p},y_{b/p})}$ for some constant α dependent on initial conditions, it follows from the comparison lemma (Lemma A.5) that the nominal dynamics are also LES. Consequently, the cascaded system satisfies the conditions of Theorem A.3 and Lemma A.4, and therefore the cascaded system is GAS and LES. This implies that the origin of the error dynamics, i.e. $(\tilde{X}_1, \tilde{X}_2) = (0, 0)$, is globally asymptotically stable and locally exponentially stable. □

8.5 Case Study

This section presents a case study for the theoretical results presented in this chapter. We will apply the path-following approach to the case of following a circular path. The ocean current components are given by $V_x = -1$ [m/s] and $V_y = 1.2$ [m/s] and consequently $V_{\max} \approx 1.562$ [m/s]. The desired relative surge velocity is chosen to be constant and set to $u_{rd} = 5$ [m/s] such that Assumption 8.3 is verified. The simulation uses the ship model parameters from Fredriksen and Pettersen [63]

which are given in Section C.1 of the thesis. Using these parameters and expressions (8.2c) and (8.2d) it is straightforward to verify that the curvature bound from Lemma 8.2 is given by $\kappa_{\max} < (Y_{\min})/(2X_{\max}) \approx 0.0667$. The observer is initialised as suggested in Subsection 8.3.2 and the observer gains are selected as $k_{x_1} = k_{y_1} = 1$ and $k_{x_1} = k_{y_1} = 0.1$. The controller gains are selected as $k_{u_r} = 0.1$ for the surge velocity controller and $k_1 = 1000$ and $k_2 = 400$ for the yaw rate controller.

In this case study the vessel is required to follow a circle with a radius of 400 [m]. Consequently, the curvature of the path is given by $\kappa_p = 1/400 = 0.0025$. This implies we satisfy our constraint on the curvature $\kappa_p < (Y_{\min})/(2X_{\max}) \approx 0.0667$. The required value for μ can be calculated as suggested in Lemma 8.3 to obtain $\mu > 62.3468$ [m], which can be satisfied by taking $\mu = 70$ [m]. The initial conditions are taken as

$$[u_r(t_0), v_r(t_0), r(t_0), x(t_0), y(t_0), \psi(t_0)]^T = [0, 0, 0, 700, 10, \pi/2]^T. \tag{8.65}$$

The resulting trajectory of the ship can be seen in Figure 8.3. The dashed blue line is the trajectory of the vessel and the red cicle is the reference. The yellow ships represent the orientation of the ship at certain times. From Figure 8.3 it can clearly be seen that the orientation of the ship is not tangent to the circle, which is indeed what is needed to compensate for the ocean current.

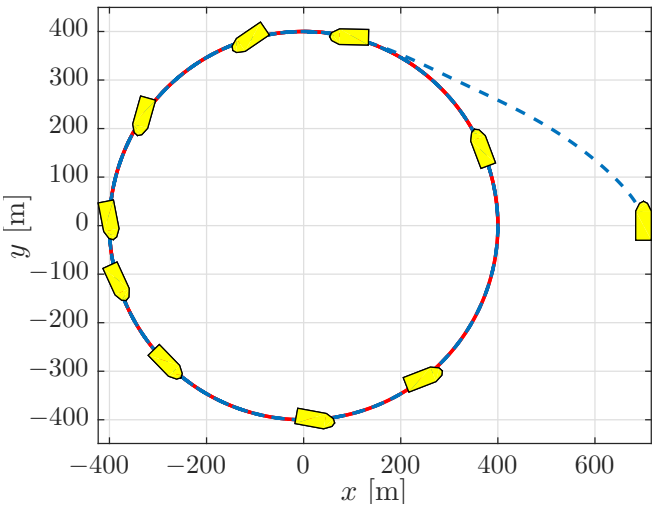

Figure 8.3: Path of the vessel in the $x - y$-plane. The dashed blue line is the trajectory of the path and the red line is the reference. The yellow ships denote the orientation of the vessel at certain times.

The path-following errors in tangential direction, $x_{b/p}$, and in normal direction, $y_{b/p}$ can be seen in the top plot of Figure 8.4 from which it can clearly be seen that the path-following error converge to zero after a transient period. A detail of the last portion of the simulation is given to illustrate the errors converge to zero.

The estimates for the ocean current components obtained from the ocean current observer are given in the second plot from the top in Figure 8.4. From this plot it can clearly be seen that the estimates converge to the desired values without overshoot, which illustrates the conservativeness of the bound $2V_{\max} < u_{rd}(t),\ \forall t$, derived in the analysis of the observer-error dynamics in Subsection 8.3.2. The yaw rate r and sway velocity v_r are plotted together in the third plot of Figure 8.4. These plots show that due to the curvature of the path the yaw rate and sway velocity do not converge to zero but follow a periodic motion induced by the motion along the circle. The periodic signals are not symmetric due to the ocean current affecting the ship's motion, i.e. on part of the circle the ship moves against the current and on part of the circle it moves with the current. The relative surge velocity is plotted in the fourth plot from the top of Figure 8.4. This plot clearly shows the exponential convergence of the velocity as it moves to the desired value of $u_{rd} = 5$ [m/s]. Especially interesting is the coupling of the relative surge velocity with the value of C_r from Condition 8.1, which is plotted in the bottom plot of Figure 8.4. From this plot it can clearly be seen that C_r is bounded away from zero throughout the motion.

To compared the result and case study in Chapter 7 to the approach presented here it is most interesting to study the transient when the vehicle converges to the path. In particular, since when the vehicle is on the path the guidance laws become equivalent. If we compare the transients in Figure 7.3 and Figure 8.3 it is evident that the vessel takes a much wider approach to the circle in the global case then in the local case from Chapter 7. This is caused by the fact that the look-ahead distance Δ in the local case is always smaller then the look-ahead distance in the global case. Even when the μ of the global case is equal to the Δ of the local case, the look-ahead distance in the global case will be increased by the values of the errors during transient. Consequently, the global case will lead to slower convergence. In fact the faster convergence is confirmed by the plots of $x_{b/p}$ and $y_{b/p}$ in Figure 7.4 and Figure 8.4.

8.6 Conclusion

In this chapter curved-path following for underactuated marine vessels in the presence of constant ocean currents has been considered. In this approach the path is parametrised by a path variable with a globally defined update law. The vessel is steered using a line-of-sight like guidance law where the lookahead-distance depends on the path-following errors. To compensate for the unknown ocean currents the guidance law is aided by an ocean current observer. The closed-loop system with the controllers and observer was analysed. This was done by first showing boundedness of the underactuated sway velocity dynamics under certain conditions. It was then shown that if these conditions are satisfied and the sway velocity is bounded the path-following errors are globally asymptotically stable and locally exponentially stable.

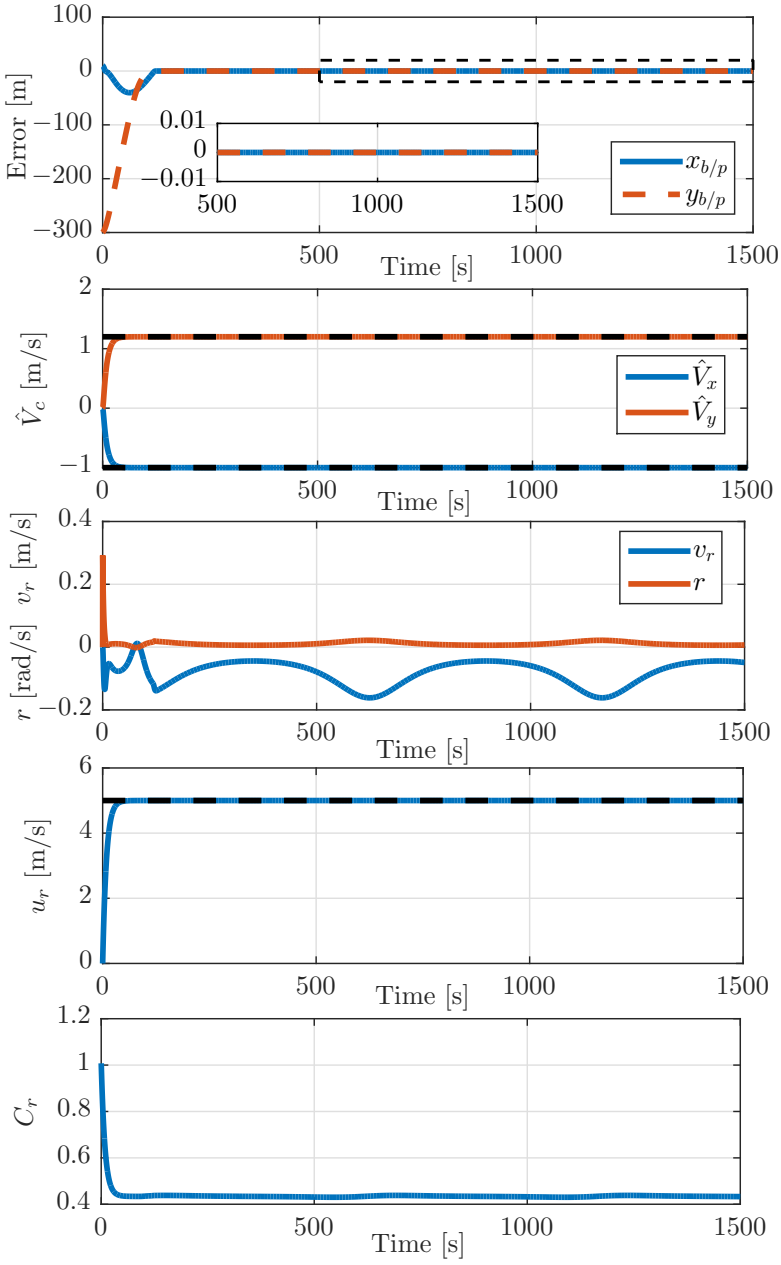

Figure 8.4: Path following errros plotted agains time (top), current estimates against time (second), sway velocity and yaw rate against time (third), surge velocity against time (fourth), and size of C_r over time (bottom).

8.A Proof of Lemma 8.1

Consider the following part of the global closed-loop system:

$$\begin{aligned}\begin{bmatrix}\dot{\tilde{\psi}}\\ \dot{\tilde{r}}\end{bmatrix} =& \begin{bmatrix} C_r\tilde{r} \\ -k_1\tilde{r} - k_2C_r\tilde{\psi}\end{bmatrix} \\ &+ \underbrace{\begin{bmatrix} G_2(\Delta, y_{b/p}, x_{b/p}, g, \hat{V}_N, \hat{V}_T, \tilde{V}_N, \tilde{V}_T) \\ -\frac{\partial r_d}{\partial \tilde{\psi}}G_2(\cdot) - \frac{\partial r_d}{\partial y_{b/p}}\tilde{V}_N - \frac{\partial r_d}{\partial x_{b/p}}\tilde{V}_T + \frac{\partial r_d}{\partial \tilde{x}}\tilde{V}_x + \frac{\partial r_d}{\partial \tilde{y}}\tilde{V}_y\end{bmatrix}}_{R(h, y_{b/p}, \delta_x, \tilde{\psi}, \tilde{x}, \tilde{y})} \qquad (8.66a)\end{aligned}$$

$$\dot{v}_r = X(u_{rd}+\tilde{u})r_d(h, y_{b/p}, \delta_x, \tilde{\psi}, \tilde{x}, \tilde{y}) + X(u_{rd}+\tilde{u})\tilde{r} + Y(u_{rd}+\tilde{u})v_r \qquad (8.66b)$$

where

$$\begin{aligned}G_2(\cdot) =& \frac{\Delta}{\Delta^2 + \left(y_{b/p}+g\right)^2}\left[1 + \frac{\partial g}{\partial c}2y_{b/p} + \frac{\partial g}{\partial b}2\hat{V}_N\right]\tilde{V}_N \\ &+ \left(\frac{2\Delta^2}{\Delta^2 + \left(y_{b/p}+g\right)^2}\frac{\partial g}{\partial c} - \frac{y_{b/p}+g}{\Delta^2 + (y_{b/p}+g)^2}\right)\frac{\partial \Delta}{\partial \boldsymbol{p}_{b/p}}\left[\tilde{V}_T, \tilde{V}_N\right]^T\end{aligned} \qquad (8.67)$$

From the boundedness of the vector $[\tilde{X}_2^T, \kappa(\theta), u_{rd}, \dot{u}_{rd}, V_T, V_N]^T$ we know that $\left\|[\tilde{X}_2^T, \kappa(\theta), u_{rd}, \dot{u}_{rd}, V_T, V_N]^T\right\| \leq \beta_0$, and from (8.41) we can conclude the existence of positive functions $a_{r_d}(\cdot)$, $b_{r_d}(\cdot)$, $a_R(\cdot)$, and $b_R(\cdot)$ which are all continuous in their arguments and are such that such the following inequalities hold:

$$|r_d(\cdot)| \leq a_{r_d}(\mu, \beta_0)\,|v_r| + b_{r_d}(\mu, \beta_0) \qquad (8.68)$$

and,

$$\|R(\cdot)\| \leq a_R(\mu, \beta_0)\,|v_r| + b_R(\mu, \beta_0) \qquad (8.69)$$

Then we choose the following Lyapunov function candidate:

$$V_1(\tilde{\psi}, \tilde{r}, v_r) = \frac{1}{2}\left(k_2\tilde{\psi}^2 + \tilde{r}^2 + v_r^2\right) \qquad (8.70)$$

whose time derivative along the solutions of (8.66) is

$$\begin{aligned}\dot{V}_1(\cdot) =& \; k_2C_r\tilde{r}\tilde{\psi} - k_1\tilde{r}^2 - k_2C_r\tilde{r}\tilde{\psi} + [\tilde{\psi} \;\; \tilde{r}]R(\cdot) \\ &+ Y(u_{rd}+\tilde{u})v_r^2 + X(u_{rd}+\tilde{u})\tilde{r}v_r + X(u_{rd}+\tilde{u})r_d(\cdot)v_r\end{aligned} \qquad (8.71)$$

Using Young's inequality we note that

$$\begin{aligned}\dot{V}_1(\cdot) &\leq k_1\tilde{r}^2 + \tilde{\psi}^2 + \tilde{r}^2 + R^2(\cdot) + Y(u_{rd}+\tilde{u})v_r^2 \\ &\quad + |X(u_{rd}+\beta_0)|\left(\tilde{r}^2 + v_r^2\right) + |X(u_{rd}+\beta_0)|\left(r_d^2(\cdot) + v_r^2\right) \\ &\leq \alpha V_1 + \beta, \quad \alpha \geq 0, \quad \beta \geq 0\end{aligned} \qquad (8.72)$$

Note that since the differential inequality (8.72) is scaler we can invoke the comparison lemma Khalil [82, Lemma 3.4] given as Lemma A.5 in Appendix A. From Lemma A.5 we know that the solutions of differential inequality (8.72) are bounded by the solutions of the linear system:

$$\dot{x} = \alpha x + \beta \tag{8.73}$$

which has solutions

$$x(t) = \frac{\|x(t_0)\|\alpha + \beta}{\alpha} e^{\alpha(t-t_0)} - \frac{\beta}{\alpha} \tag{8.74}$$

Hence, from Lemma A.5 we have that

$$V_1(\cdot) \leq \frac{\|V_1(t_0)\|\alpha + \beta}{\alpha} e^{\alpha(t-t_0)} - \frac{\beta}{\alpha} \tag{8.75}$$

which shows the solutions of $V_1(\cdot)$ are defined up to $t_{\max} = \infty$ and consequently from (8.70) it follows that the solutions of $\tilde{\psi}$, $\tilde{r}$, and v_r must be defined up to $t_{\max} = \infty$. Hence, the solutions of (8.66) satisfy Definition A.7 and we can conclude forward completeness of trajectories of (8.66).

The forward completeness of trajectories of the global closed-loop system now depends on forward completeness of of $\dot{y}_{b/p}$ and $\dot{x}_{b/p}$ from (8.49a). We can conclude forward completeness of $\dot{y}_{b/p}$ and $\dot{x}_{b/p}$ by considering the Lyapunov function

$$V_2 = \frac{1}{2} x_{b/p}^2 + \frac{1}{2} y_{b/p}^2. \tag{8.76}$$

The time derivative of (8.76) is given by

$$\begin{aligned}
\dot{V}_2 &= x_{b/p}\dot{x}_{b/p} + y_{b/p}\dot{y}_{b/p} \\
&\leq -u_{td}\frac{y_{b/p}^2}{\sqrt{\Delta^2 + (y_{b/p}+g)^2}} - \frac{k_\delta x_{b/p}^2}{\sqrt{1+x_{b/p}^2}} + (G_1(\cdot) + \tilde{V}_N) y_{b/p} + \tilde{V}_T x_{b/p} \\
&\leq (G_1 + \tilde{V}_N) y_{b/p} + \tilde{V}_T x_{b/p}
\end{aligned} \tag{8.77}$$

where using the bound on $G_1(\cdot)$ from (8.28) and Young's inequality we obtain

$$\dot{V}_2 \leq V_2 + \frac{1}{2}\left(\zeta^2(u_{td})\|[\tilde{\psi}, \tilde{r}]^T\|^2 + \tilde{V}_N^2 + \tilde{V}_T^2\right) \tag{8.78}$$

$$\leq V_2 + \sigma_2(v_r, \tilde{\psi}, \tilde{r}, \tilde{V}_N, \tilde{V}_T) \tag{8.79}$$

with $\sigma_2(\cdot) \in \mathcal{K}_\infty$. Consequently, if we view the arguments of $\sigma_2(\cdot)$ as input to the $x_{b/p}$ and $y_{b/p}$ dynamics, then (8.78) satisfies Theorem A.6 and hence $\dot{x}_{b/p}$ and $\dot{y}_{b/p}$ are forward complete. Note that the arguments of $\sigma_2(\cdot)$ are all forward complete and therefore fit the definition of an input signal given in Definition A.7. We have now shown forward completeness of (8.49a) and (8.49c) and since (8.49b) is GES is is trivially forward complete. We can therefore claim forward completeness of the entire closed-loop system (8.49) and the proof of Lemma 8.1 is complete.

8.B Proof of Lemma 8.2

Recall the sway velocity dynamics (8.49c):

$$\dot{v}_r = X(\tilde{u} + u_{rd})(r_d + \tilde{r}) + Y(u_{rd} + \tilde{u})v_r, \quad Y(u_{rd}) < 0$$

Consider the following Lyapunov function candidate:

$$V_3(v_r) = \frac{1}{2}v_r^2 \tag{8.80}$$

The derivative of (8.80) along the solutions of (8.49c) is given by

$$\begin{aligned}\dot{V}_3 &= v_r\dot{v}_r = v_r X(u_{rd} + \tilde{u})r_d + X(u_{rd} + \tilde{u})v_r\tilde{r} + Y(u_{rd} + \tilde{u})v_r^2 \\ &\leq X(u_{rd})r_d v_r + a_x\tilde{u}r_d v_r + X(u_{rd})v_r\tilde{r} + a_x\tilde{u}v_r\tilde{r} + a_y\tilde{u}v_r^2 + Y(u_{rd})v_r^2\end{aligned} \tag{8.81}$$

where we used the fact that:

$$Y(u_r) = a_y u_r + b_y \tag{8.82}$$
$$X(u_r) = a_x u_r + b_x \tag{8.83}$$

The term $r_d v_r$ is given by

$$\begin{aligned}r_d v_r = &- \frac{v_r}{C_r}\Bigg[\kappa(\theta)\left(u_t\cos(\psi + \beta - \gamma_p(\theta)) + k_\delta\frac{x_{b/p}}{\sqrt{1 + x_{b/p}^2}} + \hat{V}_T\right) \\ &+ \frac{Y(u_r)v_r u_{rd} - \dot{u}_{rd}v_r}{u_{rd}^2 + v_r^2} + \frac{\Delta}{\Delta^2 + \left(y_{b/p} + g\right)^2}\Bigg[\dot{\hat{V}}_N\frac{b + \sqrt{b^2 - ac}}{-a} \\ &+ \frac{\partial g}{\partial b}\left(2\hat{\dot{V}}_N y_{b/p}\right) + \frac{\partial g}{\partial a}\left(2\hat{V}_N\dot{\hat{V}}_N - 2u_{rd}\dot{u}_{rd} - 2v_r Y(u_r)v_r\right) \\ &+ \left[1 + \frac{\partial g}{\partial c}2y_{b/p} + \frac{\partial g}{\partial b}2\hat{V}_N\right]\left(\frac{-u_{td}y_{b/p}}{\sqrt{\Delta^2 + (y_{b/p} + g)^2}} + G_1(\cdot) - x_{b/p}\kappa(\theta)\dot{\theta}\right) \\ &+ \frac{\partial g}{\partial c}2\Delta\Bigg[\frac{\partial\Delta}{\partial x_{b/p}}\left(-k_\delta\frac{x_{b/p}}{\sqrt{1 + x_{b/p}^2}} + y_{b/p}\kappa(\theta)\dot{\theta}\right) \\ &+ \frac{\partial\Delta}{\partial y_{b/p}}\left(-u_{td}\frac{y_{b/p}}{\sqrt{\Delta^2 + (y_{b/p} + g)^2}} + G_1(\cdot) - x_{b/p}\kappa(\theta)\dot{\theta}\right)\Bigg]\Bigg] \\ &- \frac{y_{b/p} + g}{\Delta^2 + (y_{b/p} + g)^2}\Bigg[\frac{\partial\Delta}{\partial x_{b/p}}\left(-k_\delta\frac{x_{b/p}}{\sqrt{1 + x_{b/p}^2}} + y_{b/p}\kappa(\theta)\dot{\theta}\right) \\ &+ \frac{\partial\Delta}{\partial y_{b/p}}\left(-u_{td}\frac{y_{b/p}}{\sqrt{\Delta^2 + (y_{b/p} + g)^2}} + G_1(\cdot) - x_{b/p}\kappa(\theta)\dot{\theta}\right)\Bigg]\Bigg]\end{aligned} \tag{8.84}$$

We now introduce a term $F(\tilde{X}_1, \tilde{X}_2, \Delta, V_T, V_T, u_{rd}, v_r)$ to collect all the terms that grow linearly with v_r and the terms that grow quadratically with v_r but vanish when $\tilde{X}_1$ and $\tilde{X}_2$ are zero. Consequently we rewrite (8.84) to obtain

$$\begin{aligned} r_d v_r = &- \frac{v_r}{C_r}\left[1 + \frac{\Delta x_{b/p}}{\Delta^2 + \left(y_{b/p} + g\right)^2}\right]\kappa(\theta)\left(u_t \cos(\psi + \beta - \gamma_p(\theta))\right) \\ &- \frac{1}{C_r}\left(\frac{u_{rd}}{u_{rd}^2 + v_r^2} - \frac{2\Delta v_r}{\Delta^2 + (y_{b/p} + g)^2}\frac{\partial g}{\partial a}\right) Y(u_r) v_r^2 \\ &+ F(\tilde{X}_1, \tilde{X}_2, \Delta, V_T, V_T, u_{rd}, v_r) \end{aligned} \tag{8.85}$$

where

$$\begin{aligned} F(\cdot) = &- \frac{v_r}{C_r}\left[\kappa(\theta)\left(k_\delta \frac{x_{b/p}}{\sqrt{1 + x_{b/p}^2}} + \hat{V}_T\right) - \frac{\dot{u}_{rd} v_r}{u_{rd}^2 + v_r^2}\right. \\ &+ \frac{\Delta}{\Delta^2 + \left(y_{b/p} + g\right)^2}\left[\dot{\hat{V}}_N \frac{b + \sqrt{b^2 - ac}}{-a} + \frac{\partial g}{\partial b}\left(2\dot{\hat{V}}_N y_{b/p}\right)\right. \\ &+ 2\frac{\partial g}{\partial a}\left(\hat{V}_N \dot{\hat{V}}_N - u_{rd}\dot{u}_{rd}\right) - x_{b/p}\kappa(\theta)\left(\frac{k_\delta x_{b/p}}{\sqrt{1 + x_{b/p}^2}} + \hat{V}_T\right) \\ &+ \left[\frac{\partial g}{\partial c} 2 y_{b/p} + \frac{\partial g}{\partial b}\left(2\hat{V}_N\right)\right]\left(\frac{-u_{td} y_{b/p}}{\sqrt{\Delta^2 + (y_{b/p} + g)^2}} + G_1(\cdot) - x_{b/p}\kappa(\theta)\dot{\theta}\right) \\ &\left.\left. - \frac{\partial g}{\partial c} 2\Delta\left[\frac{\partial \Delta}{\partial x_{b/p}}\frac{k_\delta x_{b/p}}{\sqrt{1 + x_{b/p}^2}} + \frac{\partial \Delta}{\partial y_{b/p}}\left(\frac{u_{td} y_{b/p}}{\sqrt{\Delta^2 + (y_{b/p} + g)^2}} + G_1(\cdot)\right)\right]\right] \\ &+ \frac{y_{b/p} + g}{\Delta^2 + (y_{b/p} + g)^2}\left[\frac{\partial \Delta}{\partial x_{b/p}}\frac{k_\delta x_{b/p}}{\sqrt{1 + x_{b/p}^2}}\right. \\ &\left.\left. + \frac{\partial \Delta}{\partial y_{b/p}}\left(\frac{u_{td} y_{b/p}}{\sqrt{\Delta^2 + (y_{b/p} + g)^2}} + G_1(\cdot)\right)\right]\right] \end{aligned} \tag{8.86}$$

Note here that using our definition of Δ in (8.53) all the terms in $r_d v_r$ with partial derivatives of Δ multiplied by $\dot{\theta}$ are cancelled due to skew-symmetry. It is straightforward to verify that the function $F(\cdot)$ satisfies the following inequality:

$$|F(\cdot)| \leq F_2(\tilde{X}_1, \tilde{X}_2, \Delta, V_T, V_N, u_{rd}) v_r^2 + F_1(\tilde{X}_1, \tilde{X}_2, \Delta, V_T, V_N, u_{rd})\,|v_r| \tag{8.87}$$

where $F_{1,2}(\cdot)$ are positive functions continuous in their arguments with:

$$F_2(0, 0, \Delta, V_T, V_N, u_{rd}) = 0. \tag{8.88}$$

Consequently, using (8.85) the term $r_d v_r$ can be bounded as a function of v_r as follows

$$\begin{aligned} r_d v_r &\leq \sqrt{u_r^2 + v_r^2} \left| \frac{v_r}{C_r} \right| |\kappa(\theta)| \left| \left[-1 + \frac{\Delta x_{b/p}}{\Delta^2 + \left(y_{b/p} + g\right)^2} \right] \right| + |F(\cdot)| \\ &\quad - \frac{1}{C_r} \left(\frac{u_{rd}}{u_{rd}^2 + v_r^2} - \frac{2\Delta v_r}{\Delta^2 + (y_{b/p} + g)^2} \frac{\partial g}{\partial a} \right) Y(u_r) v_r^2 \\ &\leq \left| \frac{v_r^2}{C_r} \right| |\kappa(\theta)| \left| \left[-1 + \frac{\Delta x_{b/p}}{\Delta^2 + \left(y_{b/p} + g\right)^2} \right] \right| + |F(\cdot)| \\ &\quad + \left| \frac{v_r}{C_r} \right| |\kappa(\theta)| \, |u_r| \left| \left[-1 + \frac{\Delta x_{b/p}}{\Delta^2 + \left(y_{b/p} + g\right)^2} \right] \right| \\ &\quad - \frac{1}{C_r} \left(\frac{u_{rd}}{u_{rd}^2 + v_r^2} - \frac{2\Delta v_r}{\Delta^2 + (y_{b/p} + g)^2} \frac{\partial g}{\partial a} \right) Y(u_r) v_r^2 \end{aligned} \tag{8.89}$$

Remark 8.7. The necessity for the choice of Δ as in (8.53) becomes evident from (8.85). The choice of Δ constant would make all partial derivatives of Δ equal to zero. However, from $v_r/C_r x_{b/p} \kappa(\theta) \dot{\theta}$ we obtain a term of the form

$$\frac{v_r^2}{C_r} \kappa(\theta) \frac{\Delta^2 x_{b/p}}{(\Delta^2 + (y_{b/f} + g)^2)^{3/2}} \tag{8.90}$$

which grows quadratically in v_r with a gain that cannot be bounded independent of $x_{b/f}$ if Δ is independent of $x_{b/f}$. Therefore, boundedness of v_r cannot be shown independently of $x_{b/f}$. With the choice of $\Delta = \sqrt{\mu^2 + x_{b/p}^2}$ as proposed in Moe et al. [100], the partial derivatives with respect to $y_{b/p}$ would be zero. The term in (8.90) would now be upper-bounded by one. However, a new term would then be introduced from the partial derivative of Δ

$$\frac{v_r^2}{C_r} \frac{\partial \Delta}{\partial x_{b/p}} \kappa(\theta) \frac{\Delta y_{b/p} (y_{b/p} + g)}{(\Delta^2 + (y_{b/f} + g)^2)^{3/2}} \tag{8.91}$$

where it should be noted that this term can grow unbounded in $y_{b/p}$ near the manifold where $g = -(y_{b/p} + 1)$. Hence, the growth of this quadratic term in v_r cannot be upper-bounded independent of $y_{b/p}$.

To avoid the issues describe in Remark 8.7, we choose Δ as defined in (8.53). Using the definition of $\Delta(x_{b/p}, y_{b/p})$ given in (8.53) it is straightforward to verify

that

$$\begin{aligned} r_d v_r \leq & \left|\frac{v_r^2}{C_r}\right| |\kappa(\theta)| \left|\left[-1+\frac{\Delta x_{b/p}}{\Delta^2+\left(y_{b/p}+g\right)^2}\right]\right| + |F(\cdot)| \\ & + \left|\frac{v_r}{C_r}\right| |\kappa(\theta)|\,|u_r| \left|\left[-1+\frac{\Delta x_{b/p}}{\Delta^2+\left(y_{b/p}+g\right)^2}\right]\right| \\ & - \frac{1}{C_r}\left(\frac{u_{rd}}{u_{rd}^2+v_r^2} - \frac{2\Delta v_r}{\Delta^2+(y_{b/p}+g)^2}\frac{\partial g}{\partial a}\right) Y(u_r) v_r^2 \\ \leq & \, 2\left|\frac{v_r^2}{C_r}\right| |\kappa(\theta)| + 2\,|u_r| \left|\frac{v_r}{C_r}\right| |\kappa(\theta)| + |F(\cdot)| \\ & - \frac{1}{C_r}\left(\frac{u_{rd}}{u_{rd}^2+v_r^2} - \frac{2\Delta v_r}{\Delta^2+(y_{b/p}+g)^2}\frac{\partial g}{\partial a}\right) Y(u_r) v_r^2 \end{aligned} \tag{8.92}$$

When substituting (8.92) in (8.81) we obtain

$$\begin{aligned} \dot{V}_3 = v_r \dot{v}_r \leq & \frac{1}{C_r}\Big[2\,|X(u_{rd})|\,|\kappa(\theta)| + Y(u_{rd})\Big] v_r^2 + a_y \tilde{u} v_r^2 + a_x \tilde{u} v_r \tilde{r} \\ & + X(u_{rd})\left(F(\cdot) + 2\,|u_r|\left|\frac{v_r}{C_r}\right|\right) + a_x \tilde{u} r_d v_r + X(u_{rd}) v_r \tilde{r} \end{aligned} \tag{8.93}$$

Consequently, on the manifold where $(\tilde{X}_1, \tilde{X}_2) = 0$ we have

$$\dot{V}_3 \leq \frac{1}{C_r^*}\Big(2X_{\max}\,|\kappa(\theta)| + Y_{\min}\Big) v_r^2 + X(u_{rd}) F_1(0,0,\Delta,V_T,V_N,u_{rd}) |v_r| \tag{8.94}$$

where $C_r^*(v_r, x_{b/p}, y_{b/p}, \Delta, V_N, u_{rd}) = C_r(v_r, x_{b/p}, y_{b/p}, \Delta, \hat{V}_N = V_N, u_r = u_{rd})$. Boundedness of (8.94) is guaranteed as long as

$$2X_{\max}\,|\kappa(\theta)| + Y_{\min} < 0 \tag{8.95}$$

Hence, satisfaction of (8.54) renders the quadratic term in (8.94) negative and since the quadratic term is dominant for sufficiently large v_r, (8.94) is negative definite for sufficiently large v_r. If $\dot{V}_3$ is negative for sufficiently large v_r this implies that V_3 decreases for sufficiently large v_r. Since $V_3 = 1/2 v_r^2$, a decrease in V_3 implies a decrease in v_r^2 and by extension in v_r. Therefore, v_r cannot increase above a certain value and v_r is bounded near the manifold where $(\tilde{X}_1, \tilde{X}_2) = 0$.

Remark 8.8. Note that $C_r^*(v_r, y_{b/f}, \Delta, V_N, u_{rd})$ can be found independently of $y_{b/p}$ and $x_{b/p}$ since the terms in C_r are bounded with respect to these variables.

Consequently, close to the manifold where $(\tilde{X}_1, \tilde{X}_2) = 0$ the sufficient and necessary condition for local boundedness of (8.49c) is the following:

$$2X_{\max}\,|\kappa(\theta)| + Y_{\min} < 0 \tag{8.96}$$

which is satisfied if and only if the condition in Lemma 8.2 is satisfied. This completes the proof of Lemma 8.2.

8.C Proof of Lemma 8.3

Recall the sway velocity dynamics (8.49c):

$$\dot{v}_r = X(\tilde{u} + u_{rd})(r_d + \tilde{r}) + Y(u_{rd} + \tilde{u})v_r, \quad Y(u_{rd}) < 0$$

Consider the following Lyapunov function candidate:

$$V_3(v_r) = \frac{1}{2}v_r^2 \tag{8.97}$$

The derivative of (8.97) along the solutions of (8.49c) is given by

$$\begin{aligned}\dot{V}_3 &= v_r\dot{v}_r = v_r X(u_{rd} + \tilde{u})r_d + X(u_{rd} + \tilde{u})v_r\tilde{r} + Y(u_{rd} + \tilde{u})v_r^2 \\ &\leq X(u_{rd})r_d v_r + a_x\tilde{u}r_d v_r + X(u_{rd})v_r\tilde{r} + a_x\tilde{u}v_r\tilde{r} + a_y\tilde{u}v_r^2 + Y(u_{rd})v_r^2\end{aligned} \tag{8.98}$$

where we used the fact that:

$$Y(u_r) = a_y u_r + b_y \tag{8.99}$$
$$X(u_r) = a_x u_r + b_x \tag{8.100}$$

The term $r_d v_r$ is given by:

$$\begin{aligned}r_d v_r = &- \frac{v_r}{C_r}\Bigg[\kappa(\theta)\left(u_t\cos(\psi + \beta - \gamma_p(\theta)) + k_\delta\frac{x_{b/p}}{\sqrt{1 + x_{b/p}^2}} + \hat{V}_T\right) \\ &+ \frac{Y(u_r)v_r u_{rd} - \dot{u}_{rd}v_r}{u_{rd}^2 + v_r^2} + \frac{\Delta}{\Delta^2 + \left(y_{b/p} + g\right)^2}\Bigg[\dot{\hat{V}}_N\frac{b + \sqrt{b^2 - ac}}{-a} \\ &+ \frac{\partial g}{\partial b}\left(2\hat{V}_N y_{b/p}\right) + \frac{\partial g}{\partial a}\left(2\hat{V}_N\dot{\hat{V}}_N - 2u_{rd}\dot{u}_{rd} - 2v_r Y(u_r)v_r\right) \\ &+ \left[1 + \frac{\partial g}{\partial c}2y_{b/p} + \frac{\partial g}{\partial b}2\hat{V}_N\right]\left(\frac{-u_{td}y_{b/p}}{\sqrt{\Delta^2 + (y_{b/p} + g)^2}} + G_1(\cdot) - x_{b/p}\kappa(\theta)\dot{\theta}\right) \\ &+ \frac{\partial g}{\partial c}2\Delta\Bigg[\frac{\partial\Delta}{\partial x_{b/p}}\left(-k_\delta\frac{x_{b/p}}{\sqrt{1 + x_{b/p}^2}} + y_{b/p}\kappa(\theta)\dot{\theta}\right) \\ &+ \frac{\partial\Delta}{\partial y_{b/p}}\left(-u_{td}\frac{y_{b/p}}{\sqrt{\Delta^2 + (y_{b/p} + g)^2}} + G_1(\cdot) - x_{b/p}\kappa(\theta)\dot{\theta}\right)\Bigg]\Bigg] \\ &- \frac{y_{b/p} + g}{\Delta^2 + (y_{b/p} + g)^2}\Bigg[\frac{\partial\Delta}{\partial x_{b/p}}\left(-k_\delta\frac{x_{b/p}}{\sqrt{1 + x_{b/p}^2}} + y_{b/p}\kappa(\theta)\dot{\theta}\right) \\ &+ \frac{\partial\Delta}{\partial y_{b/p}}\left(-u_{td}\frac{y_{b/p}}{\sqrt{\Delta^2 + (y_{b/p} + g)^2}} + G_1(\cdot) - x_{b/p}\kappa(\theta)\dot{\theta}\right)\Bigg]\Bigg]\end{aligned} \tag{8.101}$$

We can now collect the terms that have less than quadratic growth in v_r and/or vanish when $\tilde{X}_2 = 0$.

$$\begin{aligned}
r_d v_r = &- \frac{v_r}{C_r}\kappa(\theta)\left(\sqrt{u_r^2+v_r^2}\cos(\psi+\beta-\gamma_p(\theta))\right) \\
&+ \frac{v_r}{C_r}\frac{\Delta x_{b/p}}{\Delta^2+\left(y_{b/p}+g\right)^2}\left(\kappa(\theta)\sqrt{u_r^2+v_r^2}\cos(\psi+\beta-\gamma_p)\right) \\
&- \frac{v_r}{C_r}\frac{\Delta}{\Delta^2+\left(y_{b/p}+g\right)^2}\left(-u_{td}\frac{y_{b/p}}{\sqrt{\Delta^2+(y_{b/p}+g)^2}}+G_1(\cdot)\right) \\
&+ \frac{v_r}{C_r}\frac{y_{b/p}+g}{\Delta^2+(y_{b/p}+g)^2}\frac{\partial\Delta}{\partial y_{b/p}}\left(-u_{td}\frac{y_{b/p}}{\sqrt{\Delta^2+(y_{b/p}+g)^2}}+G_1(\cdot)\right) \\
&- \frac{1}{C_r}\left(\frac{u_{rd}}{u_{rd}^2+v_r^2}-\frac{2\Delta v_r}{\Delta^2+(y_{b/p}+g)^2}\frac{\partial g}{\partial a}\right)Y(u_r)v_r^2 \\
&+ G(\tilde{X}_1,\tilde{X}_2,\Delta,V_T,V_N,u_{rd},v_r)
\end{aligned} \tag{8.102}$$

where,

$$\begin{aligned}
G(\cdot) \triangleq &- \frac{v_r}{C_r}\left[\kappa(\theta)\left(k_\delta\frac{x_{b/p}}{\sqrt{1+x_{b/p}^2}}+\hat{V}_T\right)-\frac{k_\delta x_{b/p}}{\sqrt{1+x_{b/p}^2}}\right. \\
&- \frac{\dot{u}_{rd}v_r}{u_{rd}^2+v_r^2}-\frac{y_{b/p}+g}{\Delta^2+(y_{b/p}+g)^2}\frac{\partial\Delta}{\partial x_{b/p}} \\
&+ \frac{\Delta}{\Delta^2+\left(y_{b/p}+g\right)^2}\left[\dot{\hat{V}}_N\frac{b+\sqrt{b^2-ac}}{-a}+\frac{\partial g}{\partial b}\left(2\dot{\hat{V}}_N y_{b/p}\right)\right. \\
&- \frac{\partial g}{\partial c}2\Delta\left[\frac{\partial\Delta}{\partial x_{b/p}}\frac{k_\delta x_{b/p}}{\sqrt{1+x_{b/p}^2}}+\frac{\partial\Delta}{\partial y_{b/p}}\left(\frac{u_{td}y_{b/p}}{\sqrt{\Delta^2+(y_{b/p}+g)^2}}+G_1(\cdot)\right)\right] \\
&+ 2\left[\frac{\partial g}{\partial c}y_{b/p}+\frac{\partial g}{\partial b}\hat{V}_N\right]\left(\frac{-u_{td}y_{b/p}}{\sqrt{\Delta^2+(y_{b/p}+g)^2}}+G_1(\cdot)-x_{b/p}\kappa(\theta)\dot{\theta}\right) \\
&+ \left.\left.2\frac{\partial g}{\partial a}\left(\hat{V}_N\dot{\hat{V}}_N-u_{rd}\dot{u}_{rd}\right)-x_{b/p}\kappa(\theta)\left(\frac{k_\delta x_{b/p}}{\sqrt{1+x_{b/p}^2}}+\hat{V}_T\right)\right]\right]
\end{aligned} \tag{8.103}$$

where $G(\cdot)$ is the function introduced to collect the terms that have less than quadratic growth in v_r and/or vanish when $\tilde{X}_2 = 0$. Note here that using our definition of Δ in (8.53) all the terms in $r_d v_r$ with partial derivatives of Δ multiplied by $\dot{\theta}$ are cancelled due to skew-symmetry. We can now find the following bound on

(8.101)

$$
\begin{aligned}
r_d v_r \leq & \left|\frac{v_r}{C_r}\right| |\kappa(\theta)| \sqrt{u_r^2+v_r^2} \left| \frac{\Delta x_{b/p}}{\Delta^2 + \left(y_{b/p}+g\right)^2} - 1 \right| \\
& + \left|\frac{v_r}{C_r}\right| \left|\frac{1}{\Delta}\right| \left(4\sqrt{u_r^2+v_r^2} + |\tilde{u}|\right) \\
& + \left|\frac{v_r}{C_r}\right| \left|\frac{y_{b/p}+g}{\Delta^2+(y_{b/p}+g)^2}\right| \left(4\sqrt{u_r^2+v_r^2} + |\tilde{u}|\right) + |G(\cdot)| \\
& - \frac{1}{C_r}\left(\frac{u_{rd}}{u_{rd}^2+v_r^2} - \frac{2\Delta v_r}{\Delta^2+(y_{b/p}+g)^2}\frac{\partial g}{\partial a}\right) Y(u_r) v_r^2 \\
\leq & \left|\frac{v_r^2}{C_r}\right| \left[|\kappa(\theta)| \left| \frac{\Delta x_{b/p}}{\Delta^2 + \left(y_{b/p}+g\right)^2} - 1 \right| + \frac{8}{\Delta} \right] + |G(\cdot)| \\
& + \left|\frac{v_r}{C_r}\right| |\kappa(\theta)| \, |u_r| \left| \frac{\Delta x_{b/p}}{\Delta^2 + \left(y_{b/p}+g\right)^2} - 1 \right| + \left|\frac{v_r}{C_r}\right| \left|\frac{2}{\Delta}\right| (4\,|u_r| + |\tilde{u}|) \qquad (8.104) \\
& - \frac{1}{C_r}\left(\frac{u_{rd}}{u_{rd}^2+v_r^2} - \frac{2\Delta v_r}{\Delta^2+(y_{b/p}+g)^2}\frac{\partial g}{\partial a}\right) Y(u_r) v_r^2 \\
\leq & \left|\frac{v_r^2}{C_r}\right| \left[|\kappa(\theta)| \left| \frac{\Delta x_{b/p}}{\Delta^2 + \left(y_{b/p}+g\right)^2} - 1 \right| + \frac{8}{\Delta} \right] + \Phi(\cdot) \\
& - \frac{1}{C_r}\left(\frac{u_{rd}}{u_{rd}^2+v_r^2} - \frac{2\Delta v_r}{\Delta^2+(y_{b/p}+g)^2}\frac{\partial g}{\partial a}\right) Y(u_r) v_r^2 \\
\leq & \left|\frac{v_r^2}{C_r}\right| \left[2\,|\kappa(\theta)| + \frac{8}{\Delta} \right] + \Phi(\cdot) \\
& - \frac{1}{C_r}\left(\frac{u_{rd}}{u_{rd}^2+v_r^2} - \frac{2\Delta v_r}{\Delta^2+(y_{b/p}+g)^2}\frac{\partial g}{\partial a}\right) Y(u_r) v_r^2
\end{aligned}
$$

where,

$$
\Phi(\cdot) \triangleq |G(\cdot)| + 2\left|\frac{v_r}{C_r}\right| |\kappa(\theta)| \, |u_r| + 2\left|\frac{v_r}{C_r}\right| \left|\frac{1}{\Delta}\right| (4\,|u_r| + |\tilde{u}_r|) \qquad (8.105)
$$

The function $\Phi(\cdot)$ is introduced to collect the remaining terms that have less than quadratic growth in v_r and/or vanish when $\tilde{X}_2 = 0$. Note also the terms in $G(\cdot)$ with partial derivatives of g that appear to have quadratic growth. Although the overall terms appear to have quadratic growth, the partial derivatives of g actually decrease for increasing v_r giving the entire term less than quadratic growth. From the definitions of $\Phi(\cdot)$ and $G(\cdot)$ one can easily conclude the existence of three continuous positive functions $F_{0,2}(\tilde{X}_1, \tilde{X}_2, u_{rd}, \dot{u}_{rd}, V_T, V_N, \Delta)$ which are bounded under the boundedness of the vector $[\tilde{X}_2^T, u_{rd}, \dot{u}_{rd}, V_T, V_N, \Delta]^T$, with

$$
F_2(\tilde{X}_1, \tilde{X}_2 = 0, u_{rd}, \dot{u}_{rd}, V_{x_e}, V_{y_e}, \Delta) = 0,
$$

such that:

$$
\Phi(\cdot) \leq F_2(\cdot) v_r^2 + F_1(\cdot) v_r + F_0(\cdot). \qquad (8.106)
$$

When we substitute the bound on $r_d v_r$ from (8.104) in (8.98) we obtain:

$$\begin{aligned}\dot{V}_3 = v_r \dot{v}_r \leq & |X(u_{rd})| \left(\left| \frac{v_r^2}{C_r} \right| \left[2 |\kappa(\theta)| + \frac{8}{\Delta} \right] + \Phi(\cdot) \right) + a_x \tilde{u} r_d v_r \\ & + X(u_{rd}) v_r \tilde{r} + a_x \tilde{u} v_r \tilde{r} + a_y \tilde{u} v_r^2 + Y(u_{rd}) v_r^2 \\ & - \frac{1}{C_r} \left(\frac{u_{rd}}{u_{rd}^2 + v_r^2} - \frac{2\Delta v_r}{\Delta^2 + (y_{b/p} + g)^2} \frac{\partial g}{\partial a} \right) Y(u_r) v_r^2 \\ \leq & \left| \frac{1}{C_r} \right| \left[|X(u_{rd})| \left[2 |\kappa(\theta)| + \frac{8}{\Delta} \right] - |Y(u_{rd})| \right] v_r^2 \\ & + a_x \tilde{u} r_d v_r + X(u_{rd})(v_r \tilde{r} + \Phi(\cdot)) + a_x \tilde{u} v_r \tilde{r} + a_y \tilde{u} v_r^2\end{aligned} \tag{8.107}$$

Consequently, on the manifold where $\tilde{X}_2 = 0$ we obtain

$$\begin{aligned}\dot{V}_3 \leq & \left| \frac{1}{C_r} \right| \left[X_{\max} \left[2\kappa_{\max} + \frac{8}{\Delta} \right] - Y_{\min} \right] v_r^2 \\ & + X(u_{rd}) (F_1(\tilde{X}_1, 0, u_{rd}, \dot{u}_{rd}, V_T, V_N, \Delta) |v_r| \\ & + F_0(\tilde{X}_1, 0, u_{rd}, \dot{u}_{rd}, V_T, V_N, \Delta))\end{aligned} \tag{8.108}$$

To have boundedness of v_r for small values of $\tilde{X}_2$ we have to satisfy the following inequality:

$$X_{\max} \left[2\kappa_{\max} + \frac{8}{\Delta} \right] - Y_{\min} < 0 \tag{8.109}$$

such that the quadratic term in (8.108) is negative. Using (8.53) we need to choose μ, such that:

$$\mu > \frac{8 X_{\max}}{Y_{\min} - 2\kappa_{\max} X_{\max}} \tag{8.110}$$

which is the condition given in Lemma 8.3. Note that the denominator of μ is nonzero and positive as long of the conditions of Lemma 8.2 are satisfied. Consequently, near the manifold $\tilde{X}_2 = 0$ it holds that (8.108) is negative definite for sufficiently large v_r. Consequently, near the manifold $\tilde{X}_2 = 0$ it holds that (8.107) is negative definite for sufficiently large v_r. If $\dot{V}_3$ is negative for sufficiently large v_r this implies that V_3 decreases for sufficiently large v_r. Since $V_3 = 1/2 v_r^2$, a decrease in V_3 implies a decrease in v_r^2 and by extension in v_r. Consequently, v_r cannot increase above a certain value and v_r is bounded near $\tilde{X}_2 = 0$ if μ is chosen such that (8.55) holds, which completes the proof of Lemma 8.3.

Chapter 9

Path Following of Unparametrized Paths for Underactuated Marine Vessels

This chapter presents a control methodology for underactuated marine vessels with two control inputs (thrust and torque) and three degrees-of-freedom (position and rotation). This chapter has its own modelling section. This choice is made since there are no ocean currents considered in this work and therefore the model is slightly different with respect to the models presented in Chapter 2. The control specification is path following: make the ship approach a path and follow it with nonzero speed without requiring any time parametrization. While in the trajectory tracking problem one would seek to make the ship follow a moving reference point, in path following one wants to stabilize a suitable controlled-invariant subset of the state space (see [104]), and no exogenous signal drives the control loop.

The papers listed in Subsection 1.1.3 consider path following of straight-line paths or path-following/trajectory-tracking of curved paths that are parametrized by time or a path variable. To the best of our knowledge, in the context of marine vessels, the problem of finding a smooth, static, and time-invariant feedback solving the path-following problem for general paths, remains open. In this work, we make an initial step towards its solution. Our approach leverages the hierarchical control methodology presented in El-Hawwary and Maggiore [55], a methodology which has been used in Roza and Maggiore [123] to derive almost global position controllers for underactuated flying vehicles. The idea is to first design a path following control law for a kinematic point-mass. Then from this feedback extract a desired heading angle, and view it as a reference for a torque controller. Carrying out these two separate design steps corresponds to the simultaneous stabilization of two nested subsets of the state space, and the a reduction theorem from El-Hawwary and Maggiore [55] is used to show overall stability. In particular, we show that if the curvature of the path is not too large in relation to a constant that depends on the ship's parameters, then the sideways velocity is uniformly bounded.

The challenge in solving the path-following problem for marine vessels is that, due to the presence of sideways motion, in order to stay on a curved path the ship

cannot head tangent to it, and its angle of attack relative to the path's tangent depends on the sway speed.

9.1 Preliminaries and notation

In this chapter we adopt the following notation. We denote by $\mathbb{S}^1$ the set of real numbers modulo 2π, with the differentiable manifold structure making it diffeomorphic to the unit circle. If $\psi \in \mathbb{S}^1$, R_ψ is the rotation matrix

$$R_\psi = \begin{bmatrix} \cos(\psi) & -\sin(\psi) \\ \sin(\psi) & \cos(\psi) \end{bmatrix}.$$

If $f(x, y)$ is a differentiable function of two scalar variables, we denote by $\partial_x f$, $\partial_y f$ the partial derivatives with respect to x and y, respectively. Similarly, we define $\partial^2_{xy} f := \partial_x \partial_y f$, and similarly for the other second-order partial derivatives. If $f : \mathbb{R}^n \to \mathbb{R}^m$ is a differentiable vector function and $p \in \mathbb{R}^n$, df_p is the $m \times n$ Jacobian matrix of f at p. If Γ is a closed subset of a metric space (M, d) and $x \in M$, then we denote by $\|x\|_M$ the point-to-set distance of x to M, $\|x\|_M = \inf_{y \in M} d(x - y)$.

The following stability definitions are taken from El-Hawwary and Maggiore [55]. Let $\Sigma : \dot{\chi} = f(\chi)$ be a smooth dynamical system with state space a Riemannian manifold $\mathcal{X}$ with associated metric d. Let $\phi(t, \chi_0)$ denote the local phase flow generated by Σ, and let $B_\delta(x)$ denote the ball of radius δ centred at $x \in M$.

Consider a closed set $\Gamma \subset \mathcal{X}$ which is positively invariant for Σ, i.e., for all $\chi_0 \in \Gamma$, $\phi(t, \chi_0) \in \Gamma$ for all $t > 0$ for which $\phi(t, \chi_0)$ is defined. Then we have the following stability definitions taken from El-Hawwary and Maggiore [55].

Definition 9.1. The set Γ is *s*table for Σ if for any $\varepsilon > 0$, there exists a neighborhood $\mathcal{N}(\Gamma) \subset \mathcal{X}$ such that, for all $\chi_0 \in \mathcal{N}(\Gamma)$, $\phi(t, \chi_0) \in B_\varepsilon(\Gamma)$, for all $t > 0$ for which $\phi(t, \chi_0)$ is defined. The set Γ is *a*ttractive for Σ if there exists a neighborhood $\mathcal{N}(\Gamma) \subset \mathcal{X}$ such that for all $\chi_0 \in \mathcal{N}(\Gamma)$, $\lim_{t\to\infty} \|\phi(t, \chi_0)\|_\Gamma = 0$. The *d*omain of attraction of Γ is the set $\{\chi_0 \in \mathcal{X} : \lim_{t\to\infty} \|\phi(t, \chi_0)\|_\Gamma = 0\}$. The set Γ is *g*lobally attractive for Σ if it is attractive with domain of attraction $\mathcal{X}$. The set Γ is *l*ocally asymptotically stable (LAS) for Σ if it is stable and attractive. The set Γ is *g*lobally asymptotically stable for Σ if it is stable and globally attractive. If $\Gamma_1 \subset \Gamma_2$ are two closed positively invariant sets, then Γ_1 is *asymptotically stable relative to* Γ_2 if Γ_1 is asymptotically stable for the restriction of Σ to Γ_2. System Σ is *locally uniformly bounded (LUB) near* Γ if for each $x \in \Gamma$ there exist positive scalars λ and m such that $\phi(\mathbb{R}_+, B_\lambda(x)) \subset B_m(x)$. △

The following result is key in the development of this work.

Theorem 9.1 (El-Hawwary and Maggiore [55])**.** *Let Γ_1, Γ_2, $\Gamma_1 \subset \Gamma_2 \subset \mathcal{X}$, be two closed sets that are positively invariant for Σ and suppose that Γ_1 is not compact. If*

(i) Γ_1 is asymptotically stable relative to Γ_2,

(ii) Γ_2 is asymptotically stable, and

(iii) Σ is LUB near Γ_1,

then Γ_1 is asymptotically stable for Σ.

9.2 The Problem

Consider the 3-degrees-of-freedom vessel depicted in Figure 9.1, which may describe an ASV or an AUV moving in the horizontal plane. We denote by $p \in \mathbb{R}^2$ the position of the vessel on the plane and $\psi \in \mathbb{S}^1$ its heading (or yaw) angle. The yaw rate $\dot{\psi}$ is denoted by r.

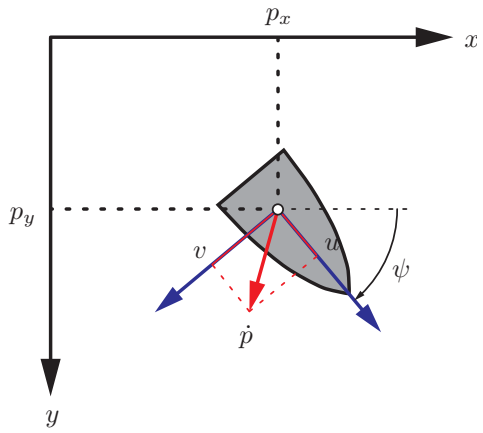

Figure 9.1: Illustration of the ship's kinematic variables.

We attach at the point p of the vessel a body frame aligned with the main axes of the vessel, as depicted in the figure, with the standard convention that the z-axis points into the plane (towards the sea bottom). We represent the velocity vector $\dot{p}$ in body frame coordinates as (u, v), where u, the longitudinal component of the velocity vector, is called the surge speed, while v, the lateral component, is called the sway speed. Finally, the control inputs of the vessel are the surge trust T_u and the rudder angle T_r. In terms of these variables, the model derived in Fossen [60] is

$$\begin{aligned} \dot{\boldsymbol{\eta}} &= \begin{bmatrix} R_\psi & 0 \\ 0 & 1 \end{bmatrix} \boldsymbol{\nu} \\ \boldsymbol{M}\dot{\boldsymbol{\nu}} + \boldsymbol{C}(\boldsymbol{\nu})\boldsymbol{\nu} + \boldsymbol{D}\boldsymbol{\nu} &= \boldsymbol{B}\boldsymbol{f} \end{aligned} \tag{9.1}$$

with $\boldsymbol{\eta} \triangleq [p, \psi]^\top$, $\boldsymbol{\nu} \triangleq [u, v, r]^\top$, and $\boldsymbol{f} \triangleq [T_u, T_r]^\top$. The matrices $\boldsymbol{M}$, $\boldsymbol{D}$, and $\boldsymbol{B}$ are given by

$$\boldsymbol{M} \triangleq \begin{bmatrix} m_{11} & 0 & 0 \\ 0 & m_{22} & m_{23} \\ 0 & m_{23} & m_{33} \end{bmatrix},$$

$$\boldsymbol{D} \triangleq \begin{bmatrix} d_{11} & 0 & 0 \\ 0 & d_{22} & d_{23} \\ 0 & d_{32} & d_{33} \end{bmatrix}, \boldsymbol{B} \triangleq \begin{bmatrix} b_{11} & 0 \\ 0 & b_{22} \\ 0 & b_{32} \end{bmatrix}$$

with $\boldsymbol{M} = \boldsymbol{M}^\top > 0$ the symmetric positive definite inertia matrix including added mass, $\boldsymbol{D} > 0$ is the hydrodynamic damping matrix, and $\boldsymbol{B}$ is the actuator config-

uration matrix. The matrix $\boldsymbol{C}(\boldsymbol{\nu})$ is the matrix of Coriolis and centripetal forces and can be obtained from $\boldsymbol{M}$ (see [60]). We place the origin of the body frame at a point on the center-line of the vessel with distance ϵ from the centre of mass. Following Fredriksen and Pettersen [64], assuming that the vessel is starboard symmetric, there exists ϵ such that the resulting dynamics have mass and damping matrices satisfying this relation: $\boldsymbol{M}^{-1}\boldsymbol{B}\boldsymbol{f} = [\tau_u, 0, \tau_r]^\top$. Thus, with this choice of origin of the body frame, the sway dynamics become decoupled from the rudder control input, making it easier to analyze the stability properties of the sway dynamics. Using this convention, the model of the marine vessel (9.1) can be represented as

$$\begin{aligned} \dot{p} &= R_\psi \begin{bmatrix} u \\ v \end{bmatrix} \\ \begin{bmatrix} \dot{u} \\ \dot{v} \end{bmatrix} &= \begin{bmatrix} F_u(v,r) - \frac{d_{11}}{m_{11}} u + \tau_u \\ X(u)r + Y(u)v \end{bmatrix} \\ \dot{\psi} &= r \\ \dot{r} &= F_r(u,v,r) + \tau_r. \end{aligned} \tag{9.2}$$

The functions $X(u)$ and $Y(u)$ are linear. Their expressions are given in Appendix 9.A together with those of F_u and F_r. Denoting by $\chi := (p, u, v, \psi, r)$ the state of the vessel, the state space is $\mathcal{X} := \mathbb{R}^2 \times \mathbb{R} \times \mathbb{R} \times \mathbb{S}^1 \times \mathbb{R}$.

Assumption 9.1. We assume that $Y(u) < 0$ for all $u \in [0, U_{\max}]$.

This is a realistic assumption, since $Y(\bar{u}) \geq 0$ would imply that the sway dynamics are undamped or unstable when the yaw rate r is zero.

Assumption 9.2. The ocean current is zero.

This assumption is made to simplify the exposition of the ideas. The results of this work can be adapted to handle unknown constant current.

Consider a planar Jordan[1] curve γ expressed in implicit form as $\gamma = \{p : h(p) = 0\}$, where h is a C^1 function whose gradient never vanishes on γ. We assume that $h : \mathbb{R}^2 \to \mathbb{R}$ is a proper function, i.e., all its sublevel sets $\{p : h(p) \leq c\}$, $c \in \mathbb{R}$, are compact. Since γ is assumed to be compact, there is no loss of generality in this assumption.

Path-Following Problem (PFP). Design a smooth time-invariant feedback such that, for suitable initial conditions, the position vector $p(t) \to \{p : h(p) = 0\}$, and the speed $\|\dot{p}(t)\|$ satisfies $0 < \|\dot{p}(t)\| \leq \sup_t \|\dot{p}(t)\| < \infty$. In other words, we want to make the position of the ship converge to the path, travel along it without stopping, while guaranteeing that its speed is bounded.

Geometric objects. Associated with the implicit representation $h(p) = 0$ of γ there are three geometric objects: the unit tangent and normal vectors, and the signed curvature. The unit normal vector at p is

$$N(p) := dh_p^\top / \|dh_p\|.$$

[1] A curve is said to be Jordan if it is closed and has no self-intersections.

The unit tangent vector at p is the counterclockwise rotation of $N(p)$ by $\pi/2$,

$$T(p) := R_{\pi/2} N(p).$$

Finally, the signed curvature $\kappa(p)$ is defined as

$$\kappa(p) = -\frac{(\partial_y h)^2\, \partial^2_{xx} h - 2\partial^2_{xy} h\, \partial_x h\, \partial_y h + \partial^2_{yy} h\, (\partial_x h)^2}{\left((\partial_x h)^2 + (\partial_y h)^2\right)^{(3/2)}}. \tag{9.3}$$

The quantities $N(p), T(p), \kappa(p)$ are defined not just on γ, but at all points p such that $dh_p \neq [0 \;\; 0]$. If $p_0 \notin \gamma$, then $N(p_0), T(p_0), \kappa(p_0)$ are the normal vector, tangent vector, and curvature at p_0 of the curve $\{p : h(p) = p_0\}$.

9.3 Hierarchical Control Approach

The idea of the proposed solution is hierarchical in nature.

1. We regulate the surge speed u to a desired constant $\bar{u} > 0$.
2. We consider the kinematic point-mass system

   $$\dot{p} = \mu,$$

   and we solve the PFP with the constraint that $\|\mu\| = (\bar{u}^2 + v^2)^{(1/2)}$. The result of this design is a function $\mu(p, v)$.
3. Having found $\mu(p, v)$, we find the desired heading angle $\psi_d(p, v)$ such that

   $$R_{\psi_d} \begin{bmatrix} \bar{u} \\ v \end{bmatrix} = \mu.$$

   This equation has a solution because, by construction, $\|\mu\| = (\bar{u}^2 + v^2)^{(1/2)}$. Intuitively, when $\psi = \psi_d$ and $u = \bar{u}$, the marine vessel behaves like a kinematic point-mass subject to a path-following control law.
4. Having found $\psi_d(p, v)$, we define the output function $e = \psi - \psi_d$ and we show that, under certain conditions on $\bar{u}$ (possibly any $\bar{u} > 0$), the system with input τ_r and output e has relative degree 2. We thus define a controller $\tau_r(\chi)$ that stabilizes the set where $e = \dot{e} = 0$.
5. We show that, if the curvature of the path is not too large, then the sway speed v remains bounded. We use Theorem 9.1 to prove that the hierarchical approach described above does indeed solve the PFP if the curvature of the path is not too large.

9.4 Control Design

In this section we carry out the design steps 1-4 outlined above. The stability analysis of step 5 is carried out in the next section.

Step 1: regulation of surge speed. This step is trivial, we choose the feedback linearizing control law

$$\tau_u = -F_u(v,r) + \frac{d_{11}}{m_{11}}u - K_u(u-\bar{u}),\ K_u > 0. \tag{9.4}$$

Step 2: solution of the PFP for a kinematic point-mass. Consider the kinematic point-mass system

$$\dot{p} = \mu, \tag{9.5}$$

where the velocity vector $\mu \in \mathbb{R}^2$ is the control input. We are to design μ such that $\|\mu\| = (\bar{u}^2 + v^2)^{(1/2)}$ and the set $\{h(p)\}$ is asymptotically stable. To this end, consider the output $z = h(p)$. The derivative is

$$\dot{z} = dh_p\mu = \|dh_p\|N(p)^\top\mu. \tag{9.6}$$

Define

$$\mu(p,v) := -\Big[\bar{u}\sigma(h(p))\Big]N(p) + w(p,v)T(p). \tag{9.7}$$

This control input is composed of two terms. The first term is orthogonal to all level sets of h (in particular, to γ) and is responsible for making $z \to 0$, as we shall see in a moment. The second term is tangent to the level sets of h and it will be designed to guarantee that $\|\mu\| = (\bar{u}^2 + v^2)^{(1/2)}$. The function $\sigma : \mathbb{R} \to (-a, a)$, $a \in (0,1)$, is a saturation function, chosen to be smooth, monotonically increasing, zero in zero, and such that $\lim_{|z|\to\infty} |\sigma(z)| = a$. The positive scalar a is a design parameter.

Since $\{T(p), N(p)\}$ is an orthonormal frame, substitution of (9.7) into (9.6) gives

$$\dot{z} = -\|dh_p\|\bar{u}\sigma(z).$$

Since, by assumption, $\|dh_p\| \neq 0$ on γ, by continuity of h we have that $\|dh_p\| \neq 0$ in a neighborhood of γ. Therefore, for any $\bar{u} > 0$, the set $\{p : h(p) = 0\}$ is asymptotically stable.

Next we design $w(p,v)$ such that $\|\mu(p,v)\| = (\bar{u}^2 + v^2)^{(1/2)}$. Referring to the identity (9.7), since $\{T(p), N(p)\}$ form an orthonormal frame, we have

$$\|\mu\|^2 = \bar{u}^2\sigma^2(h(p)) + w^2(p,v).$$

Setting

$$w(p,v) := \left(\bar{u}^2(1 - \sigma^2(h(p))) + v^2\right)^{(1/2)}, \tag{9.8}$$

we have $\|\mu(p,v)\| = (\bar{u}^2 + v^2)^{(1/2)}$, as required. Note that the above expression of $w(p,v)$ is well-defined and smooth because, by construction, $|\sigma| < a \leq 1$.

In conclusion, we have the following result.

Lemma 9.2. *The feedback $\mu(p,v)$ defined in* (9.7) *and* (9.8) *makes the set $\{p \in \mathbb{R}^2 : h(p) = 0\}$ asymptotically stable for the kinematic point-mass system* (9.5).

Step 3: definition of ψ_d. We need to find a smooth function $\psi_d(p, v)$ such that

$$R_{\psi_d} \begin{bmatrix} \bar{u} \\ v \end{bmatrix} = \mu(p, v).$$

The vector on the left-hand side of the identity above has norm $(\bar{u}^2 + v^2)^{(1/2)}$ and, by construction, so does the vector on the right-hand side. Thus ψ_d is just the phase of the vector μ,

$$\psi_d(p, v) := \text{atan2}(\mu_2(p, v), \mu_1(p, v)), \tag{9.9}$$

where atan2 is the four-quadrant arctangent function such that

$$\text{atan2}(\sin(\theta), \cos(\theta)) = \theta \text{mod} 2\pi.$$

Step 4: regulation of ψ to ψ_d. We define the output function $e = \psi - \psi_d$. Then

$$\dot{e} = g(p, u, v)r + f(p, u, v, \psi), \tag{9.10}$$

where

$$g(p, u, v) = 1 - \big(\partial_v \psi_d(p, v)\big) X(u),$$
$$f(p, u, v, \psi) = -\big(\partial_p \psi_d(p, v)\big) R_\psi \begin{bmatrix} u \\ v \end{bmatrix} - \partial_v \psi_d Y(u) v.$$

Taking one more time derivative along (9.2) we get

$$\ddot{e} = g(p, u, v)\big(F_r(v, r) + \tau_r\big) + \dot{g}(\chi)r + \dot{f}(\chi).$$

Lemma 9.3. *The following identity holds:*

$$\partial_v \psi_d = -\frac{\bar{u}}{\bar{u}^2 + v^2} \left[1 + \frac{\sigma(h(p))v}{w(p, v)}\right], \tag{9.11}$$

where $w(p, v)$ is given in (9.8)*. Suppose that*

$$1 - \frac{\bar{u}|X(\bar{u})|}{\bar{u}^2 + v^2} > 0 \tag{9.12}$$

for all $v \in \mathbb{R}$. Then, the parameter $a \in (0, 1]$ in the saturation σ can be chosen small enough that system (9.2) *with input τ_r and output $e = \psi - \psi_d(p, v)$ has relative degree 2 at any point $\chi = (p, u, v, \psi, r)$ such that $u = \bar{u}$.*

Remark 9.1. Condition (9.12) is met for all $\bar{u}$, for the ship parameters listed in the appendix and used in our simulations.

Proof. Recall that, by definition, ψ_d satisfies the following identity

$$R_{\psi_d} \begin{bmatrix} \bar{u} \\ v \end{bmatrix} = \mu,$$

from which we deduce that

$$\begin{bmatrix}\cos(\psi_d)\\ \sin(\psi_d)\end{bmatrix} = \frac{1}{\bar{u}^2+v^2}\begin{bmatrix}\bar{u} & v\\ -v & \bar{u}\end{bmatrix}\mu.$$

Now using the identity

$$\partial_v\psi_d = \begin{bmatrix}-\sin(\psi_d) & \cos(\psi_d)\end{bmatrix}\begin{bmatrix}\partial_v\cos(\psi_d)\\ \partial_v\sin(\psi_d)\end{bmatrix},$$

and the expressions for $\cos(\psi_d)$, $\sin(\psi_d)$ found above, after some manipulation one gets

$$\partial_v\psi_d = -\frac{\bar{u}}{\bar{u}^2+v^2} + \frac{1}{\bar{u}^2+v^2}\mu^\top\begin{bmatrix}0 & 1\\ -1 & 0\end{bmatrix}\partial_v\mu.$$

Substituting in the above the expression for μ given in (9.7), after some algebra one obtains identity (9.11).

Now we turn to the relative degree property. System (9.2) with input τ_r and output e has relative degree 2 when $u=\bar{u}$ if $1-\partial_v\psi_d(p,v)X(\bar{u})>0$, or

$$1+\frac{X(\bar{u})\bar{u}}{\bar{u}^2+v^2}\left[1+\frac{\sigma(h(p))v}{w(p,v)}\right]>0.$$

Using the fact that $|\sigma(\cdot)|<a\leq 1$ and $|v/w(p,v)|<1$, we have the inequality

$$1+\frac{X(\bar{u})\bar{u}}{\bar{u}^2+v^2}\left[1+\frac{\sigma(h(p))v}{w(p,v)}\right] > 1-\frac{|X(\bar{u})|(1+a)\bar{u}}{\bar{u}^2+v^2}.$$

If condition (9.12) holds, there exists $a\in(0,1]$, such that the lower bound above is greater than zero, implying that the system (9.2) with output e has relative degree 2. □ □

Assuming that (9.12) holds, we define the smooth feedback linearizing control law

$$\begin{aligned}\tau_r = -F_r(v,r) + \frac{1}{g(p,u,v)}\Big(&-\dot{f}(\chi)-\dot{g}(\chi)r\\ &-K_p\sin(\psi-\psi_d(p,v))-K_d(r-\dot{\psi}_d(\chi))\Big),\end{aligned} \tag{9.13}$$

where dot on a function denotes the time derivative of the function along the vector field (9.2) with τ_u as in (9.4). With the feedback above, we obtain

$$\ddot{e}+K_p\sin(e)+K_d\dot{e}=0.$$

This is the equation of a pendulum with friction. Thus the equilibrium $(e,\dot{e})=(0,0)$ is almost globally asymptotically stable. This implies that the set $\{\chi\in\mathcal{X}:\psi=\psi_d(p,v), r=\dot{\psi}_d(\chi)\}$ is stable. Moreover, this set is also asymptotically stable if the original system (9.2) with the chosen feedbacks τ_u and τ_r has no finite escape times. The absence of finite escape times will be proved in the next section.

Summary of feedback design. We have designed the following feedback control law

$$\begin{aligned}\tau_u &= -F_u(v,r) + \frac{d_{11}}{m_{11}}u - K_u(u-\bar{u}),\\ \tau_r &= -F_r(v,r) + \frac{1}{g(p,u,v)}\Big(- \dot{f}(\chi) - \dot{g}(\chi)r \\ &\qquad - K_p \sin(\psi - \psi_d(p,v)) - K_d(r - \dot{\psi}_d(\chi))\Big),\end{aligned} \tag{9.14}$$

where $\bar{u}, K_u, K_p, K_d > 0$ are design parameters and

$$\begin{aligned}\psi_d(p,v) &= \operatorname{atan2}(\mu_2(p,v), \mu_1(p,v)),\\ \mu(p,v) &= -\Big[\bar{u}\sigma(h(p))\Big]N(p)\\ &\qquad + \left(\bar{u}^2(1-\sigma^2(h(p))) + v^2\right)^{(1/2)} T(p).\end{aligned}$$

Finally, $\sigma(z)$ is any smooth, monotonically increasing function such that $\sigma(0) = 0$ and $\lim_{|z|\to\infty} |\sigma(z)| = a$, where $a \in (0,1]$ is sufficiently small as in Lemma 9.3. For instance, $\sigma(z) = a\tanh(Kz)$, $K > 0$, has the desired properties.

As we discussed, in the absence of finite escape times the feedback above asymptotically stabilizes the set $\Gamma_2 := \{\chi \in \mathcal{X} : u = \bar{u}, \psi = \psi_d(p,v), r - \dot{\psi}_d(p,u,v,r) = 0\}$. In Theorem 9.5 below we show that it solves the PFP.

9.5 Stability Analysis

As we shall see in a moment, the control design procedure developed in the previous section amounts to the simultaneous stabilization of the two nested closed sets $\Gamma_1 \subset \Gamma_2$

$$\begin{aligned}\Gamma_2 &= \{\chi \in \mathcal{X} : u = \bar{u}, \psi = \psi_d(p,v), r = \dot{\psi}_d(\chi)\},\\ \Gamma_1 &= \{\chi \in \Gamma_2 : h(p) = 0\}.\end{aligned}$$

On Γ_2, the ship behaves like a kinematic point-mass subject to a path-following control law. On Γ_1, the ship is on the path with a desired surge speed $\bar{u}$. Showing that the feedback (9.14) solves the PFP amounts to showing that Γ_1 is asymptotically stable. To prove this property, we will use Theorem 9.1.

To begin, we observe that, by design, Γ_2 is stable, and asymptotically stable if solutions starting in a neighborhood of Γ_2 have no finite escape times. Assume for a moment that this is the case. On Γ_2, we have

$$\dot{p} = R_{\psi_d}\begin{bmatrix}\bar{u}\\ v\end{bmatrix}.$$

By the construction in step 2,

$$R_{\psi_d}\begin{bmatrix}\bar{u}\\ v\end{bmatrix} = \mu(p,v),$$

and thus

$$\dot{p} = \mu(p,v).$$

By Lemma 9.2, the set $\{h(p) = 0\}$ is asymptotically stable for the above dynamics. In the absence of finite escape times, this implies that Γ_1 is asymptotically stable relative to Γ_2. Therefore, in order to prove asymptotic stability of Γ_1, we will prove that the closed-loop system has no finite escape times near Γ_2 and, in addition, property (iii) of Theorem 9.1 holds. This is done in the next lemma.

Lemma 9.4. *Consider system* (9.2) *with the feedbacks defined in* (9.14)*, and suppose Assumptions 9.1 and 9.2 hold. Suppose further that the desired surge speed* $\bar{u} \in [0, U_{\max}]$ *is such that* $1 + \bar{u}X(\bar{u})/(\bar{u}^2 + v^2) \neq 0$*. Then for any initial condition in a neighborhood of* Γ_2*, the solution is defined for all* $t \geq 0$*. Moreover, if the curvature* κ *of* γ *satisfies the bound*

$$\max_{p \in \gamma} |\kappa(p)| < \frac{|Y(\bar{u})|}{|X(\bar{u})|},$$

then the closed-loop system is LUB near Γ_1*.*

Proof. We first show that the closed-loop system has no finite escape times near Γ_2. Since Γ_2 is stable, for any $\delta > 0$ there exists a positively invariant neighborhood of Γ_2, $\mathcal{N}(\Gamma_2)$, such that all solutions originating in $\mathcal{N}(\Gamma_2)$ satisfy $|u(t) - \bar{u}| < \delta$, $|\psi(t) - \psi_d(p(t), v(t))| < \delta$, $|\dot{r}(t) - \dot{\psi}_d(\chi(t))| < \delta$. From now on, consider an arbitrary solution $\chi(t)$ originating in $\mathcal{N}(\Gamma_2)$. Since $u - \bar{u}$ is bounded, u has no finite escape times. Since $\psi \in \mathbb{S}^1$, a compact set, the same holds for ψ. Recalling that on Γ_2 we have $\dot{p} = \mu(p, v)$, we may write

$$\begin{aligned} \dot{p} &= \mu(p, v) + \left(R_\psi \begin{bmatrix} u \\ v \end{bmatrix} - R_{\psi_d} \begin{bmatrix} \bar{u} \\ v \end{bmatrix} \right) \\ &= R_{\psi - \psi_d} \mu(p, v) + R_\psi \begin{bmatrix} u - \bar{u} \\ 0 \end{bmatrix}. \end{aligned}$$

Letting, as in the previous section, $z = h(p)$, we have

$$\begin{aligned} \dot{z} &= -\|dh_p\| \left(\bar{u}\sigma(z) N^\top R_{\psi - \psi_d} N - N^\top R_\psi \begin{bmatrix} u - \bar{u} \\ 0 \end{bmatrix} \right) \\ &= -\|dh_p\| \left(\bar{u}\sigma(z) \cos(\psi - \psi_d) - N^\top R_\psi \begin{bmatrix} u - \bar{u} \\ 0 \end{bmatrix} \right). \end{aligned}$$

Using the fact that $z\sigma(z) \geq 0$, $\cos(\psi - \psi_d) > \cos(\delta)$, and $|u - \bar{u}| < \delta$, we deduce the following inequality

$$z\dot{z} \leq -\|dh_p\| |z| \left(\bar{u}\sigma(z) \cos(\delta) - \delta \right). \tag{9.15}$$

Pick δ small enough that $\delta / (\bar{u} \cos(\delta)) < 1$, then we see that $z\dot{z} \leq 0$ whenever $z > \rho(\delta) := \sigma^{-1}(\delta / \bar{u} \cos \delta)$. This implies that all trajectories of the z-dynamics are bounded and, moreover, the interval $\{z : |z| < \rho(\delta)\}$ is positively invariant for the z-dynamics. Recalling that $z = h(p)$ and that h is proper, we deduce that all trajectories of the p subsystem are bounded and hence have no finite escape times. Moreover, the neighborhood of Γ_1 defined as $\{\chi \in \mathcal{N}(\Gamma_2) : |h(p)| < \rho(\delta)\}$,

is positively invariant. Since $\rho(\cdot)$ is a class-$\mathcal{K}$ function, Γ_1 is stable. In the rest of the proof we denote

$$\mathcal{N}(\Gamma_1) = \{\chi \in \Gamma_2 : |h(p)| < \rho(\delta)\}.$$

By the construction above, for any $\delta > 0$ this set is a neighborhood of Γ_1 and trajectories originating in it satisfy the bounds

$$|u - \bar{u}| < \delta, |\psi - \psi_d(p, v)| < \delta, |\dot{r} - \dot{\psi}_d(\chi)| < \delta, |h(p)| < \rho(\delta).$$

We now turn our attention to the v-subsystem. For convenience, we denote $\alpha(p, v) := \partial_v \psi_d$, whose expression is given in Lemma 9.3. On $\mathcal{N}(\Gamma_2)$, $\dot{e}$ is bounded. Using (9.10) and Lemma 9.3, we have

$$r = \frac{1}{1 - \alpha(p, v)X(u)} \left(\alpha(p, v)Y(u)v + (\partial_p \psi_d) R_\psi \begin{bmatrix} u \\ v \end{bmatrix} + \dot{e} \right),$$

where $\dot{e}$ is bounded. Since condition (9.12) is assumed to hold, the quantity $1 - \alpha(p, v)X(\bar{u}) > 0$. Therefore, for small enough $\delta > 0$, the quantity $1 - \alpha(p, v)X(u) > 0$ as well, implying that r above is well defined. Substituting the expression for r in the $\dot{v}$ equation in (9.2) and rearranging terms, we get

$$\dot{v} = \frac{1}{1 - \alpha(p, v)X(u)} \Big(Y(u)v + X(u) \Big((\partial_p \psi_d) R_\psi \begin{bmatrix} u \\ v \end{bmatrix} + \dot{e} \Big) \Big).$$

We argue that $|\dot{v}| \leq C_1 + C_2|v|$, for suitable $C_1, C_2 > 0$. Indeed, on $\mathcal{N}(\Gamma_2)$ the coefficient in front of the parenthesis is upper bounded by a constant. The term $Y(u)v$ is linear in v and u is bounded. The term $\partial_p \psi_d$ is a continuous function of (p, v). Since we have established that $p(t)$ is bounded, $\partial_p \psi_d$ is bounded with respect to p. Moreover, using the definition of ψ_d and μ it is possible to show that $\sup_v |\partial_p \psi_d| < \infty$. Thus the term $X(u)\partial_p \psi_d R_\psi [u \quad v]^\top$ grows linearly with v, proving the claim. Since $|\dot{v}|$ grows linearly with v, the v subsystem has no finite escape times. Finally, concerning $r(t)$, we have expressed it as function of $(p(t), u(t), v(t), \psi(t), \dot{e}(t))$, signals that are defined for all $t \geq 0$, and therefore $r(t)$ has no finite escape times. In conclusion, all solutions originating on $\mathcal{N}(\Gamma_2)$ are defined for all $t \geq 0$.

Now we prove that the closed-loop system is LUB near Γ_1. Consider a generic solution $\chi(t)$ originating in $\mathcal{N}(\Gamma_1)$. Since $|h(p(t))| < \rho(\delta)$, and since h is proper, $\|p(t)\|$ has a bound independent of the initial condition in $\mathcal{N}(\Gamma_1)$. Consider now the $\dot{v}$ equation above, and in particular the term $(\partial_p \psi_d) R_\psi [u \quad v]^\top$. On Γ_2, this term reduces to

$$(\partial_p \psi_d) R_{\psi_d} \begin{bmatrix} \bar{u} \\ v \end{bmatrix} = (\partial_p \psi_d) \mu(p, v).$$

We show in Appendix 9.B that

$$(\partial_p \psi_d) \mu(p, v) = -\kappa(p) w(p, v) + \Delta_1(p, v),$$

where $\kappa(p)$ is the curvature at p of the level set of h through p, $w(p, v)$ is defined in (9.8), and $\Delta_1(p, v)$ is a smooth function that vanishes on γ and is bounded with

respect to v. Since $p(t)$ has a uniform bound over initial conditions in $\mathcal{N}(\Gamma_1)$, so does $\Delta_1(p(t), v(t))$. Back to the $\dot{v}$ equation, using the identity

$$R_\psi \begin{bmatrix} u \\ v \end{bmatrix} = R_{\psi_d} \begin{bmatrix} \bar{u} \\ v \end{bmatrix} + (R_{\psi-\psi_d} - I) \begin{bmatrix} \bar{u} \\ v \end{bmatrix} + R_\psi \begin{bmatrix} u - \bar{u} \\ 0 \end{bmatrix},$$

we have

$$\begin{aligned} \dot{v} = \frac{1}{1 - \alpha X} \Big(& Y(u)v - w(p, v)X(u)\kappa(p) \\ & + X(u)(\partial_p \psi_d)(R_{\psi-\psi_d} - I) \begin{bmatrix} \bar{u} \\ v \end{bmatrix} + \Delta_2(\chi) \Big), \end{aligned}$$

where $\Delta_2(\chi) = X(u)(\Delta_1(p, v) + \partial_p \psi_d (R_\psi [u - \bar{u} \;\; 0]^\top) + \dot{e})$ is uniformly bounded along solutions originating in $\mathcal{N}(\Gamma_1)$. We now derive two bounds valid on the positively invariant set $\mathcal{N}(\Gamma_1)$. First, the boundedness of p yields

$$\big| w(p, v)X(u)\kappa(p) \big| \leq C_1 + |X(u)||\kappa||v|$$

for some $C_1 > 0$. Also, it is possible to show that $\|\partial_p \psi_d(p, v)\|$ is bounded. Then, since $|\psi - \psi_d| < \delta$, we have the second bound

$$\big| X(u)(\partial_p \psi_d)(R_{\psi-\psi_d} - I)[\bar{u} \;\; v]^\top \big| \leq |X(u)|\delta|v| + C_2,$$

for some $C_2 > 0$. Recall that, by Assumption 9.1, $\bar{u} \in [0, V_{\max}]$, so that $Y(\bar{u}) < 0$ and for sufficiently small δ, $Y(u) < 0$ as well. Define the Lyapunov function $V = v^2/2$, then

$$\begin{aligned} \dot{V} \leq \frac{-1}{1 - \alpha X} \Big(& |Y(u)| - |X(u)|(|\kappa| + \delta) \Big) v^2 \\ & + \Big((C_1 + C_2) + \sup_{\chi \in \mathcal{N}(\Gamma_1)} \Delta_2(\chi) \Big) |v|. \end{aligned}$$

By assumption, $|Y(\bar{u})| - |X(\bar{u})||\kappa(p)| > 0$ for all $p \in \gamma$. Since κ is a continuous function and since, on $\mathcal{N}(\Gamma_1)$, $|u - \bar{u}| < \delta$ and $|h(p)| < \rho(\delta)$, we have that for small enough δ,

$$|Y(u)| - |X(u)|(|\kappa(p)| + \delta) > 0.$$

Thus $v(t)$ is uniformly bounded. Since r is a continuous function of $(p, u, v, \psi, \dot{e})$, r is uniformly bounded as well. This proves the LUB property near Γ_1. □

Application of Theorem 9.1 gives the following result.

Theorem 9.5. *Consider system* (9.2) *with the feedbacks defined in* (9.14)*, suppose that Assumptions 9.1 and 9.2 hold, and assume that the desired surge speed* $\bar{u} \in [0, V_{\max}]$ *is chosen such that condition* (9.12) *holds. If the curvature* κ *of* γ *satisfies the bound*

$$\max_{p \in \gamma} |\kappa(p)| < \frac{|Y(\bar{u})|}{|X(\bar{u})|},$$

then Γ_1 *and* Γ_2 *are asymptotically stable, implying that feedback* (9.14) *solves the PFP.*

Remark 9.2. It is interesting to note that in Moe et al. [100, Theorem 1], the authors present a stability result for a path-following control law with a similar, but more restrictive, curvature bound, $\max|\kappa| < (1/3)|Y(\bar{u})/X(\bar{u})|$ compared to that in Theorem 9.5.

9.6 Simulation Results

In this section two case studies are presented to verify the proposed path-following strategy. For this purpose we consider a supply vessel described by the model (9.2) with the function descriptions and model parameters given in Appendix 9.A. In the first case study we consider the case of following of following a straight-line path. Note that in the proof we assume the curves are Jordan, which the straight-line is not since it is not closed. However, the straight-line is a common test case and serves as a good proof of concept of the control strategy. The second case study considers following of a Cassini oval.

9.6.1 Case 1: Straight-Line Path

In this case study the goal is to follow a straight-line path aligned with the inertial x-axis. Hence, $h(p) \triangleq -p_y$ and the implicit representation of the path is given by $\gamma = \{p : -p_y = 0\}$. This assures that the unit normal vector, $N(p)$, points in the negative y-direction and the unit tangent vector, $T(p)$, points in the positive x-direction. The desired velocity is chosen as $\bar{u} = 2$ [m/s] and the saturation function is set to $\sigma(h(p)) = 2/\pi \tan^{-1}(h(p))$. The initial conditions are given by $\chi_0 := ([0, 100], 0, 0, \pi/2, 0)$ and the controller gains from (9.14) are given by $K_u = 0.5$, $K_p = 0.4$, and $K_d = 2$. The trajectory of the ship in the x-y plane can be seen in Figure 9.2, where the ship icons superimposed on the path give the orientation of the ship at those points. From Figure 9.2 it can be seen that the trajectory converges to the x-axis and that the ship travels in the direction of the unit tangent vector $T(p)$. The positional error of the ship w.r.t. the path, i.e. p_y, can be seen in Figure 9.3, from which it can clearly be seen that the error converges to zero.

9.6.2 Case 2: Cassini Oval

In this case study the goal is to follow a Cassini oval. This implies that $h(p) \triangleq (p_x^2 + p_y^2)^2 - 2a^2(p_x^2 - p_y^2) + a^4 - b^4$ and that the path is implicitly described by

$$\gamma = \{p : (p_x^2 + p_y^2)^2 - 2a^2(p_x^2 - p_y^2) + a^4 - b^4 = 0\}.$$

where in this case study $a = 22.5$ [m] and $b = 24.9$ [m]. This results in a curve for which the maximum curvature $\max_{p\in\gamma}|\kappa(p)| = 0.0785$ and with a desired velocity $\bar{u} = 2$ [m/s] the ratio $|Y(\bar{u})|/|X(\bar{u})| = 0.2483$. Note that this curve satisfies the curvature condition of Theorem 9.5 showing that this is not a very restrictive condition, since it allows a ship with a length of approximately 83 meters to follow a curve whose diameter (the maximum distance between any two of its points) is approximately 70 metres. The saturation function is set to $\sigma(h(p)) = 2/\pi \tan^{-1}(\alpha h(p))$,

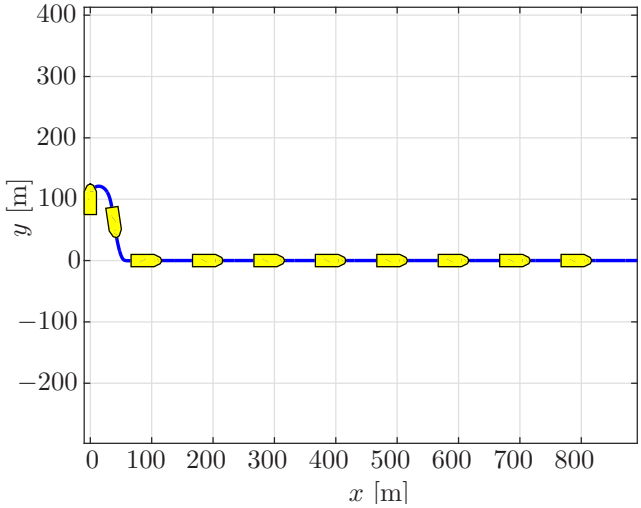

Figure 9.2: Path of the ship (the ship is not to scale).

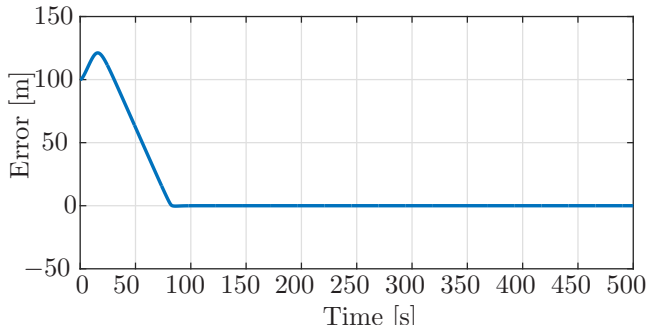

Figure 9.3: Path-following error of the ship.

where α is a parameter that can be used to tune the slope of the saturation function. In this case the magnitude of $h(p)$ is large, therefore α needs to be small to make the saturation effective close to the path and we choose $\alpha = 10^{-4}$. The initial conditions are given by $\chi_0 := ([15, 45], 0, 0, -2/3\pi, 0)$ and the controller gains from (9.14) are given by $K_u = 1$, $K_p = 30$, and $K_d = 5$. The trajectory of the ship and the desired oval can be seen in Figure 9.4. From Figure 9.4 we can clearly see convergence to the desired oval and from the superimposed ships it can be seen that the heading of the vessel is not tangent to the oval. Its velocity vector, on the other hand, is tangent to the path. From the plot of the sway velocity in Figure 9.5 it can be seen that this motion induces quite large sway velocities relative to the desired surge velocity $\bar{u} = 2$ [m/s]. The value of $h(p)$ is plotted in Figure 9.6 which shows that $h(p)$ is driven to zero as the ship converges to the path, showing that

the ship is able to track the specified Cassini oval in accordance with the theoretical analysis.

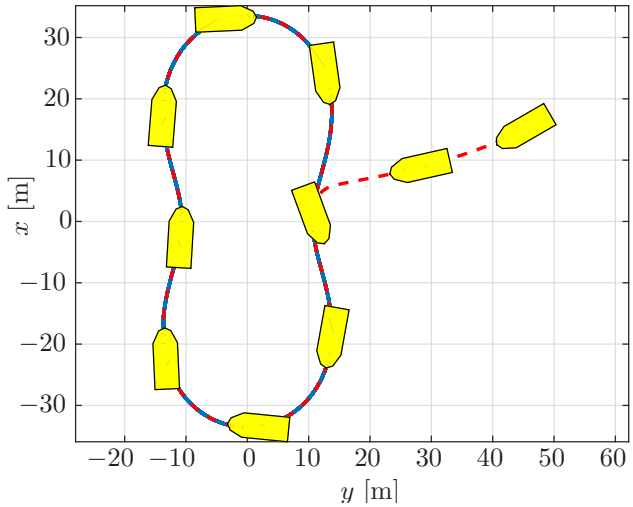

Figure 9.4: Path of the ship and the cassini oval (the ship is not to scale).

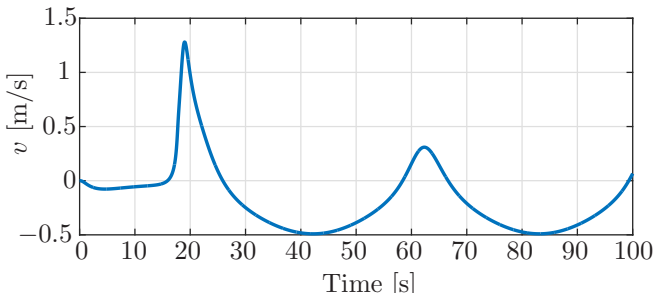

Figure 9.5: Sway velocity of the ship.

9.7 Conclusions

In this chapter we presented a methodology to design path-following controllers for a class of underactuated marine vessels. This methodology allows one to migrate a path-following controller designed for a point-mass to one that is guaranteed to work for the underactuated vessel. As we mentioned in the introduction, the proposed solution is an initial step. For simplicity, we assumed the curve to be Jordan and the ocean current to be absent. We will remove these assumptions in future work.

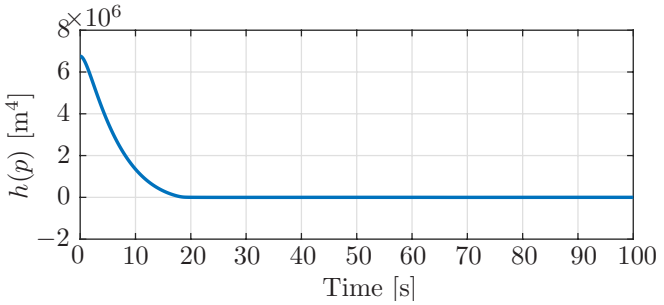

Figure 9.6: Magnitude of $h(p)$ as the vessel converges to the path.

9.A Functions used in the Model

The functions F_u, $X(u)$, $Y(u)$, and F_r are given by:

$$\begin{aligned}
F_u &\triangleq \frac{1}{m_{11}}(m_{22}v + m_{23}r)r, \\
X(u) &\triangleq \frac{m_{23}^2 - m_{11}m_{33}}{m_{22}m_{33} - m_{23}^2}u + \frac{d_{33}m_{23} - d_{23}m_{33}}{m_{22}m_{33} - m_{23}^2}, \\
Y(u) &\triangleq \frac{(m_{22} - m_{11})m_{23}}{m_{22}m_{33} - m_{23}^2}u - \frac{d_{22}m_{33} - d_{32}m_{23}}{m_{22}m_{33} - m_{23}^2}, \\
F_r(u,v,r) &\triangleq \frac{m_{23}d_{22} - m_{22}(d_{32} + (m_{22} - m_{11})u)}{m_{22}m_{33} - m_{23}^2}v \\
&\quad + \frac{m_{23}(d_{23} + m_{11}u) - m_{22}(d_{33} + m_{23}u)}{m_{22}m_{33} - m_{23}^2}r.
\end{aligned}$$

The numerical expressions for the matrices $\boldsymbol{M}$, $\boldsymbol{D}$, and $\boldsymbol{B}$ used in the simulations are

$$\boldsymbol{M} \triangleq \begin{bmatrix} 7.22e6 & 0 & 0 \\ 0 & 1.21e7 & -5.6446e7 \\ 0 & -5.6446e7 & 4.9044e9 \end{bmatrix},$$

$$\boldsymbol{D} \triangleq \begin{bmatrix} 9.507e4 & 0 & 0 \\ 0 & 4.34e6 & -9.6961e6 \\ 0 & -2.6026e7 & 8.0445e8 \end{bmatrix} \quad \boldsymbol{B} \triangleq \begin{bmatrix} 1 & 0 \\ 0 & -1.13e6 \\ 0 & 9.8181e9 \end{bmatrix}$$

which are the model parameters from Fredriksen and Pettersen [63] translated from the center of gravity to the point ϵ, where $\epsilon = 1.6650$ m.

9.B Curvature Computation for Lemma 9.4

We need to find an expression for $(\partial_p \psi_d)\mu(p,v)$. We begin by recalling the expressions for $\cos(\psi_d)$ and $\sin(\psi_d)$ from the proof of Lemma 9.3:

$$\begin{bmatrix} \cos(\psi_d) \\ \sin(\psi_d) \end{bmatrix} = \frac{1}{\bar{u}^2 + v^2} \begin{bmatrix} \bar{u} & v \\ -v & \bar{u} \end{bmatrix} \mu.$$

Then we write

$$\begin{aligned}\partial_p \psi_d &= \begin{bmatrix} -\sin(\psi_d) & \cos(\psi_d) \end{bmatrix} \begin{bmatrix} \partial_p \cos(\psi_d) \\ \partial_p \sin(\psi_d) \end{bmatrix} \\ &= \frac{1}{(\bar{u}^2+v^2)^2} \mu^\top \begin{bmatrix} v & \bar{u} \\ -\bar{u} & v \end{bmatrix} \begin{bmatrix} \bar{u} & v \\ -v & \bar{u} \end{bmatrix} \partial_p \mu \\ &= \frac{1}{(\bar{u}^2+v^2)} \mu^\top \begin{bmatrix} 0 & 1 \\ -1 & 0 \end{bmatrix} \partial_p \mu.\end{aligned}$$

Thus

$$(\partial_p \psi_d)\mu(p,v) = \frac{1}{(\bar{u}^2+v^2)} \mu^\top \begin{bmatrix} 0 & 1 \\ -1 & 0 \end{bmatrix} (\partial_p \mu)\mu.$$

At this point we substitute in the expression for $\mu(p,v)$ in (9.7), using $w(p,v)$ in (9.8) and the fact that

$$N(p) = \frac{1}{((\partial_x h)^2 + (\partial_y h)^2)^{(1/2)}},\ T(p) = \begin{bmatrix} 0 & -1 \\ 1 & 0 \end{bmatrix} N(p).$$

After some algebra we obtain

$$(\partial_p \psi_d)\mu = -\kappa(p) w(p,v) + \Delta_1(p,v),$$

where κ is given in (9.3) and

$$\begin{aligned}\Delta_1(p,v) = &-\frac{\bar{u}\sigma(h(p))}{((\partial_x h)^2 + (\partial_y h)^2)^{3/2}} \Big[\partial^2_{xy} h \left((\partial_x h)^2 - (\partial_y h)^2\right) \\ &+ (\partial_x h)(\partial_y h)(\partial^2_{yy} h - \partial^2_{xx} h)\Big] - \frac{\bar{u}^2 \sigma(h(p))\sigma'(h(p))}{w(p,v)((\partial_x h)^2 + (\partial_y h)^2)^{3/2}} \\ &\cdot \left[(\partial_x h)^4 + (\partial_y h)^4 + 2(\partial_x h)^2 (\partial_y h)^2\right].\end{aligned}$$

We see that $\Delta_1(p,v)$ vanishes when $h(p) = 0$. Moreover, its dependence on v arises in the term $w(p,v)$ in one denominator. Since the function $1/w(p,v)$ is bounded with respect to v, so is Δ_1.

Chapter 10

Conclusions and Future Work

This thesis has considered various topics subdivided into three parts. Some concluding remarks are given in this chapter together with some suggestions for future developments on these topics.

The first part considered the modelling of marine vehicles and environmental disturbances. In this part novel results were introduced to estimate the wave encounter frequency for a marine vessel. Rather than using models of the vessel or using spectral analysis techniques, this estimator is based on measurements of the ship motion that are readily available for the vessel such as the roll and pitch angle of the ship. These signals are sinusoidal in nature and their frequency is coupled directly to the frequency of the waves exciting the vessel. Therefore, a frequency estimator for the frequency of sinusoidal signals was adapted for application to ship motion signals. In particular, the estimator was equipped with a gain-switching mechanism that allows the estimator to function in situations of low excitation by switching to a higher gain and in situations of high excitation by doing the converse. Moreover, it was shown that the stability properties of the estimator still hold for time-varying amplitudes as long as the signal is persistently exciting. The origin of the estimation error dynamics were shown to be globally exponentially stable for the new estimator. The estimator was verified using an experimental case study. The case study considered several data sets gathered in towing tank tests with a model ship and data from an Atlantic passage with a container ship. The frequency estimator was successfully applied to two data sets of pitch angle measurements and two sets of heave displace measurements gathered in the towing tank tests and a data set of pitch angle measurements from the Atlantic passage. Future developments of interest for this work would be the investigation of multi-frequency estimators to be able to estimate the peaks of multi-peak wave spectra. Moreover, it can be of interest to unify this result with other model based results and spectral analysis results such that more information of the sea state can be extracted.

The second part of the thesis considered multi-vehicle approaches. Straight line coordinated path following in the presence of constant ocean currents is considered both for marine surface vessels and for autonomous underwater vehicles. The aim of this work was to combine the results for straight-line path following in the presence

of constant ocean currents using integral line-of-sight guidance, and a coordination law that had been successfully applied to straight-line path following in the absence of disturbances. The combination of the disturbance rejection algorithm with the formation control approach breaks the cascaded systems stability proof that was used for both strategies individually. It was shown, using a result from the literature that allows feedback-interconnections to be studied as cascades under certain conditions, that stability of the closed-loop system can still be shown. The theoretical results were supported by numerical simulations and an experimental case study using three autonomous underwater vehicles. It was shown that due to the lack of continuous communication in practice the performance degrades. However, these problems should be resolvable by appropriate tuning. As future work some of the measures suggested in the experimental case study might be implemented to see if the performance can be increased in practical circumstances. Moreover, the influence of time-delays and communication failures can be studied to extend the theoretical results. This part also considered a leader-follower type motion synchronisation. A constant bearing guidance algorithm from the literature, that is intended for straight-line target tracking, was analysed for applications of curved trajectories in this work. First, a proof was given to show that the constant bearing guidance algorithm results in USGES tracking error dynamics for which we can give an explicit bound on the synchronisation error, rather than UGAS and ULES by linearisation about the origin as previously shown which provided no such bound. The remainder of the chapter analysed the closed-loop system when the constant bearing guidance algorithm is used for curved leader trajectories. It was shown that for a straight line, synchronisation can be achieved, while on a curved trajectory only integral input-to-state stability of the synchronisation error with respect to the sway velocity can be shown. Simulation results were given to verify the theoretical results. As future work string stability of leader-follower vehicle strings could be investigated.

The third part of the thesis considered curved path following for underactuated marine vessels. Two strategies were presented for path following in the presence of an ocean current disturbance, and one strategy was presented that does not consider environmental disturbances. The two approaches in which ocean currents were considered were based on a line-of-sight type guidance laws aided by an ocean current observer to estimate the unknown disturbances. Path following was achieved by parametrising the path using a path variable that is used to propagate a path-tangential reference frame. The path-following errors are then expressed with respect to this frame and path following is achieved when the vessel converges to the frame. One of the strategies has a parametrisation that aims to keep the vessel on the normal of the path-tangential frame. The advantage of this approach is that the path-following error is always defined as the shortest distance to the path. However, the parametrisation has a singularity and therefore only a local result can be realised. The other approach has a parametrisation that is globally valid. However, in this case the path-following error is not the shortest distance to the path and there is no direct control over the rate of convergence. It was shown that the stability proof can be done along the same lines and allows us to conclude asymptotic stability for the local approach and global asymptotic stability for the global approach. This was done by first considering the sway velocity dynamics

and show that these dynamics are bounded under certain conditions. Stability of the path-following errors was then shown by recursively applying a cascaded systems argument. The theoretical results were supported by numerical simulations. Future development for this work might include substituting the ocean current observer with an adaptive algorithm that can compensate for the ocean current much like the integral line-of-sight for straight-line paths. The curved path-following approach that did not consider ocean currents disturbances presented novel results that allow path following without the need for parametrisation of the path. Consequently, this is the purest form of path following that only aims at stabilising a manifold of the state space. The approach is based on principles from geometric control and principles from hierarchical control design. It was shown that based on a condition on the curvature, the sway velocity remains bounded and the path is an asymptotically stable manifold for the vehicle and path-following can be achieved. The theoretical results were supported by numerical simulations. Future work on this topic could be to make the strategy globally valid and adding an ocean current disturbance.

Appendices

Appendix A

Mathematical References

This appendix contains some of the mathematical definitions and notations that are used in the thesis.

A.1 Notation

We denote by $\mathbb{R}^n$ the n-dimensional Euclidean space and by $\mathbb{R}^+$ the set of all non-negative real numbers. The absolute value of a scalar x is denoted by $|x|$. The p-norm of a vector $x \in \mathbb{R}^n$ is denoted by $\|x\|_p$, for $p \in [1, \infty]$, when no subscript is given, i.e. $\|x\|$, the Euclidean norm is implied. The following definitions of comparison functions, known as class $\mathcal{K}$ and $\mathcal{KL}$ functions, are used throughout the thesis.

Definition A.1 (Khalil [82, Definition 4.2])**.** A continuous function $\alpha : [0, a) \to [0, \infty)$ is said to belong to class $\mathcal{K}$ if it is strictly increasing and $\alpha(0) = 0$. It is said to belong to class $\mathcal{K}_\infty$ if $a = \infty$ and $\alpha(r) \to \infty$ as $r \to \infty$.

Definition A.2 (Khalil [82, Definition 4.3])**.** A continuous function $\beta : [0, a) \times [0, \infty) \to [0, \infty)$ is said to belong to class $\mathcal{KL}$ if, for each fixed s, the mapping $\beta(r, s)$ belongs to class $\mathcal{K}$ with respect to r and, for each fixed r, the mapping $\beta(r, s)$ is decreasing with respect to s and $\beta(r, s) \to 0$ as $s \to \infty$.

Lemma A.1 (Khalil [82, Lemma 4.2])**.** *Let α_1 and α_2 be class $\mathcal{K}$ functions on $[0, a)$, α_1 and α_2 be class $\mathcal{K}_\infty$ functions on $[0, a)$, and β be a class $\mathcal{KL}$ function. Denote the inverse of α_i by α_i^{-1}. Then,*

- *α_1^{-1} is defined on $[0, \alpha_1(a))$ and belongs to class $\mathcal{K}$.*
- *α_3^{-1} is defined on $[0, \infty)$ and belongs to class $\mathcal{K}_\infty$.*
- *$\alpha_1 \circ \alpha_2$ belongs to class $\mathcal{K}$.*
- *$\alpha_3 \circ \alpha_4$ belongs to class $\mathcal{K}_\infty$.*
- *$\sigma(r, s) = \alpha_1(\beta(\alpha_2(r), s))$ belongs to class $\mathcal{KL}$.*

A.2 Stability Definitions

We now presents some notions of stability for a nonautonomous system

$$\dot{x} = f(t, x) \tag{A.1}$$

where $f : [0, \infty) \times D \to \mathbb{R}^n$ is piecewise continuous in t and locally Lipschitz in x on $[0, \infty) \times D$, with $D \subset \mathbb{R}^n$ a domain that contains the origin $x = 0$. The following definitions are obtained from Khalil [82]

Definition A.3. The equilibrium point $x = 0$ of (A.1) is

- uniformly stable (US) if and only if there exist a class $\mathcal{K}$ function α and a positive constant c, independent of t_0, such that

$$\|x(t)\| \leq \alpha(\|x(t)\|), \ \forall t \geq t_0 \geq 0, \ \forall \|x(t_0)\| < c \tag{A.2}$$

- globally uniformly stable (UGS) if an only if inequality (A.2) is satisfied for any initial state $x(t_0)$.
- uniformly asymptotically stable (UAS) if and only if there exist a class $\mathcal{KL}$ function β and a positive constant c, independent of t_0, such that

$$\|x(t)\| \leq \beta(\|x(t_0)\|, t - t_0), \ \forall t \geq t_0 \geq 0, \ \forall \|x(t_0)\| < c \tag{A.3}$$

- globally uniformly asymptotically stable (UGAS) if an only if inequality (A.3) is satisfied for any initial state $x(t_0)$.

Definition A.4 (Khalil [82, Definition 4.5])**.** The equilibrium point $x = 0$ of (A.1) is locally exponentially stable (LES) if there exist positive constants c, k, and λ such that

$$\|x(t)\| \leq k\|x(t_0)\|e^{-\lambda(t-t_0)}, \ \forall \|x(t_0)\| < c \tag{A.4}$$

and globally exponentially stable (GES) if (A.4) is satisfied for any initial state $x(t_0)$.

A.3 Cascaded Systems

Consider the following nonlinear time-varying cascaded system:

$$\dot{x} = f_1(t, x) + g(t, x, y) \tag{A.5a}$$
$$y = f_2(t, y) \tag{A.5b}$$

where $x \in \mathbb{R}^n$, $y \in \mathbb{R}^m$, and $f_1(t, x)$ and $f_2(t, x)$ continuously differentiable in their arguments. The following results characterise the stability properties of the system (A.5).

Lemma A.2 (Panteley and Loría [112, Lemma 2])**.** *Consider the cascaded system* (A.5)*. If both* $\dot{x} = f_1(t, x)$ *and* $\dot{y} = f_2(t, y)$ *are UGAS and the solutions of* (A.5a) *and* (A.5b) *are globally uniformly bounded, then the cascaded system* (A.5) *is UGAS.*

Theorem A.3 (Panteley and Loria [111, Theorem 2]). *Consider the cascaded system* (A.5). *Assume that the system* $\dot{x} = f_1(t,x)$ *is UGAS with a Lyapunov function* $V(t,x)$ *satisfying*

$$\left\| \frac{\partial V}{\partial x} \right\| \|x\| \leq c_1 V(t,x), \quad \forall \|x\| \geq \eta > 0, \tag{A.6}$$

and that Assumptions (A1)-(A2) below are satisfied. Then the cascaded system (A.5) *is UGAS.*

(A1) The function $g(t,x,y)$ *satisfies*

$$\|g(t,x,y)\| \leq \theta_1(\|y\|) + \theta_2(\|y\|)\|x\|, \tag{A.7}$$

where $\theta_1, \theta_2 : \mathbb{R}^+ \to \mathbb{R}^+$ *are continuous.*

(A2) The system $\dot{y} = f_2(t,y)$ *is UGAS and for all* $t \geq t_0$,

$$\int_{t_0}^{t} \|x(s)\| \mathrm{d}s \leq \phi(\|x(t_0)\|), \tag{A.8}$$

where $\phi(\cdot) \in \mathcal{K}$.

Remark A.1. If the nominal system $\dot{x} = f_1(t,x)$ is UGAS with a quadratic Lyapunov function, then the condition (A.6) is satisfied trivially.

Remark A.2. If the perturbing system $\dot{y} = f_2(t,y)$ is UGAS and ULES (or equivalently exponentially stable in any ball of initial conditions), then the integrability condition (A.8) is satisfied trivially

Lemma A.4 (Panteley et al. [113, Lemma 8]). *If in addition to the assumptions in Theorem A.3, both* $\dot{x} = f_1(t,x)$ *and* $\dot{y} = f_2(t,y)$ *are UGAS and ULES then the cascaded system* (A.5) *is UGAS and ULES.*

Proposition A.1 (Loría and Panteley [94, Proposition 2.3]). *If in addition to the assumptions in Theorem A.3, both* $\dot{x} = f_1(t,x)$ *and* $\dot{y} = f_2(t,y)$ *are UGES then the cascaded system* (A.5) *is UGES.*

A.4 Integral Input-to-State Stability

Consider the system

$$\dot{x} = f(x,u) \tag{A.9}$$

with states $x(t) \in \mathbb{R}^n$ and the inputs are measurable locally essentially bounded functions $u : \mathbb{R}^+ \to \mathbb{R}^m$, and $f : \mathbb{R}^n \times \mathbb{R}^m \to \mathbb{R}^n$ locally Lipschitz. Given any control u and any $\xi \in \mathbb{R}^n$, there is a unique maximal solution of the intial value problem $\dot{x} = f(x,u)$, $x(0) = \xi$. This solution is defined on some maximal open interval, and it is denoted by $x(\cdot, \xi, u)$.

Definition A.5 (Angeli et al. [6, Definition 2.2]). The system (A.9) is integral input-to-state stable (iISS) if there exists functions $\alpha \in \mathcal{K}_\infty$, $\beta \in \mathcal{KL}$, and $\gamma \in \mathcal{K}$, such that, for all $\xi \in \mathbb{R}^n$ and all u, the solution $x(t, \xi, u)$ is defined for all $t \geq 0$, and

$$\alpha(\|x(t, \xi, u)\|) \leq \beta(\|\xi\|, t) + \int_0^t \gamma(\|u(s)\|)\mathrm{d}s \tag{A.10}$$

for all $t \geq 0$, all $\xi \in \mathbb{R}^n$, and all u.

Definition A.6 (Angeli et al. [6, Definition 2.2]). A continuously differentiable function $V : \mathbb{R}^n \to \mathbb{R}$ is called an iISS-Lyapunov function for system (A.9) if there exist functions $\alpha_1, \alpha_2 \in \mathcal{K}$, and a continuous positive definite function α_3, such that

$$\alpha_1(\|\xi\|) \leq V(\xi) \leq \alpha_2(\|\xi\|) \tag{A.11}$$

for all $\xi \in \mathbb{R}^n$ and

$$DV(\xi)f(\xi, \mu) \leq -\alpha_3(\|\xi\|) + \sigma(\|\mu\|) \tag{A.12}$$

for all $\xi \in \mathbb{R}^n$ and all $\mu \in \mathbb{R}^m$.

A.5 Additional Tools

Lemma A.5 (Comparison Lemma, Khalil [82, Lemma 3.4]). *Consider the scalar differential equation*

$$\dot{u} = f(t, u), \quad u(t_0) = u_0$$

where $f(t, u)$ is continuous in t and locally Lipschitz in u, for all $t \geq 0$ and all $u \in J \subset \mathbb{R}$. Let $[t_0, T)$ (T could be infinity) be the maximal interval of existence of the solution $u(t) \in J$ for all $t \in [t_0, T)$. Let $v(t)$ be a continuous function whose upper right-hand derivative $D^+v(t)$ satisfies the differential inequality

$$D^+v(t) \leq f(t, v(t)), \quad v(t_0) \leq u_0$$

with $v(t) \in J$ for all $t \in [t_0, T)$. Then, $v(t) \leq u(t)$ for all $t \in [t_0, T)$.

Definition A.7 (Angeli and Sontag [5]). Consider a general nonlinear system of the form

$$\dot{x} = f(x, u), \quad y = h(x) \tag{A.13}$$

with states $x \in \mathbb{R}^n$, inputs $u \in \mathbb{R}^m$, and outputs $y \in \mathbb{R}^p$. The maps $f : \mathbb{R}^n \times \mathbb{R}^m \to \mathbb{R}^n$ and $h : \mathbb{R}^n \to \mathbb{R}^m$ are locally Lipschitz continuous. By an input signal for (A.13) we mean any measurable locally essentially bounded function of time, $u(\cdot) : \mathbb{R} \to \mathbb{R}^m$. The system (A.13) is called forward complete if for every initial condition and every input signal u, the corresponding solution is defined for all $t \geq 0$.

Theorem A.6 (Angeli and Sontag [5, Corollary 2.11]). *System* (A.13) *is forward complete if and only if there exists a smooth and proper function* $V : \mathbb{R}^n \to \mathbb{R}_{\geq 0}$ *and such that*

$$\frac{\partial V(x)}{\partial x} f(x,u) \leq V(x) + \sigma(\|u\|), \quad \forall x \in \mathbb{R}^n, \ \forall u \in \mathbb{R}^m \tag{A.14}$$

holds for some $\sigma \in \mathcal{K}_\infty$.

Lemma A.7 (Khalil [82, Lemma 8.2]). *Let* $\phi : \mathbb{R} \to \mathbb{R}$ *be a uniformly continuous function on* $[0, \infty)$. *Suppose that* $\lim_{t\to\infty} \int_0^t \phi(\tau)\mathrm{d}\tau$ *exists and is finite. Then,*

$$\phi(t) \to 0 \tag{A.15}$$

as $t \to \infty$.

Appendix B

Translation of Equations of Motion

This appendix presents the detail on how to perform the translation of the equations of motion for both the surface vessel model considered in Section 2.2 and the model for the AUV considered in Section 2.3. This translation is applied to remove the effect of the yaw rate controller on the representation of the sway velocity dynamics. This significantly simplifies the process of control design and the stability analysis. The coordinate transformation for a surface vessel can be found in Fredriksen and Pettersen [64] and is given Section B.1 of this appendix. The transformation for an AUV can be found in Børhaug et al. [29] and is given in Section B.2 of this appendix.

B.1 Translation for the Manoeuvring Model in 3-DOF

Recall the model given in Section 2.2;

$$\dot{\boldsymbol{\eta}} = \boldsymbol{R}(\psi)\boldsymbol{\nu}_r + [V_x, V_y, 0]^T \tag{B.1}$$

$$\boldsymbol{M}\dot{\boldsymbol{\nu}}_r + \boldsymbol{C}(\boldsymbol{\nu}_r)\boldsymbol{\nu}_r + \boldsymbol{D}\boldsymbol{\nu}_r = \boldsymbol{B}\boldsymbol{f}. \tag{B.2}$$

where $\boldsymbol{\eta} \triangleq [x, y, \psi]^T$, $\boldsymbol{\nu}_r \triangleq [u_r, v_r, r]^T$, $\boldsymbol{f} \triangleq [T_u, T_r]^T$, and

$$\boldsymbol{M} \triangleq \begin{bmatrix} m_{11} & 0 & 0 \\ 0 & m_{22} & m_{23} \\ 0 & m_{23} & m_{33} \end{bmatrix}, \boldsymbol{D} \triangleq \begin{bmatrix} d_{11} & 0 & 0 \\ 0 & d_{22} & d_{23} \\ 0 & d_{32} & d_{33} \end{bmatrix}, \boldsymbol{B} \triangleq \begin{bmatrix} b_{11} & 0 \\ 0 & b_{22} \\ 0 & b_{32} \end{bmatrix}.$$

From the structure of $\boldsymbol{M}$, $\boldsymbol{B}$, and $\boldsymbol{f}$ it is straightforward to verify that in this model the rudder angle input T_r influences not only the dynamics of the yaw but also the dynamics of the sway velocity. The transformation presented here allows us to transform the equations of motions to a point where it holds that $\boldsymbol{M}^{-1}\boldsymbol{B}\boldsymbol{f} = [\tau_u, 0, \tau_r]^T$. Hence, in this point the sway velocity dynamics are decoupled from the yaw control.

For the case of a surface vessel the following transformation is proposed in Fredriksen and Pettersen [64]

$$\bar{v}_r = v_r + \epsilon r, \tag{B.3}$$

where ϵ is a constant given by

$$\epsilon \triangleq -\frac{m_{33}b_{22} - m_{23}b_{32}}{m_{22}b_{32} - m_{23}b_{22}} \tag{B.4}$$

where as pointed out in Børhaug [26] this transformation is well-defined if the system is initially controllable in yaw. This transformation corresponds to moving the body-frame along the center line of the vessel, for a distance ϵ, to a point where the yaw control input generates a pure rotation and no sway force. Therefore, as in Caharija [39] we translate the body-fixed frame to the point where yaw and sway are decoupled and consider motion around this point in this thesis. This can be done without loss of generality, since the transformation is invertible and the structure and properties of the inertia and damping matrices are not changed.

The transformation results in a transformed body-frame velocity vector $\bar{\boldsymbol{\nu}}_r \triangleq [u_r, \bar{v}_r, r]^T$. As in Caharija [39] we note that there exists a corresponding transformation matrix $\boldsymbol{H}_{3DOF}$ such that $\boldsymbol{\nu}_r = \boldsymbol{H}_{3DOF}\bar{\boldsymbol{\nu}}_r$ where

$$\boldsymbol{H}_{3DOF} \triangleq \begin{bmatrix} 1 & 0 & 0 \\ 0 & 1 & -\epsilon \\ 0 & 0 & 1 \end{bmatrix}. \tag{B.5}$$

The transformation of the equations of motion using $\boldsymbol{H}_{3DOF}$ is preformed as described in Fossen [60] and results in

$$\dot{\boldsymbol{\eta}} = \boldsymbol{R}(\psi)\boldsymbol{\nu}_r + [V_x, V_y, 0]^T \tag{B.6}$$

$$\boldsymbol{M}^H\dot{\boldsymbol{\nu}}_r + \boldsymbol{C}^H(\boldsymbol{\nu}_r)\boldsymbol{\nu}_r + \boldsymbol{D}^H\boldsymbol{\nu}_r = \boldsymbol{B}^H\boldsymbol{f}. \tag{B.7}$$

where $\boldsymbol{M}^H \triangleq \boldsymbol{H}_{3DOF}^T\boldsymbol{M}\boldsymbol{H}_{3DOF}$, $\boldsymbol{D}^H \triangleq \boldsymbol{H}_{3DOF}^T\boldsymbol{D}\boldsymbol{H}_{3DOF}$, and $\boldsymbol{B}^H \triangleq \boldsymbol{H}_{3DOF}^T\boldsymbol{B}$. The model now corresponds to the motion around the point where the yaw rudder control is now decoupled from the sway dynamics. Consequently, it can now be verified that

$$(\boldsymbol{M}^H)^{-1}\boldsymbol{B}^H\boldsymbol{f} = \begin{bmatrix} \frac{b_{11}}{m_{11}}T_u \\ 0 \\ \frac{m_{22}b_{32} - m_{23}b_{22}}{m_{22}m_{33} - m_{23}^2}T_r \end{bmatrix} \tag{B.8}$$

such that we can define

$$\begin{bmatrix} \tau_u \\ \tau_r \end{bmatrix} \triangleq \begin{bmatrix} \frac{b_{11}}{m_{11}} & 0 \\ 0 & \frac{m_{22}b_{32} - m_{23}b_{22}}{m_{22}m_{33} - m_{23}^2} \end{bmatrix} \begin{bmatrix} T_u \\ T_r \end{bmatrix}. \tag{B.9}$$

The controllers in this thesis are developed in terms on τ_u and τ_r, but can be easily be transformed back in terms of T_u and T_r using the inverse of transformation of (B.9) which is well defined since $\boldsymbol{M}$ is positive definite.

B.2 Translation for the Manoeuvring Model in 5-DOF

Recall the model given in Section 2.3;

$$\begin{aligned} \dot{\boldsymbol{\eta}} &= \boldsymbol{J}(\boldsymbol{\eta})\boldsymbol{\nu}_r + [V_x, V_y, V_z, 0, 0]^T, \\ \boldsymbol{M}\dot{\boldsymbol{\nu}}_r + \boldsymbol{C}(\boldsymbol{\nu}_r)\boldsymbol{\nu}_r + \boldsymbol{D}\boldsymbol{\nu}_r + \boldsymbol{g}(\boldsymbol{\eta}) &= \boldsymbol{B}\boldsymbol{f} \end{aligned} \tag{B.10}$$

where $\boldsymbol{\eta} = [x, y, z, \theta, \psi]^T$, $\boldsymbol{\nu}_r = [u_r, v_r, w_r, q, r]^T$, $\boldsymbol{f} \triangleq [T_u, T_q, T_r]^T$, and the matrices $\boldsymbol{M}$ and $\boldsymbol{B}$ have the following structure

$$\boldsymbol{M} = \begin{bmatrix} m_{11} & 0 & 0 & 0 & 0 \\ 0 & m_{22} & 0 & 0 & m_{25} \\ 0 & 0 & m_{33} & m_{34} & 0 \\ 0 & 0 & m_{43} & m_{44} & 0 \\ 0 & m_{52} & 0 & 0 & m_{55} \end{bmatrix}, \quad \boldsymbol{B} \triangleq \begin{bmatrix} b_{11} & 0 & 0 \\ 0 & 0 & b_{23} \\ 0 & b_{32} & 0 \\ 0 & b_{42} & 0 \\ 0 & 0 & b_{53} \end{bmatrix}.$$

From the structure of $\boldsymbol{M}$, $\boldsymbol{B}$, and $\boldsymbol{f}$ it is straightforward to verify that the yaw rudder angle input T_r influences not only the dynamics of the yaw but also the dynamics of the sway velocity. Moreover, the pitch rudder angle T_q does not only influence the pitch dynamics but also the dynamics of the heave velocity. The transformation presented here allows us to transform the equations of motions to a point where it holds that $\boldsymbol{M}^{-1}\boldsymbol{B}\boldsymbol{f} = [\tau_u, 0, 0, \tau_q, \tau_r]^T$. Hence, in this point the sway velocity dynamics are decoupled from the yaw control and the heave velocity dynamics are decoupled from the pitch control.

Inspired by the work in Fredriksen and Pettersen [64] the following coordinate transform was proposed in Børhaug et al. [29]

$$\bar{v}_r = v_r + \epsilon_1 r, \quad \bar{w}_r = w_r + \epsilon_2 q, \tag{B.11}$$

where ϵ_1 and ϵ_2 are constants defined as

$$\epsilon \triangleq -\frac{m_{55}b_{23} - m_{25}b_{53}}{m_{22}b_{53} - m_{25}b_{23}}, \quad \epsilon \triangleq -\frac{m_{44}b_{32} - m_{34}b_{42}}{m_{33}b_{42} - m_{34}b_{32}}. \tag{B.12}$$

Note that ϵ_1 and ϵ_2 are well-defined if the original system is controllable in yaw and pitch. As pointed out in Børhaug [26] and Caharija [39] it is intresting to note that if $m_{22} = m_{33}$, $m_{44} = m_{55}$, $m_{25} = -m_{34}$, $b_{23} = -b_{32}$, and $b_{42} = b_{53}$ then it holds that $\epsilon_1 = -\epsilon_2$. Interestingly enough this holds for most AUVs of cylindrical shape since they satisfy symmetry properties in the body and in the diving control surfaces. Examples include the HUGIN AUV ([26]), the LAUV ([45]), and the ISiMI ([81]). If this is the case than the transformation reduces to a translation along the center-line of the body by a distance ϵ_1. Therefore, as in Caharija [39] we translate the body-fixed frame to the point where yaw and sway, and pitch and heave are decoupled and consider motion around this point in this thesis. This can be done without loss of generality, since the transformation is invertible and the structure and properties of the inertia and damping matrices are not changed.

As for the 3-DOF case we now introduce a transformed body-frame velocity vector $\bar{\boldsymbol{\nu}}_r \triangleq [u_r, \bar{v}_r, \bar{w}_r, q, r]^T$. As in Caharija [39] we note that there exists a corresponding transformation matrix $\boldsymbol{H}_{5DOF}$ such that $\boldsymbol{\nu}_r = \boldsymbol{H}_{5DOF}\bar{\boldsymbol{\nu}}_r$ where

$$\boldsymbol{H}_{5DOF} \triangleq \begin{bmatrix} 1 & 0 & 0 & 0 & 0 \\ 0 & 1 & 0 & 0 & -\epsilon_1 \\ 0 & 0 & 1 & -\epsilon_2 & 0 \\ 0 & 0 & 0 & 1 & 0 \\ 0 & 0 & 0 & 0 & 1 \end{bmatrix}. \tag{B.13}$$

The transformation of the equations of motion using $\boldsymbol{H}_{5DOF}$ is preformed as described in Fossen [60] and results in

$$\begin{aligned} \dot{\boldsymbol{\eta}} &= \boldsymbol{J}(\boldsymbol{\eta})\boldsymbol{\nu}_r + [V_x, V_y, V_z, 0, 0]^T, \\ \boldsymbol{M}^H\dot{\boldsymbol{\nu}}_r + \boldsymbol{C}^H(\boldsymbol{\nu}_r)\boldsymbol{\nu}_r + \boldsymbol{D}^H\boldsymbol{\nu}_r + \boldsymbol{g}^H(\boldsymbol{\eta}) &= \boldsymbol{B}^H\boldsymbol{f} \end{aligned} \tag{B.14}$$

where $\boldsymbol{M}^H \triangleq \boldsymbol{H}_{5DOF}^T\boldsymbol{M}\boldsymbol{H}_{5DOF}$, $\boldsymbol{D}^H \triangleq \boldsymbol{H}_{5DOF}^T\boldsymbol{D}\boldsymbol{H}_{5DOF}$, $\boldsymbol{g}^H(\boldsymbol{\nu}) = \boldsymbol{H}_{5DOF}^H\boldsymbol{g}(\boldsymbol{\nu})$, and $\boldsymbol{B}^H \triangleq \boldsymbol{H}_{5DOF}^T\boldsymbol{B}$. The model now corresponds to the motion around the point where the yaw rudder control and pitch rudder control are decoupled from the sway and heave dynamics respectively. Consequently, it can now be verified that

$$(\boldsymbol{M}^H)^{-1}\boldsymbol{B}^H\boldsymbol{f} = \begin{bmatrix} \frac{b_{11}}{m_{11}}T_u \\ 0 \\ 0 \\ \frac{m_{33}b_{42}-m_{34}b_{32}}{m_{33}m_{44}-m_{34}^2}T_q \\ \frac{m_{22}b_{53}-m_{25}b_{23}}{m_{22}m_{55}-m_{25}^2}T_r \end{bmatrix} \tag{B.15}$$

such that we can define

$$\begin{bmatrix} \tau_u \\ \tau_q \\ \tau_r \end{bmatrix} \triangleq \begin{bmatrix} \frac{b_{11}}{m_{11}} & 0 & 0 \\ 0 & \frac{m_{33}b_{42}-m_{34}b_{32}}{m_{33}m_{44}-m_{34}^2} & 0 \\ 0 & 0 & \frac{m_{22}b_{53}-m_{25}b_{23}}{m_{22}m_{55}-m_{25}^2} \end{bmatrix} \begin{bmatrix} T_u \\ T_q \\ T_r \end{bmatrix}. \tag{B.16}$$

The controllers in this thesis are developed in terms on τ_u, τ_q, and τ_r, but can be easily be transformed back in terms of T_u, T_q, and T_r using the inverse of transformation of (B.16) which is well defined since $\boldsymbol{M}$ is positive definite.

Appendix C

Numerical Simulation Models

This appendix presents the models used for the numerical simulations in the thesis. The first model is for a supply vessel, this a 3-DOF model and corresponds to the model in Section 2.2. The second model is a model for an AUV, this model corresponds to the 5-DOF model in Section 2.3.

C.1 Numerical Model for a Supply Vessel

This section presents a simulation model for an underactuated supply vessel. In particular, we consider the model derived in Fossen et al. [62] and Fredriksen and Pettersen [63]. Recall the dynamics of the model given by

$$\boldsymbol{M}\dot{\boldsymbol{\nu}}_r + \boldsymbol{C}(\boldsymbol{\nu}_r)\boldsymbol{\nu}_r + \boldsymbol{D}\boldsymbol{\nu}_r = \boldsymbol{B}\boldsymbol{f}. \tag{C.1}$$

The numerical values of $\boldsymbol{M}$, $\boldsymbol{B}$, and $\boldsymbol{C}(\boldsymbol{\nu}_r)$ are given by

$$\boldsymbol{M} = \begin{bmatrix} 7.22 \cdot 10^6 & 0 & 0 \\ 0 & 1.21 \cdot 10^7 & -3.63 \cdot 10^7 \\ 0 & -3.63 \cdot 10^7 & 4.75 \cdot 10^9 \end{bmatrix}, \quad \boldsymbol{B} = \begin{bmatrix} 1 & 0 \\ 0 & -1.13 \cdot 10^6 \\ 0 & 9.63 \cdot 10^7 \end{bmatrix},$$

$$\boldsymbol{C}(\boldsymbol{\nu}_r) = \begin{bmatrix} 0 & 0 & -1.21 \cdot 10^7 v_r + 3.63 \cdot 10^7 r \\ 0 & 0 & 7.22 \cdot 10^6 u_r \\ 1.21 \cdot 10^7 v_r - 3.63 \cdot 10^7 r & -7.22 \cdot 10^6 u_r & 0 \end{bmatrix}$$

The linear damping matrix from Fredriksen and Pettersen [63] is given by

$$\boldsymbol{D} = \begin{bmatrix} 95070 & 0 & 0 \\ 0 & 4.34 \cdot 10^6 & -2.47 \cdot 10^6 \\ 0 & -1.88 \cdot 10^7 & 7.57 \cdot 10^8 \end{bmatrix}. \tag{C.2}$$

The control input vector $\boldsymbol{f}$ is defined as $\boldsymbol{f} = [T_u, T_r]^T$ and contains the surge thrust T_u and the yaw rudder angle T_r.

C.2 Numerical Model for AUV

This section presents a simulation model for an AUV. The AUV under consideration is the light autonomous underwater vehicle (LAUV) developed at Laboratório de Sistemas e Tecnologia Subaquática (LSTS) from the electrical engineering and computer science department at the university of Porto in cooperation with the spin-off company OceanScan - Marine Systems and Technology, Lda. The model parameters are obtained from da Silva et al. [45]. An image of the LAUV can be seen in Figure C.1.

Figure C.1: Image of the LAUV.

Recall the dynamics of the model given in Section 2.3:

$$\boldsymbol{M}\dot{\boldsymbol{\nu}}_r + \boldsymbol{C}(\boldsymbol{\nu}_r)\boldsymbol{\nu}_r + \boldsymbol{D}\boldsymbol{\nu}_r + \boldsymbol{g}(\boldsymbol{\eta}) = \boldsymbol{B}\boldsymbol{f}. \tag{C.3}$$

The numerical values for the matrices $\boldsymbol{M}$, $\boldsymbol{C}(\boldsymbol{\nu}_r)$, $\boldsymbol{D}$, and $\boldsymbol{B}$ are given by

$$\boldsymbol{M} = \begin{bmatrix} 19.0 & 0 & 0 & 0 & 0 \\ 0 & 34.0 & 0 & 0 & 0 \\ 0 & 0 & 34.0 & 0 & 0 \\ 0 & 0 & 0 & 2.1 & 0 \\ 0 & 0 & 0 & 0 & 2.1 \end{bmatrix},$$

$$\boldsymbol{D} = \begin{bmatrix} 2.4 & 0 & 0 & 0 & 0 \\ 0 & 23.0 & 0 & 0 & -11.5 \\ 0 & 0 & 23.0 & 11.5 & 0 \\ 0 & 0 & -3.1 & 9.7 & 0 \\ 0 & 3.1 & 0 & 0 & 9.7 \end{bmatrix}, \quad \boldsymbol{B} = \begin{bmatrix} 1 & 0 & 0 \\ 0 & 0 & -39.8783 \\ 0 & 39.8783 & 0 \\ 0 & 18.1446 & 0 \\ 0 & 0 & 18.1446 \end{bmatrix}$$

$$\boldsymbol{C}(\boldsymbol{\nu}_r) = \begin{bmatrix} 0 & 0 & 0 & 34.0 \cdot w_r & -34.0 \cdot v_r \\ 0 & 0 & 0 & 0 & 19 \cdot u_r \\ 0 & 0 & 0 & -19.0 \cdot u_r & 0 \\ -34.0 \cdot w_r & 0 & 19.0 \cdot u_r & 0 & 0 \\ 34.0 \cdot v_r & -19.0 \cdot u_r & 0 & 0 & 0 \end{bmatrix}.$$

The gravity vector is given by $\boldsymbol{g}(\boldsymbol{\eta}) = [0, 0, 0, BG_z W \sin(\theta), 0]^T$, where $BG_z = 0.017$ [m] is the vertical distance between centre of gravity (CG) and the centre of

buoyancy (CB), and $W = mg$ is the weight of the vehicle with mass $m = 18$ [kg] and gravitational acceleration $g = 9.81$ [m/s^2]. The control input vector $\boldsymbol{f}$ is defined as $\boldsymbol{f} = [T_u, T_q, T_r]^T$ and contains the surge thrust T_u, the pitch rudder angle T_q, and the yaw rudder angle T_r.

References

[1] A. P. Aguiar and J. P. Hespanha. Trajectory-tracking and path-following of underactuated autonomous vehicles with parametric modeling uncertainty. *IEEE Transactions on Automatic Control*, 52(8):1362–1379, 2007.

[2] A. P. Aguiar and A. M. Pascoal. Dynamic positioning and way-point tracking of underactuated AUVs in the presence of ocean currents. *International Journal of Control*, 80(7):1092–1108, 2007.

[3] A. A. Aguirre. *Remote Control and Motion Coordination of Mobile Robots*. PhD thesis, Technische Universiteit Eindhoven, 2011.

[4] J. Almeida, C. Silvestre, and A. Pascoal. Cooperative control of multiple surface vessels in the presence of ocean currents and parametric model uncertainty. *International Journal of Robust and Nonlinear Control*, 20(14): 1549–1565, 2010.

[5] D. Angeli and E. D. Sontag. Forward completeness, unboundedness observability, and their lyapunov characterizations. *Systems & Control Letters*, 38 (4):209–217, 1999.

[6] D. Angeli, E. D. Sontag, and Y. Wang. A characterization of integral input-to-state stability. *IEEE Transactions on Automatic Control*, 45(6):1082–1097, 2000.

[7] S. Aranovskiy and A. Bobtsov. Output harmonic disturbance compensation for nonlinear plant. In *20th Mediterranean Conference on Control & Automation (MED)*, pages 386–391. IEEE, 2012.

[8] S. V. Aranovskiy, A. A. Bobtsov, A. S. Kremlev, and G. V. Luk'yanova. A robust algorithm for identification of the frequency of a sinusoidal signal. *Journal of Computer and Systems Sciences International*, 46(3):371–376, 2007.

[9] F. Arrichiello, S. Chiaverini, and T. I. Fossen. Formation control of marine surface vessels using the null-space-based behavioral control. In *Group coordination and cooperative control*, pages 1–19. Springer, 2006.

[10] H. Bai, M. Arcak, and J. T. Wen. *Cooperative control design*, volume 89. Springer, 2011.

[11] T. Balch and R. C. Arkin. Behavior-based formation control for multirobot teams. *IEEE Transactions on Robotics and Automation*, 14(6):926–939, 1998.

[12] R. W. Beard, J. Lawton, and F. Y. Hadaegh. A coordination architecture for spacecraft formation control. *IEEE Transactions on Control Systems Technology*, 9(6):777–790, 2001.

[13] D. J. W. Belleter and K. Y. Pettersen. Path following for formations of underactuated marine vessels under influence of constant ocean currents. In *Proceedings of the 53th IEEE Conference on Decision and Control, Los Angeles, USA, Dec. 15-17*, pages 4521–4528, 2014.

[14] D. J. W. Belleter and K. Y. Pettersen. 3D coordinated path following with disturbance rejection for formations of under-actuated agents. In *54th IEEE Conference on Decision and Control (CDC)*, pages 1040–1047. IEEE, 2015.

[15] D. J. W. Belleter and K. Y. Pettersen. Path following with disturbance rejection for inhomogeneous formations with underactuated agents. In *European Control Conference (ECC), Linz, Austria*, pages 1023–1030. IEEE, 2015.

[16] D. J. W. Belleter and K. Y. Pettersen. Underactuated leader-follower synchronisation for multi-agent systems with rejection of unknown disturbances. In *American Control Conference (ACC), Chicago, USA*, pages 3094–3100, 2015.

[17] D. J. W. Belleter and K. Y. Pettersen. Leader-follower synchronisation for a class of underactuated systems. In N. van de Wouw, E. Lefeber, and I. Lopez Arteaga, editors, *Nonlinear Systems*, chapter 8, pages 157–179. Springer, 2017.

[18] D. J. W. Belleter, D. A. Breu, T. I. Fossen, and H. Nijmeijer. Nonlinear observer design for parametric roll resonance. In *Proceedings of the 11th International Conference on the Stability of Ships and Ocean Vehicles*, pages 699–705, 2012.

[19] D. J. W. Belleter, D. A. Breu, T. I. Fossen, and H. Nijmeijer. A globally K-exponentially stable nonlinear observer for the wave encounter frequency. *IFAC Proceedings Volumes, Presented at: 9th IFAC Conference on Control Applications in Marine Systems*, 46(33):209–214, 2013.

[20] D. J. W. Belleter, R. Galeazzi, and T. I. Fossen. Experimental verification of a global exponential stable nonlinear wave encounter frequency estimator. *Ocean Engineering*, 97:48–56, 2015.

[21] D. J. W. Belleter, J. Braga, and K. Y. Pettersen. Experimental verification of a coordinated path following strategy for underactuated marine vehicles. *To be submitted to Elsevier Ocean Engineering*, 2016.

[22] D. J. W. Belleter, M. Maghenem, C. Paliotta, and K. Y. Pettersen. Observer based path following for underactuated marine vessels in the presence of ocean currents: a global approach. *To be submitted to IEEE Transactions of Control Systems Technology*, 2016.

[23] D. J. W. Belleter, C. Paliotta, M. Maggiore, and K. Y. Pettersen. Path following for underactuated marine vessels. In *10th IFAC Symposium on Nonlinear Control Systems (NOLCOS), To Appear*. IFAC, 2016.

[24] A. A. Bobtsov. New approach to the problem of globally convergent frequency estimator. *International Journal of Adaptive Control and Signal Processing*, 22(3):306–317, 2008.

[25] M. Bodson and S. C. Douglas. Adaptive algorithms for the rejection of sinusoidal disturbances with unknown frequency. *Automatica*, 33(12):2213–2221, 1997.

[26] E. Børhaug. *Nonlinear Control and Synchronisation of Mechanical Systems*. PhD thesis, Norwegian University of Science and Technology, 2008.

[27] E. Børhaug and K. Y. Pettersen. Los path following for underactuated underwater vehicle. *Proceedings of the 7th IFAC Conference on Manoeuvering and Control of Marine Craft MCMC, Lisbon, Portugal*, 2006.

[28] E. Børhaug, A. Pavlov, and K. Y. Pettersen. Cross-track formation control of underactuated surface vehicles. In *Proceedings of the 45th IEEE Conference on Decision and Control*, pages 5955–5961, 2006.

[29] E. Børhaug, A. Pavlov, and K. Y. Pettersen. Straight line path following for formations of underactuated underwater vehicles. In *Proceedings of the 46th IEEE Conference on Decision and Control*, pages 2905–2912, 2007.

[30] E. Børhaug, A. Pavlov, and K. Y. Pettersen. Integral LOS control for path following of underactuated marine surface vessels in the presence of ocean currents. In *Proceedings of the 47th IEEE Conference on Decision and Control*, pages 4984–4991, 2008.

[31] E. Børhaug, A. Pavlov, E. Panteley, and K. Y. Pettersen. Straight line path following for formations of underactuated marine surface vessels. *IEEE Transactions on Control Systems Technology*, 19(3):493–506, 2011.

[32] M. Breivik and T. I. Fossen. Path following of straight lines and circles for marine surface vessels. *Proceeding of the 6th IFAC Control Applications in Marine Systems*, 2004.

[33] M. Breivik and T. I. Fossen. Guidance-based path following for autonomous underwater vehicles. In *Proceedings of OCEANS 2005 MTS/IEEE*, pages 2807–2814. IEEE, 2005.

[34] M. Breivik and T. I. Fossen. Principles of guidance-based path following in 2d and 3d. In *Proceedings of the 44th IEEE Conference on Decision and Control*, pages 627–634. IEEE, 2005.

[35] M. Breivik and T. I. Fossen. Guidance laws for planar motion control. In *Proceedings of the 47th IEEE Conference on Decision and Control, Cancun, Mexico*, pages 570–577, 2008.

[36] M. Breivik, V. E. Hovstein, and T. I. Fossen. Ship formation control: A guided leader-follower approach. *IFAC Proceedings Volumes*, 41(2):16008–16014, 2008.

[37] M. Breivik, V. E. Hovstein, and T. I. Fossen. Straight-line target tracking for unmanned surface vehicles. *Modeling Identification and Control*, 29(4): 131–149, 2008.

[38] M. Burger, A. Pavlov, E. Borhaug, and K. Y. Pettersen. Straight line path following for formations of underactuated surface vessels under influence of constant ocean currents. In *Proceedings of the American Control Conference*, pages 3065–3070, 2009.

[39] W. Caharija. *Integral Line-of-Sight Guidance and Control of Underactuated Marine Vehicles*. PhD thesis, Norwegian University of Science and Technology, 2014.

[40] W. Caharija, M. Candeloro, K. Y. Pettersen, and A. J. Sørensen. Relative velocity control and integral los for path following of underactuated surface vessels. In *Proceedings of the 9th IFAC Conference on Manoeuvring and Control of Marine Craft*, 2012.

[41] W. Caharija, K. Y. Pettersen, J. T. Gravdahl, and E. Børhaug. Path following of underactuated autonomous underwater vehicles in the presence of ocean currents. In *Proceedings of the 51th IEEE Conference on Decision and Control*, pages 528–535, 2012.

[42] W. Caharija, K. Y. Pettersen, A. J. Sørensen, M. Candeloro, and J. T. Gravdahl. Relative velocity control and integral line of sight for path following of autonomous surface vessels: Merging intuition with theory. *Proceedings of the Institution of Mechanical Engineers, Part M: Journal of Engineering for the Maritime Environment*, 228(2):180–191, 2014.

[43] W. Caharija, K. Y. Pettersen, M. Bibuli, P. Calado, E. Zereik, J. Braga, J. T. Gravdahl, A. J. Sørensen, M. Milovanović, and G. Bruzzone. Integral line-of-sight guidance and control of underactuated marine vehicles: Theory, simulations and experiments. *IEEE Transactions on Control Systems Technology*, 24(5):1623–1642, 2016.

[44] Y. Q. Chen and Z. Wang. Formation control: a review and a new consideration. In *2005 IEEE/RSJ International Conference on Intelligent Robots and Systems*, pages 3181–3186, 2005.

[45] J. E. da Silva, B. Terra, R. Martins, and J. B. de Sousa. Modeling and simulation of the lauv autonomous underwater vehicle. In *13th IEEE IFAC International Conference on Methods and Models in Automation and Robotics*, 2007.

[46] J. Dasdemir and A. Loria. Robust formation-tracking control of mobile robots via one-to-one time-varying communication. *International Journal of Control*, pages 1–17, 2014. doi: 10.1080/00207179.2014.889856.

[47] J. P. Desai, J. Ostrowski, and V. Kumar. Controlling formations of multiple mobile robots. In *Proceedings of the 1998 IEEE International Conference on Robotics and Automation*, volume 4, pages 2864–2869. IEEE, 1998.

[48] J. P. Desai, J. P. Ostrowski, and V. Kumar. Modeling and control of formations of nonholonomic mobile robots. *IEEE Transactions on Robotics and Automation*, 17(6):905–908, 2001.

[49] K. D. Do and J. Pan. State-and output-feedback robust path-following controllers for underactuated ships using serret–frenet frame. *Ocean Engineering*, 31(5):587–613, 2004.

[50] K. D. Do and J. Pan. Global tracking control of underactuated ships with nonzero off-diagonal terms in their system matrices. *Automatica*, 41(1):87–95, 2005.

[51] K. D. Do and J. Pan. Global robust adaptive path following of underactuated ships. *Automatica*, 42(10):1713–1722, 2006.

[52] K. D. Do and J. Pan. Nonlinear formation control of unicycle-type mobile robots. *Robotics and Autonomous Systems*, 55(3):191–204, 2007.

[53] K. D. Do, Z.-P. Jiang, and J. Pan. Underactuated ship global tracking under relaxed conditions. *IEEE Transactions on Automatic Control*, 47(9):1529–1536, 2002.

[54] K. D. Do, Z.-P. Jiang, and J. Pan. Universal controllers for stabilization and tracking of underactuated ships. *Systems & Control Letters*, 47(4):299–317, 2002.

[55] M. I. El-Hawwary and M. Maggiore. Reduction theorems for stability of closed sets with application to backstepping control design. *Automatica*, 49 (1):214–222, 2013.

[56] P. Encarnaçao and A. Pascoal. 3d path following for autonomous underwater vehicle. In *Proceedings of the 39th IEEE Conference on Decision and Control*, 2000.

[57] P. Encarnaçao, A. Pascoal, and M. Arcak. Path following for marine vehicles in the presence of unknown currents. In *Proceedings of SYROCO 6th IFAC Symposium on Robot Control*, pages 469–474, 2000.

[58] H. Enshaei and R. Brimingham. Monitoring dynamic stability via ship's motion responses. In *Proceedings of the 11th international conference on the stability of ships and ocean vehicles*, pages 707–717, 2012.

[59] T. Fossen, M. Breivik, and R. Skjetne. Line-of-sight paht following of underactuated marine craft. In *Proceedings of the 6th IFAC Conference on Manoeuvering and Control of Marine Craft*, pages 244–249, 2003.

[60] T. I. Fossen. *Handbook of Marine Craft Hydrodynamics and Motion Control.* Wiley, 2011.

[61] T. I. Fossen and J. P. Strand. Passive nonlinear observer design for ships using lyapunov methods: full-scale experiments with a supply vessel. *Automatica*, 35(1):3–16, 1999.

[62] T. I. Fossen, S. I. Sagatun, and A. J. Sørensen. Identification of dynamically positioned ships. *Control Engineering Practice*, 4(3):369–376, 1996.

[63] E. Fredriksen and K. Y. Pettersen. Global κ-exponential way-point manoeuvering of ships. In *Proceeding of the 43rd IEEE Conference on Decision and Control (CDC)*, volume 5, pages 5360–5367. IEEE, 2004.

[64] E. Fredriksen and K. Y. Pettersen. Global κ-exponential way-point maneuvering of ships: Theory and experiments. *Automatica*, 42(4):677–687, 2006.

[65] S. H. Fu and W. M. Haddad. Nonlinear adaptive tracking of surface vessels with exogenous disturbances. *Asian Journal of Control*, 5(1):88–103, 2003.

[66] R. Ghabcheloo, A. P. Aguiar, A. Pascoal, C. Silvestre, I. Kaminer, and J. Hespanha. Coordinated path-following control of multiple underactuated autonomous vehicles in the presence of communication failures. In *Proceedings of the 45th IEEE Conference on Decision and Control*, pages 4345–4350, 2006.

[67] R. Ghabcheloo, A. P. Aguiar, A. Pascoal, C. Silvestre, I. Kaminer, and J. Hespanha. Coordinated path-following in the presence of communication losses and time delays. *SIAM Journal on Control and Optimization*, 48(1):234–265, 2009.

[68] C. Godcil and G. Royle. Algebraic graph theory. *Series Springer Graduate Texts in Mathematics*, 207, 2001.

[69] V. Hassani, A. J. Sørensen, and A. M. Pascoal. A novel methodology for robust dynamic positioning of marine vessels: Theory and experiments. In *American Control Conference (ACC)*, pages 560–565. IEEE, 2013.

[70] C. Holden, R. Galeazzi, C. Rodríguez, T. Perez, T. I. Fossen, M. Blanke, and M. de Almeida Santos Neves. Nonlinear container ship model for the study of parametric roll resonance. *Modeling, Identification and Control*, 28 (4):87–103, 2007.

[71] M. Hou. Parameter identification of sinusoids. *IEEE Transactions on Automatic Control*, 57(2):467–472, 2012.

[72] L. Hsu, R. Ortega, and G. Damm. A globally convergent frequency estimator. *IEEE Transactions on Automatic Control*, 44(4):698–713, 1999.

[73] I.-A. F. Ihle, R. Skjetne, and T. I. Fossen. Nonlinear formation control of marine craft with experimental results. In *Proceeding of the 43rd IEEE Conference on Decision and Control*, volume 1, pages 680–685. IEEE, 2004.

[74] I.-A. F. Ihle, R. Skjetne, and T. I. Fossen. Output feedback control for maneuvering systems using observer backstepping. In *Proceedings of the 2005 IEEE International Symposium on, Mediterrean Conference on Control and Automation Intelligent Control, 2005.*, pages 1512–1517. IEEE, 2005.

[75] I.-A. F. Ihle, J. Jouffroy, and T. I. Fossen. Formation control of marine surface craft: A lagrangian approach. *IEEE Journal of Oceanic Engineering*, 31(4):922–934, 2006.

[76] I.-A. F. Ihle, M. Arcak, and T. I. Fossen. Passivity-based designs for synchronized path-following. *Automatica*, 43(9):1508–1518, 2007.

[77] T. Iseki and K. Ohtsu. Bayesian estimation of directional wave spectra based on ship motions. *Control Engineering Practice*, 8(2):215–219, 2000.

[78] A. Jadbabaie, J. Lin, and A. S. Morse. Coordination of groups of mobile autonomous agents using nearest neighbor rules. *IEEE Transactions on Automatic Control*, 48(6):988–1001, 2003.

[79] Z.-P. Jiang. Global tracking control of underactuated ships by lyapunov's direct method. *Automatica*, 38(2):301–309, 2002.

[80] Z.-P. Jiang and H. Nijmeijer. A recursive technique for tracking control of nonholonomic systems in chained form. *IEEE Transactions on Automatic control*, 44(2):265–279, 1999.

[81] B.-H. Jun, J.-Y. Park, F.-Y. Lee, P.-M. Lee, C.-M. Lee, K. Kim, Y.-K. Lim, and J.-H. Oh. Development of the auv 'isimi'and a free running test in an ocean engineering basin. *Ocean Engineering*, 36(1):2–14, 2009.

[82] H. Khalil. *Nonlinear Systems*. Prentice Hall, 2002.

[83] V. Kumar, N. Leonard, and A. Morse. *Cooperative Control*. Springer-Verlag, 2005.

[84] E. Kyrkjebø. *Motion Coordination of Mechanical Systems*. PhD thesis, Norwegian University of Science and Technology, 2007.

[85] E. Kyrkjebø, K. Y. Pettersen, M. Wondergem, and H. Nijmeijer. Output synchronization control of ship replenishment operations: Theory and experiments. *Control Engineering Practice*, 15(6):741–755, 2007.

[86] L. Lapierre and D. Soetanto. Nonlinear path-following control of an AUV. *Ocean Engineering*, 34(11):1734–1744, 2007.

[87] L. Lapierre, D. Soetanto, and A. Pascoal. Nonlinear path following with applications to the control of autonomous underwater vehicles. In *Proceedings of the 42nd IEEE Conference on Decision and Control (CDC)*, volume 2, pages 1256–1261. IEEE, 2003.

[88] L. Lapierre, D. Soetanto, and A. Pascoal. Coordinated motion control of marine robots. In *Proceedings of the 6th IFAC Conference on Manoeuvering and Control of Marine Craft*, 2004.

[89] E. Lefeber, K. Y. Pettersen, and H. Nijmeijer. Tracking control of an underactuated ship. *IEEE Transactions on Control Systems Technology*, 11(1): 52–61, 2003.

[90] M. A. Lewis and K.-H. Tan. High precision formation control of mobile robots using virtual structures. *Autonomous Robots*, 4(4):387–403, 1997.

[91] Z. Lin, B. Francis, and M. Maggiore. Necessary and sufficient graphical conditions for formation control of unicycles. *IEEE Transactions on Automatic Control*, 50(1):121–127, 2005.

[92] Z. Lin, B. Francis, and M. Maggiore. State agreement for continuous-time coupled nonlinear systems. *SIAM Journal on Control and Optimization*, 46 (1):288–307, 2007.

[93] A. Loría. From feedback to cascade-interconnected systems: Breaking the loop. In *Proceedings of the 47th IEEE Conference on Decision and Control (CDC)*, pages 4109–4114. IEEE, 2008.

[94] A. Loría and E. Panteley. Cascaded nonlinear time-varying systems: Analysis and design. In *Advanced topics in control systems theory*, pages 23–64. Springer, 2004.

[95] A. Loría and E. Panteley. Cascaded nonlinear time-varying systems: Analysis and design. In *Advanced topics in control systems theory*, pages 23–64. Springer, 2005.

[96] M. Maghenem, D. J. W. Belleter, C. Paliotta, and K. Y. Pettersen. Observer based path following for underactuated marine vessels in the presence of ocean currents: a local approach. *Submitted to IFAC world congress*, 2017.

[97] R. Marino and P. Tomei. Global estimation of n unknown frequencies. *IEEE Transactions on Automatic Control*, 47(8):1324–1328, 2002.

[98] M. Mesbahi and M. Egerstedt. *Graph theoretic methods in multiagent networks*. Princeton University Press, 2010.

[99] A. Micaelli and C. Samson. *Trajectory tracking for unicycle-type and two-steering-wheels mobile robots*. PhD thesis, INRIA, 1993.

[100] S. Moe, W. Caharija, K. Y. Pettersen, and I. Schjølberg. Path following of underactuated marine surface vessels in the presence of unknown ocean currents. In *American Control Conference (ACC)*, pages 3856–3861. IEEE, 2014.

[101] L. Moreau. Stability of continuous-time distributed consensus algorithms. In *Proceedings of the 43rd IEEE Conference on Decision and Control (CDC)*, volume 4, pages 3998–4003. IEEE, 2004.

[102] L. Moreau. Stability of multiagent systems with time-dependent communication links. *IEEE Transactions on Automatic Control*, 50(2):169–182, 2005.

[103] K. Narendra and A. Annaswamy. A new adaptive law for robust adaptation without persistent excitation. *IEEE Transactions on Automatic control*, 32 (2):134–145, 1987.

[104] C. Nielsen, C. Fulford, and M. Maggiore. Path following using transverse feedback linearization: Application to a maglev positioning system. *Automatica*, 46(3):585–590, 2010.

[105] U. D. Nielsen. Estimations of on-site directional wave spectra from measured ship responses. *Marine Structures*, 19(1):33–69, 2006.

[106] H. Nijmeijer and A. Rodriguez-Angeles. *Synchronization of mechanical systems*. World Scientific, 2003.

[107] V. O. Nikiforov. Adaptive servomechanism controller with an implicit reference model. *International Journal of Control*, 68(2):277–286, 1997.

[108] K.-K. Oh, M.-C. Park, and H.-S. Ahn. A survey of multi-agent formation control. *Automatica*, 53:424–440, 2015.

[109] R. Olfati-Saber. Flocking for multi-agent dynamic systems: Algorithms and theory. *IEEE Transactions on Automatic Control*, 51(3):401–420, 2006.

[110] C. Paliotta, D. J. W. Belleter, and K. Y. Pettersen. Adaptive source seeking with leader-follower formation control. *IFAC-PapersOnLine, Presented at: 10th IFAC Conference on Manoeuvring and Control of Marine Craft*, 48(16): 285–290, 2015.

[111] E. Panteley and A. Loría. On global uniform asymptotic stability of nonlinear time-varying systems in cascade. *Systems & Control Letters*, 33(2):131–138, 1998.

[112] E. Panteley and A. LorıA. Growth rate conditions for uniform asymptotic stability of cascaded time-varying systems. *Automatica*, 37(3):453–460, 2001.

[113] E. Panteley, E. Lefeber, A. Loría, and H. Nijmeijer. Exponential tracking control of a mobile car using a cascaded approach. In *Proceedings of the IFAC workshop on motion control*, pages 221–226. Grenoble, France Grenoble, France, 1998.

[114] Z. Peng, D. Wang, Z. Chen, X. Hu, and W. Lan. Adaptive dynamic surface control for formations of autonomous surface vehicles with uncertain dynamics. *IEEE Transactions on Control Systems Technology*, 21(2):513–520, 2013.

[115] K. Y. Pettersen and H. Nijmeijer. Tracking control of an underactuated surface vessel. In *Proceedings of the 37th IEEE Conference on Decision and Control*, volume 4, pages 4561–4566. IEEE, 1998.

[116] K. Y. Pettersen and H. Nijmeijer. Underactuated ship tracking control: theory and experiments. *International Journal of Control*, 74(14):1435–1446, 2001.

[117] K. Y. Pettersen, J. T. Gravdahl, and H. Nijmeijer. *Group coordination and cooperative control*, volume 336. Springer Berlin, 2006.

[118] H. A. Poonawala, A. C. Satici, and M. W. Spong. Leader-follower formation control of nonholonomic wheeled mobile robots using only position measurements. In *Proceedings of the 9th Asian Control Conference (ASCC), Istanbul, Turkey*, pages 1–6, June 2013. doi: 10.1109/ASCC.2013.6606313.

[119] P. A. Regalia. An improved lattice-based adaptive iir notch filter. *IEEE Transactions on signal processing*, 39(9):2124–2128, 1991.

[120] W. Ren and R. Beard. Decentralized scheme for spacecraft formation flying via the virtual structure approach. *Journal of Guidance, Control, and Dynamics*, 27(1):73–82, 2004.

[121] W. Ren, R. W. Beard, and E. M. Atkins. A survey of consensus problems in multi-agent coordination. In *Proceedings of the American Control Conference*, pages 1859–1864. IEEE, 2005.

[122] C. W. Reynolds. Flocks, herds and schools: A distributed behavioral model. *ACM SIGGRAPH computer graphics*, 21(4):25–34, 1987.

[123] A. Roza and M. Maggiore. A class of position controllers for underactuated VTOL vehicles. *IEEE Transactions on Automatic Control*, 59(9):2580–2585, 2014.

[124] C. Samson. Path following and time-varying feedback stabilization of a wheeled mobile robot. In *Proceedings of the International Conference on Control, Automation, Robotics and Vision*, 1992.

[125] R. Skejic, M. Breivik, T. I. Fossen, and O. Faltinsen. Modeling and control of underway replenishment operations in calm water. In *Proceedings of the 8th IFAC Conference on Manoeuvring and Control of Marine Craft, Guarujá, Brazil*, pages 78–85, 2009.

[126] R. Skjetne, T. I. Fossen, and P. Kokotović. Output maneuvering for a class of nonlinear systems. *IFAC Proceedings Volumes*, 35(1):501–506, 2002.

[127] R. Skjetne, S. Moi, and T. I. Fossen. Nonlinear formation control of marine craft. In *Proceedings of the 41st IEEE Conference on Decision and Control*, volume 2, pages 1699–1704. IEEE, 2002.

[128] R. Skjetne, T. I. Fossen, and P. V. Kokotović. Robust output maneuvering for a class of nonlinear systems. *Automatica*, 40(3):373–383, 2004.

[129] R. Skjetne, T. I. Fossen, and P. V. Kokotović. Adaptive maneuvering, with experiments, for a model ship in a marine control laboratory. *Automatica*, 41(2):289–298, 2005.

[130] D. Soetanto, L. Lapierre, and A. Pascoal. Adaptive, non-singular path-following control of dynamic wheeled robots. In *42nd IEEE Conference on Decision and Control*, volume 2, pages 1765–1770. IEEE, 2003.

[131] A. J. Sørensen. Structural issues in the design and operation of marine control systems. *Annual Reviews in Control*, 29(1):125–149, 2005.

[132] D. M. Stipanović, G. Inalhan, R. Teo, and C. J. Tomlin. Decentralized overlapping control of a formation of unmanned aerial vehicles. *Automatica*, 40 (8):1285–1296, 2004.

[133] A. Stotsky. Frequency determination in control applications: excitation-based approach. *Proceedings of the Institution of Mechanical Engineers, Part I: Journal of Systems and Control Engineering*, 226(8):1142–1148, 2012.

[134] K.-H. Tan and M. A. Lewis. Virtual structures for high-precision cooperative mobile robotic control. In *Proceedings of the 1996 IEEE/RSJ International Conference on Intelligent Robots and Systems', IROS 96*, volume 1, pages 132–139. IEEE, 1996.

[135] H. G. Tanner, A. Jadbabaie, and G. J. Pappas. Flocking in fixed and switching networks. *IEEE Transactions on Automatic Control*, 52(5):863–868, 2007.

[136] E. A. Tannuri, J. V. Sparano, A. N. Simos, and J. J. Da Cruz. Estimating directional wave spectrum based on stationary ship motion measurements. *Applied Ocean Research*, 25(5):243–261, 2003.

[137] T. Vicsek, A. Czirók, E. Ben-Jacob, I. Cohen, and O. Shochet. Novel type of phase transition in a system of self-driven particles. *Physical Review Letters*, 75(6):1226, 1995.

[138] X. Xia. Global frequency estimation using adaptive identifiers. *IEEE Transactions on Automatic Control*, 47(7):1188–1193, 2002.

[139] B. J. Young, R. W. Beard, and J. M. Kelsey. A control scheme for improving multi-vehicle formation maneuvers. In *Proceedings of the American Control Conference*, volume 2, pages 704–709. IEEE, 2001.